

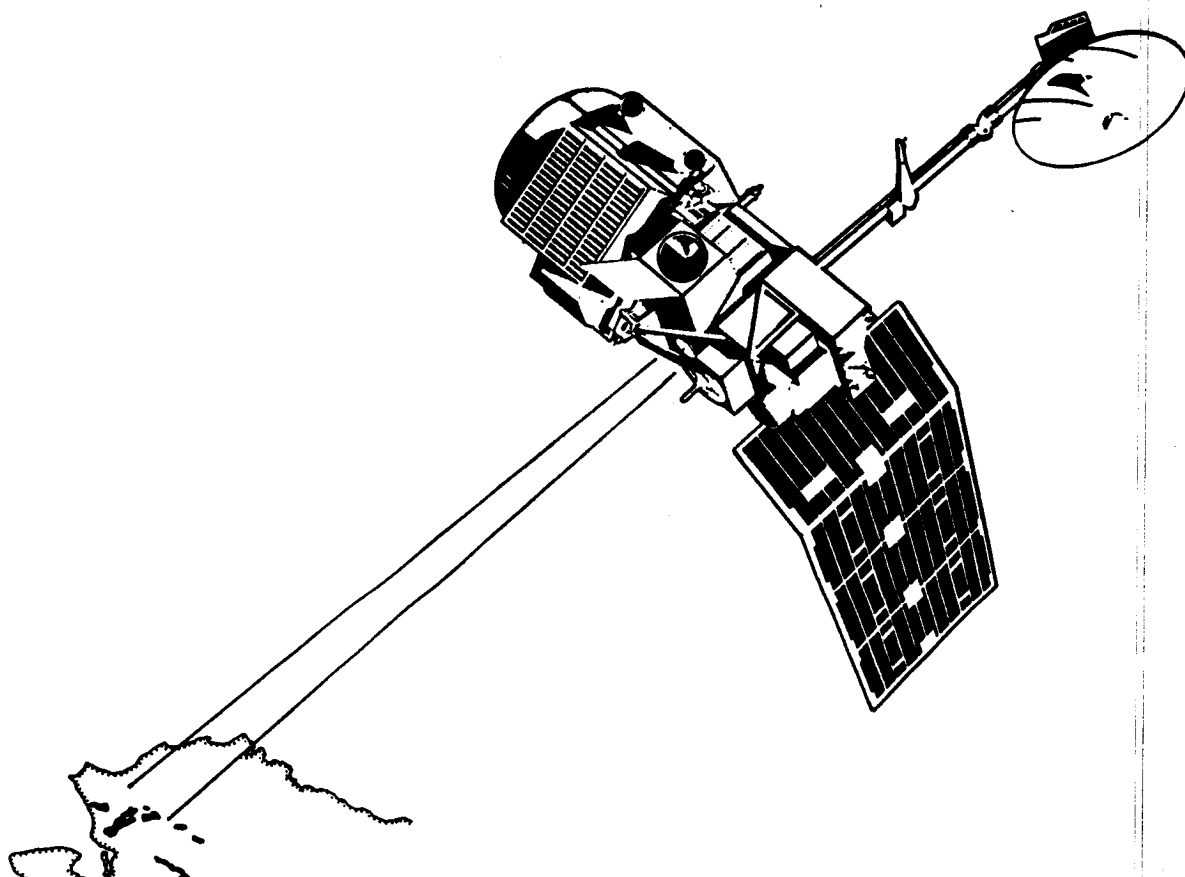
Thematic Mapper Study of Alaskan Ophiolites

Final Report ✓

to the

National Aeronautics and Space Administration

Contract NAS5-28739



(NASA-CR-182554) THEMATIC MAPPER STUDY OF
ALASKAN OPHIOLITES Final Report (Cornell
Univ.) 296 p CSCI 08G

N88-18584

Unclas
G3/43 0128283

Cornell University
February 1988

Thematic Mapper Study of Alaskan Ophiolites

Final Report
to the
National Aeronautics and Space Administration
Contract NAS5-28739

Department of Geological Sciences
Snee Hall
Cornell University
Ithaca, New York 14853

Principal Investigator: John M. Bird

24 February 1988

Preface

This document is the final report for "Thematic Mapper Study of Alaskan Ophiolites", NASA research project NAS5-28739, that was conducted from 26 July 1985 to 1 November 1987. The project was administered by Cornell University, and the Cornell University Department of Geological Sciences. The following Cornell personnel participated on the project:

John M. Bird	Professor of Geology, P.I.
David J. Harding	Graduate Research Assistant
Karl R. Wirth	Graduate Research Assistant
Ann E. Blythe	Graduate Research Assistant
Deborah H. Shelton	Field Assistant
Jan Zender-Romick	Field Assistant

Many people have assisted our work on this project. We especially thank Vincent Salomonson, Harold Oseroff, Locke Stuart, John Barker, and Maria Mackie of the NASA Goddard Space Flight Center for providing essential support. We also thank the following people for information, field logistics and analytical work: Irving Tailleux, Inyo Ellersieck, John Pallister, and David Barnes of the United States Geological Survey, Paul Hartel, Ray Bain, Kate Roney, and Jim Pepper, of the United States Park Service, Roy McMichael and Tim O'Toole of Cominco, Inc., Tom Eggert, Chris Meisling, and Peter Barker of ARCO Alaska, Inc., and Mark Harrison and Mat Heizler of the State University of New York at Albany. Additional graduate student support for work incorporated in this NASA project was provided by the Geological Society of America, the American Association of Petroleum Geologists, the Society of Sigma Xi, the NASA Graduate Student Researchers Program, and the Graduate School of Cornell University.

Table of Contents

	page
Preface	i
 Landsat Thematic Mapper Studies	 1-84
Introduction	1
Method for Mapping from Thematic Mapper Images	12
Spectral Variations	16
Maps of the Ophiolite Exposures	36
Gravity Modelling of Western Brooks Range Ophiolites	72
 Manuscripts in Preparation, sections A-E	
A. Recognition of Hydrothermal Metamorphism and Alteration of Basalts in the Brooks Range, Alaska, Using Landsat Thematic Mapper Data	 A1-A14
B. Geology and Geochemistry of Mafic Volcanic Rocks, Western Brooks Range Alaska	 B1-B35
C. Ophiolite Crystallization, Thrusting, and Uplift, Western Brooks Range, Alaska	 C1-C61
D. Regional Cross-Section of the Eastern Brooks Range, Northern Alaska	 D1-D12
E. Analysis of Digital Aeromagnetic and Topographic Data from the Josephine Peridotite, Southwestern Oregon	 E1-E24
 Appendices, sections I-IV	
A. Appendix I - TM data received at Cornell University -- NASA project NAS5-28739	 I1-I2
B. Appendix II - 1985 Field Studies and Rock Samples Collected	 II-1, II-1b, II-2 to II-17
C. Appendix III - 1987 Field Studies and Rock Samples Collected	 III-1, III-1b, III-1c, III-2 to III-17
D. Appendix IV - Publications, Meetings Attended	IV-1 to IV-3
 References Cited, section R	 R1-R12

Landsat Thematic Mapper Studies

Introduction

The two principle objectives of the project Thematic Mapper Study of Alaskan Ophiolites were to further develop techniques for producing geologic maps from Landsat Thematic Mapper data, and to study the tectonics of the ophiolite terrains of the Brooks Range and Ruby Geanticline, northern Alaska. Ophiolites, sections of oceanic lithosphere tectonically emplaced along island arcs and continental margins, are important to the understanding of mountain belt evolution. Ophiolites also provide an opportunity to study the structural, lithologic, and geochemical characteristics of oceanic lithosphere, yielding a better understanding of the processes that form lithosphere. We proposed the following to be reasonable expectations for this NASA project:

- 1) an efficient and reliable production of accurate geologic maps from Thematic Mapper data that discriminate the major rock-types and structures of the ophiolites,
- 2) improved regional lithologic and structural maps of the Brooks Range - Ruby Geanticline region,
- 3) an improved understanding of the three-dimensional character of the crust provided by combining TM images with gravity, magnetic and seismic reflection data,
- 4) recognition of regional structural features and fabrics visible only with high resolution, synoptic satellite images, and
- 5) recognition of key localities for more detailed field study of the ophiolites and regional tectonics.

Our expectations evolved and were modified as the project proceeded. The major use of the TM data was directed toward mapping the ophiolite exposures in the greatest detail possible, in combination with field mapping and sampling that provided "ground truth" to guide our interpretation of the images. Rock units were differentiated on the basis of spectral differences, and structures that effect the spatial distribution of the ophiolitic rocks were identified. Our mapping was concentrated on the large and well-exposed ophiolites of the western Brooks Range; ophiolites of the eastern Brooks Range and Ruby Geanticline are poorly exposed and cannot be as effectively mapped using remote sensing data. Regional lithologic and structural mapping was not extensively pursued because, logistically, it proved to be unrealistic for us to attempt to improve upon the existing mapping, available for most of the Brooks Range at a scale of 1:250,000, primarily because detailed knowledge of local stratigraphies and structures is required to accurately interpret the TM images. Rather than assuming an untenable task of understanding all aspects of northern Alaskan geology, we concentrated our work on the ophiolites of the Brooks Range. An integrated study of the ophiolites was pursued by combining the TM mapping with other techniques, including gravity modelling of their subsurface geometries, radiometric age dating, and geochemical analyses.

The first part of this report is a description of the methods and results of the TM mapping and gravity modelling. The second part of the report includes papers, being prepared for publication, that are either completed or are nearing completion. These papers are: 1) an analysis of basalt spectral

variations (Harding and Bird), 2) a study of basalt geochemical variations (Wirth, Bird, and Harding), 3) an examination of the cooling history of the ophiolites using radiometric age data (Wirth, Bird, and Harding), 4) an analysis of shortening produced by thrusting during the Brooks Range orogeny (Blythe and Bird), and 5) a study of an ophiolite using digital aeromagnetic and topographic data (Harding and Bird). Additional papers on our Thematic Mapper work, and the gravity modelling, are being prepared as our research continues. Appendices are included in the report that list TM data received, samples collected in the field, published abstracts and papers, and meetings attended.

Ophiolites of the Western Brooks Range

The term ophiolite (GSA Penrose Conference definition, Anonymous, 1972) refers to a distinctive assemblage of ultramafic to mafic rocks occurring in a sequence, from bottom to top, of:

- i) Ultramafic complex, consisting of variable proportions of harzburgite, lherzolite and dunite, usually with a metamorphic tectonite fabric (more or less serpentinized).
- ii) Gabbroic complex, ordinarily with cumulus textures commonly containing cumulus peridotites and pyroxenites and usually less deformed than the ultramafic complex.
- iii) Mafic sheeted dike complex.
- iv) Mafic volcanic complex, commonly pillowed.

Associated rock types include: (1) an overlying sedimentary section typically including ribbon cherts, thin shale interbeds, and minor limestones;

(2) podiform bodies of chromite generally associated with dunite; (3) sodic felsic intrusive and extrusive rocks.

In the now generally accepted model of plate tectonics, an ophiolite is considered to be an exposure of oceanic crust and upper mantle that has been tectonically emplaced into an orogenic belt. The oceanic crust is comprised of the gabbroic, mafic sheeted dike, and mafic volcanic complexes and the associated sediments. The upper mantle is comprised of the ultramafic tectonite complex. Together, the crust and upper mantle comprise a section of oceanic lithosphere.

The ophiolite exposures of northern Alaska were selected for study because the exposures are large and they have been little studied in the past. Also, northern Alaska is remote and inaccessible, and it is thus an appropriate site for utilizing remote sensing data in a geologic study. The scale of the northern Alaskan ophiolites is compared to other better known ophiolite terranes in Figure 1. The ophiolites of northern Alaska have been divided into three terranes (Figure 1), the western Brooks Range, the Angayucham Terrane, and the Rampart Belt of the Ruby Geanticline (Patton et al., 1977). The Angayucham Terrane ophiolites form a thin belt, comprised dominantly of basalt, that borders the margins of the Yukon-Koyukuk basin (Figure 2). The Angayucham Terrane ophiolites dip toward the basin, under Cretaceous sediments. The Yukon-Koyukuk Basin is thought to be floored by oceanic lithosphere that is exposed at the margins of the basin as the Angayucham Terrane. The ophiolites of the western Brooks Range and Rampart Belt are

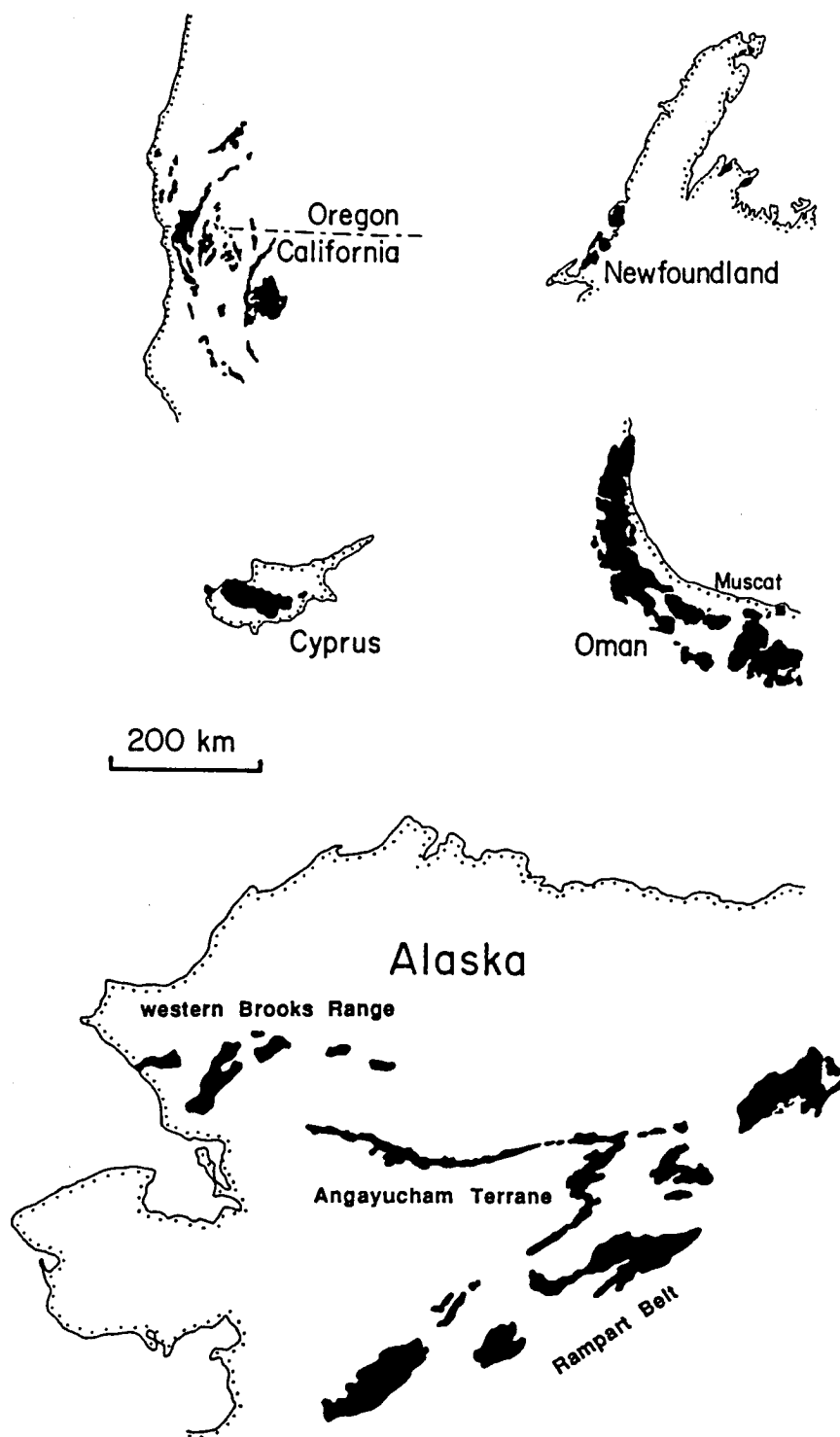


Figure 1. Distribution of ophiolites (black) in northern Alaska compared, at the same scale, to four better-known ophiolite terranes.

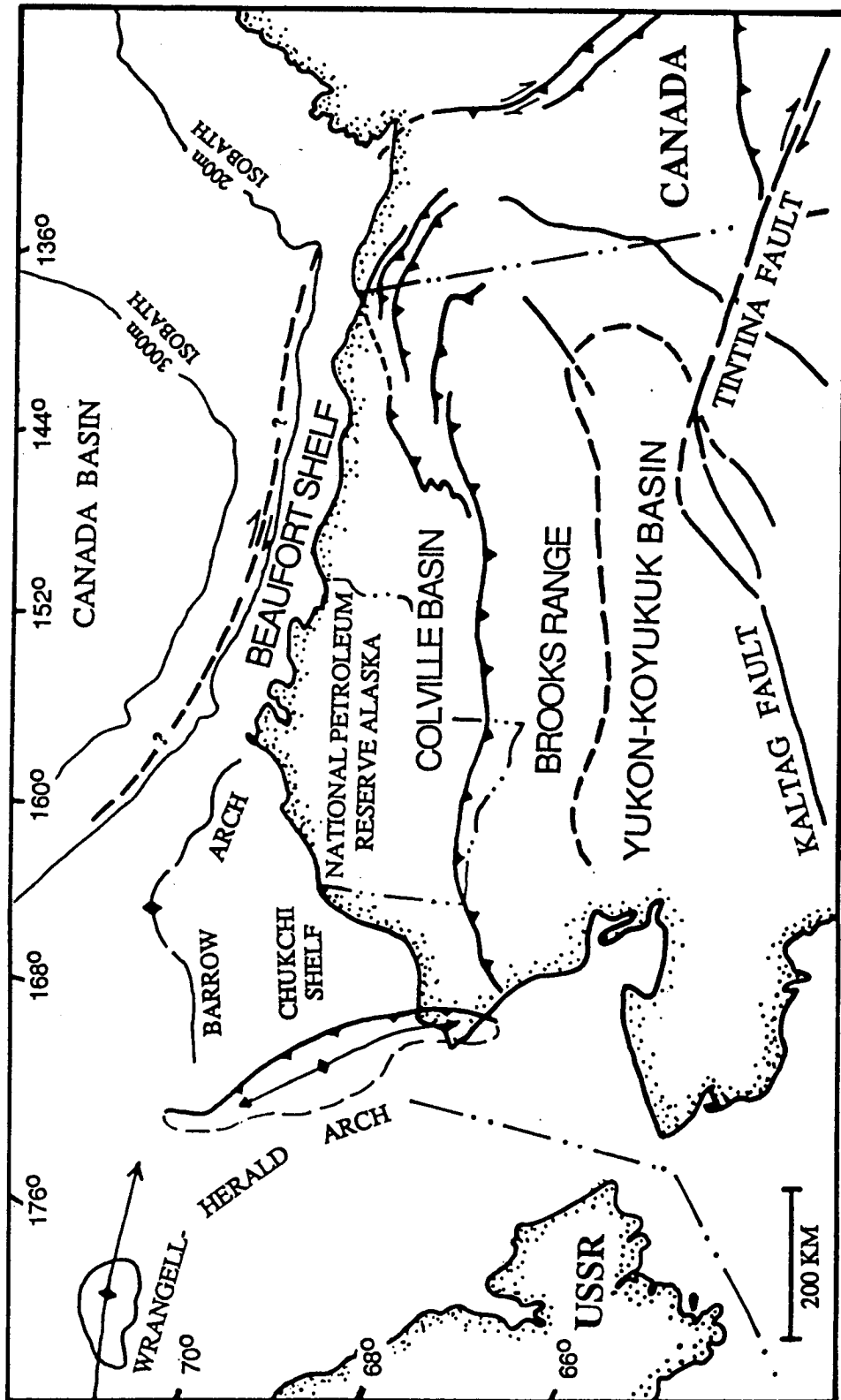


Figure 2. Arctic Alaska, reference map.

large sheets that have been thrust over continental margin sediments. It has been suggested that the western Brooks Range and Rampart Belt ophiolites are erosional remnants of very large thrust sheets that once covered the entire Brooks Range and Rampart Belt and that were continuous with the Angayucham Terrane ophiolites (Roeder and Mull, 1978).

This project emphasized study of the well-exposed western Brooks Range ophiolites. The Brooks Range is a Late Jurassic to Early Cretaceous fold and thrust belt that is thought to have been formed by subduction of a continental margin beneath the oceanic rocks now preserved in the Yukon-Koyukuk Basin. The subduction of the Australian continental lithosphere beneath the Banda arc is an active, analogous example of the origin inferred for the Brooks Range. The western Brooks Range is comprised of a stack of thrust sheets, or allochthons. The lower thrust sheets are comprised of sedimentary rocks of the continental margin, whereas the two structurally highest thrust sheets are comprised of oceanic rocks, that, together, make up the western Brooks Range ophiolites. The lower of the two oceanic-rock thrust sheets, termed the Copter Peak Allochthon, consists of mafic sheeted dikes, mafic volcanics, and minor chert, whereas the upper thrust sheet, termed the Misheguk Allochthon, consists of ultramafic and gabbroic rocks (Mayfield et al., 1973). Thus, the ophiolite stratigraphy has been disrupted and inverted by thrusting. Geochemical variations in the Copter Peak rocks (see Document B) indicate that the Copter Peak and Misheguk Allochthons are not a single section of oceanic lithosphere with its upper and lower portions inverted by thrusting, but rather that disparate pieces of oceanic lithosphere from several oceanic

sites have been juxtaposed by thrusting. Thus, the Copter Peak and Misheguk Allochthon rocks may not be petrogenetically related.

The distribution of Copter Peak and Misheguk Allochthon rocks, as mapped from TM images, is shown in Figure 3 for a part of the western Brooks Range; Figure 4 is a black-and-white mosaic of TM band 7 for the same area. Field mapping and sampling for petrographic and geochemical studies were done in the Asik Mountain, Maiyumerak Mountains, and Avan Hills ophiolite exposures in order to provide data to constrain our interpretation of the Thematic Mapper images. These sites were selected because of their accessibility and because, together, they provide exposures of all the major ophiolitic rock types in the Brooks Range. Residual and cumulate ultramafic rocks are extensively exposed in the Avan Hills, gabbro is well exposed at Asik Mountain, and mafic sheeted dikes and flows are exposed in the Maiyumerak Mountains. Composite sections for these three localities are shown in Figure 5. The thicknesses represented in these columns are not the thickness of the thrust sheets, but rather these are thicknesses measured perpendicular to compositional layers that are thought to have originally been formed in a horizontal, or near-horizontal, orientation (ultramafic cumulate layers and mafic flows). Thus, the columns represent "stratigraphic" thicknesses with the rocks restored to their orientation when they were a part of the oceanic lithosphere. The mafic dikes and flows have also been restored to their original position, forming the upper part of the oceanic lithosphere. In their present configuration, the mafic volcanics of the Copter Peak Allochthon at

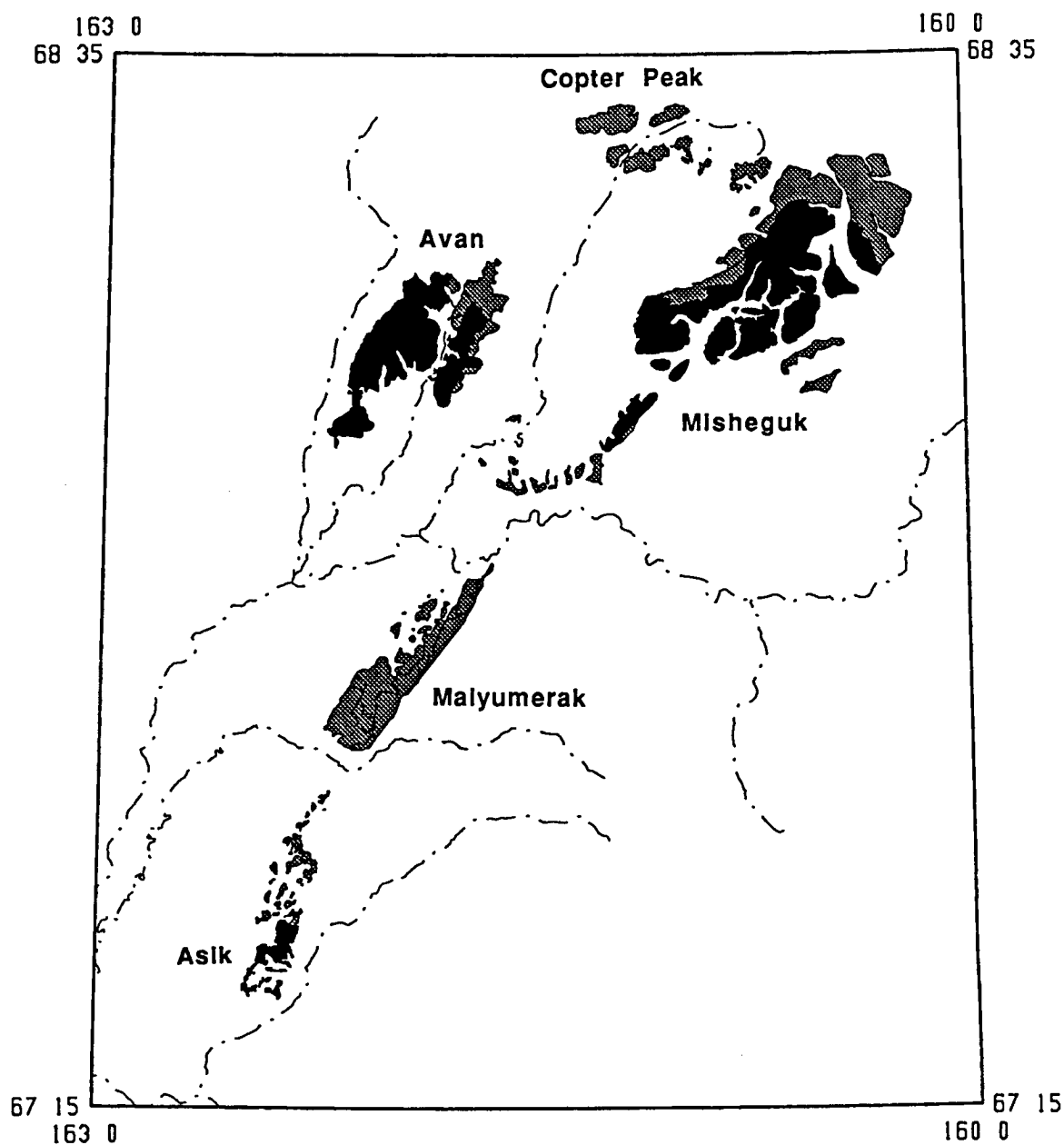


Figure 3. Distribution of Misheguk (black) and Copter Peak (grey) Allochthon exposures for a part of the western Brooks Range, as interpreted from Landsat Thematic Mapper images. Dash-dot lines are rivers.

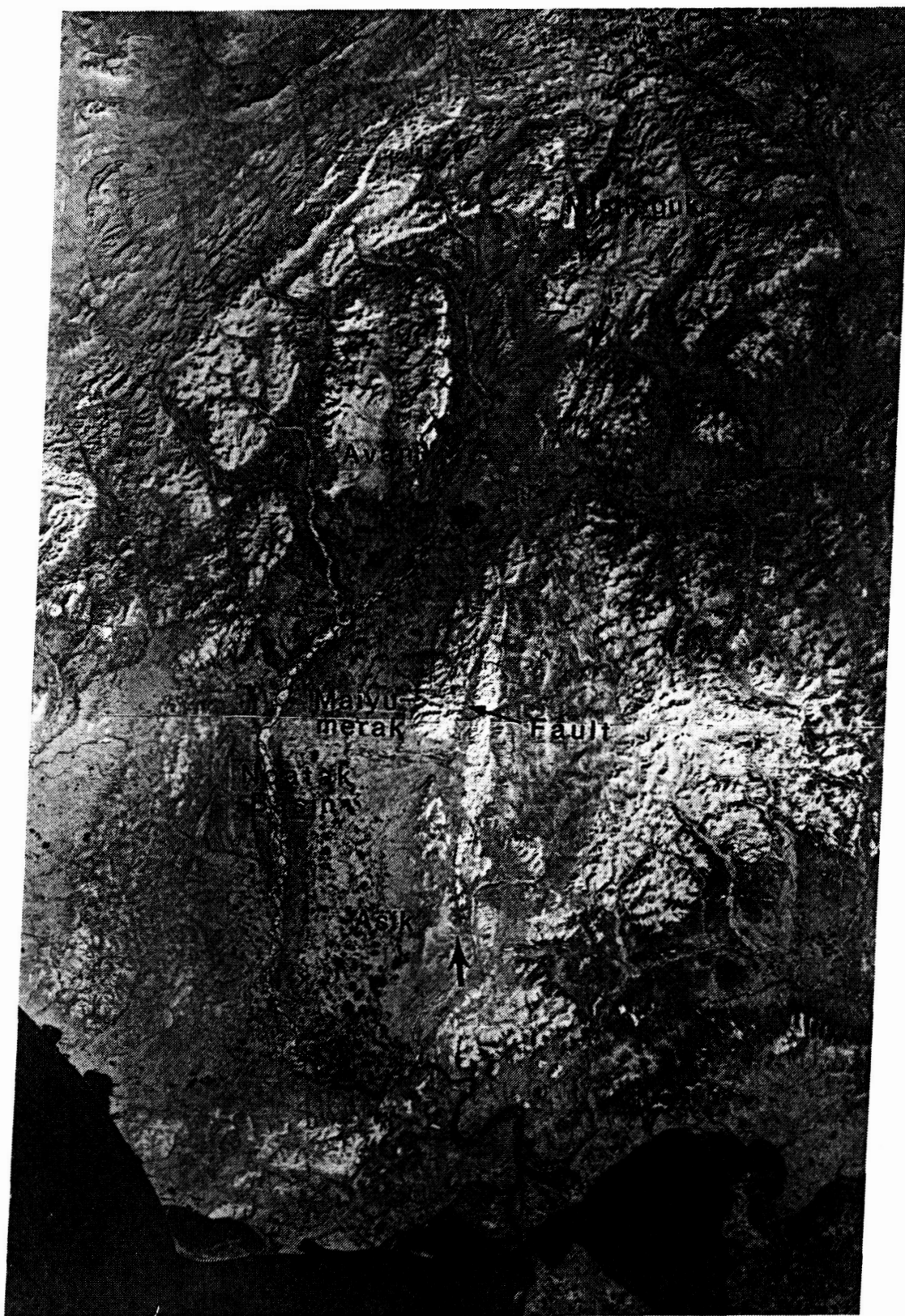


Figure 4. Thematic Mapper band 7 mosaic of two TM scenes showing the ophiolite exposures at Asik Mountain, Maiyumerak Mountains, Avan Hills, and Misheguk Mountain. The arcuate lineament indicated by the arrows is inferred to be a high-angle fault bounding the east side of the Noatak Basin. The region shown is 185 km wide.

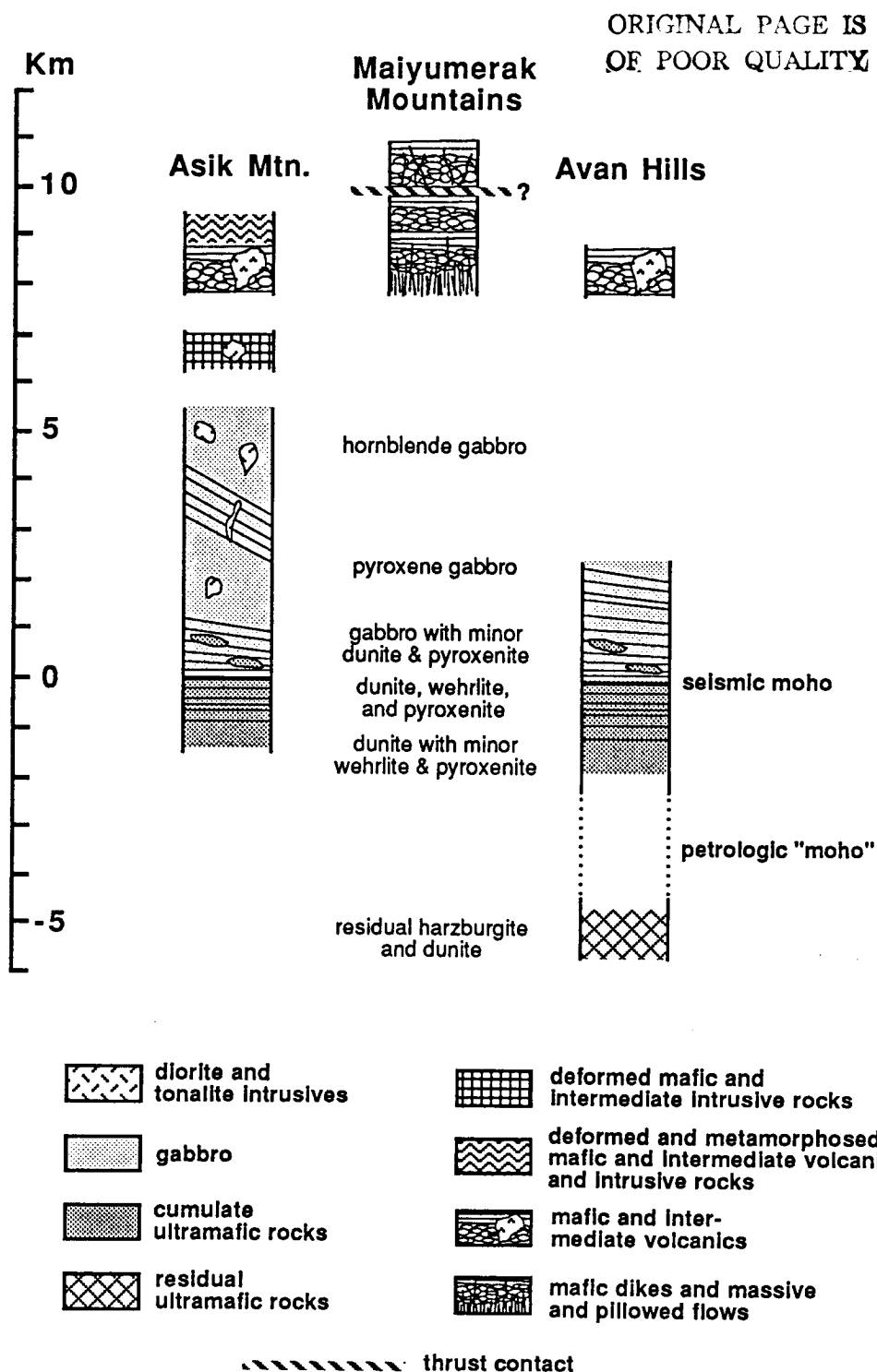


Figure 5. Restored sections of ophiolite exposures at Asik Mountain, Maiyumerak Mountains, and Avan Hills. Thicknesses are measured perpendicular to compositional layers that are inferred to have been formed in a horizontal, or near horizontal, orientation (ultramafic cumulate layers and mafic flows).

Asik Mountain and Avan Hills are thrust sheets occurring structurally below the ultramafic and gabbroic rocks of the Misheguk Allochthon.

Method for Mapping from Thematic Mapper Images

The geologic maps of the Brooks Range ophiolites were produced by visual interpretation of enhanced Thematic Mapper images. One person (D. Harding) interpreted all of the images in order to ensure systematic and consistent mapping. Differentiation of the rock units was based primarily on spectral differences, which are described in the following section. Morphologic features such as drainage density and texture are additional features that were used to differentiate units. Criteria used for the identification of faults were conservative; high-angle faults were inferred where morphologically defined lineaments (eg. aligned drainages, scarps, and/or gullies) delineate a boundary between spectrally differentiated rock units, at least along a part of the lineament. Morphologic lineaments that do not separate units were generally not inferred to be high-angle faults, although they might be. The sense of offset along inferred high-angle faults (eg. strike-slip, normal, reverse, or composite) could not be determined from the images. Low-angle faults (eg. thrusts and low-angle reverse faults) were not interpreted from the images; low-angle faults, because they are not delineated by linear geomorphic features, can not be differentiated on the TM images from low-angle igneous or depositional contacts. From field work, it is known that the rocks of the Copter Peak Allochthon occur structurally below, and are in thrust contact with, the rocks of the Misheguk Allochthon.

Therefore, for all of the ophiolite maps, a thrust contact can reasonably be inferred to occur everywhere between the rocks of the Copter Peak and Misheguk Allochthons.

The geologic interpretations were done interactively on a CRT screen, using International Image Systems (I²S) Model 75 hardware and System 600 software with a VAX 750 host. With the I²S system, entire quadrants of TM data can be examined as three-band color composites at full resolution by scrolling a 512 x 512 window across the quadrant, applying any predefined radiometric enhancement to the data. The geologic interpretation is produced as a registered graphics overlay by selecting vertices that define polygons, that outline rock units, and lines, that delineate faults. The TM image was typically displayed at a scale of 1:28,500 while drawing the interpretation (a 2x enlargement of the pixels on a 27 cm wide, 512 x 512 CRT). The graphics overlay can be displayed with any image, so that the geologic interpretation can be constructed sequentially from a variety of three-band color composites with various radiometric enhancements applied.

The utility of various image enhancements for visual differentiation of rock types was evaluated for regions where we have field constraints on the distribution of rocks (Asik Mountain for gabbro, Maiyumerak Mountains for basalt, and Avan Hills for ultramafic rocks and gabbro). Scaled three-band composites, principal component transformations, and band-ratio images were evaluated, and it was found that scaled three-band composite images were most easily interpreted and that they adequately differentiated the

ophiolite rock types. The most useful band combinations for rock differentiation were 7,3,1 and 3,2,1 displayed as red, green, blue composites. A 5,4,2 composite was useful for differentiating exposed rock and vegetation, and for identifying areas of hydrothermal alteration. These band composites are discussed more fully in the next section. Scaling was performed based on statistics for training regions of illuminated ophiolite rock exposures, rather than on whole-scene statistics, in order to maximize color differences between ophiolitic rocks. Both linear and histogram-normalization functions were used to scale the images. The scalings that best differentiated the ophiolitic rocks, as determined for our field study areas, were saved and applied to all the ophiolite images during interpretation so that the color of spectrally similar exposures would be constant from image to image (additive atmospheric radiance and sun angle do not vary significantly between the TM scenes).

An interactive, visual method of image interpretation was used, as opposed to a computer classification method, because several characteristics of the data render classification methods ineffective: 1) the gabbros are spectrally heterogeneous at the pixel-scale due to variable mineralogy; a human interpreter can better group spectrally heterogeneous pixels into a single unit, 2) the range of spectral variation for gabbro and basalt has significant overlap; these units can, in part, be distinguished by geomorphic characteristics, 3) many areas have radiance that is too low to permit accurate classification because of extensive shadows, resulting from the rugged relief and the low sun angle at these high latitudes (typically 45° for our mid-summer scenes);

a human interpreter can extrapolate contacts through shaded areas, and 4) mixed pixels of vegetation and rock, which are especially common for basalt, might not be accurately classified; a human interpreter can recognize these pixels and include them within a rock unit.

After the geologic interpretation of an image was completed, the x-y image coordinants of the vertices defining the polygons and lines were transformed to latitude and longitude using map projection software. The transformation was based on four control points selected in the image for which the latitude and longitude could be determined from 1:63,360 scale topographic sheets. The latitude and longitude were obtained from the topographic sheets by using a digitizing table and inverse map projection software that is accurate to within tens of meters. Limited tests indicate that the transformation from image x-y coordinates to latitude and longitude is accurate to within 1 to 2 pixels (30 to 60 m). Maps were generated from the latitude and longitude data using mapping software initially developed by J. Gephart, of the Institute for the Study of the Continents at Cornell University, and extensively modified for this NASA project by D. Harding. The mapping software consists of 2300 lines of Fortran code which uses subroutine calls to HOOPS, a commercial graphics package by Ithaca Software. The maps can be displayed for viewing on a high-resolution, color graphics device before final plotting to a laser printer or pen plotter.

An advantage of this on-screen approach to mapping, as opposed to mapping on photographic prints, is that the geologic interpretation becomes a

part of a digital geographic database; the interpretation can be merged and plotted with other information, such as sample localities or geophysical data, and the boundaries and scales of maps can be readily changed.

The mapping procedure described above was developed during the course of this NASA project and now provides the Department of Geological Sciences at Cornell University with an efficient method for producing geologic interpretations from digital remote sensing data.

Spectral Variations

Spectral differences between rock units in the six Thematic Mapper reflectance bands (bands 1 through 5, and 7) were used both to differentiate units within single ophiolite exposures and to correlate units between exposures. Rock units, as used in this report, refer to bodies of rock that 1) consist dominantly of one lithologic type or combination of types, 2) are characterized by a distinctive and substantially homogeneous spectral reflectance, 3) have easily recognizable boundaries, and 4) are large enough to be represented on a geologic map.

The spectral reflectance of rock units was evaluated by extracting Digital Number means and standard deviations from the digital TM data for selected "training" sites. (Digital Number, or DN, is an eight-bit integer (0-255) that is a measure of radiance received by the Thematic Mapper sensors from a ground resolution element, or pixel, with 0 corresponding to low radiance and 255 corresponding to high radiance.) Training sites were selected from

similarly-oriented, directly-illuminated, south-southeast facing slopes in order to minimize DN variations due to albedo differences caused by varying solar zenith angle, or due to weathering differences that are dependent on slope orientation. The training sites were typically 50 to several hundred pixels in size. DN values for training sites were first obtained from areas known to consist of a single, vegetation-free, homogeneous lithology, identified by us during field mapping. DN values from unknown areas were then compared to these reference training sites in order to correlate rock units between exposures. A correction was applied to the DN values to remove the effect of additive radiance, due to atmospheric scattering, by subtracting the DN values for deep, clear lakes located near the training sites. (Water is assumed to be a specular reflector, so that DN values for clear lakes are thought to be a measure only of additive atmospheric scattering, without any component of reflected light from the lake surface.) DN values, corrected for atmospheric scattering, were sufficient for our study; it was not necessary to convert DN values to absolute radiance, or absolute reflectance, because our objective was to differentiate rock units based on a comparison of relative reflectance.

Seigel and Goetz (1977) have shown that small amounts of vegetation mixed with rock can greatly affect reflectance, particularly for near-infrared wavelengths (eg. TM band 4) where vegetation reflectance is very high as compared to typical rock reflectance. Areas of rock including any vegetation would, therefore, be inappropriate for selection as training sites. However, the terrain of the western Brooks Range is characterized by isolated, unvegetated, rock exposures separated by tundra covered expanses. Areas of mixed

vegetation and exposed rock are rare, so that areas of pixels consisting only of rock are common and easily selected for training sites. Training sites were examined using a scaled band 5, 4, 2 composite, displayed as red, green, and blue, in which vegetation appears bright green, to ensure that pixels of mixed vegetation and rock were not included. Also, the band 4 mean for training sites was compared to the band 4 mode; the mean for sites including vegetation and rock mixed pixels is greater than the mode, due to vegetation causing the histogram of band 4 DN values to be skewed to higher values.

Gabbro and basalt in the Brooks Range commonly have extensive lichen growth on exposed surfaces; the large effect on rock reflectance by vegetation, discussed above, is in reference to chlorophyll-rich vegetation. Lichens, being chlorophyll-poor and having low albedo, undoubtedly affect rock reflectance less than chlorophyll-rich vegetation. However, the reflectance of exposed gabbro and basalt surfaces will be a composite of the reflectance of the minerals comprising the rock weathered surfaces and of the lichen cover. Reflectance measurements of lichen-covered rock surfaces, collected by us from the Brooks Range ophiolites, are being done by K. Wirth, as part of a NASA Graduate Student Researchers Program fellowship, in order to evaluate the effects of mineralogy, weathering, and lichen on reflectance. Ultramafic rocks in the Brooks Range have no vegetation cover, including an absence of lichen, because ultramafic rocks typically have high concentrations of elements toxic to vegetation and because the high concentrations of magnesium inhibits the uptake of calcium by most plants.

Within the Misheguk Allochthon, the following rock units were spectrally differentiated: diorite to granite stocks (gr), gabbro (gb), pyroxenite (px), "cumulate" ultramafic rocks (dn) that consist primarily of dunite with some pyroxenite and wehrlite, and "residual" ultramafic rocks (hz) that consist primarily of harzburgite. Ultramafic rocks are comprised dominantly of three mafic minerals (olivine, orthopyroxene, and clinopyroxene), and ultramafic-rock names are defined by the proportions of these minerals (Figure 6). The "residual" ultramafic rocks are strongly deformed, as indicated by well-developed mineral lineations and foliations, and by tight folds. These rocks are interpreted to have been a part of uppermost oceanic mantle that was deformed plastically and partially melted, with melts being extracted to form the overlying oceanic crust, leaving refractory, residual harzburgite. The "cumulate" ultramafic rocks, pyroxenite, and gabbro are compositionally layered and show a progression upward in composition from ultramafic to mafic. These rocks are interpreted to have crystallized in magma chambers from melts derived from the underlying residual mantle. The ultramafic rock units were further subdivided, based on the intensity of serpentinization (alteration of olivine and pyroxene to serpentine-group minerals by hydration). The gabbro is spectrally heterogeneous and was divided into numerous subunits.

Rocks of the Copter Peak Allochthon were divided into two red-weathering basalts (lg1 and lg2), a black-weathering basalt (ug). The difference in weathering color is subtle and generally not easily recognized in the field. In paper A, included in the second part of this report, the weathering color of the basalts is interpreted to be a result of metamorphic facies, with black-

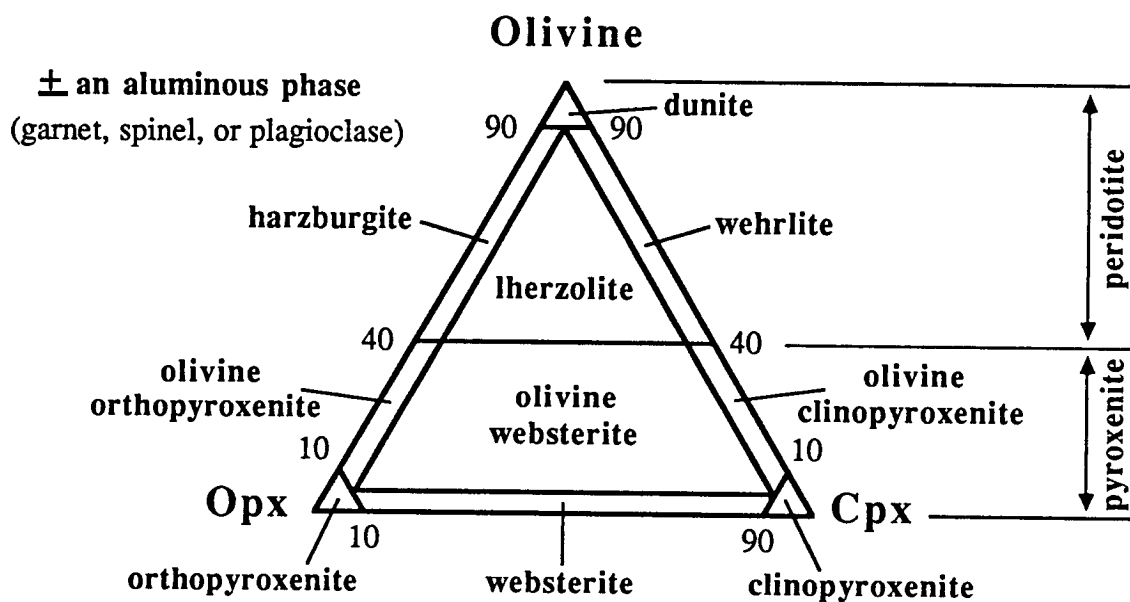


Figure 6. International Union of Geological Scientists ternary classification of rocks composed of olivine, orthopyroxene, and clinopyroxene \pm an aluminous phase.

weathering basalts being actinolite-bearing upper-greenschist facies rocks and with red-weathering basalts being actinolite-free lower-greenschist facies rocks. Subsequent petrographic observations suggest that the pyroxene content may also be correlated with weathering color; black-weathering basalt generally lack igneous pyroxene phenocrysts whereas the red-weathering basalt generally contain pyroxene phenocrysts. Phenocryst assemblages are indicative of magma crystallization conditions; thus, weathering color might differentiate basalts formed from different melts. The basalts were also subdivided based on the intensity of hydrothermal alteration (see paper A).

Several other units were identified locally in the Copter Peak Allochthon during field mapping, including amphibolite-grade metamorphic rocks derived from basalt and associated sedimentary rocks (ms), and a complex unit of variably metamorphosed and deformed mafic- and intermediate-composition volcanic and intrusive rocks (mv). These units occur at or near the thrust contact with the the overlying Misheguk Allochthon and might have been formed during thrusting (see paper C for a discussion of the thermal histories of these rocks). A second complex unit, that consists of variably deformed mafic- and intermediate-composition intrusive rocks (mi), was identified during our field mapping. However, it is uncertain whether this unit is a part of the Misheguk Allochthon or the Copter Peak Allochthon.

Mafic igneous rocks of the Ipnavik Sequence (Ip) were mapped locally from the Thematic Mapper images. The sequence consists of mafic sills and dikes intrusive into chert and limestone. The sequence is not a part of the ophiolite

exposures; rather, it occurs in the structurally-lower sedimentary allochthons. Mafic rocks of the sequence were mapped because they crop out near several of the ophiolite exposures and because they are spectrally similar to some of the ophiolite mafic rocks.

Mean DN values, for representative training sites on the various mapped rock units, corrected for atmospheric scattering, are shown in Table 1 . Plots of the range of corrected DN values versus TM band for several of the map units are shown in Figure 7. Several differences are apparent, such as the lower albedo of serpentinite versus non-hydrated ultramafic rocks, and of unaltered basalt versus altered basalt. However, other units, such as the gabbros and basalts, show considerable overlap, and subtle differences between rock units are not illustrated by such plots (for an example, see Document A on very small DN differences between basalts having different mineralogies). Alternative methods, including ternary plots and normalized plots, were developed to accentuate small DN differences between rock units.

The application of ternary plots to remote sensing data is illustrated in Figure 8. Ternary plots, on which the relative proportions of three variables normalized to 100 are plotted, are convenient for representing the three DN values of a pixel displayed in a red, green, and blue composite image. For example, the point in Figure 8a represents a pixel with DN values for bands 7, 3, and 1 occurring in the proportions 60:10:30. The absolute DN values for such a pixel could be 30, 5, and 15, or 120, 20, and 60, as examples. Such a pixel would appear reddish magenta in a composite with band 7 displayed in red,

Table 1 Mean Digital Number Minus Atmospheric Correction						
UNIT	BAND 1	BAND 2	BAND 3	BAND 4	BAND 5	BAND 7
			BASALT			
MY alt lg2	26.9	21.2	40.7	43.0	126.3	64.2
MY alt lg1	22.4	18.0	35.8	38.7	123.9	70.0
MY alt ug	31.3	20.4	34.2	36.5	131.6	75.1
MY ug	28.1	18.5	29.7	30.3	77.0	45.5
MY lg2	23.8	17.5	30.0	35.8	70.7	38.1
MY lg1	26.1	18.9	33.1	32.6	85.4	53.3
AN alt lg2	25.4	20.8	36.2	39.5	116.6	61.1
AN alt ug	28.5	21.2	33.9	43.1	127.1	66.9
MS lg2	22.2	17.7	31.9	33.0	84.0	44.4
AS alt lg	30.5	23.9	37.8	48.2	114.5	58.8
AS alt ug	24.0	19.3	27.1	66.9	107.5	46.8
AV lg	14.4	11.1	22.3	28.9	75.4	39.8
AV alt ug	31.0	21.1	34.7	32.1	101.3	58.5
			GABBRO			
AS gb1	22.3	15.4	24.1	36.6	89.8	42.8
AS gb2	24.4	15.6	23.8	36.6	97.3	50.2
AS gb3	24.4	16.1	25.1	28.4	78.3	41.3
AS gb4	26.6	19.1	29.9	37.3	101.7	53.5
AV gb1	28.8	17.9	30.3	31.8	101.2	55.0
MS gb1	31.7	20.9	35.1	37.8	109.0	54.9
MS gb2	45.8	29.7	46.7	44.0	104.6	52.3
MS gb3	26.0	17.7	30.1	33.5	124.6	72.7
MS gb4	43.7	26.1	39.9	38.3	105.1	57.3
MS gb5	26.4	20.0	33.6	31.5	72.5	35.7
SK gb1a	29.7	17.4	26.7	25.6	103.5	56.1
SK gb1b	46.6	26.2	37.2	31.7	121.3	66.0
SK gb2	24.1	15.0	24.2	24.8	104.6	60.0
SK gb3	31.6	19.7	31.0	28.8	106.8	58.2
SK gb4	23.0	15.5	26.1	26.6	84.4	44.7
SK gb5	18.0	11.7	20.9	24.5	78.0	41.3

Table 1 Continued						
UNIT	BAND 1	BAND 2	BAND 3	BAND 4	BAND 5	BAND 7
CUMULATE ULTRAMAFIC ROCKS						
AV dn1	29.2	28.1	52.2	44.3	82.5	44.9
AV dn2	28.7	29.6	56.7	49.0	104.8	61.3
AV dn3	26.9	26.9	50.3	42.9	85.8	46.6
AV dn4	37.9	39.2	74.3	65.1	140.5	77.2
AV dn5	42.6	42.2	77.4	61.1	127.0	72.4
AV px	14.7	10.9	20.6	27.8	87.2	36.2
SK dn1a	26.0	26.0	51.2	49.8	132.6	68.3
SK dn1b	25.5	26.0	49.7	42.8	88.6	49.6
SK dn2	39.1	39.6	74.6	66.0	143.7	71.8
RESIDUAL ULTRAMAFIC ROCKS						
AV hz1	31.6	30.9	61.1	60.2	156.5	79.9
AV hz2	32.0	32.1	66.7	64.7	144.4	71.9
AV hz3	26.5	27.9	57.6	53.6	130.6	70.6
AV hz4	34.8	37.1	72.7	64.9	156.7	86.8
AV hz5	26.6	26.8	55.3	53.0	125.6	68.4
SERPENTINITE						
AV serp1	27.3	25.1	45.6	38.2	74.0	41.8
AV serp2	29.2	24.5	42.3	35.1	70.0	37.0
AV serp3	25.4	21.7	38.7	34.3	62.0	32.6
SK serp1	25.7	22.4	38.6	33.7	66.7	37.4
MISCELLANEOUS						
AS Ip	28.8	20.3	30.3	47.7	114.5	57.2
AS mi	29.0	19.5	29.3	38.9	106.9	54.9
AS mv1	38.8	27.9	41.9	53.7	136.8	69.2
AS mv2	29.0	21.5	30.7	60.0	120.6	57.6
SK gr	20.8	15.1	25.4	23.8	93.9	56.1
MS ms	19.9	12.2	21.0	26.2	111.9	66.4

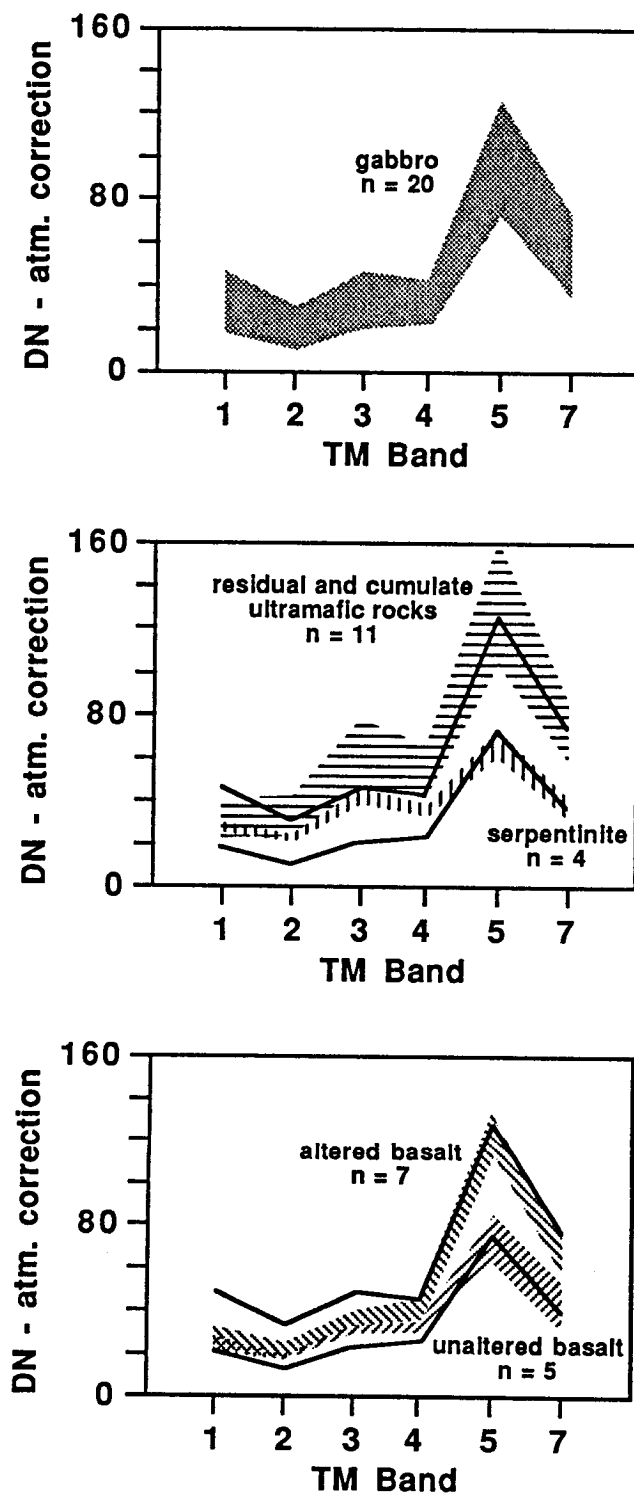


Figure 7 Fields showing the range of mean DN values, corrected for additive atmospheric radiance, for training sites on the major rock units of the ophiolite exposures. The minimum and maximum mean DN values for gabbros are repeated in the two lower plots as solid lines. N is the number of training sites used to define the ranges.

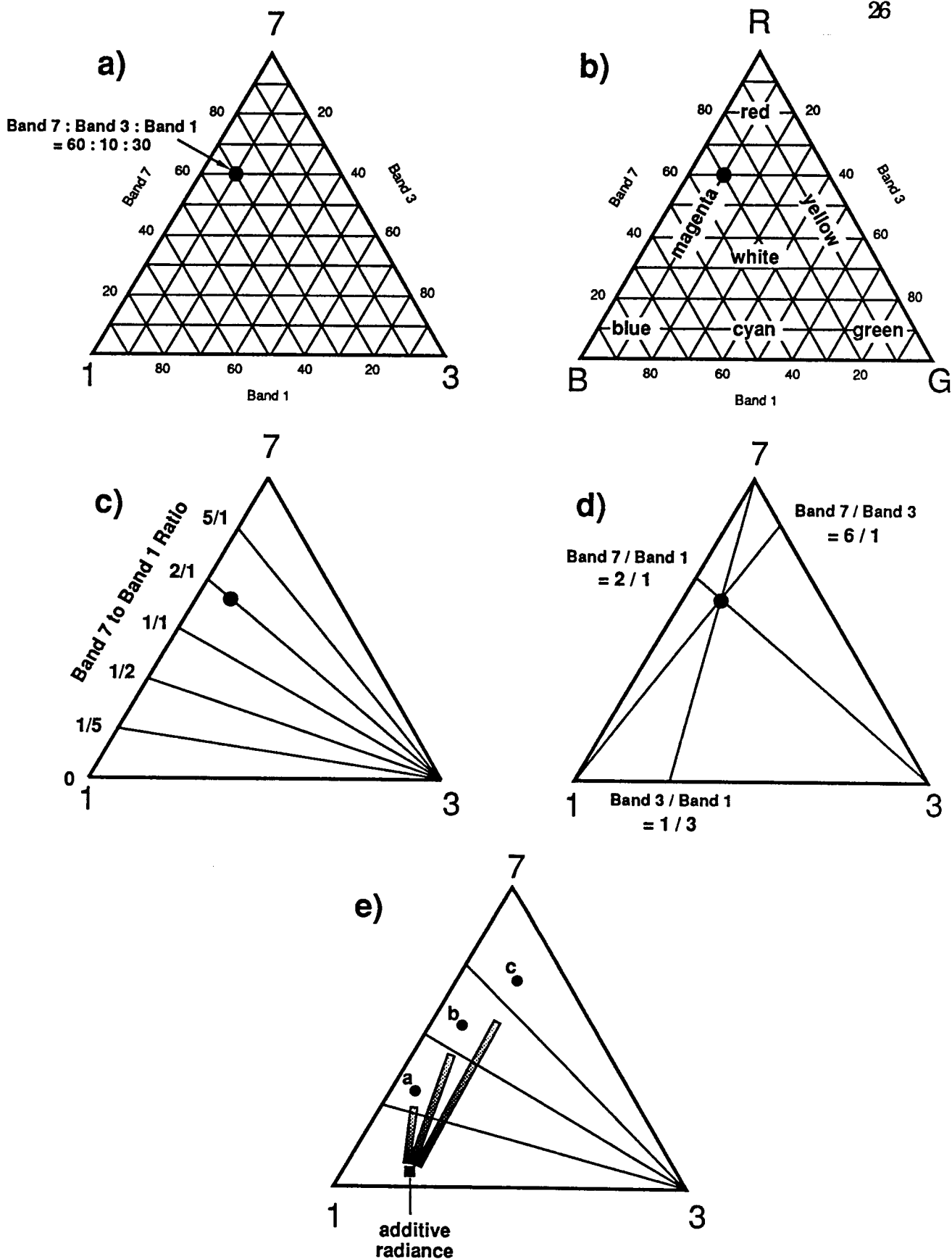


Figure 8 Application of ternary diagrams to Landsat Thematic Mapper data. See text for explanation.

band 3 in green, and band 1 in blue (Figure 8b). Band ratios are also graphically illustrated on ternary plots; ternary points with equal band 7 to band 1 ratios, for example, plot along a line radiating from the band 3 apex (Figure 8c). Ternary points can be thought of as depicting the three band ratios between three DN values. The pixel with band 7:band 3:band 1 proportions of 60:10:30, for example, has a band 7-to-band 1 ratio of 2-to-1, a band 7-to-band 3 ratio of 6-to-1, and a band 3-to-band 1 ratio of 1-to-3 (Figure 8d).

Because band ratios eliminate albedo variations, brightness differences are not represented in a ternary plot; only the hue component of an RGB triplet is represented. However, additive radiance due to atmospheric scattering must be subtracted from the DN values in order to remove the influence of slope orientation on band ratios. The influence of atmospheric scattering and slope orientation is shown in the ternary plot of Figure 8e. Points a, b, and c represent the DN values, corrected for atmospheric scattering, for pixels from three training sites that would be effectively differentiated by a band 7 to band 1 ratio. The training sites are assumed to contain pixels from slopes of varying orientations. However, all pixels for a training site plot together because it is assumed that each site is spectrally homogeneous and that the effect of atmospheric scattering has been perfectly corrected. The filled square is the ternary point for typical DN values in bands 7, 3, and 1 for additive radiance from atmospheric scattering. If the additive radiance were not subtracted from the DN values of the training site pixels, the ternary points for the pixels would be shifted toward the additive radiance point. Pixels with small DN values, from dark, weakly illuminated slopes, would be shifted closer to the

additive radiance point than pixels with large DN values, from bright, strongly illuminated slopes, thus forming "mixing lines", the shaded bars in Figure 8e. The pixels of the three training sites, when arrayed in mixing lines, are not effectively differentiated by a band 7 to band 1 ratio.

Atmosphere-corrected DN values for the major rock units of the ophiolites are plotted on ternary diagrams in Figure 9, for band combinations 7, 3, 1 and 5, 4, 2 and 3, 2, 1. Patterned fields are shown that enclose the DN means for training sites on the respective rock units. The number of enclosed means, n , is listed for each unit. Portions of the full ternary diagrams have been enlarged so that the differences between fields are better resolved. The filled squares on the full ternary diagrams are typical points for additive atmospheric radiance, determined from DN values for deep, clear lakes. The letter v represents the ternary points for typical tundra vegetation.

The combination of bands 7, 3, and 1, displayed as a red, green, blue composite, was the most useful combination for visually differentiating the ophiolite rock units based on differences in hue. The differentiation of units is graphically illustrated in the ternary for bands 7, 3, and 1 of Figure 9, in which the rock-unit fields are well separated, as compared to the ternaries for bands 5, 4, 2 and 3, 2, 1. The greatest variation occurs in band 7; altered basalts, for example, show an increase in band 7 reflectance as compared to unaltered basalt. The increase in band 7 reflectance is consistent with field-spectrometer measurements of *in situ* bidirectional reflectance of hydrothermally altered, and unaltered mafic volcanic rocks (Abrams et al., 1985) Weathered surfaces

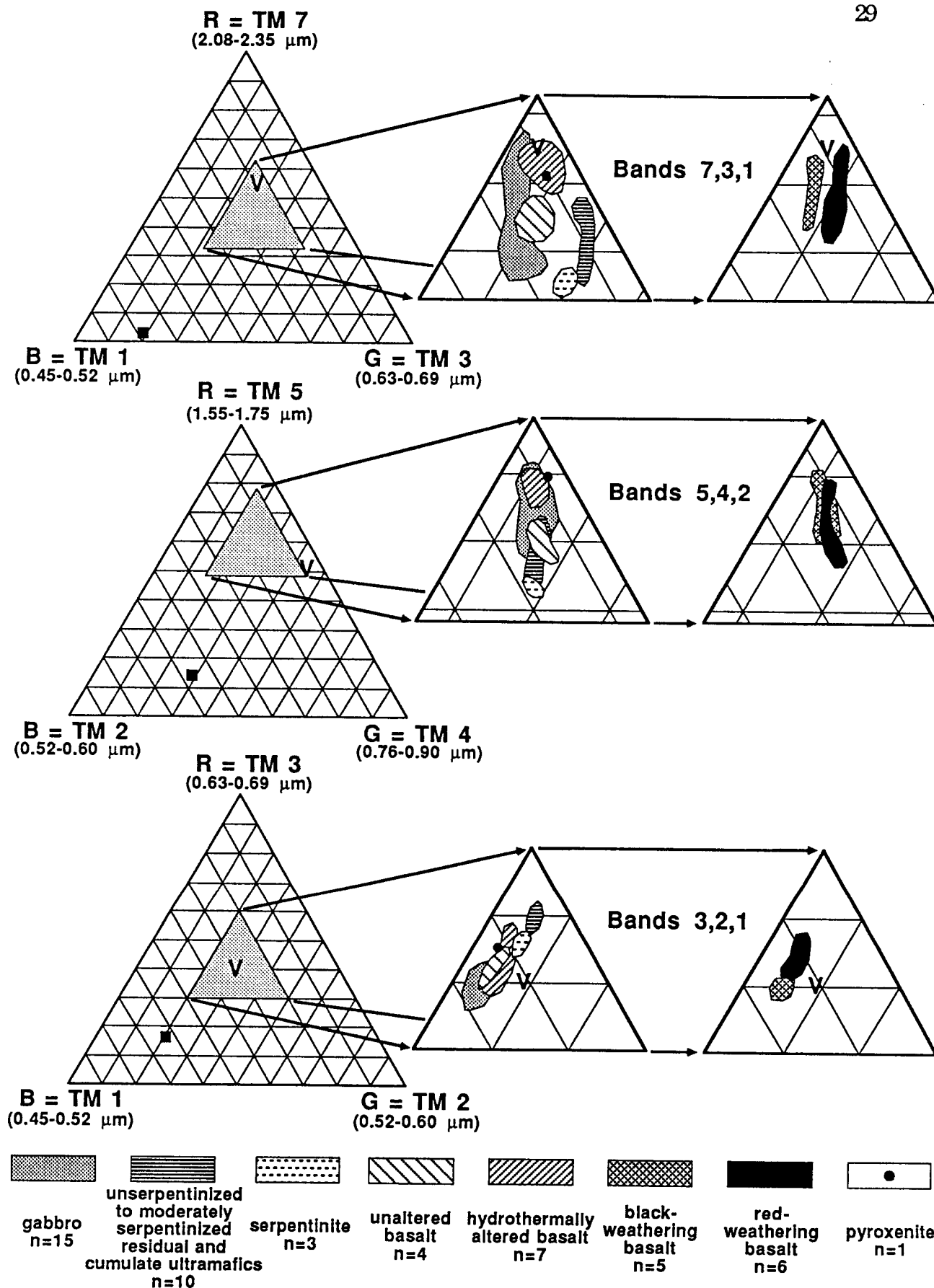


Figure 9 Ternary plots for band combinations 7,3,1 and 5,4,2 and 3,2,1, showing fields that enclose corrected mean DN values for training sites on the major ophiolite rock units. N is the number of sites used to define the fields. The solid square and the letter v are the ternary points for additive atmospheric radiance and vegetation, respectively.

of hematite-bearing, altered andesite and sulphide-bearing, altered dacite, for example, have high reflectance in TM band 5 and 7 bandwidths, as compared to unaltered andesite and dacite, due to the high albedo of hematite and fine-grained clay minerals (Abrams et al., 1985). Gabbro exhibits a similar variation in band 7 reflectance. The reflectance variation between red- and black-weathering basalt is a slight increase in the relative proportion of band 3 to band 1 reflectance, indicative of an increase in the concentration of iron hydroxide minerals.

Weathered ultramafic rock surfaces are orange to red-brown, due to the extensive formation of iron hydroxide minerals from weathered olivine and pyroxene, thus accounting for the high band 3 reflectance of the ultramafic-rock fields in Figure 9. The ternary points for the individual training sites on ultramafic rock exposures are plotted in Figure 10, for 7,3,1 and 5,4,2 band combinations. The serpentinites have low band 7 reflectance as compared with unserpentinized and moderately serpentinized ultramafic rock. This low reflectance is probably due to the Mg-O-H absorption feature at 2.3 μm , within the band 7 wavelength bandwidth. The ternary points for unserpentinized to moderately serpentinized cumulate dunite occur in a line, extending from the serpentinite field toward greater band 7 and band 5 reflectance, suggesting that this data defines a mixing line between the reflectance of serpentinite and of unserpentinized-dunite weathered-surfaces. The TM data might, therefore, provide a quantitative measure of the intensity of hydration. This possibility is being studied further. The ternary points for residual harzburgite (olivine, 10 to 30% orthopyroxene) also are arrayed in a line, extending half the distance from the dunite field (olivine only) toward the pyroxenite ternary point. This

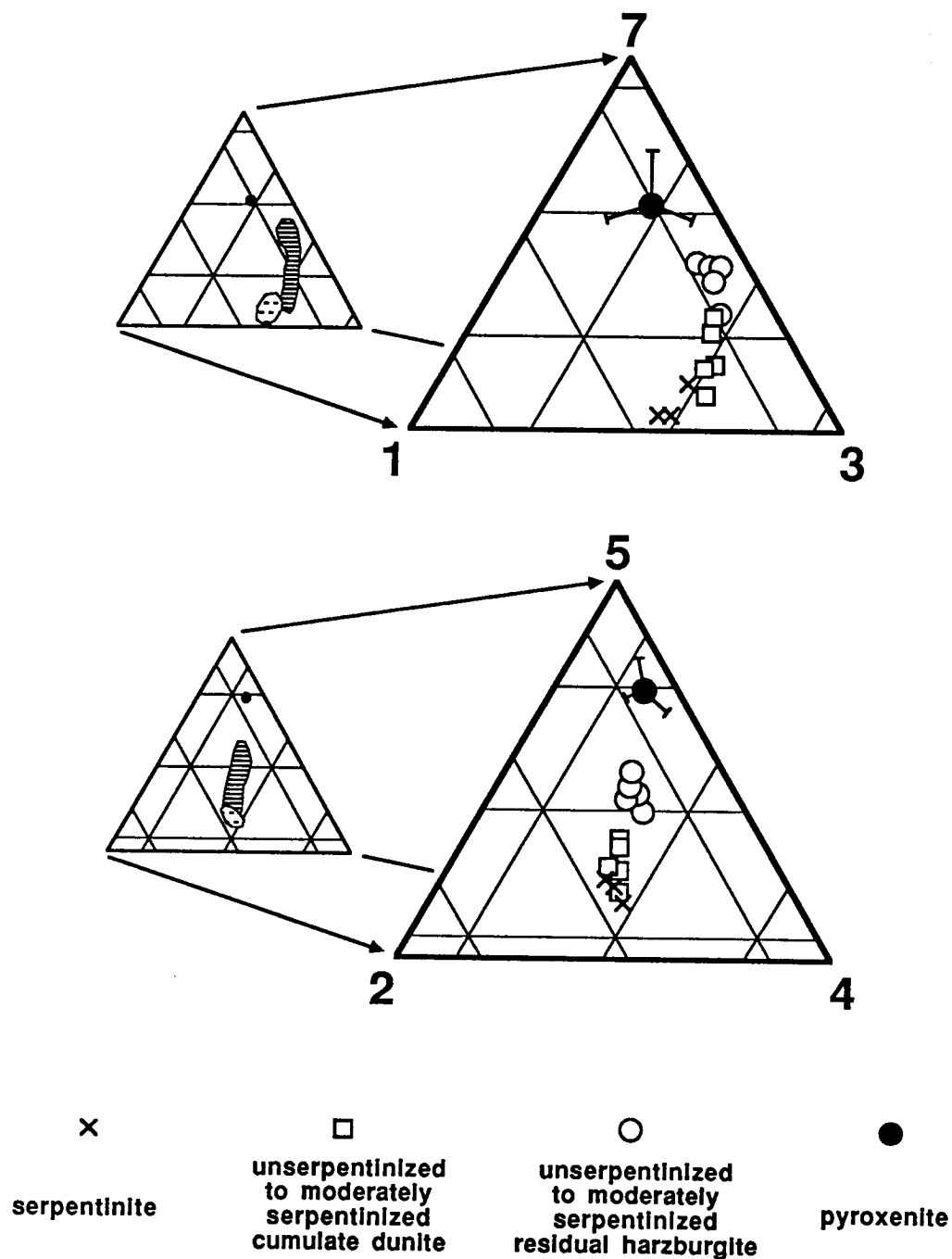


Figure 10 Parts of ternary plots for band combinations 7,3,1 and 5,4,2, with mean DN values, corrected for additive atmospheric radiance, plotted for training sites on ultramafic rocks. One sigma standard deviations are shown for the pyroxenite site.

suggests that the data defines a mixing line between the reflectance of dunite and pyroxenite, and, therefore, the TM data might also provide a quantitative measure of pyroxene content in ultramafic rocks. This possibility is also being studied further.

The rock-unit fields for the 5,4,2 ternary of Figure 9 are not well-separated, but the ternary point for vegetation (v) plots relatively far from the rock units, accounting for the poor differentiation of ophiolite rocks in 5,4,2 composites but good differentiation between exposed rock and vegetation. The rock-unit fields define a line in the 3,2,1 ternary, with varying proportions of band 3 and band 1 reflectance at a constant proportion of band 2 reflectance. These proportions might be the result of varying concentrations of iron hydroxide minerals on the rock weathered surfaces; iron hydroxides are characterized by low reflectance at band 1 wavelengths, due to ferric-iron conduction-band absorption, and high reflectance at band 3 wavelengths.

Gabbroic rocks of the ophiolites are spectrally heterogeneous and exhibit a broad range of relative reflectance, as shown in the 7,3,1 and 5,4,2 ternaries of Figure 9. Spectral variations of the gabbroic rocks were evaluated using normalized plots. Figure 11, a, shows DN values, corrected for additive atmospheric radiance, for five spectrally distinct gabbros of the Misheguk Mountain ophiolite. Spectral differences between the gabbros are difficult to recognize in this plot. Figure 11, b, shows normalized plots, in which the corrected DN values for the gabbros have been divided by the corrected DN values for a reference gabbro (Misheguk gb1). Differences between the

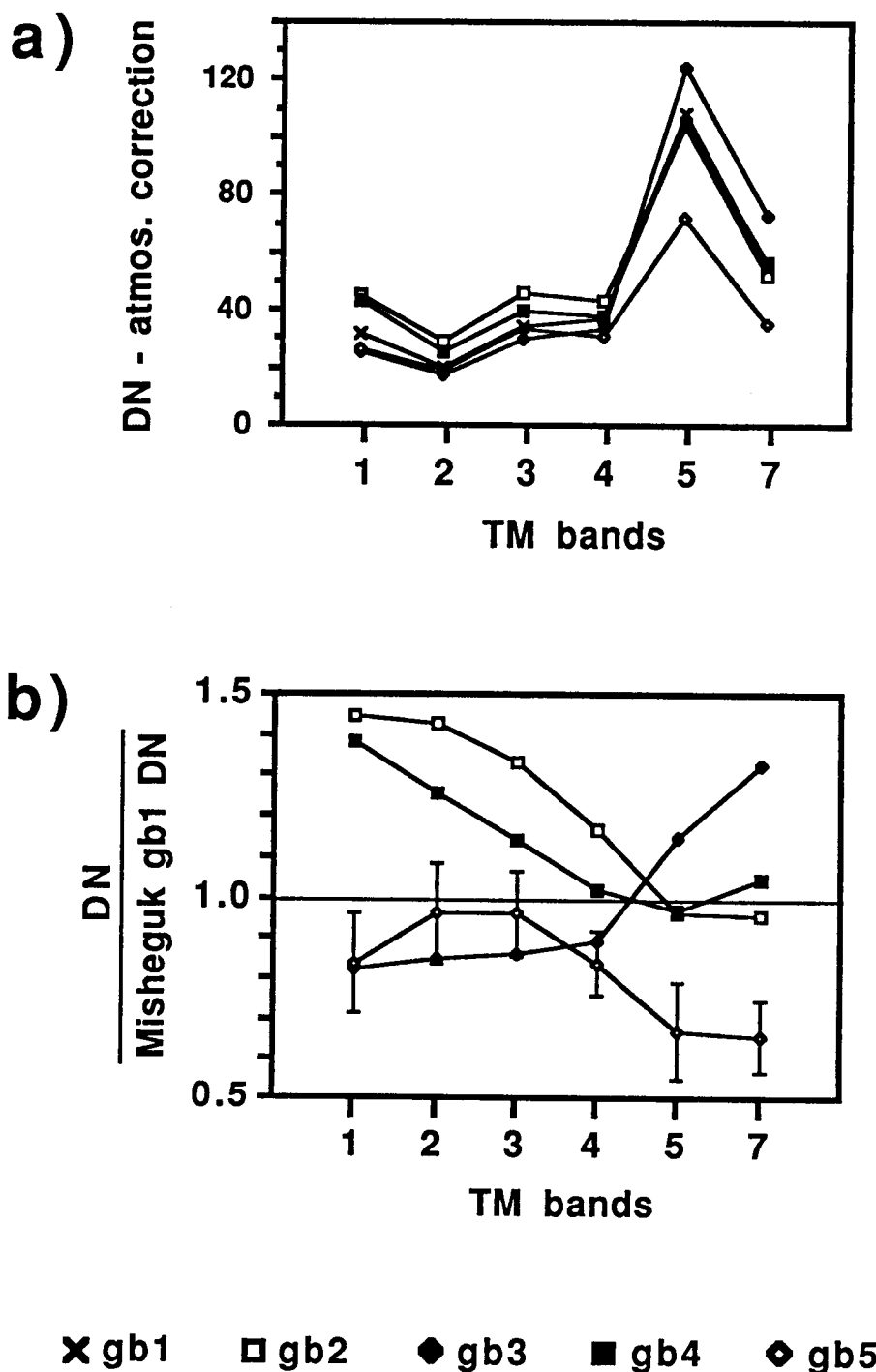


Figure 11 Mean DN values, corrected for additive atmospheric radiance, for training sites on spectrally distinct Misheguk Mountain gabbros, as a) DN value versus TM band, and b) DN values, normalized by DN values for gb1, versus TM band. One sigma standard deviations are shown for gb5; these are representative of the standard deviations for the other gabbro units.

gabbros are apparent in this plot. Unit gb3 has increasing reflectance at longer wavelengths, as compared to gb1. Units gb2 and gb4 exhibit high reflectance that decreases with increasing wavelength, relative to gb1. Unit gb5 exhibits a complex, convex-upward pattern. The origins of these spectral differences are not known. Several possible causes are, 1) varying proportions of igneous minerals (eg. decreasing olivine content up-section), 2) varying mineral composition (eg. increasing Fe to Mg ratio of pyroxene up-section), 3) varying degrees of hydrothermal alteration, or 4) varying types, or amounts, of lichen cover. The spectral differences might have geologic significance, or they might be of non-geological origin.

All the gabbro units differentiated by us in the TM maps of the ophiolites are compared, in Figure 12, using normalized plots. Six patterns are distinguished: flat, rising, high band 4, low band 4, falling, and convex-upward. Gabbros with similar patterns might be equivalent rocks; for example, gabbro units gb1 in the Avan Hills, gb5 at Siniktanneyak Mountain, gb3 at Asik Mountain, and the reference gabbro, gb1 at Misheguk Mountain, although having varying albedos, exhibit similar relative reflectance intensities between bands, as indicated by the parallel, flat patterns in Figure 12, a. However, there is a strong correlation between the normalized patterns and geographic location. For example, most gabbro units at Asik Mountain have high band 4 patterns, whereas most units at Siniktanneyak Mountain have low band 4 patterns. These correlations suggest that some factor related to geographic location, such as weathering conditions or amount of lichen cover, controls gabbro reflectance, rather than rock type. Further work is needed to determine if gabbro reflectance can be used to identify equivalent rock types between ophiolite exposures.

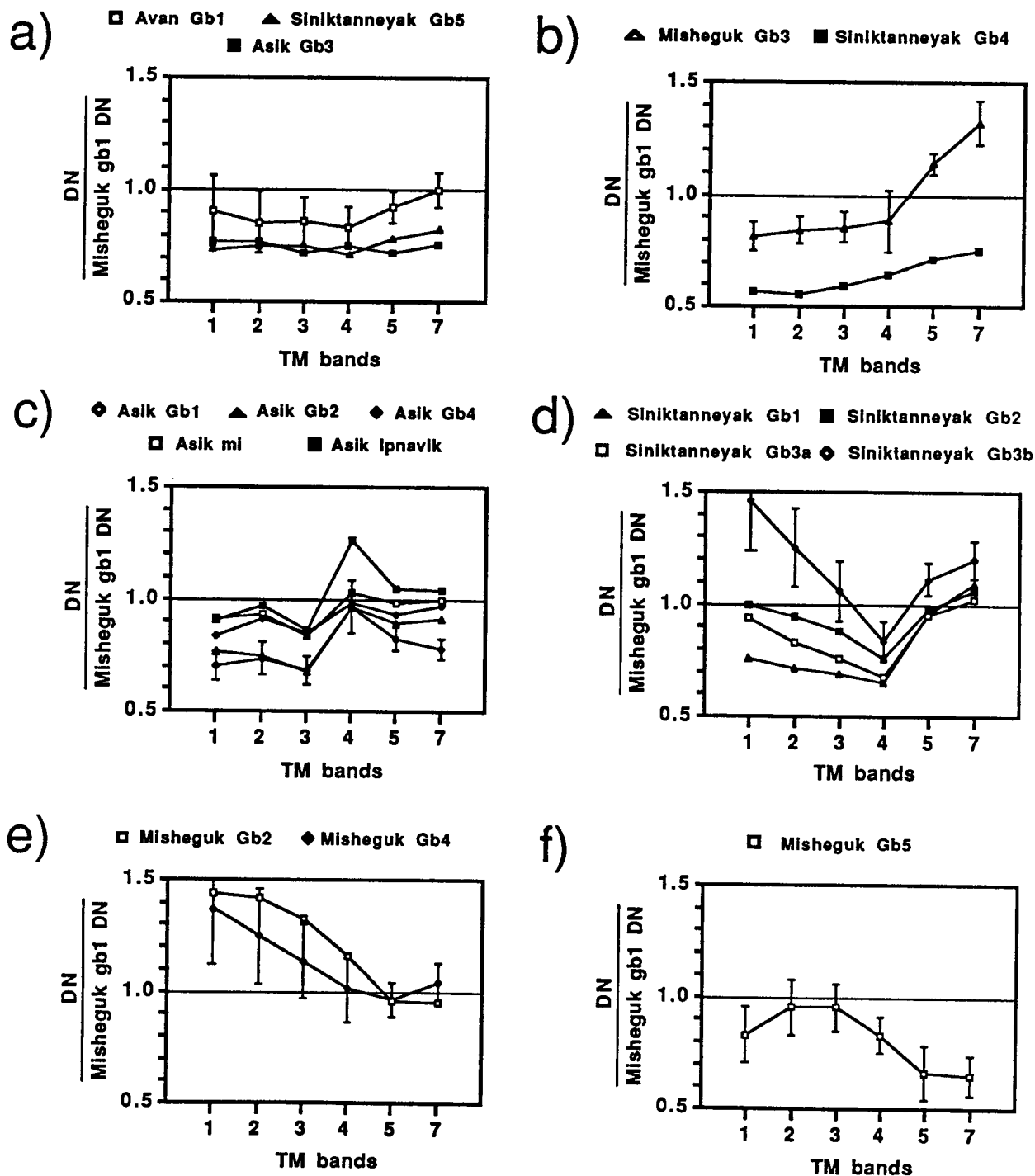


Figure 12 Mean DN values, corrected for additive atmospheric radiance and normalized by DN values for Misheguk gb1, for training sites on spectrally distinct gabbros of four ophiolite exposures, showing a) flat patterns, b) rising patterns, c) high band 4 patterns, d) low band 4 patterns, e) falling patterns, and f) a convex-upward pattern. Representative one sigma standard deviations are shown for selected units.

Maps of the Ophiolite Exposures

The locations of the ophiolite exposures that were mapped for this project are shown in Figure 13. Previous mapping of these exposures was done, both during reconnaissance field work and from aerial photographs by various other workers. The previous maps have varying levels of detail, with the ophiolite rocks differentiated using various rock nomenclatures. Our mapping has been done at a consistent level of detail, with a consistent rock nomenclature. We have differentiated a greater number of rock units than that of any of the previous maps, with a level of detail that is equal to most of the previous maps. The most detailed of the previous maps, based on relatively extensive field work, resolve smaller units and more structures than our maps. The most detailed mapping has been done in the Ambler District of the Angayucham Terrane by Hitzman et al (1982), and Pallister and Budahn (in press), at Siniktanneyak Mountain by Nelson and Nelson (1982), and in the Avan Hills, by Zimmerman (1980). Published maps for these places are shown in Figures 14, 15, and 16. The other ophiolite exposures (Misheguk Mountain, Copter Peak, Maiyumerak Mountains, and Asik Mountain) have been mapped primarily from aerial photographs, with limited field checks, by Ellersieck et al. (1984), Curtis et al. (1984), and Blanchard et al. (in prep). These maps divide the ophiolites into three main units, ultramafic rock, gabbro, and basalt.

The explanation for the ophiolite maps, interpreted by us from the TM images, is shown in Figure 17. Unpatterned areas on the maps are either of vegetated areas, and so can not be differentiated based on spectral differences

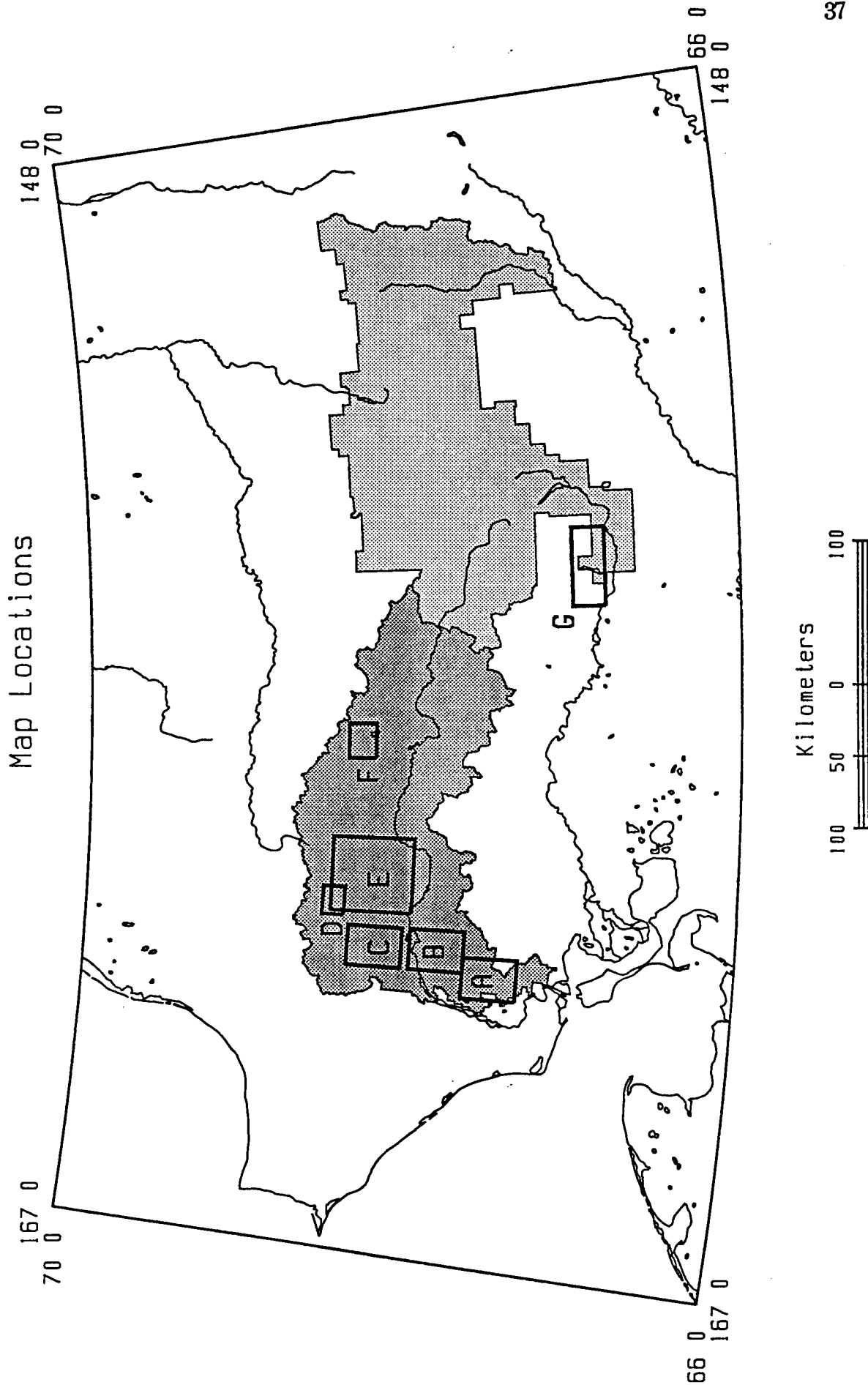


Figure 13 Locations of the ophiolite maps included in this report: A) Asik Mountain, B) Maiyumerak Mountains, C) Avan Hills, D) Copter Peak, E) Misheguk Mountain, F) Siniktanneyak Mountain, G) the Ambler District of the Angayucham Terrane. The shaded areas are the Noatak National Preserve (dark) and the Gates of the Arctic National Park (light).

ORIGINAL PAGE IS
OF POOR QUALITY

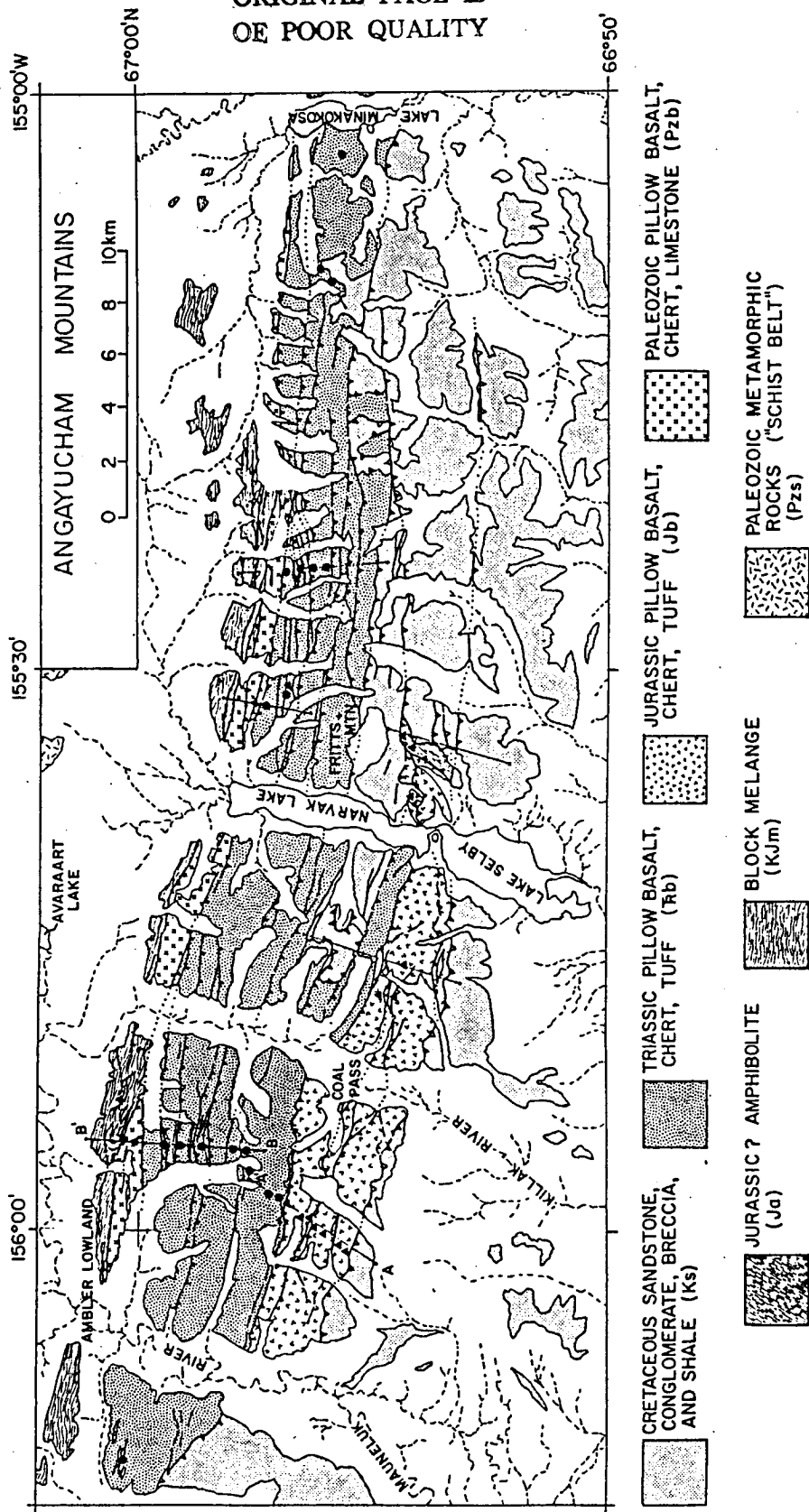
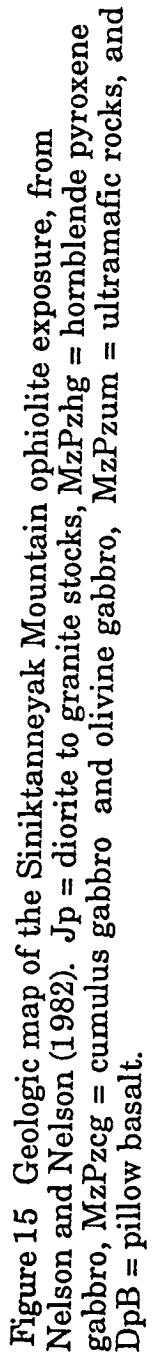


Figure 14 Geologic map of the Angayucham Terrane ophiolite exposure of the Ambler District, from Pallister and Budahn (in press).



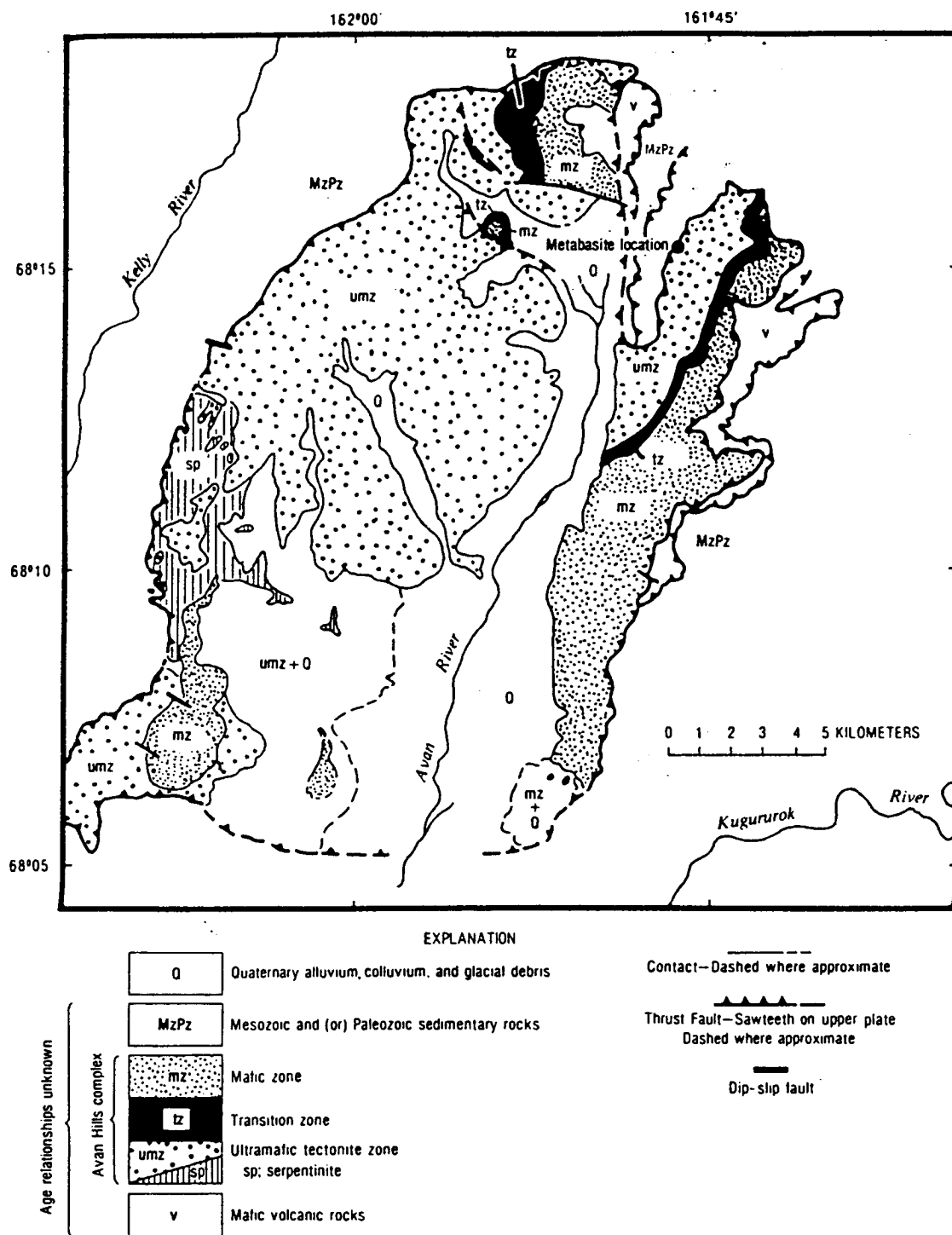


Figure 16 Geologic map of the Avan Hills ophiolite from Frank and Zimmerman (1982).

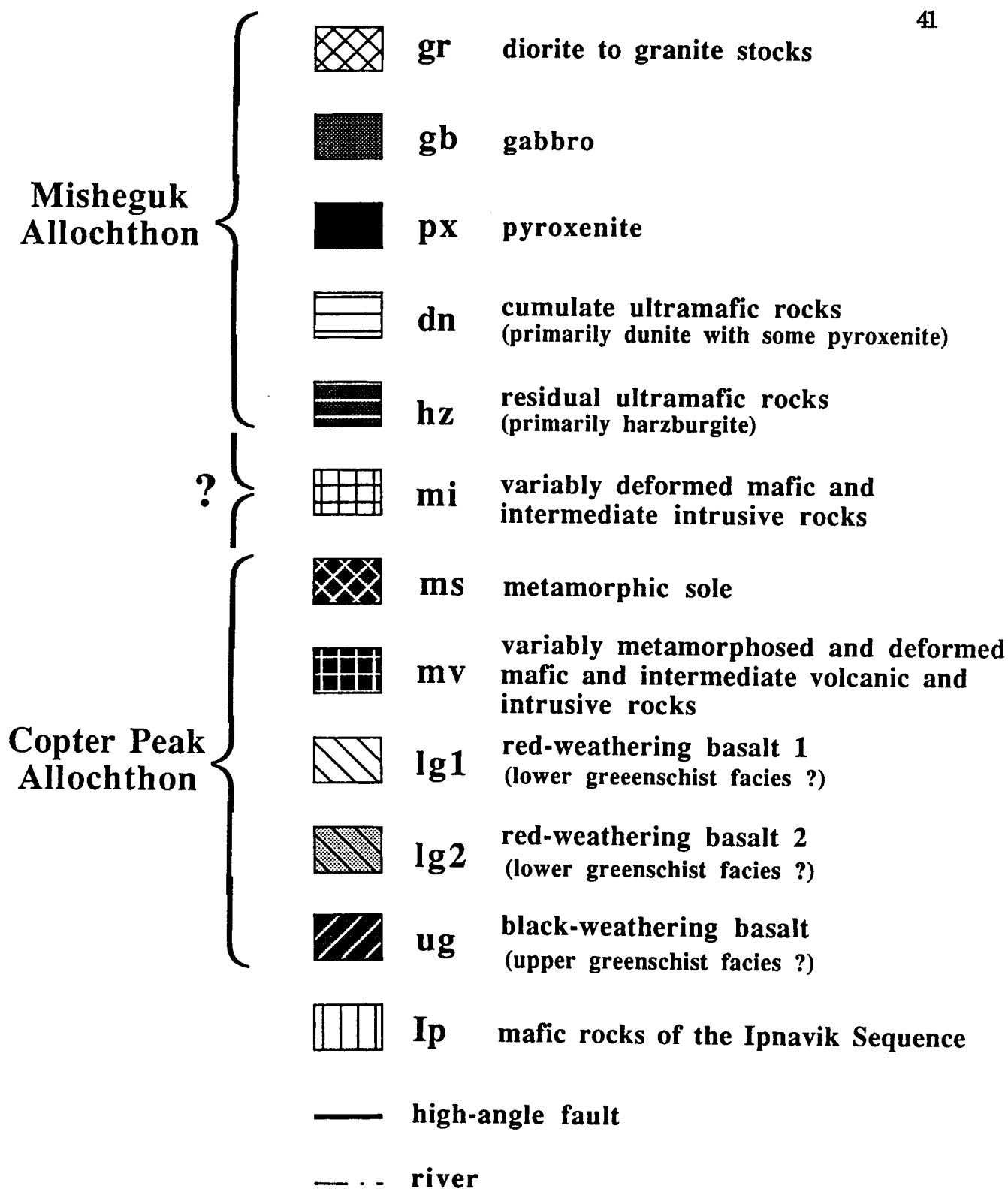


Figure 17 Explanation for the ophiolite maps interpreted from Landsat Thematic Mapper images. It is uncertain whether unit mi is a part of the Misheguk Allochthon or the Copter Peak Allochthon.

between rock units, or areas of exposed rocks of the sedimentary-rock allochthons that structurally underlie the ophiolites. Additional maps for some of the ophiolites are included, that subdivide spectrally distinct gabbros, that differentiate ultramafic rocks based on the intensity of serpentinization, that show areas of hydrothermally altered basalt, and that show the locations of rock samples we have collected. All maps are at a scale of 1:200,000, unless otherwise indicated, and are Universal Transverse Mercator projections.

Exposures of the Brooks Range ophiolites typically consist of limited ridge-crest outcrops with extensive slopes of rubble formed by ice wedging due to freeze-thaw. The rubble is most often locally derived (there is little transport or mixing of rubble by down-slope migration) so that maps of rubble distribution accurately represent bedrock geology. On some slopes, rubble has been mixed and transported long distances by solifluction. The resolution of the TM is generally not great enough to identify these solifluction areas, so the areal distribution of units may be over estimated for some exposures.

The geologic significance of the spectral variations observed in the TM images is best known for the Avan Hills, Maiyumerak Mountains, and Asik Mountain ophiolites, where we did field work during 1985 and 1987. Thirteen, eleven, and eighteen days were spent in the field at the Avan, Maiyumerak, and Asik ophiolites, respectively. Base camps were established, at various localities within the ophiolite exposures, for two to six days, with access by helicopters made available by Cominco, Inc., and ARCO Alaska, Inc. Ground traverses were done from these base camps. Measured sections for these

ophiolites are shown in Figure 18, in which the rock units are shown in their present structural positions. However, the thicknesses are not a measure of the vertical thicknesses of the thrust plates; the sections are measured perpendicular to compositional layers that are inferred to have formed in a horizontal, or near horizontal, position (ultramafic cumulates and mafic flows). Ultramafic cumulate layers, and gabbro layers, are oriented nearly vertical at Asik Mountain and the Avan Hills, and therefore the thicknesses were measured in a horizontal orientation for these rocks. The thrust plates are on the order of one kilometer thick.

Geologic maps of the Avan Hills ophiolite, interpreted from Thematic Mapper images, are shown in Figure 19 (a through c). The western part of the ophiolite consists dominantly of ultramafic rocks, including the only residual ultramafic rock recognized in any of the mapped ophiolites (residual ultramafic rock is also present at the Iykrok Mountain ophiolite, but this exposure is west of the limit for TM data acquisition). The spectral change from residual to cumulate ultramafic rocks is subtle and gradational; the boundary between these rocks, although shown on the maps of Figure 19 as being sharp, is transitional. Residual sections of ophiolites commonly grade upsection from harzburgite to dunite with decreasing amounts of pyroxene; this might account for the transitional character of the residual-cumulate boundary as seen in TM images. The exposed cumulate ultramafic rock at Avan Hills is anomalously thick as compared to ophiolites from other regions of the world; it may be thickened by thrust faulting. However, anomalously thick sections of basalt are exposed in the Angayucham Terrane (Pallister and

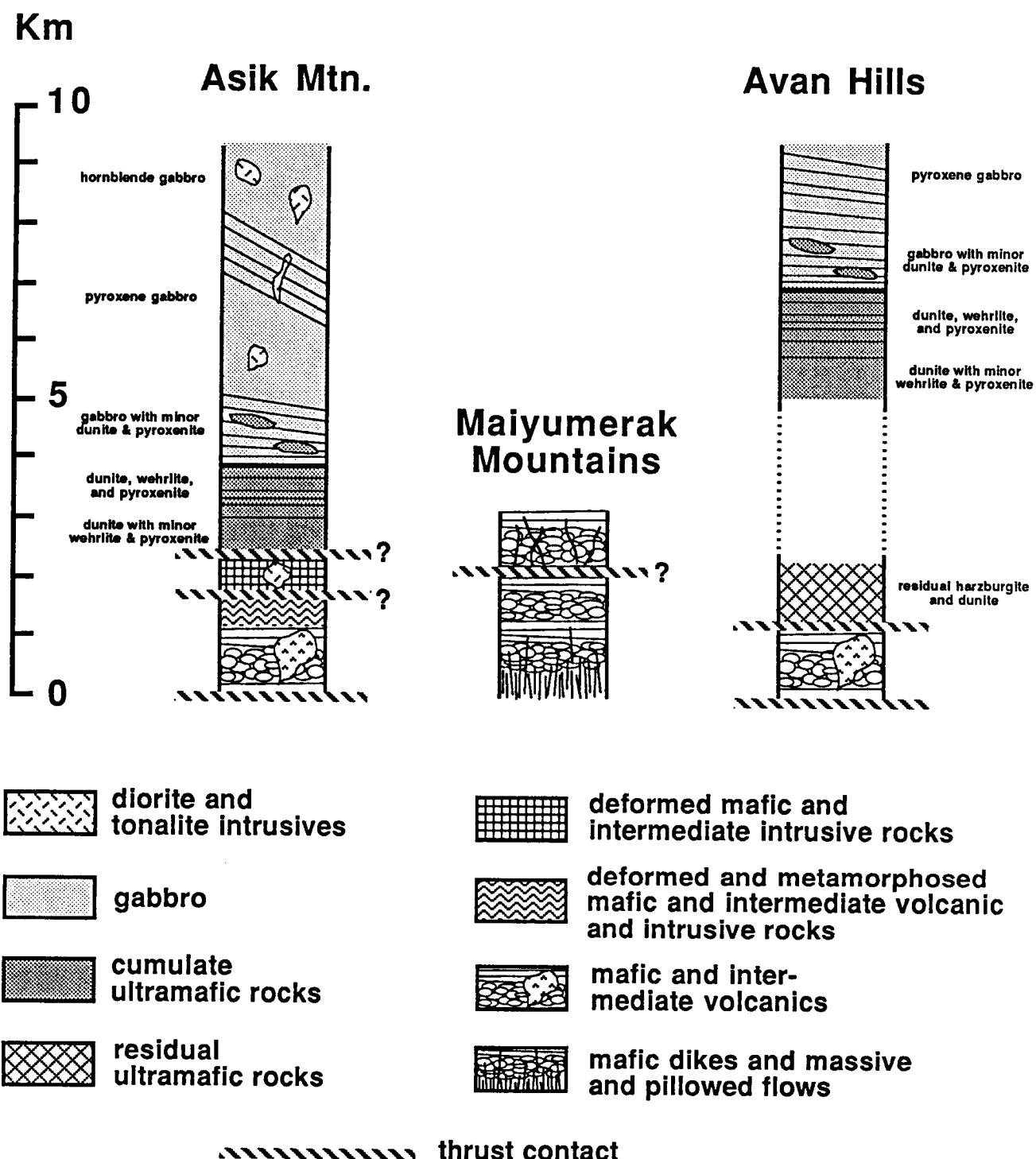


Figure 18. Sections for ophiolite exposures at Asik Mountain, Maiyumerak Mountains, and Avan Hills. Thicknesses are measured perpendicular to compositional layers that are inferred to have been formed in a horizontal, or near horizontal, orientation (ultramafic cumulate layers and mafic flows).

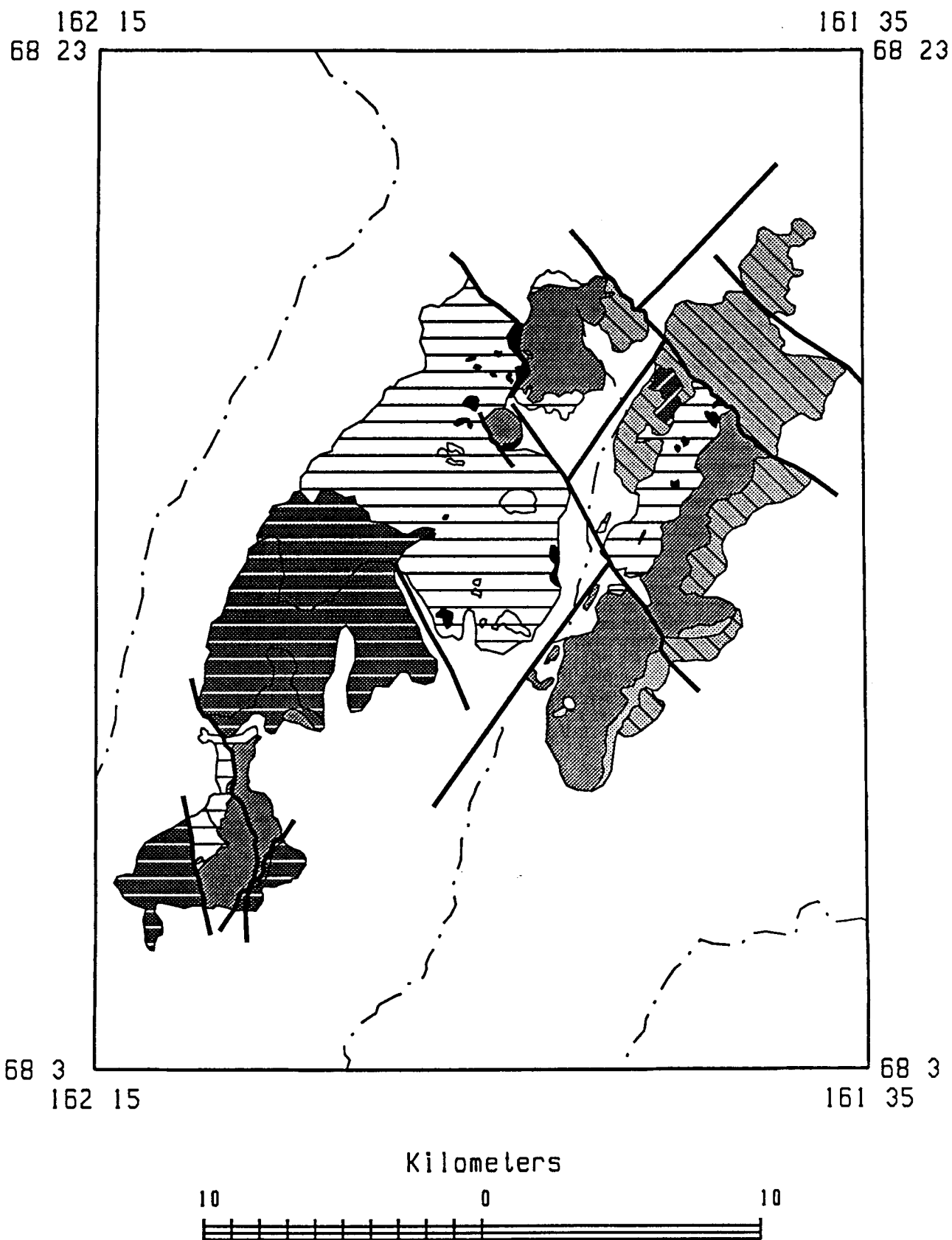


Figure 19a TM map for the Avan Hills ophiolite. See Figure 17 for explanation.



Figure 19b Intensity of serpentinization of ultramafic rocks in the Avan Hills: areas of unserpentinized rock are light grey, areas of moderately serpentinized rock are medium grey, and areas of serpentinite are dark grey.

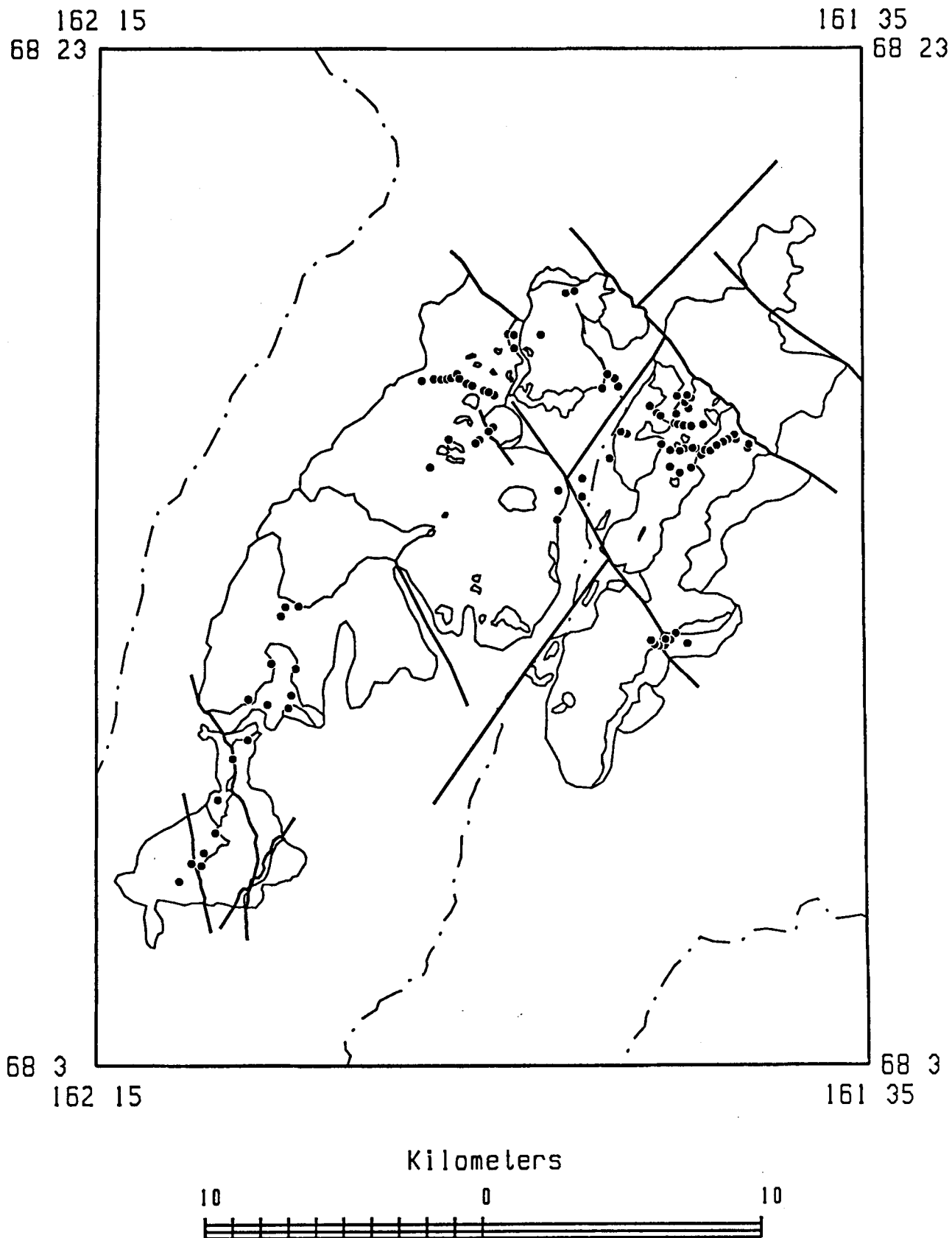


Figure 19c Sample localities (dots) in the Avan Hills.

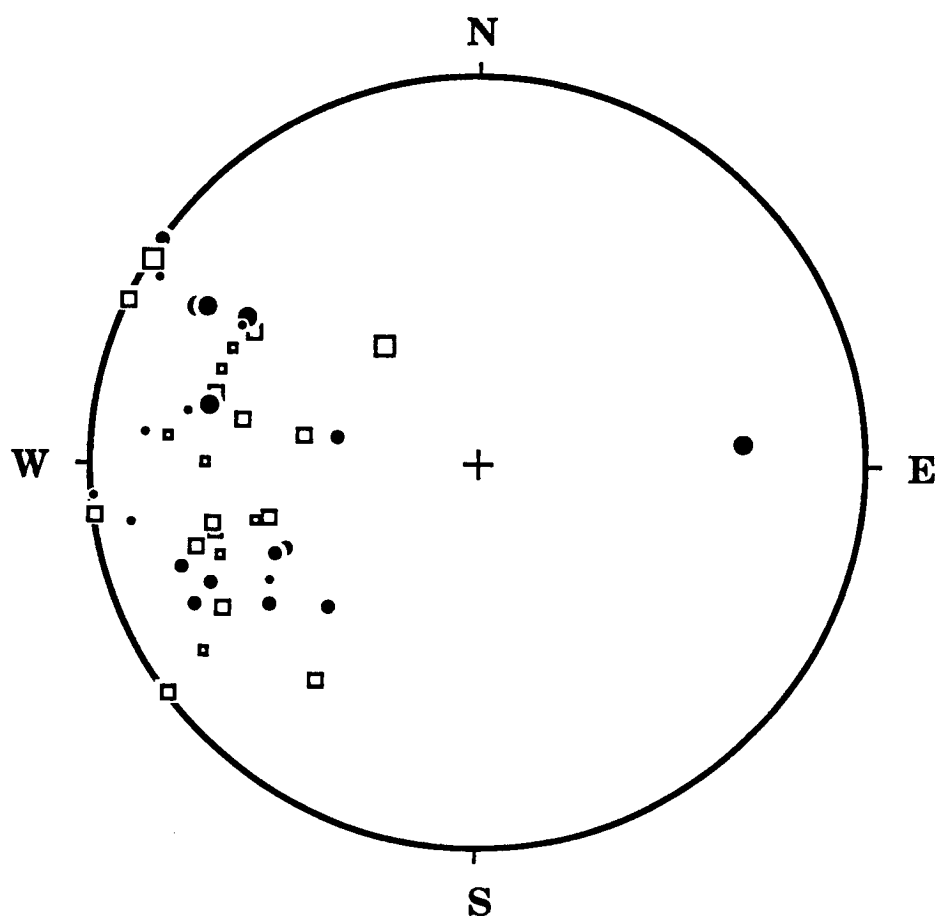


Figure 19d Lower-hemisphere, equal-area stereonet of poles to gabbro layers (solid circles) and ultramafic cumulate layers (open squares) in the north-eastern (small symbols), northwestern (medium symbols), and southwestern (large symbols) areas of the Avan Hills.

Budahn, in prep), and in the Maiyumerak Mountains, and the thick cumulate section in the Avan Hills, might be an indication that the northern Alaskan ophiolites were derived from an oceanic site with anomalously thick crust.

Field traverses in the Avan Hills showed that pyroxene occurs lower in the stratigraphic section than plagioclase. This feature can also be observed in the TM data (Figure 19a); pyroxenite units are common in the cumulate ultramafic rocks close to the contact with the overlying gabbro (the gabbro marks the appearance of plagioclase). The presence of pyroxene lower in the section than plagioclase indicates that the crystallization sequence in the "magma chamber" in which these rocks formed was olivine \Rightarrow pyroxene \Rightarrow plagioclase. This crystallization sequence is characteristic for oceanic crust formed in marginal basins or island arcs above subducted oceanic lithosphere, where water from the subducted slab is thought to suppress plagioclase crystallization (Pearce et al., 1984). The sequence is unlike that of main ocean basins (olivine \Rightarrow plagioclase \Rightarrow pyroxene). The ultramafic rocks of the Avan Hills are generally moderately serpentinized, with some areas of unserpentinized rock, and with serpentinite localized along high-angle faults (Figure 19b). Previously unrecognized high-angle faults, that trend northeast and northwest, were determined from the Thematic Mapper images. . These interpreted faults, as shown in Figure 19, affect the spatial distribution of ophiolite rock units. The most southwesterly fault in Figure 19 is well exposed and was found to be a nearly vertical fault; other fault localities examined in the field did not have good exposures.

The gabbro of Avan Hills is spectrally uniform, except for a narrow area of high albedo rock along the southeast edge of the gabbro exposure (light grey in

Figure 19a). The gabbro is compositionally layered, due to variation in the pyroxene to plagioclase ratio of the rock. The layers range from less than one meter to several tens of meters wide and are too small to be resolved by the Thematic Mapper. Compositional layers in the gabbro and ultramafic cumulate rock throughout the exposure are steeply inclined to the east. The orientations of layers, from the entire exposure, are represented by poles to the layers in the lower-hemisphere, equal-area stereonet in Figure 19d (the points are the intersection of a line, oriented perpendicular to a layer, and the lower half of a sphere).

Much of the basalt exposed in the Avan Hills is spectrally like the unaltered basalt of unit lg2 in the Maiyumerak Mountains. A small area of mafic- to intermediate-composition volcanic rocks, exposed in the northeast Avan Hills, is spectrally like the altered basalt of unit ug in the Maiyumerak Mountains.

Maps of the Maiyumerak Mountains are shown in Figure 20 (a through c). The rock units of this region are described in paper A and B. Harding et al., (1987) interpreted high-angle faults in the Maiyumerak Mountains to be part of a system of faults that bound the eastern edge of the Noatak Basin. Alternatively, these faults might have originated in the ocean basin site, before emplacement of the ophiolite onto the continental margin. The faults are parallel to the trend of sheeted dikes, recognized by us during field mapping in the Maiyumerak Mountains. The sheeted dikes trend NE-SW and dip steeply to the NW (Figure 20d). These dikes are thought to have been intruded vertically at the oceanic spreading ridge at which the ophiolite formed. The orientation of joints and fractures measured in the field, and the trend of high-

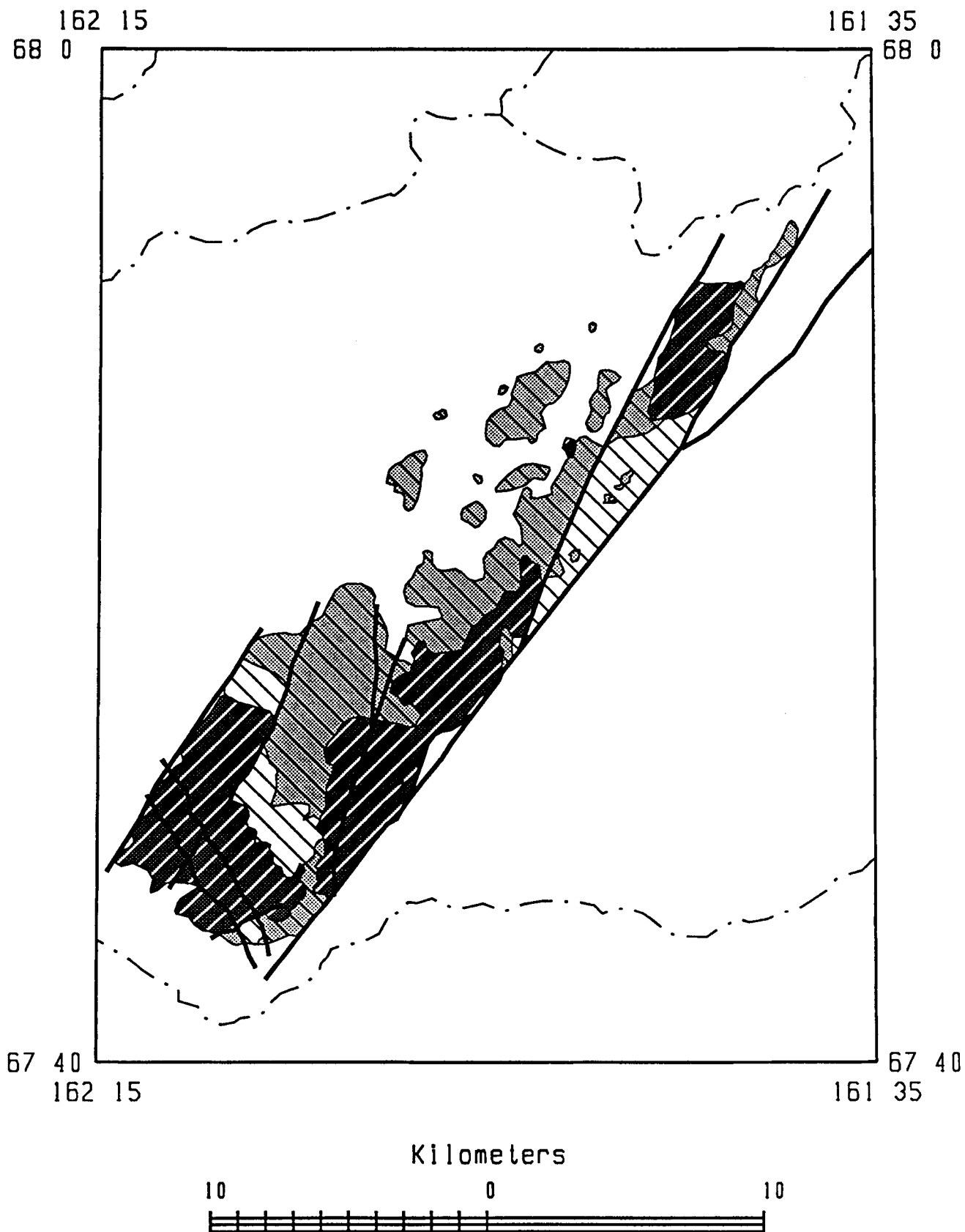


Figure 20a TM map of the Maiyumerak Mountains. See Figure 17 for explanation.

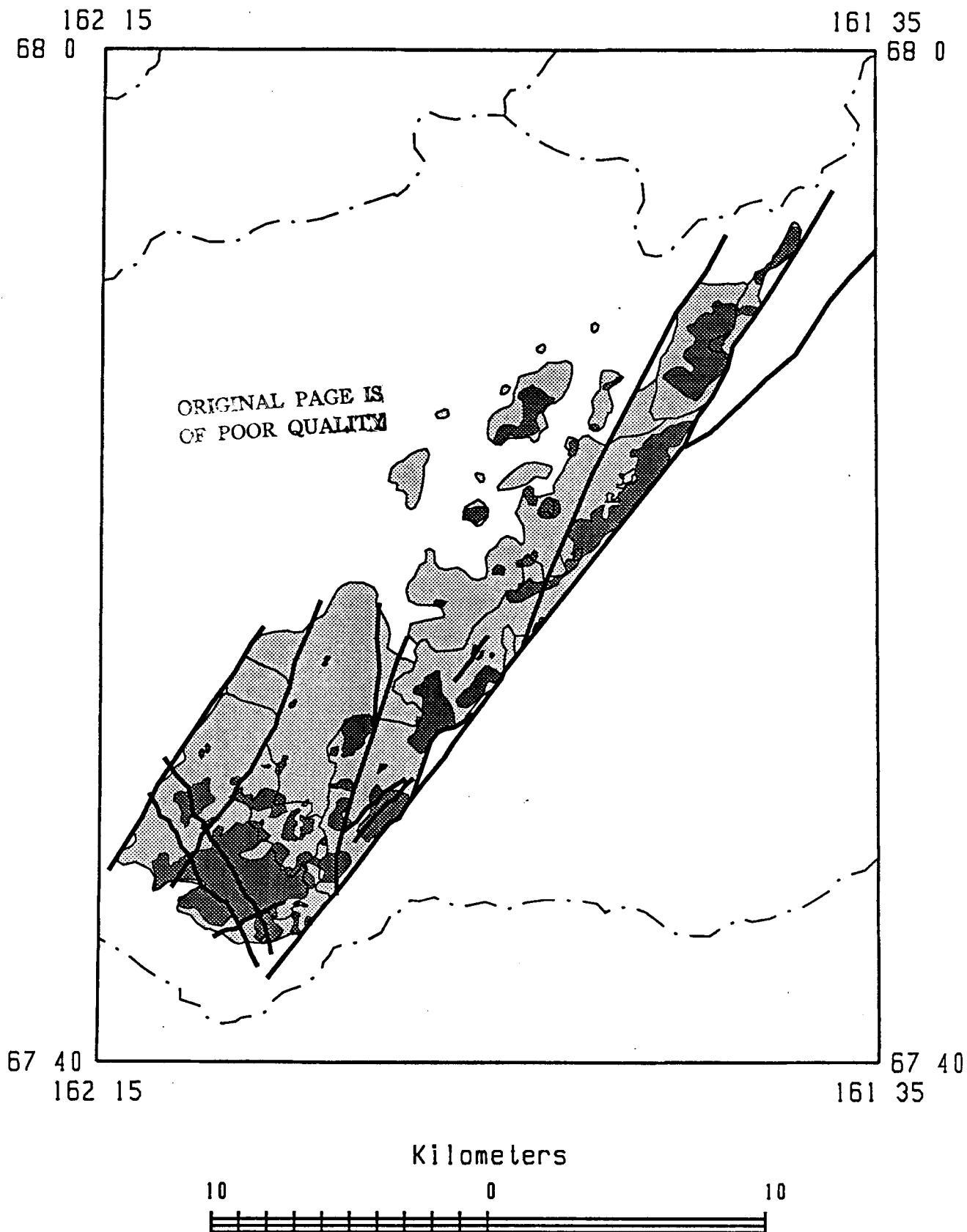


Figure 20b Hydrothermally altered (dark grey) and unaltered (light grey) basalt of the Maiyumerak Mountains. Contacts from Figure 20a are also shown.

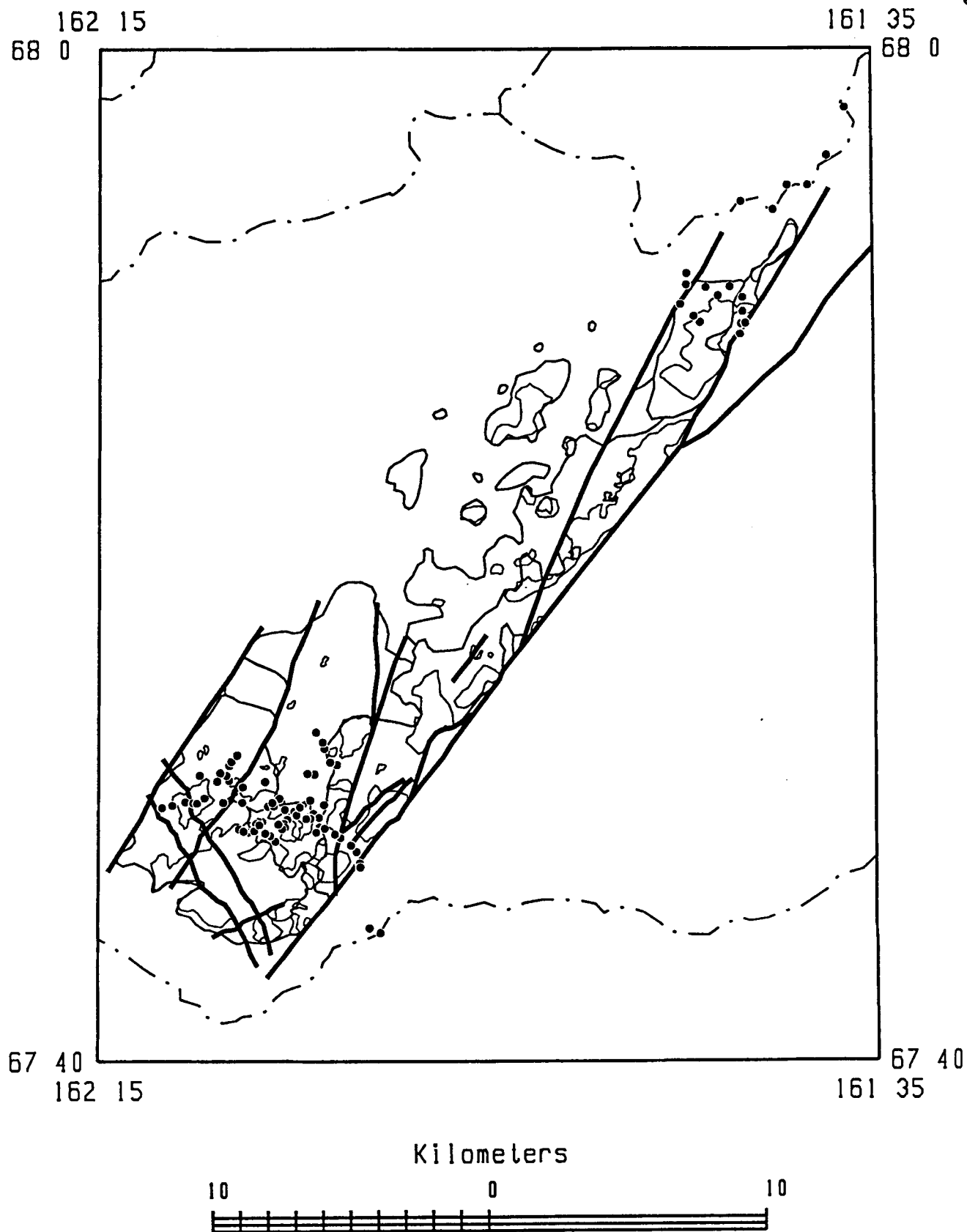


Figure 20c Sample localities (dots) of the Maiyumerak Mountains.

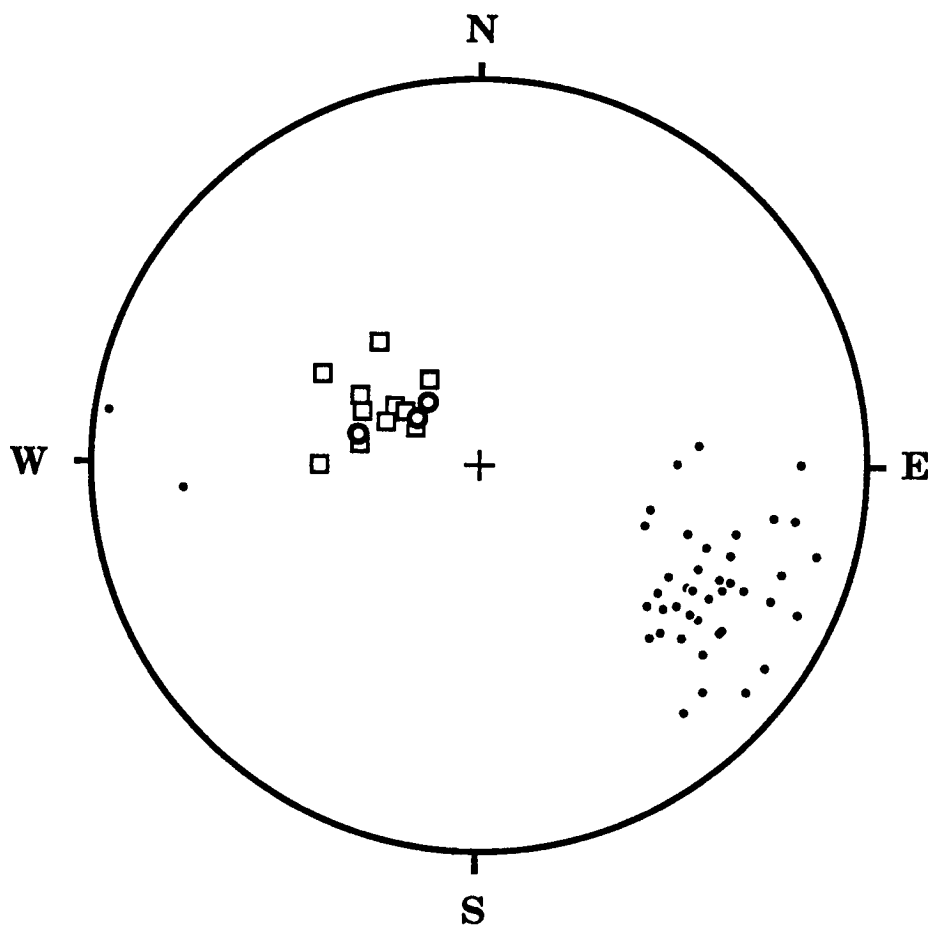


Figure 20d Lower-hemisphere, equal-area stereonet of poles to sedimentary bedding (open circles), dikes (solid circles), and flow contacts and flattened pillows (open squares) in the central Maiyumerak Mountains.

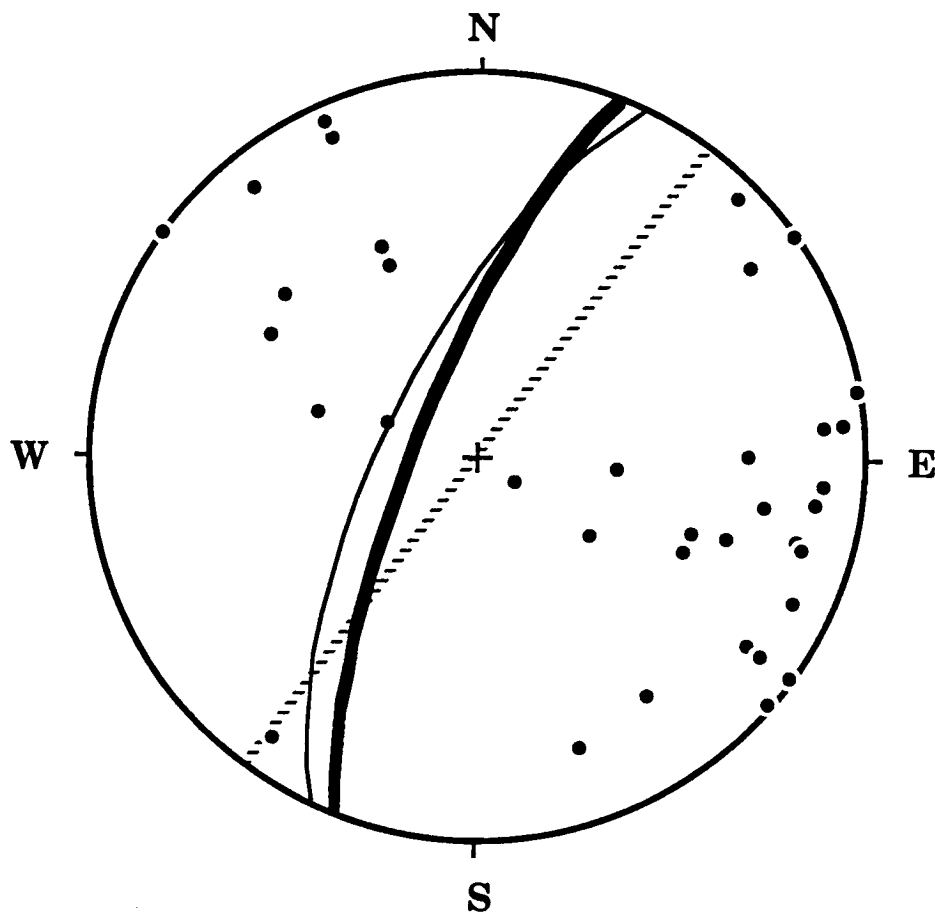


Figure 20e Lower-hemisphere, equal-area stereonet of poles to joints and fracture surfaces (solid circles), the trace of the average orientation of the joints and fracture surfaces (thick solid line), the trace of the average orientation of dikes (thin solid line), and the trend of high-angle faults interpreted from TM images (dashed line) in the Maiyumerak Mountains.

angle faults interpreted from TM images, are parallel to the sheeted dikes (Figure 20e). Normal faults along modern spreading ridges are commonly parallel to the spreading axis. These observations suggest that the faults of the Maiyumerak Mountains were ridge-parallel faults active during formation of the Maiyumerak oceanic crust.

TM maps of Asik Mountain are shown in Figure 21 (a through c). Rocks in the northern half of this region are a complex assemblage of red- and black-weathering basalt, and variably deformed and metamorphosed mafic- to intermediate-composition volcanic rocks (discussed in paper C). The southern region consists of layered gabbro and cumulate ultramafic rocks. The gabbro has been subdivided into four spectrally distinct subunits (Figure 21b). Petrographic studies indicate that gb4 is hydrothermally altered, with sauseritization of plagioclase and uralitization of pyroxene, whereas the other gabbros are not altered. Hydrothermal alteration produces increased reflectance in all TM bands, and especially in band 3 (Figure 21d), probably due to the formation of clays and iron hydroxide minerals. The origin(s) of the spectral differences between gb1, gb2, and gb3 are not known. The southwest part of Asik Mountain is comprised of interlayered dunite and pyroxenite. Some dunite layers are thick enough to be resolved in the Thematic Mapper images and are shown on Figure 21b. As at Avan Hills, the cumulate ultramafic rocks are thick, the crystallization sequence is olivine \Rightarrow pyroxene \Rightarrow plagioclase, and the compositional layers are nearly vertical (Figure 21e). The orientations of layers in the gabbro units flatten upsection. The eastern margin of Asik Mountain is bordered by a prominent topographic lineament

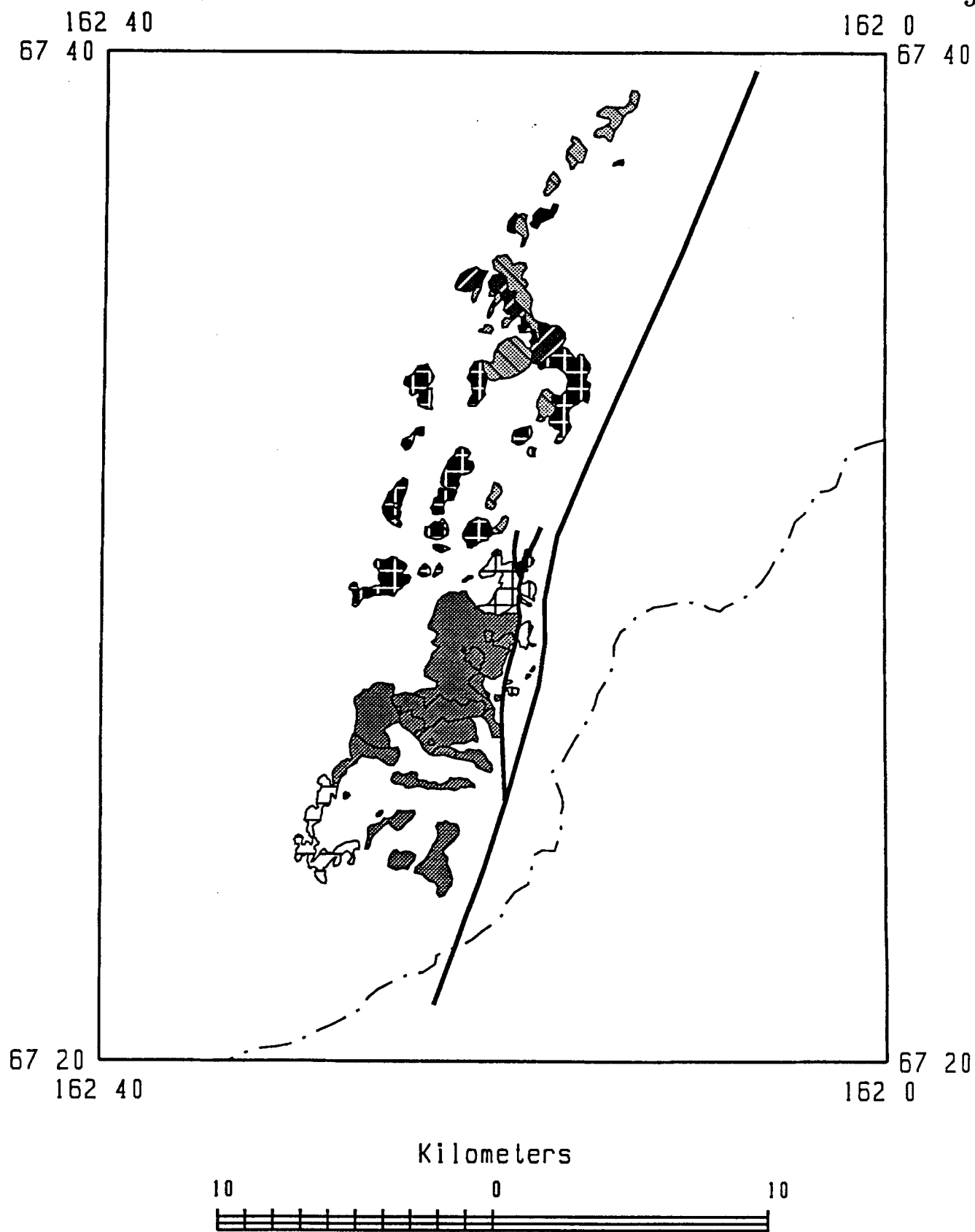


Figure 21a TM map of the Asik Mountain ophiolite. See Figure 17 for explanation.

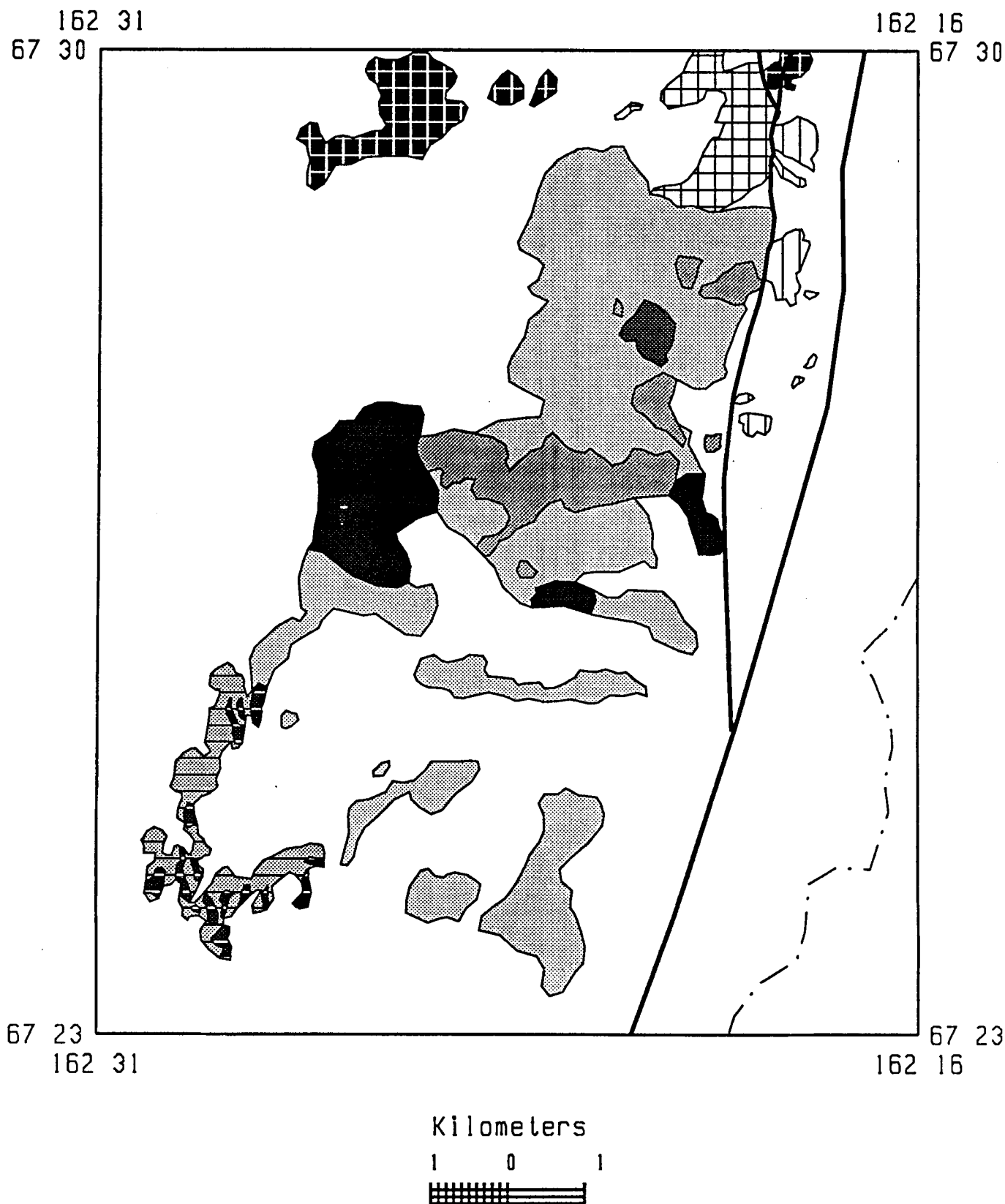


Figure 21b Rock units of Asik Mountain, with gabbros gb1 through gb4 ranging from light grey through dark grey, respectively. Cumulate dunite exposures and areas of intermixed dunite and pyroxenite are horizontally ruled and are shaded dark grey and light grey, respectively. The scale is 1:140,000.

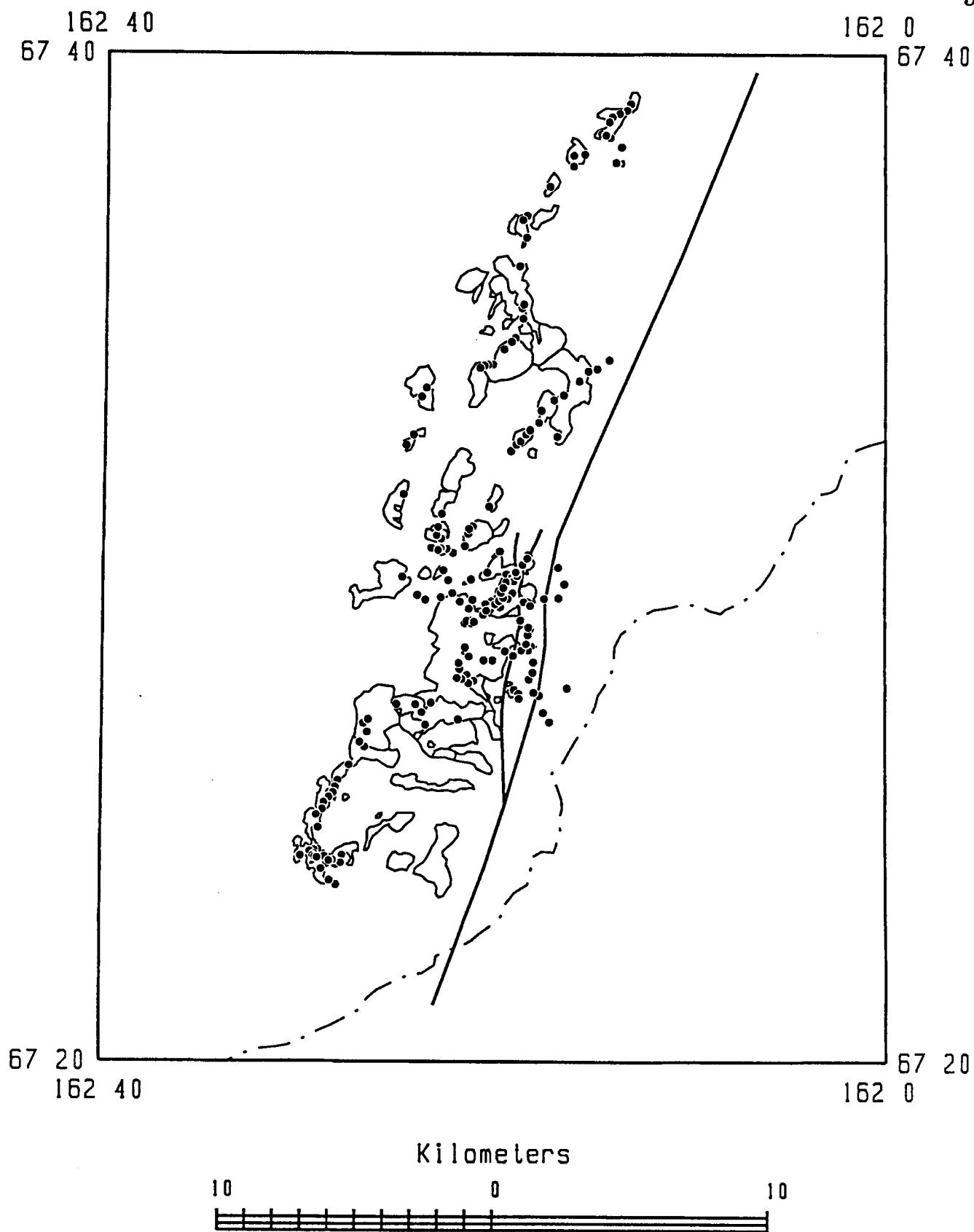


Figure 21c Sample localities (dots) at Asik Mountain.

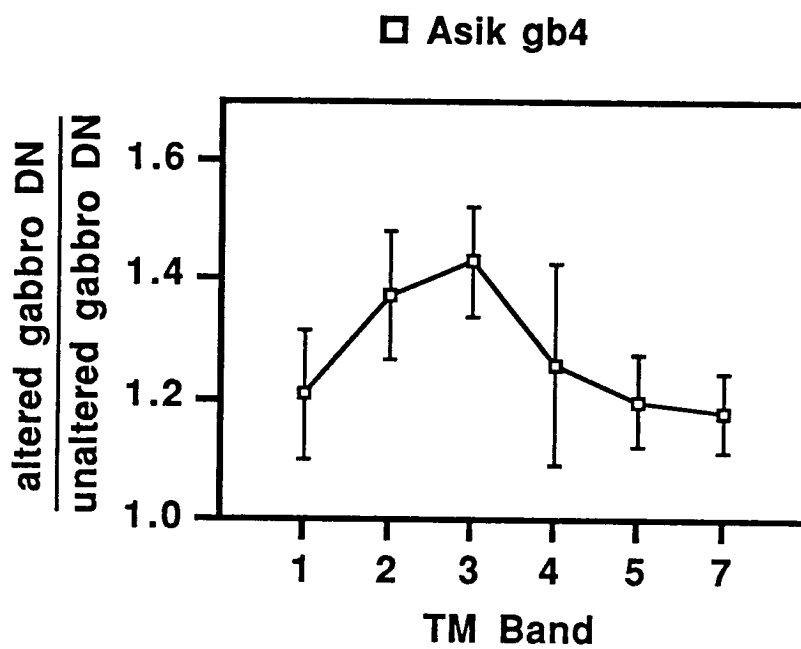


Figure 21d Effect of hydrothermal alteration on gabbro reflectance, shown in a normalized plot (note that the y-axis begins at 1.0).

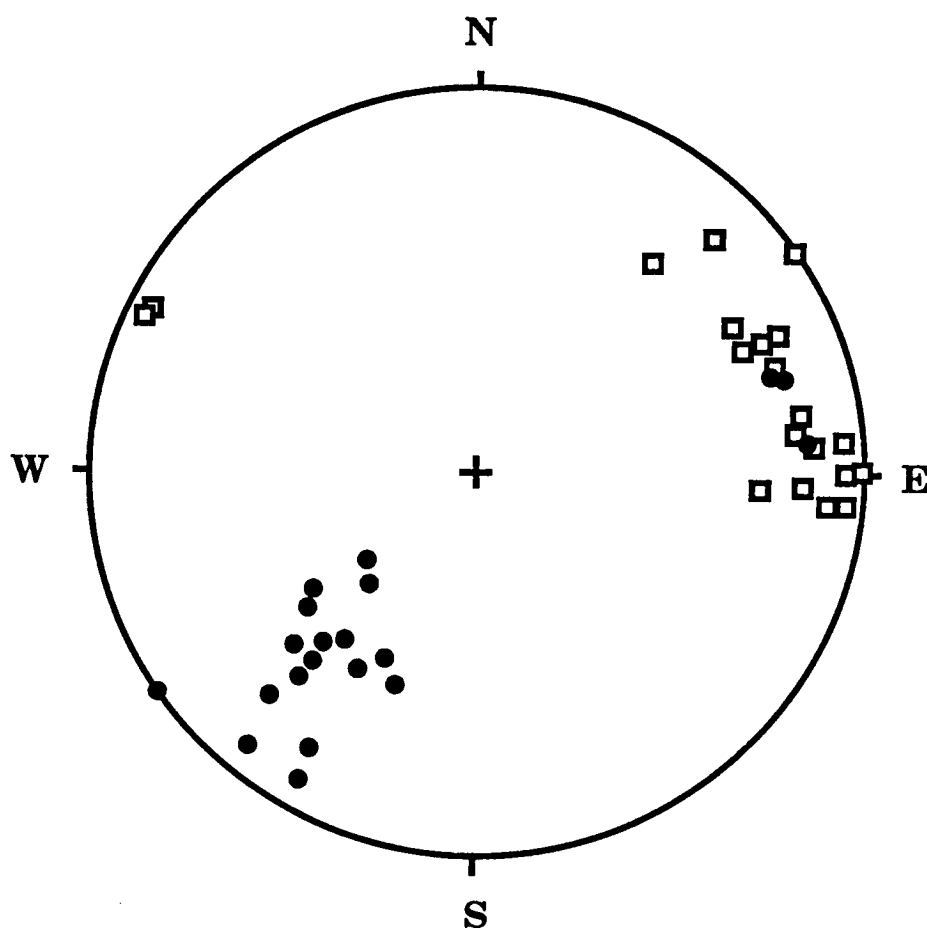


Figure 21e Lower-hemisphere, equal-area stereonet of poles to ultramafic compositional layers (open squares) and gabbroic compositional layers (solid circles) at Asik Mountain.

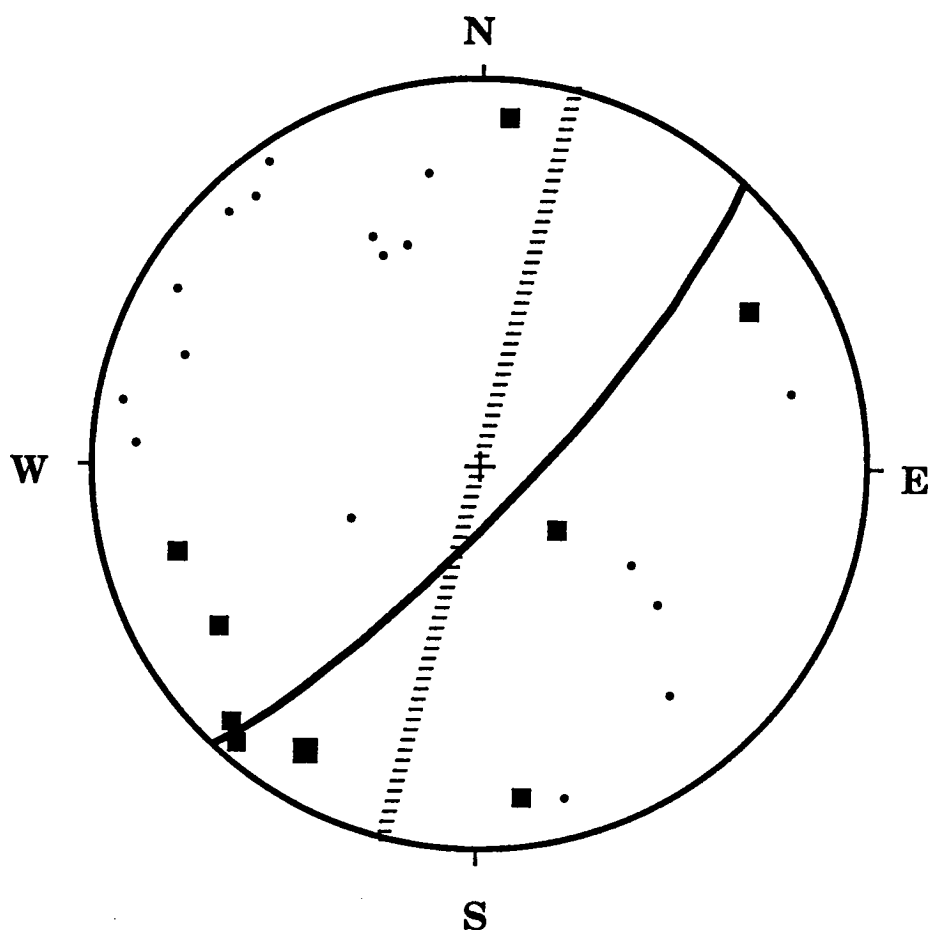


Figure 21f Lower-hemisphere, equal-area stereonet of small-scale structures of the eastern Asik Mountain area, showing poles to foliations (dots) in chert and porphyritic gabbro (of the Ipnarik Sequence), the trace of the average foliation (solid curve), the orientation of slickenside lineations (squares) and the trace of the linear valley (inferred high-angle fault) separating mafic rocks on the west from sedimentary rocks on the east (dashed line).

(Figure 4) that is interpreted to be the trace of a high-angle fault that bounds the east side of the Noatak Basin. The last fault motion was strike-slip, as determined from structures measured along a high-angle splay-fault, located to the east of the main fault (Figure 21b). The foliations in deformed rocks of the Iqnavik Sequence are nearly vertical; slickenside lineations are horizontal, and generally trend parallel to the inferred fault.

The Misheguk Mountain ophiolite is a large exposure consisting predominantly of gabbro (Figure 22, a through c). The gabbro is spectrally heterogeneous and has been divided into five subunits (Figure 22b). The causes of the spectral variations are not known, because we have not examined this exposure in the field. Our TM mapping could be used to guide future work in the Misheguk Mountains to investigate possible mineralogic variations between gabbros. Ultramafic rocks occur along the northwestern edge of the exposure. These rocks are interpreted to be cumulates because of their proximity to the gabbro contact. Pyroxenite exposures are not apparent in the ultramafic rock, indicating that the crystallization sequence for this ophiolite might have been olivine \Rightarrow plagioclase \Rightarrow pyroxene. A large exposure of metamorphic-sole rock occurs between the ultramafic rocks and the underlying basalt of the Copter Peak Allochthon. The basalt is spectrally like the unaltered lg2 unit of the Maiyumerak Mountains. The predominant topographic lineament bounding the east side of the Noatak Basin ends within the Misheguk Mountain ophiolite. The amount of slip on the inferred fault might have decreased to the north, with no slip occurring at the location of the ophiolite. Alternatively, slip on the fault may have been transferred,



EOLDOUT FRAME

68 5 161 20

68 5 160 5

Kilometers

10 0 10

FOLDOUT FRAME

Figure 22a TM map of the Misheguk Mountain ophiolite. See Figure 17 for explanation.

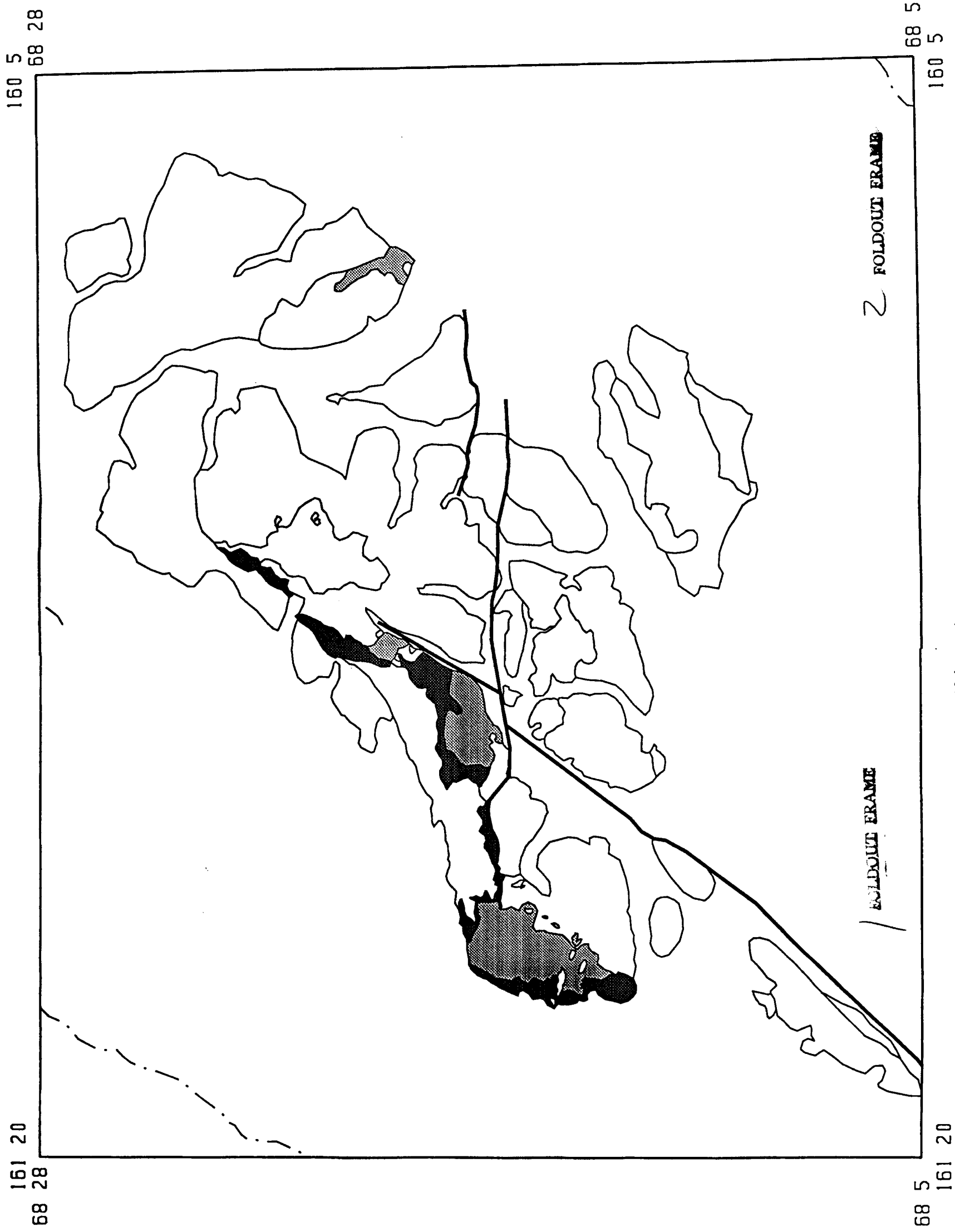


Figure 22c Intensity of serpentinitization of ultramafic rock in the Misheguk Mountain ophiolite: areas of moderately serpentinitized rock are medium grey, and areas of serpentinized rock are dark grey.

en echelon, to some other fault. A narrow, linear belt of serpentinite in the northern part of the ophiolite, occurring between basalt and gabbro, is parallel to the topographic lineament, and might be located along an en echelon fault (Figure 22c).

The Siniktanneyak Mountain exposure also consists predominantly of gabbro, with a small amount of exposed ultramafic rock and basalt (Figure 23, a, b, c). The gabbro of this ophiolite is divided into six spectral subunits (Figure 23b). Unit gb2 is equivalent to the hornblende pyroxene gabbro of Nelson and Nelson (1982) (MzPzhg of Figure 15). Units gb1, gb3, gb4, and gb5 are mapped as undivided gabbro and olivine gabbro (MzPzcg) by Nelson and Nelson (1982). Northeast-trending contacts between spectrally distinct rock, in unit gb1, were observed in the TM images. These contacts are parallel to compositional layers measured by Nelson and Nelson (1982). Unit gb6 is mapped as basalt by Nelson and Nelson (1982); this unit is poorly exposed but it is, spectrally, more like gabbro than basalt. The diorite to granite stocks of Nelson and Nelson (1982) are spectrally complex; the stocks consist of small areas of several spectrally distinct rocks, but the areas are too small to show on the TM maps. Nelson and Nelson (1982), apparently, mislocated the western stock on their map by approximately three kilometers.

Copter Peak is the type locality for the basalt of the Copter Peak Allochthon. The Copter Peak area includes several small exposures of basalt that are spectrally similar to the lg2 basalt unit of the Maiyumerak Mountains (Figure 24). The thrust contact between the basalt and the underlying

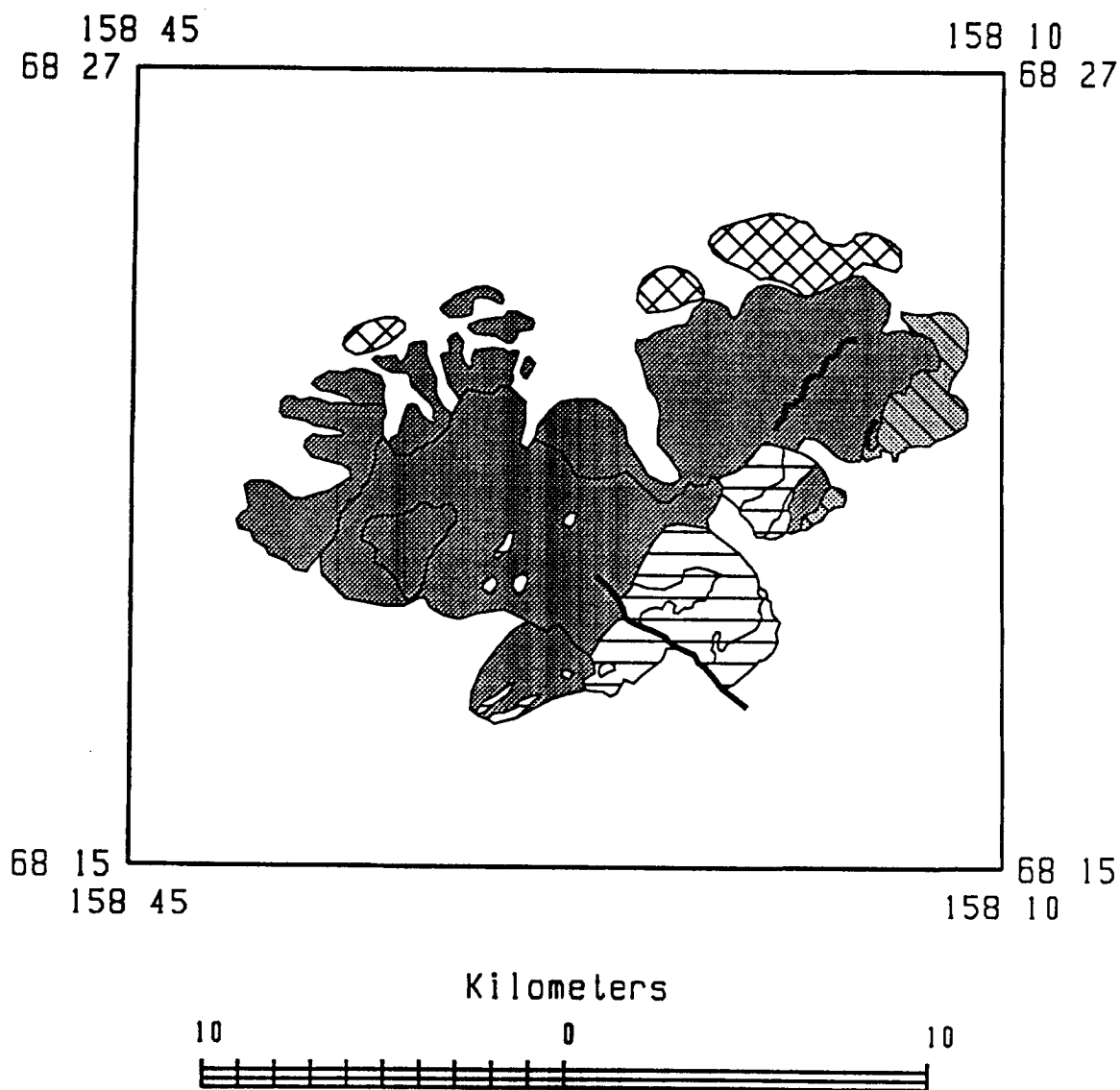


Figure 23a TM map of the Siniktanneyak Mountain ophiolite. See Figure 17 for explanation. Shaded solid lines are the trace of contacts between compositional layers.

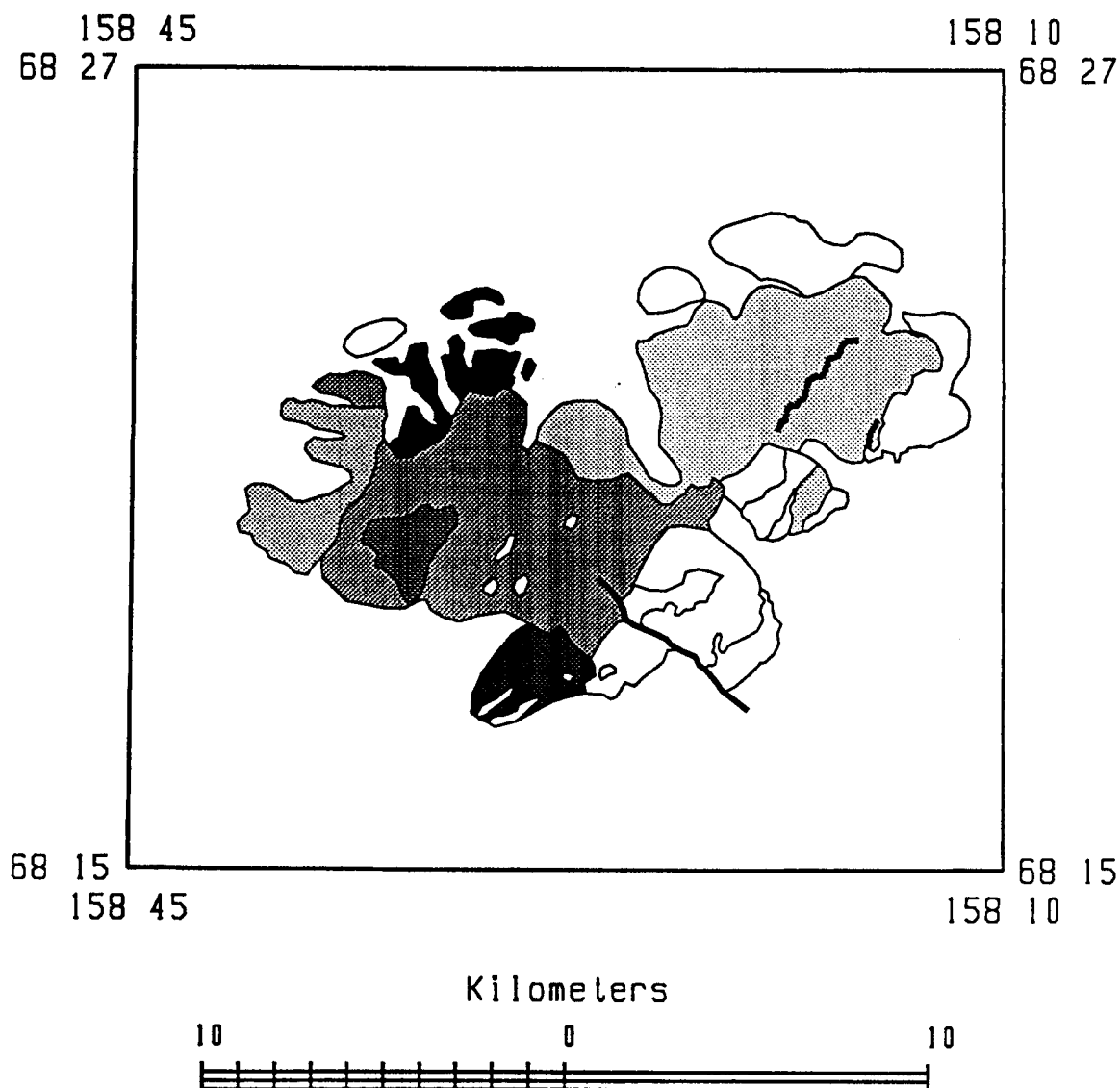


Figure 23b Spectrally distinct gabbros of the Siniktanneyak Mountain ophiolite, with units gb1 through gb6 ranging from light grey through dark grey, respectively. The shaded lines in unit gb1 are the trace of contacts between compositional layers.

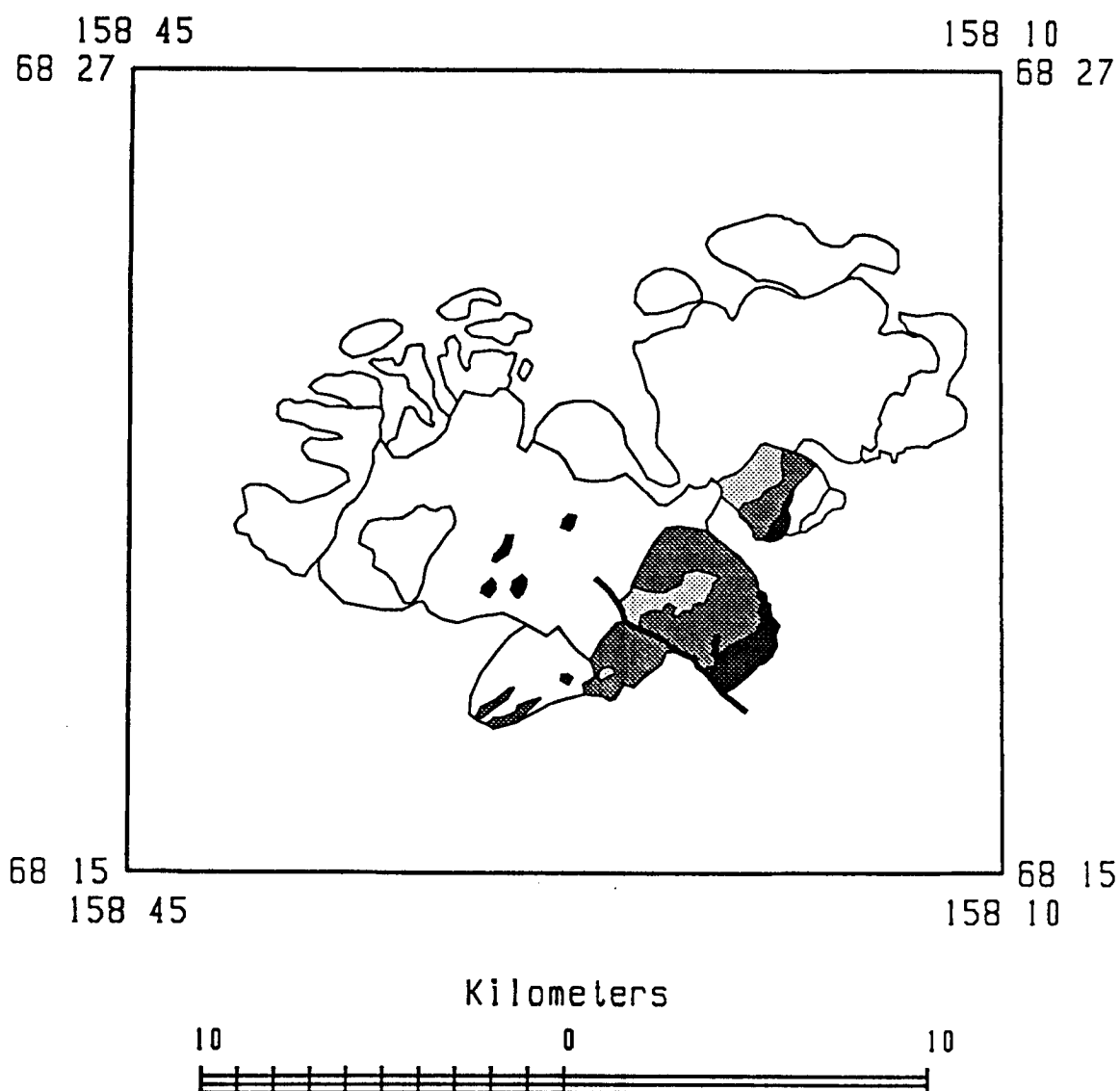


Figure 23c Intensity of serpentinization of ultramafic rocks in the Siniktanneyak Mountain ophiolite: areas of unserpentinized rock are light grey, areas of moderately serpentinized rock are medium grey, and areas of serpentinite are dark grey.

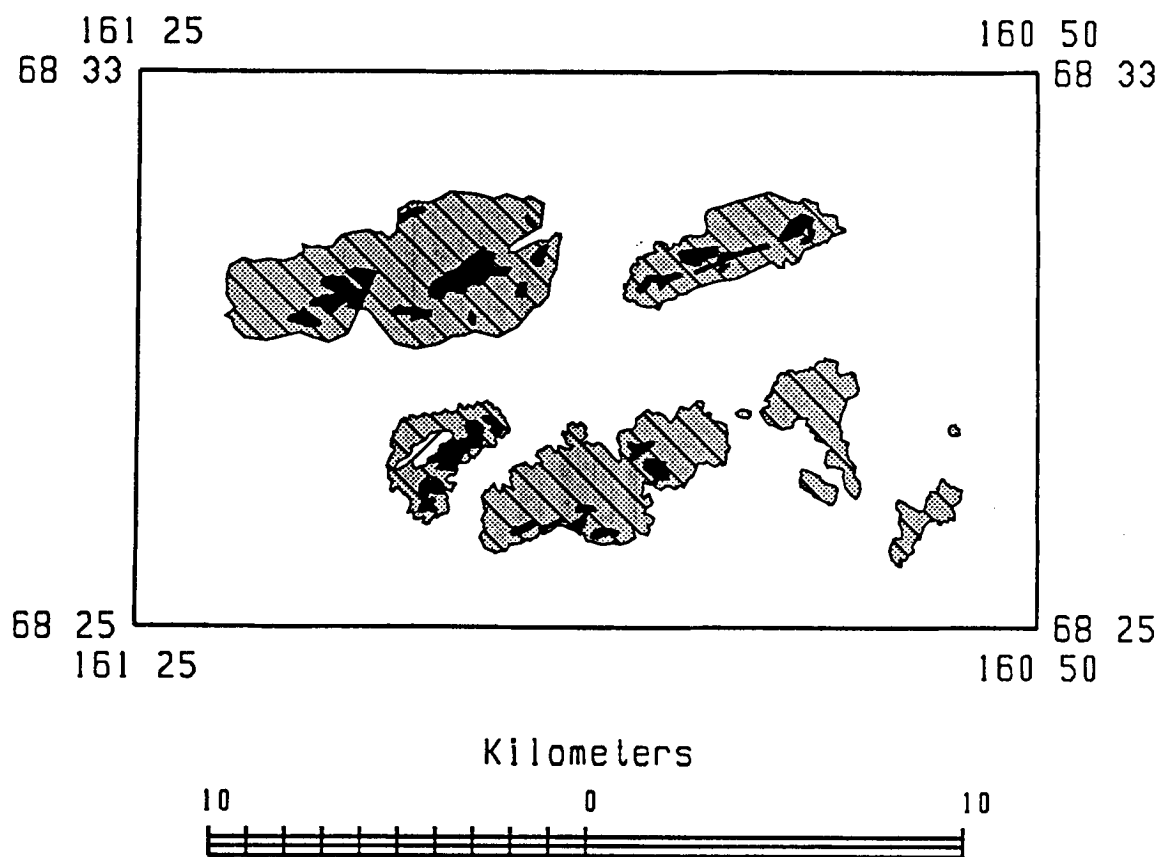


Figure 24 TM map of the Copter Peak basalt exposures. See Figure 17 for explanation. Black areas are interpreted to be hydrothermally altered.

sedimentary- rock allochthon is well-expressed in the TM images, with the trace of the contact across the topography indicating that the thrust surface is horizontal and planar. The basalts include relatively narrow, east-northeast trending, tabular exposures that are spectrally like hydrothermally altered rock of the Maiyumerak Mountains (high band 5 and 7 reflectance). The tabular character of these exposures suggests that they might be thick flows, or packets of east-northeast trending sheeted dikes.

Mapping from TM images in the Ambler District of the Angayucham Terrane (Figure 25) was difficult due to scattered cloud cover, extensive shadowing due to steep topographic relief, and extensive vegetation. However, two spectrally distinct basalts were recognized that are similar in reflectance to the altered parts of the lg2 and ug units of the Maiyumerak Mountains. The two spectrally distinct basalts correspond to dissimilar Triassic and Jurassic basalts identified by Pallister and Budahn (in press), based on petrographic, geochemical, and paleontologic studies. These basalts are described in paper A.

Gravity Modelling of Western Brooks Range Ophiolites

We have incorporated geophysical data in our remote sensing study of northern Alaskan ophiolites. This section illustrates the use of Bouger gravity data to study the subsurface boundaries of the ophiolites. Figure 26 shows Bouger gravity contours of the Noatak Basin region, of the western Brooks Range, and the surface distribution of rocks of the Misheguk and Copter Peak Allochthons, mapped from TM images. The gravity data, which is not terrain

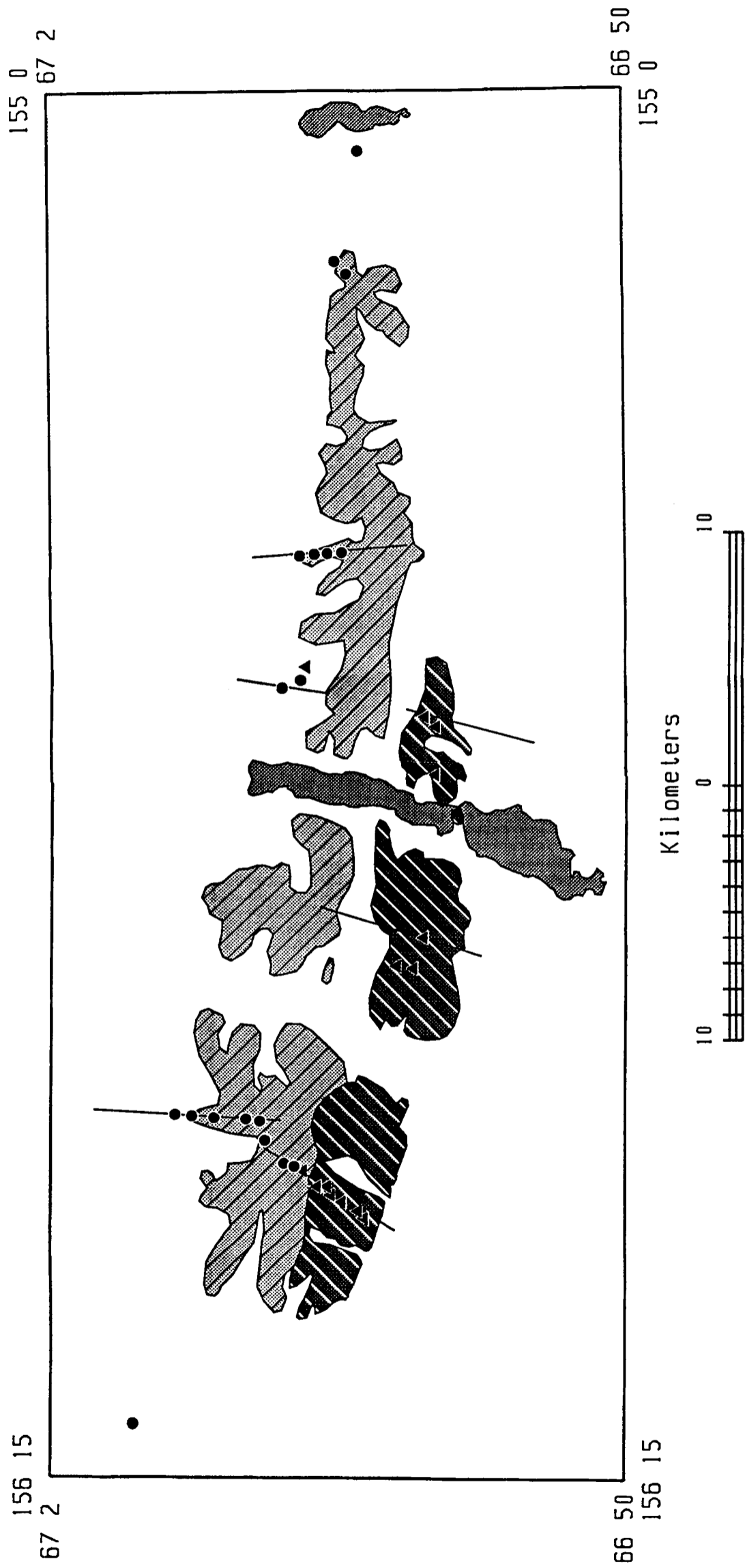


Figure 25 TM map of the basalts of the Angayucham Terrane in the Ambler District. See Figure 17 for explanation. Geochemical sample localities, along traverses (solid lines) of Pallister and Budahn (in press), are shown by triangles (light rare-earth enriched basalt) and filled circles (unenriched, flat rare-earth pattern basalt). Areas that are shaded grey and are not diagonally patterned are lakes.

(FOLDOUT FRAME

2 FOLDOUT FRAME

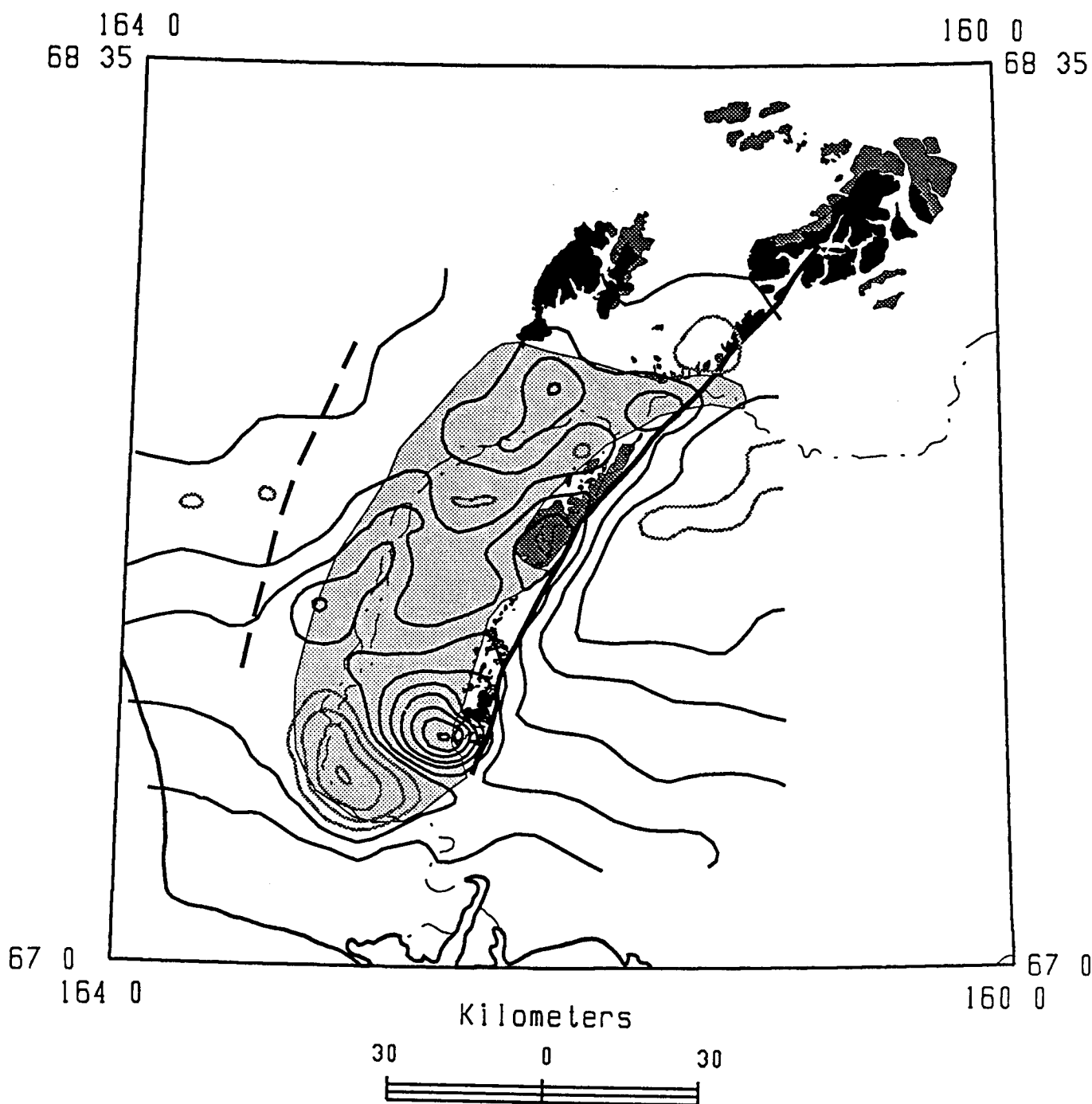


Figure 26 Bouguer gravity contours of the Noatak Basin region. The contour interval is 12.5 mgal. The maximum contour is 62.5 mgal. Contours are shaded where they indicate gravity lows. Exposures of Misheguk and Copter Peak Allochthon rocks, interpreted from Thematic Mapper images, are shown as black and dark grey areas, respectively. The Noatak Basin is shaded light grey. The prominent topographic lineament on the east margin of the basin is shown as a thick, solid line. A less prominent topographic lineament of the west side of the basin is shown as a thick, dashed line. Major rivers are shown as thin, dashed-dotted lines.

corrected, was provided by D. Barnes of the United States Geological Survey. The Noatak Basin is characterized by high-amplitude, short-wavelength gravity anomalies, as compared to the gravity field outside the basin.

Barnes (1970) and Barnes and Tailleur (1970) discussed gravity, and aeromagnetic, anomalies of the Noatak Basin. They investigated the origin of the very large-amplitude, paired gravity-high and gravity-low anomalies in the southern part of the Noatak Basin. The gravity-high, which is coincident with an aeromagnetic-high, is centered in an area Quaternary sediments just east of the Asik Mountain exposure of gabbroic and ultramafic rock (Figure 27). Barnes (1970) and Barnes and Tailleur (1970) assumed that these anomalies are produced by gabbroic rocks that extend, in the subsurface, down to the west from Asik Mountain. Our field and TM mapping strongly indicate that the aeromagnetic high centered in the area of Quaternary sediments is produced by ultramafic rock; the elongate aeromagnetic-high projects to surface exposures of ultramafic rock in the southwestern part of Asik Mountain, and the contact between gabbro and ultramafic rocks (Figure 27), and compositional layers within the ultramafic rocks (Figure 21e), are parallel to the trend of the elongate aeromagnetic-high.

The relationship between the ultramafic rock of Asik Mountain and the aeromagnetic-high is important to the interpretation of the geophysical anomalies. Barnes (1970) and Barnes and Tailleur (1970) concluded from modelling of the aeromagnetic and gravity data that the highs, if produced by gabbro, must be caused by a large mass that extends to a depth of six

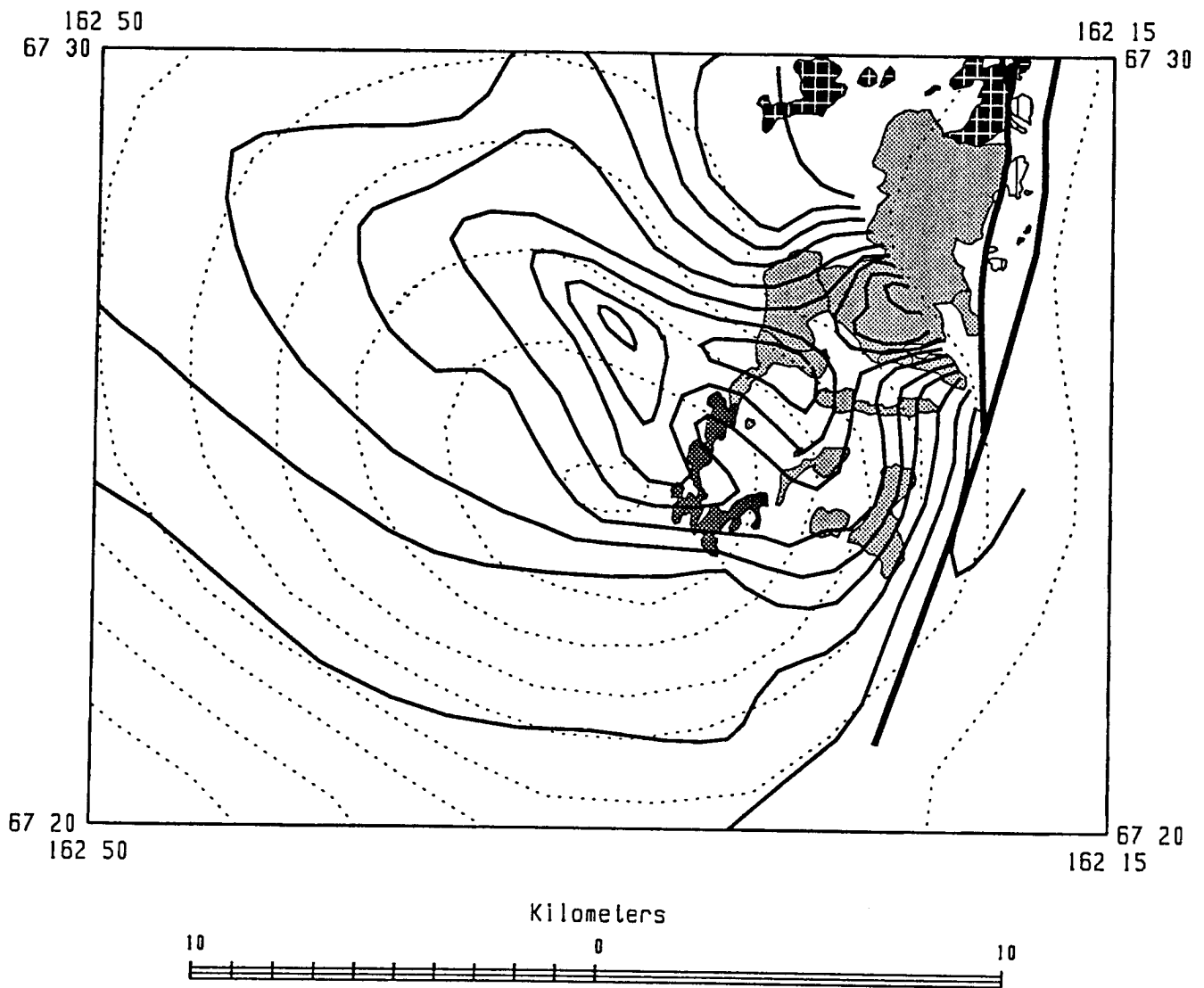


Figure 27 Aeromagnetic (solid) and gravity (dotted) contours of the southern Noatak Basin. The aeromagnetic contour interval is 200 gammas, and the maximum contour is 3300 gammas. The gravity contour interval is 12.5 mgal, and the maximum contour is 62.5 mgal. Exposed rocks, mapped from Thematic Mapper images, are gabbro (light grey), ultramafic rock (dark grey), variably deformed and metamorphosed volcanic and intrusive rock (gridded pattern) and the Ipnarik Sequence (vertical line pattern). High-angle faults are shown as thick, solid lines.

kilometers. They infer from this thickness that the mass must be an autochthonous intrusive body. This inference is not compatible with field observations that demonstrate that the gabbroic rocks of the western Brooks Range are components of thin (≤ 1 km) allochthonous thrust sheets. The base of the gabbroic rocks at Asik Mountain is not exposed, so it is possible that the gabbro is autochthonous and extends to great depths. However, the similarities between measured sections (Figure 5), and the orientations of compositional layers, at Asik Mountain and at Avan Hills, which is demonstrably a thin thrust sheet, strongly suggests that the Asik Mountain exposure is also allochthonous. A solution to the incompatibility of the geophysical modelling and the field observations would be to attribute the gravity and aeromagnetic highs, not to an extension into the subsurface of rocks of Asik Mountain, but to some unrelated mass of dense rock buried beneath the Quaternary sediments of the Noatak Basin. However, this solution is incompatible with our field and TM mapping that show that the aeromagnetic high, at least, is produced by an extension of the ultramafic rocks of Asik Mountain.

A solution to this geophysical question might be provided by using physical parameters for ultramafic rock, rather than gabbro, in modelling the anomalies. Barnes (1970) and Barnes and Tailleux (1970) used a magnetic susceptibility for the modelled source mass of 0.0045 cgs. This value is appropriate for gabbro, whereas the average magnetic susceptibility of ultramafic rock is reported to be 0.013 cgs (Telford et al., 1976). Tripling the magnetic susceptibility that is assigned to the source mass will significantly

reduce the thickness of the body required to produce the observed aeromagnetic anomaly. However, the gravity anomaly can not be accounted for in a similar manner. Barnes (1970) and Barnes and TAILLEUR (1970) used a density of 3.1 gr/cm³ for the gabbro, which is not significantly less than the density of unserpentinized ultramafic rock (3.2 to 3.3 gr/cm³). Preliminary gravity modelling, incorporating an ultramafic rock body, is shown in Figure 28 for a profile extending north from Asik Mountain through the Maiyumerak Mountains to the Noatak River. The modelling was done using a program developed by the United States Geological Survey (hypermag).

Observed gravity values are from stations that are located within 2 km of the profile. A regional gradient of -0.2 mgal per 1000 feet has been removed from the observed gravity values. The regional gradient is attributed to northward thickening of the lithosphere beneath the southern part of the Brooks Range (Barnes and TAILLEUR, 1970). The width of the rock units, perpendicular to the profile, is included as a parameter in the calculation of the model gravity values. Densities used in the model for units other than ultramafic rock (gabbro = 3.1 gr/cm³, basalt = 2.85 gr/cm³, sedimentary rock = 2.67 gr/cm³) are based on measurements of samples reported by Barnes and TAILLEUR (1970). Rock units exposed at the surface along the profile are extrapolated to depth. The models are not intended to define the precise shape of the ophiolites in the subsurface; rather, the models are intended to provide a qualitative estimate of the ophiolite thicknesses. Thick ophiolite bodies, extending to a depth of approximately 3 kilometers (10,000 feet), are required to account for the observed gravity values (Figure 28a). Thin bodies

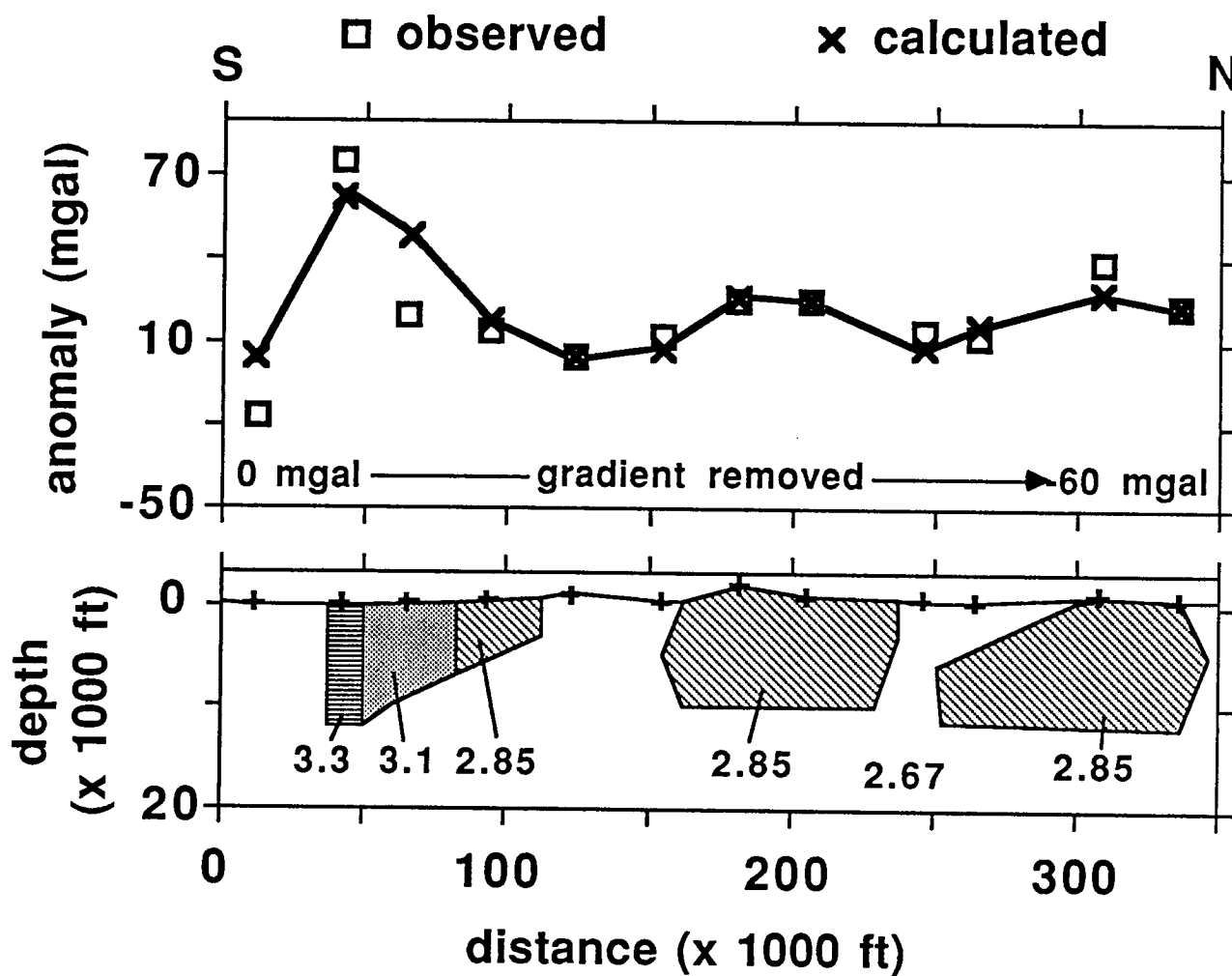


Figure 28a North-south gravity profile showing observed gravity (with gradient removed), and gravity calculated for thick ophiolite bodies. Rock units are basalt (slanted lines), gabbro (shaded), and ultramafic rock (horizontal lines). The surrounding rock is assumed to have a density of 2.67 gr/cm^3 , typical of sedimentary rock.

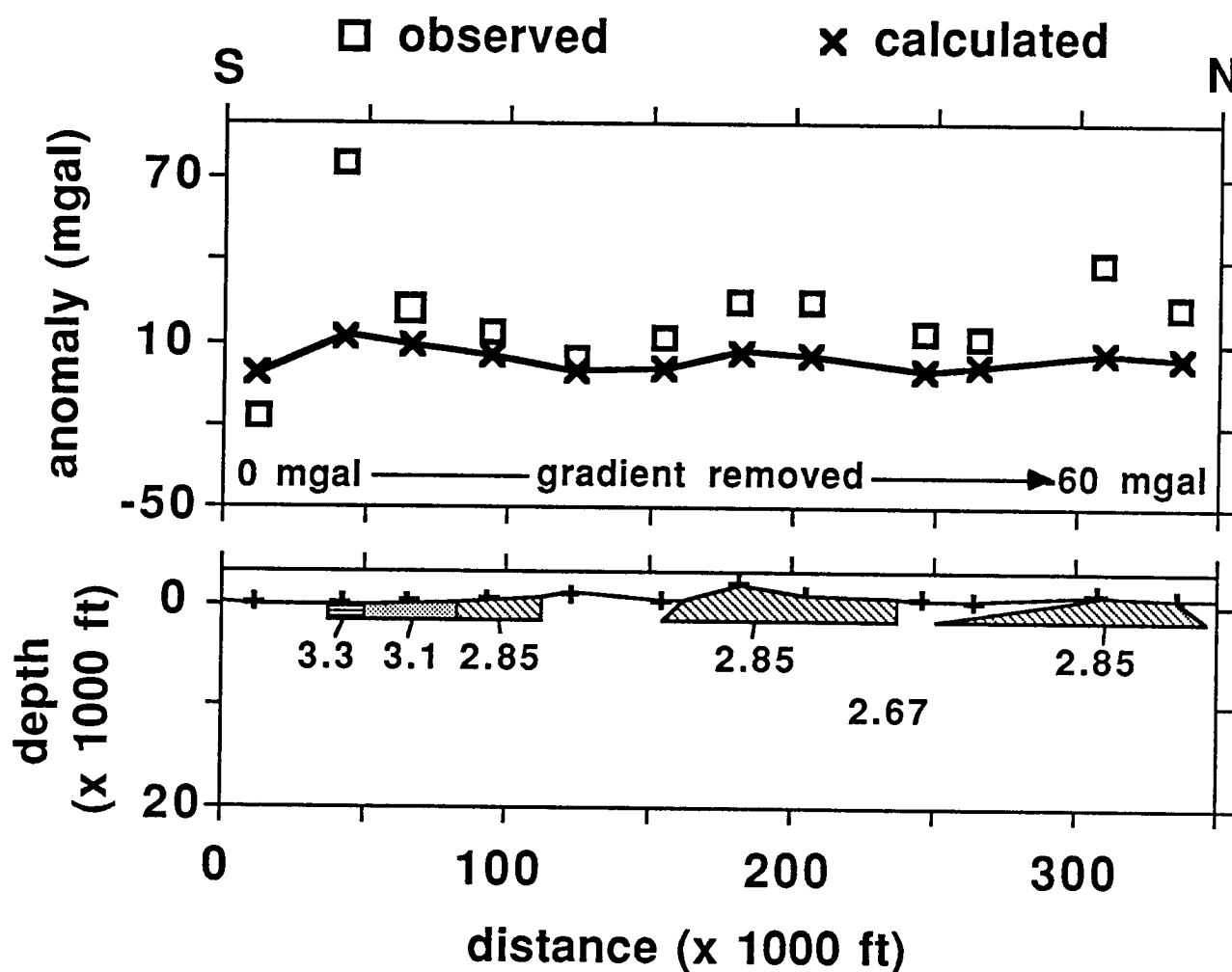


Figure 28b North-south gravity profile showing observed gravity (with gradient removed), and gravity calculated for thin ophiolite bodies. Rock units are basalt (slanted lines), gabbro (shaded), and ultramafic rock (horizontal lines). The surrounding rock is assumed to have a density of 2.67 gr/cm³, typical of sedimentary rock.

(approximately 1 km), compatible with the ophiolites being parts of allochthonous thrust sheets, produce anomalies having much smaller amplitudes than those observed (Figure 28b).

A similar conflict between gravity models and the interpretation of thin thrust sheets is seen in an east-west profile through the Maiyumerak Mountains (Figures 29, a,b c). The profile exhibits a large gravity increase that is coincident with the prominent topographic lineament identified in Figure 4. The lineament is interpreted to be the trace of a high-angle fault that separates sedimentary rocks on the east from ophiolitic rocks on the west. If the entire mass producing the observed gravity anomaly is modelled as basalt of density 2.85 gr/cm^3 , the Maiyumerak Mountain exposure must extend to great depth and it must have a steep eastern boundary (Figure 29a). If the mass in the subsurface is more dense (eg. gabbro with a density of 3.1 gr/cm^3), the thickness of the body can be significantly reduced (Figure 29b), but it is still required to be greater than the interpreted thickness of the Brooks Range ophiolites. The calculated gravity anomaly for the Maiyumerak Mountain basalts, as they are shown in a cross-section by Ellersieck (in prep), is much smaller than the observed gravity anomaly (Figure 29c).

Our preliminary gravity modelling, and the earlier work by Barnes (1970) and Barnes and TAILLEUR (1970), demonstrates that significant problems remain in understanding the subsurface geometry of the western Brooks Range ophiolites. These problems can be studied in combination with our approach to using Thematic Mapper data.

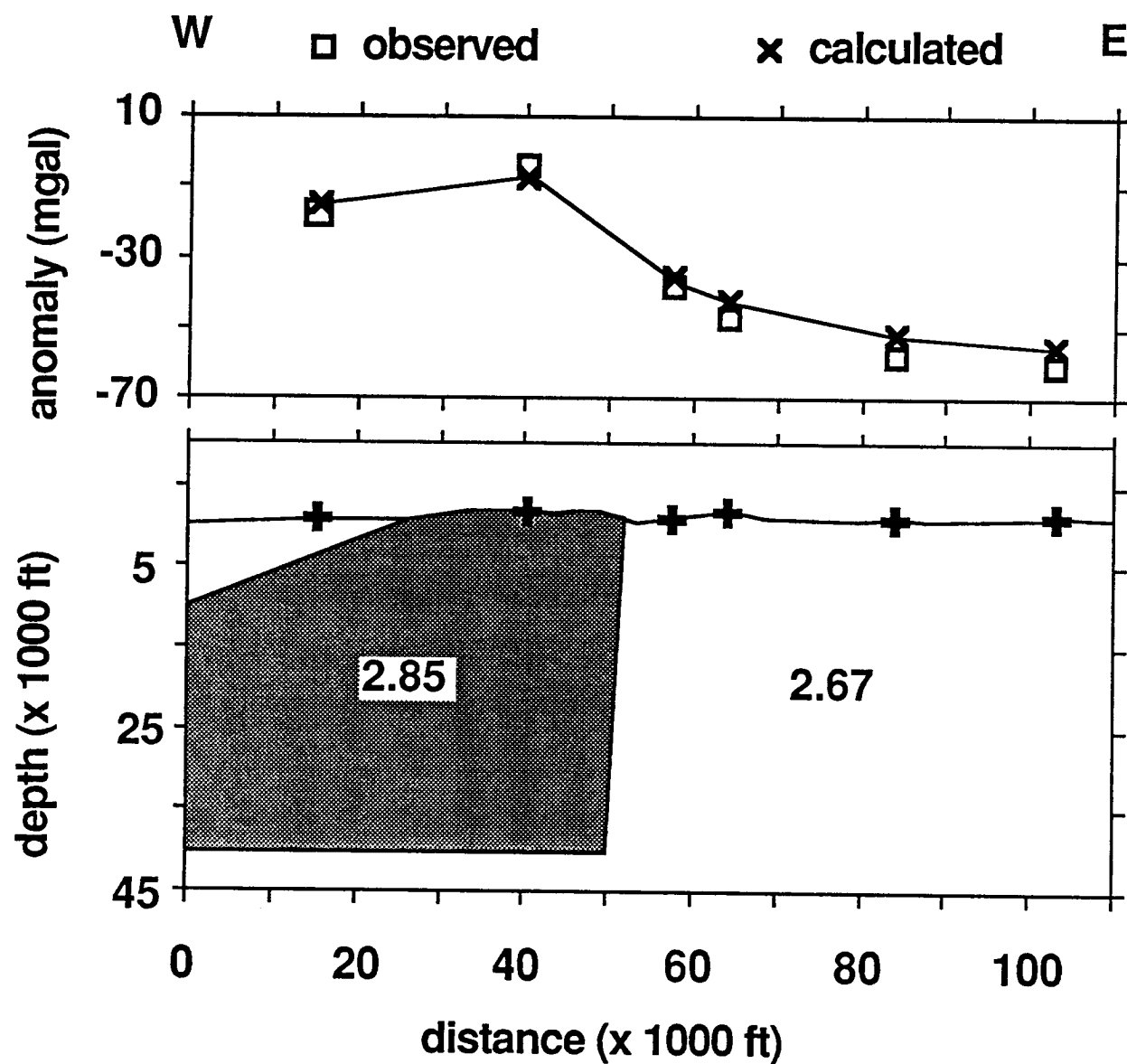


Figure 29a East-west gravity profile through the Maiyumerak Mountains, showing observed gravity, and gravity calculated for a thick body modelled as basalt of density 2.85 gr/cm^3 . The surrounding rock is assumed to have a density of 2.67 gr/cm^3 , typical of sedimentary rock.

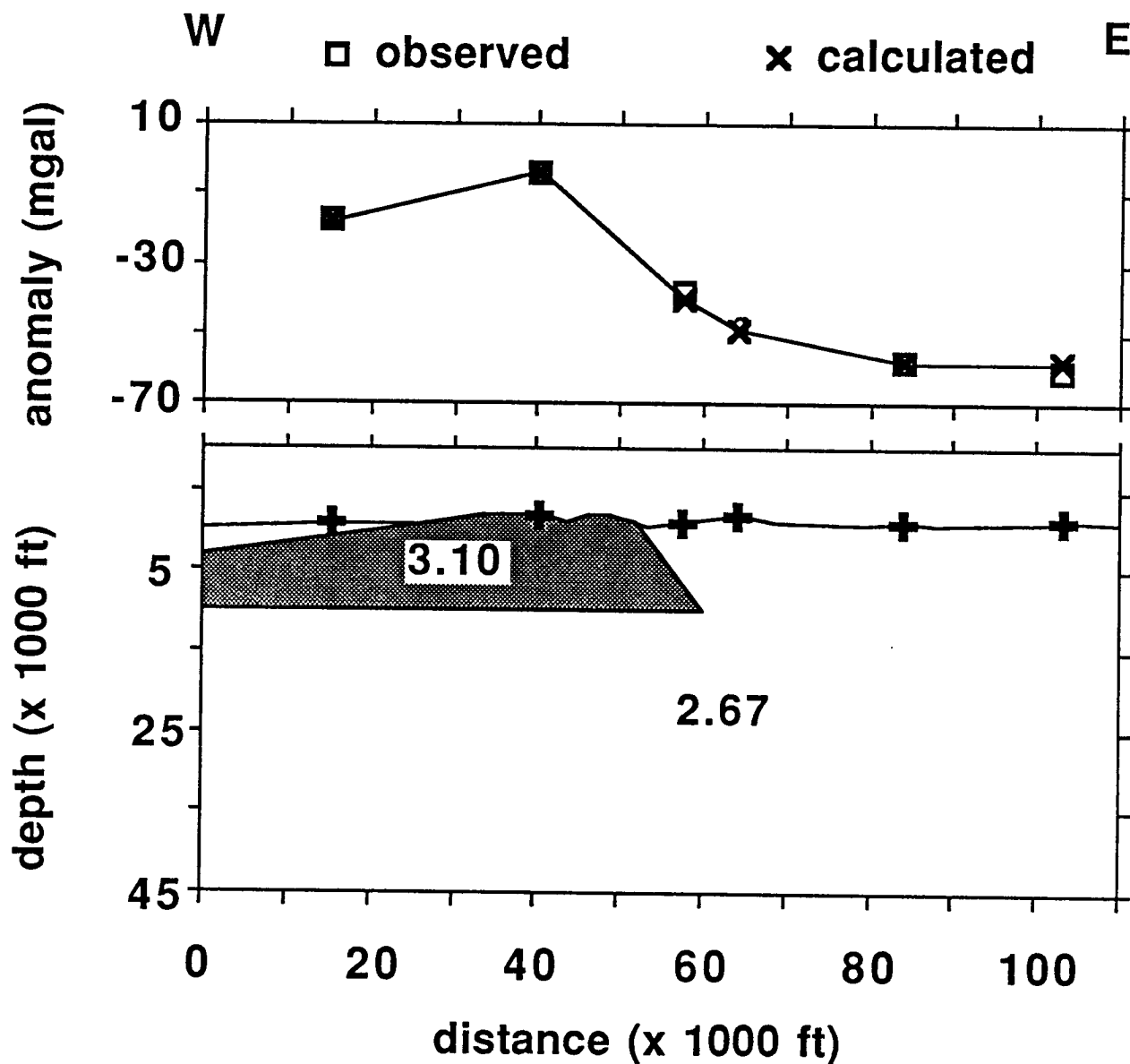


Figure 29b East-west gravity profile through the Maiyumerak Mountains, showing observed gravity, and gravity calculated for a thick body modelled as gabbro of density 3.1 gr/cm^3 . The surrounding rock is assumed to have a density of 2.67 gr/cm^3 , typical of sedimentary rock.

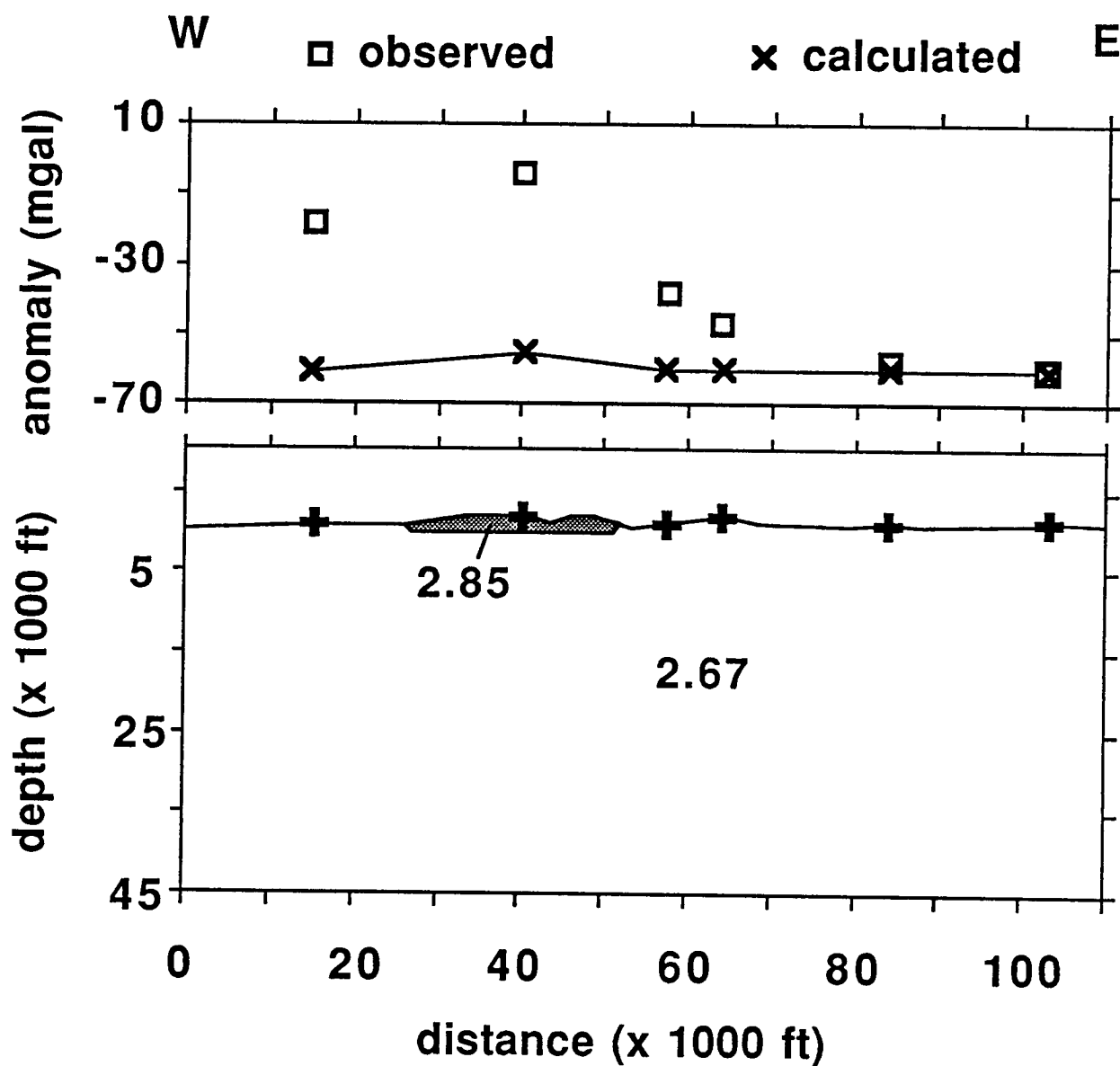


Figure 29c East-west gravity profile through the Maiyumerak Mountains, showing observed gravity, and gravity calculated for a thin body modelled as basalt of density 2.85 gr/cm^3 . The surrounding rock is assumed to have a density of 2.67 gr/cm^3 , typical of sedimentary rock.

RECOGNITION OF HYDROTHERMAL METAMORPHISM AND ALTERATION OF BASALTS IN THE BROOKS RANGE, ALASKA, USING LANDSAT THEMATIC MAPPER DATA

INTRODUCTION

Sections of oceanic lithosphere tectonically emplaced on continental margins are important to the understanding of mountain belt evolution. These rocks, generally known as ophiolites, also provide an opportunity to study the structural, lithologic, and geochemical characteristics of oceanic lithosphere, yielding a better understanding of the processes that form lithosphere. We are combining Landsat Thematic Mapper data with field mapping, geochemical analyses, geophysical data, and radiometric age studies in an investigation of oceanic lithosphere exposed by thrusting in the Brooks Range, northern Alaska. Thematic Mapper (TM) data has provided new information on mineralogic variations within these exposures, and on structures that control their spatial distribution. In this paper, we describe the use of TM data to map mineralogic and geochemical variations of basalt.

Oceanic lithosphere is comprised of a layered sequence of rocks, from bottom to top, of ultramafic rocks, gabbroic rocks, basaltic sheeted dikes, and basaltic flows. The upper portions of oceanic lithosphere are, locally, affected by hydrothermal circulation of seawater, producing metamorphism and alteration of the basaltic dikes and flows. The grade of metamorphism is dependent primarily on temperature, which increases with increasing depth

beneath the sea-floor. The resulting metamorphic facies, characterized by diagnostic mineral assemblages, typically change with depth from zeolite through greenschist to amphibolite facies (1). Hydrothermal alteration, characterized by variations of mineral and whole-rock chemical compositions, is produced by transport of ions in the circulating seawater (2). Two alteration effects of significance to remote sensing using TM data are: 1) oxidation of silicate and oxide ferrous iron to ferric iron, forming hematite, and 2) reduction of seawater sulphate-ions, forming sulphides (commonly pyrite). Both oxidized, and sulphide-bearing altered basalts, upon weathering, form reddish-colored surface coatings rich in iron-oxides and iron-hydroxides.

We have recognized spectral differences related to hydrothermal metamorphism and alteration in two regions of basalt exposures, the Maiyumerak Mountains of the western Brooks Range, and the Angayucham Mountains, located along the southern margin of the range. Both regions consist of massive and pillowed basalt flows, and basalt breccias, with interbedded tuff and chert (3,4). The flows are intruded by diabasic basalt dikes and sills. Relief in the two regions is rugged, and the exposures consist of outcrop along ridge-crests, and rubble-covered slopes. Rock surfaces are partly covered by lichen.

MAIYUMERAK MOUNTAINS SPECTRAL VARIATIONS

Previously, the Maiyumerak Mountains have been examined in reconnaissance, during regional mapping by the United States Geological Survey; neither mineralogic variations nor structures were mapped in the area. During one week of field work in 1985, we recognized a high-angle fault separating dark grey-weathering basalt from reddish brown-weathering basalt, but the rugged terrain and inaccessibility of the region constrained our mapping to a small portion of the central Maiyumerak Mountains. Subsequent examination of Thematic Mapper images demonstrated that six spectrally distinct basalts, and numerous faults, occur in the Maiyumerak Mountains (Figure 1 and Table 1).

	Maiyumerak Mountains								Angayucham Mountains			
	lower greenschist				upper greenschist				lower gr.		upper greenschist	
	altered		unaltered		altered		unaltered		altered		altered	
	lg2	lg1	lg2	lg1	ug	ug	ug	ug	Trb	Jb2	Jb1	Jb1
unit	54	126	144	52	269	86	320	68	222			
pixels												
Band 1	26.9 ± 2.5	22.4 ± 1.9	23.8 ± 1.6	26.1 ± 1.9	31.3 ± 2.6	28.1 ± 3.0	25.4 ± 2.2	28.5 ± 1.8	29.3 ± 2.5			
Band 2	21.2 2.5	18.0 0.9	17.5 1.2	18.9 1.1	20.4 1.8	18.5 1.5	20.8 1.4	21.2 1.5	21.0 1.4			
Band 3	40.7 3.6	35.8 1.9	30.0 2.2	33.1 2.4	34.2 2.7	29.7 2.3	36.2 1.7	33.9 1.7	32.6 1.8			
Band 4	43.0 4.1	38.7 1.8	35.8 2.9	32.6 2.5	36.5 2.7	30.3 3.9	39.5 3.7	43.1 7.1	39.6 5.1			
Band 5	126.3 7.9	123.9 5.9	70.7 9.2	85.4 5.7	131.6 3.8	77.0 7.4	116.6 5.6	127.1 4.3	126.9 5.4			
Band 7	64.2 3.8	70.0 3.1	38.1 5.4	53.3 4.3	75.1 4.8	45.5 4.9	61.1 2.9	66.9 2.3	68.9 4.2			

Table 1. Thematic Mapper Digital Numbers for basalts of the Maiyumerak and Angayucham Mountains, with means and one sigma standard deviations for sites on directly illuminated, south-facing slopes. The means have been corrected for atmospheric scattering by subtracting mean DN values for deep, clear water.

The largest spectral differences occur in TM band 5, with basalts having high and low reflectance appearing pink and blue, respectively, in a color composite of bands 5, 4, and 2 displayed in red, green, and blue (Figure 1A). The areas of high band 5 reflectance correlate with red-brown to orange-brown weathering basalts that have surfaces rich in iron-oxides and hydroxides, as compared to areas of basalt with low band 5 reflectance. The areas of high band 5 reflectance, which locally are gossans formed from the weathering of sulphide-bearing basalt, are interpreted to have been hydrothermally altered.

The effect of hydrothermal alteration on basalt reflectance is illustrated in plots of mean TM Digital Number (Figure 2A), and normalized Digital Number (Figure 2B), in which DN mean values for areas of altered basalt have been divided by the mean values for areas of unaltered "parent" basalt. Similarly-oriented, south-facing slopes were used to determine the mean DN values in order to minimize albedo variations due to topography. As compared to unaltered basalt, altered basalt has slightly higher DN values in bands 1-4, greatly increased band 5 DN values, and somewhat higher band 7 values. The TM DN differences are consistent with field-spectrometer measurements of *in situ* bidirectional reflectance of hydrothermally altered, and unaltered mafic volcanic rocks (5). Weathered surfaces of hematite-bearing altered andesite and sulphide-bearing altered dacite, for example, have high reflectance in TM band 5 and 7 bandwidths,

as compared to unaltered andesite and dacite, due to the high albedo of hematite and fine-grained clay minerals.

More subtle spectral variations of basalts in the Maiyumerak Mountains are related to metamorphic facies. A principal component image revealed three spectrally distinct basalts (pink, yellow, and mixed red-and-blue areas in Figure 1B). Subsequent petrographic studies demonstrated that basalt from the pink and yellow areas has lower greenschist-facies metamorphic mineral assemblages (lg₁ and lg₂), whereas basalt from the mixed red-and-blue area has upper greenschist-facies assemblages (ug). Iron-bearing minerals in the lower greenschist-facies basalt include primary clinopyroxene and iron oxides, and metamorphic chlorite and epidote. The upper greenschist-facies basalts also contain iron oxides, chlorite, and epidote, but clinopyroxene has been replaced by a green, fibrous, metamorphic amphibole of the actinolite-tremolite series.

The spectral effects of metamorphic grade are illustrated in Figure 2C, a normalized plot of DN means for areas of upper greenschist-facies basalt that were divided by the means for areas of lower greenschist-facies basalt. The DN differences, despite being very small (0 to 10 DN's), are consistent, with the upper greenschist basalt being more reflective in bands 1, 5, and 7, and less reflective in bands 3 and 4. Surprisingly, the small DN variations between lower and upper greenschist-facies basalts are similar for unaltered and hydrothermally altered basalt; the small metamorphism-dependent

A



B

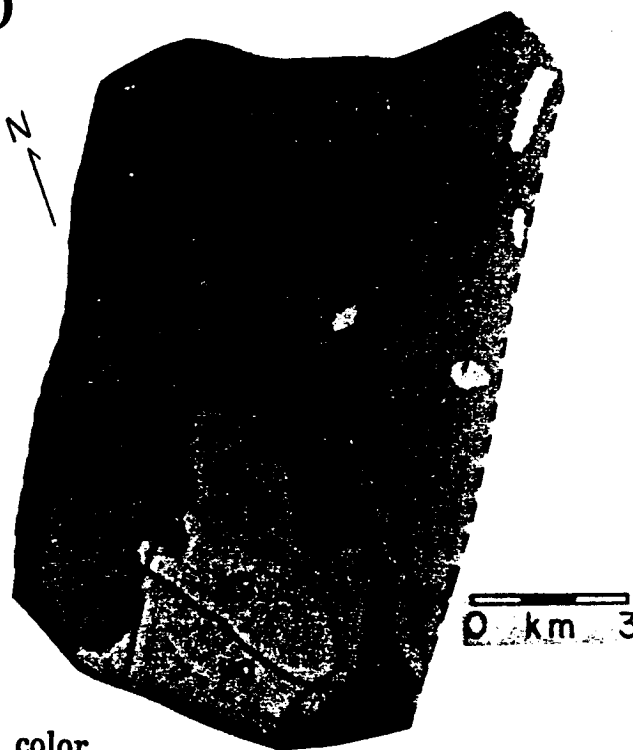
A6



C



D



original in color

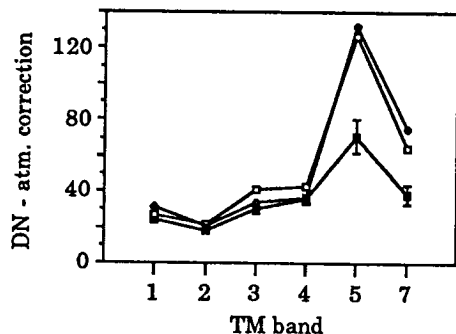
Fig. 1. Thematic Mapper images and geologic interpretation of the Maiyumerak Mountains: A) TM bands 5, 4, and 2 (linearly scaled) displayed in red, green and blue respectively. B) Principal components 5, 4, and 3, derived from a transformation of the six TM reflectance bands, displayed in red, green, and blue. Areas of shadow and vegetation have been masked, and interpreted geologic contacts are superimposed. C) TM bands 4, 3, and 2 displayed in red, green, and blue. D) Geologic interpretation with upper greenschist-facies basalt (ug) in shades of blue, and two lower greenschist-facies basalts (lg₁ and lg₂) in shades of brown and orange, respectively. Areas of hydrothermal alteration are indicated by the lighter-colored hues. Broad lines represent high-angle faults, and barbed lines represent low-angle faults, with barbs on the upper-plate side. The lines are dashed where interpretation of the images is less certain.

C-2

ORIGINAL PAGE IS
OF POOR QUALITY

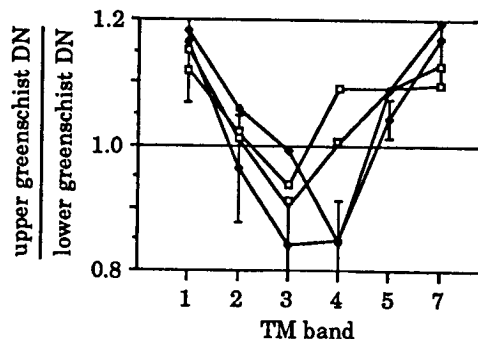
A) Representative Basalt Digital Numbers

- lower greenschist, hydrothermally altered
- lower greenschist, unaltered
- ◇ upper greenschist, hydrothermally altered



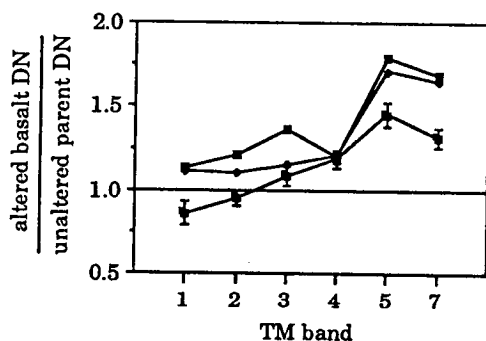
C) Effect of Metamorphic Grade

- ◇ Maiyumerak Mtns. altered basalt
- ◆ Maiyumerak Mtns. unaltered basalt
- Angayucham Mtns. altered basalt



B) Effect of Hydrothermal Alteration

- ◇ upper greenschist
- lower greenschist



D) Effect of Geographic Location

- ◇ upper greenschist
- lower greenschist

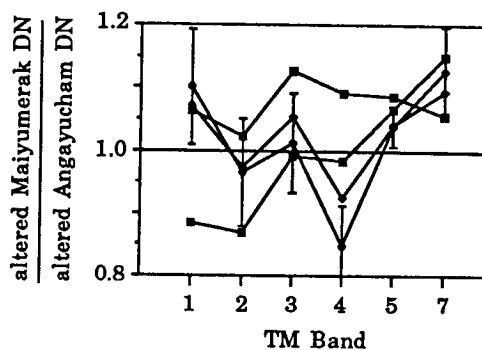


Fig. 2. Plots of A) mean Digital Number minus atmospheric scattering correction (from Table 1), and B, C, and D) normalized Digital Number for basalts of the Maiyumerak and Angayucham Mountains. Representative one sigma standard deviations are shown for selected curves.

reflectance variations are preserved despite the large variations in band 5 and 7 reflectance produced by hydro-thermal alteration. The specific mineralogic variations producing the metamorphism-dependent spectral differences are not known. However, the unaltered upper greenschist-facies basalt weathers dark grey, in comparison to the slightly redder-brown weathering, unaltered, lower greenschist-facies basalt; apparently, the presence of actinolite causes less iron to be available for the formation of iron-oxides and hydroxides during weathering.

Spectral differences of basalts in the Maiyumerak Mountains are not apparent in a standard false-color infrared display (Figure 1C). However, several NNE-trending topographic lineaments are best recognized in the false-color infrared image. Faults have been interpreted to occur in the Maiyumerak Mountains (Figure 1D), based on field observations, and the geometry of spectral boundaries and topographic lineaments identified in the TM images. The inferred sequence of events affecting the Maiyumerak basalts is: 1) hydrothermal metamorphism of oceanic basalts, producing lower and upper greenschist-facies mineral assemblages, 2) low-angle faulting (either thrusting or low-angle normal faulting) juxtaposing lower-greenschist basalt structurally above upper-greenschist basalt, 3) hydrothermal alteration of both basalts (note that the area of alteration crosses the southern low-angle contact), and 4) high-angle faulting, offsetting the low-angle fault contact.

ANGAYUCHAM MOUNTAINS SPECTRAL VARIATIONS

A similar correlation between reflectance and metamorphic facies occurs in the Angayucham Mountains, located 300 km east of the Maiyumerak Mountains. The Angayucham Mountains consist, in part, of south-dipping thrust sheets of Jurassic, upper greenschist-facies basalt and Triassic, lower greenschist-facies basalt (4). No differences between the basalts were recognized in the field, and each basalt is described as being dark green-gray to tan weathering (4). Only subsequent petrographic studies and analysis of radiolaria microfossils in interpillow cherts documented differences between the basalts (4). The metamorphic mineralogies of the two basalts are similar except that the upper greenschist basalt contains a green, fibrous amphibole of the actinolite-tremolite series, as in the Maiyumeraks, as well as stilpnomelane. Despite their reported similar weathering colors, TM images do differentiate the basalts; as in the Maiyumerak Mountains, the upper greenschist basalt is more reflective in bands 1, 5 and 7, and less reflective in band 3, as compared to the lower greenschist basalt (Figure 2C). The DN values for basalts of the same facies in the Maiyumerak and Angayucham Mountains are similar; normalized plots comparing the two regions are relatively flat and near unity (Figure 2D). Most of the basalt exposures in the Angayucham Mountains have high band 5 and 7 reflectance (Table 1), suggesting that the basalts have been hydrothermally altered. This is consistent with the report that the basalts are hematite-bearing (4).

METAMORPHIC FACIES AND TECTONIC SETTING CORRELATION

The recognition of spectral variations related to metamorphic facies led us to study the geochemistry of Maiyumerak Mountain basalts. We, and others (4), have found geochemical differences in the basalts of the Brooks Range that correlate with the spectral and metamorphic variations. This is a particularly useful result because the geochemical variations are indicative of formation of the basalts in different oceanic settings. Thus, the TM images are making it possible to map the spatial distribution of basalts of different origins. In basalt, the concentrations of various immobile trace elements and rare-earth elements (that are little affected by metamorphism and alteration) vary depending on the tectonic setting of the basalt's site of crystallization. For example (6), modern basalts from known tectonic settings are distinguished based on the concentrations of hafnium, thorium, and tantalum (Figure 3).

The Hf, Th, and Ta concentrations of the lower and upper greenschist-facies basalts in the Maiyumerak Mountains are most like those of modern tholeiitic and calc-alkaline, convergent plate-margin basalts, respectively (Figure 3). This and other trace element data, and rare-earth element patterns, suggest that the Maiyumerak basalts originated in an island arc and/or marginal basin setting within which basalt compositions varied

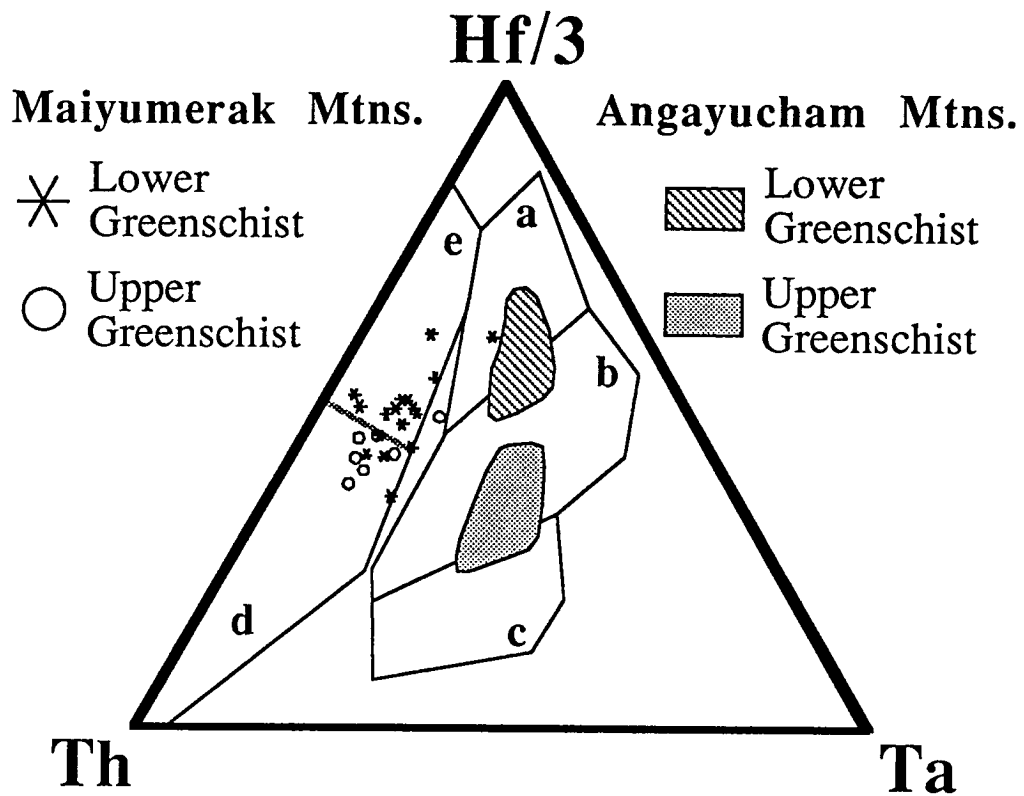
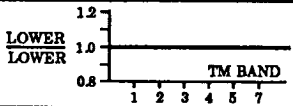
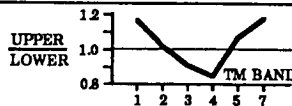
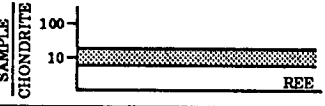



Fig. 3. Hafnium/3 vs. thorium vs. tantalum ternary plot. The fields for the Angayucham Mountains basalts are from (4). The fields of modern basaltic rocks of known tectonic setting are: a) normal mid-ocean ridge basalt, b) enriched mid-ocean ridge basalt and tholeiitic within-plate basalt, c) alkaline within-plate basalt, d) calc-alkaline convergent plate-margin basalt, and e) tholeiitic convergent plate-margin basalt (after 6).

MAIYUMERAK MOUNTAINS BASALTS

MM FACIES	LOWER GREENSCHIST	UPPER GREENSCHIST
NORMALIZED TM DIGITAL NUMBERS		
COLOR	REDDISH BROWN	DARK GREY
FE-BEARING MINERALS	CHLORITE + EPIDOTE + CLINOPYROXENE + IRON OXIDES	CHLORITE + EPIDOTE + ACTINOLITE + IRON OXIDES
RARE EARTH ELEMENT PATTERNS		
AGE	MIDDLE JURASSIC OR OLDER	MIDDLE JURASSIC OR OLDER
HF-TH-TA	CONVERGENT PLATE-MARGIN THOLEIITIC BASALT	CONVERGENT PLATE-MARGIN CALC-ALKALINE BASALT
TECTONIC SETTING	ISLAND ARC OR MARGINAL BASIN	ISLAND ARC OR MARGINAL BASIN

ANGAYUCHAM MOUNTAINS BASALTS

(from Pallister and Budahn, in press, except DN values)

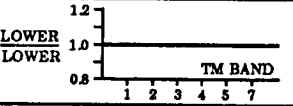
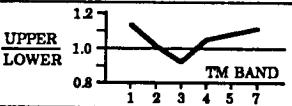
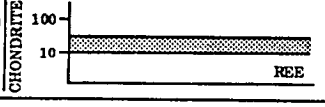

MM FACIES	LOWER GREENSCHIST	UPPER GREENSCHIST
NORMALIZED TM DIGITAL NUMBERS		
COLOR	DARK GREEN-GRAY TO TAN	DARK GREEN-GRAY TO TAN
FE-BEARING MINERALS	CHLORITE + EPIDOTE + CLINOPYROXENE + HEMATITE	CHLORITE + EPIDOTE + ACTINOLITE + STILPNOSELANE + CLINOPYROXENE + HEMATITE
RARE EARTH ELEMENT PATTERNS		
AGE	TRIASSIC	JURASSIC
HF-TH-TA	NORMAL AND ENRICHED MID-OCEAN RIDGE BASALT	THOLEIITIC WITHIN-PLATE BASALT
TECTONIC SETTING	OCEANIC PLATEAU	OCEANIC ISLAND

Fig. 4. Basalt characteristics for the Maiyumerak and Angayucham Mountains.

spatially, from tholeiitic to calc-alkaline (Figure 4). The geochemical signature of the upper greenschist-facies basalt of the Angayucham Mountains is most like modern tholeiitic within-plate basalt typical of some oceanic islands, whereas that of the lower greenschist basalt is most like normal to enriched mid-ocean ridge basalt of oceanic plateaus (using the terminology of 4). In both the Maiyumerak and Angayucham Mountains, the basalts of disparate metamorphic facies and compositions have been juxtaposed by faulting.

CONCLUSION

The combination of Thematic Mapper, mineralogic, geochemical, and field studies is providing new information regarding the geologic history of basalts in the Brooks Range. The combination of approaches is synergistic, in that each study has enhanced the effectiveness of the others. The TM images provide knowledge of the spatial distribution of different basalts not readily obtained by field mapping, nor by petrographic studies or geochemical analyses of a necessarily limited number of samples. Mineralogic studies provide an understanding of the causes of the spectral variations detected by the Thematic Mapper system, and geochemical studies provide knowledge of the tectonic significance of the spectral variations.

Acknowledgements: This work was funded by the NASA program Thematic Mapper Research in the Earth Sciences, under contract NAS 5-28739.

REFERENCES

1. Stern, C., and Elthon, D., 1979, *Tectonophysics*, v. 55, pp. 179-213.
2. Humphris, S. E., and Thompson, G., 1978, *Geochim. Cosmochim. Acta*, v. 42, pp. 107-126.
3. Wirth, K. R., Harding, D. J., and Bird, J. M., 1987, *Geol. Soc. Am. Abstracts with Programs*, v. 19, p. 464.
4. Pallister, J. S., and Budahn, J. R., in press, *J. Geophys. Res.*
5. Abrams, M. J., Conel, J. E., Lang, H. R., 1985, *The Joint NASA/Geosat Test Case Project Final Report*, The American Association of Petroleum Geologists, v. 1.
6. Wood, D. A., 1980, *Earth Plan. Sci. Lett.*, v. 50, pp. 11-30.

Geology and Geochemistry of Mafic Volcanic Rocks, Western Brooks Range, Alaska

Introduction

This is a study of the origin of mafic volcanic rocks in the western Brooks Range ophiolites. The results of mapping in three ophiolite complexes indicate that there are significant petrologic variations among them. Furthermore, during the examination and processing of Landsat Thematic Mapper images, we recognized spectral variations within and between ophiolites in the mafic volcanics (Harding et al., 1986, 1987; Bird et al., 1987). Petrographic and x-ray diffraction data from the volcanic rocks indicate that they have different metamorphic and weathering-produced mineral assemblages. These data illustrate that Thematic Mapper imagery of this region are useful for recognizing, mapping and characterizing subtle variations in mafic volcanic rocks. In order to evaluate the significance of the spectral and lithologic variations, we analysed the rocks for major and trace elements.

Major element oxide concentrations are used to distinguish various volcanic rocks (eg. Ewart, 1976; Le Maitre, 1984) and to study processes of crystallization (eg. MacDonald and Katsura, 1964; Miyashiro, 1974; Irvine and Baragar, 1971). The chemical composition of volcanic rocks, however, can be changed during metamorphism and alteration, processes that commonly occur during the formation of oceanic volcanic rocks. Some trace elements are less mobile during alteration. In particular, the rare-earth elements (REE), which have similar chemical and physical properties and are generally immobile during metamorphism, can be fractionated from each other during igneous

processes. Thus, they are more useful and reliable indicators of igneous processes than the major elements.

Analytical Methods

Rock samples free of amygdules and veins were pulverized to powder (<0.06 mm) in a Spex® shatterbox in tungsten-carbide containers. The rock powders were fused to glass beads on a strip of molybdenum in a pressurized Ar atmosphere. High-silica samples were fluxed with $\text{Li}_2\text{B}_4\text{O}_7$ and fused in open carbon crucibles at 1000°C in air. Major element oxide concentrations were determined by wavelength-dispersive analysis on a three-crystal spectrometer JEOL-733® electron microprobe; data were reduced to weight-percent oxides using a Bence-Albee matrix correction (Bence and Albee, 1968). Replicate analyses of standards indicate variations of less than 1% ($\pm 1\sigma$) for SiO_2 , Al_2O_3 , FeO^* ($\text{FeO}^* = \text{total iron as FeO}$), MgO , and CaO , and less than 5% for TiO_2 , K_2O , and P_2O_5 . Na_2O and MnO were determined by instrumental neutron activation analysis (INAA).

Trace elements were determined by INAA. Approximately 0.5 g of sample powder were encapsulated in high-purity silica tubing and irradiated in the central thimble of the Cornell TRIGA reactor. Gamma-ray spectra for each sample were collected seven and forty days after irradiation using a high-resolution GeLi coaxial detector. U.S. Geological Survey GSP-1 and Cornell PAL-889 and SIT-RK5 were the standards. Cobalt and tantalum concentrations were corrected for contamination that occurred during pulverizing. The precision of trace element analyses, estimated from analyses of standards, ranges from 1-5% ($\pm 1\sigma$) depending on the concentration of the element and on the counting statistics. The concentrations of trace elements in the Leedy

chondrite (Masuda et al., 1973; Kay and Hubbard, 1978) were used to normalize the basalt data to chondrite in some of the figures.

Acknowledgements

We thank the U.S. Park Service for permitting us to collect samples in the Noatak National Preserve. John Hunt assisted with the microprobe analysis of the samples, and Howard Adderhold provided radiation time in the Cornell TRIGA reactor for INAA. This research was funded by the NASA program "Thematic Mapper Research in the Earth Sciences", contract no. NAS5-28739.

Geology

The Brooks Range consists of Cambrian to Early Cretaceous platform carbonate and clastic sedimentary rocks that were folded and thrust during the Late Jurassic to Early Cretaceous "Brookian Orogeny" (Mayfield et al., 1983). Mafic volcanic rocks and layered gabbro and peridotite are exposed mostly in the De Long Mountains, in the northern part of the range, and comprise the uppermost thrust sheets (Patton et al., 1977). Late Precambrian-Permian(?) metamorphic rocks in the southern part of the range are probably autochthonous or parautochthonous, and might correlate with rocks that are basement to sediments deposited in the Colville Basin. The Colville Basin sediments were transported northward from the evolving Brooks Range during Late Jurassic to Late Cretaceous time.

Along the southern margin of the Brooks Range, mafic and ultramafic rocks dip southward, under the Yukon-Koyukuk Basin (Patton et al., 1977). These rocks have been interpreted to be within the "root zone" of the allochthonous mafic and ultramafic rocks in the northern part of the range (Roeder and Mull, 1978). Andesitic volcanic and sedimentary rocks in the central part of the Yukon-Koyukuk basin might be remnants of an Early to mid-Cretaceous volcanic arc (Box and Patton, 1985). These are overlain by clastic sediments that were derived from the Brooks Range during the Cenozoic (Patton, 1973).

Western Brooks Range Ophiolites

Layered mafic and ultramafic rocks, the Misheguk igneous sequence (Mayfield et al., 1983), comprise the uppermost thrust sheet in the Brooks

Range. In most exposures of ophiolite in the western Brooks Range the Misheguk igneous sequence structurally overlies, and is in fault-contact with, mafic volcanic rocks of the Copter Peak igneous sequence (Figure 1).

Metamorphic rocks occur locally along the thrust surface. The association of mafic volcanic rocks and layered mafic and ultramafic rocks in the western Brooks Range is similar to other ophiolites and to oceanic lithosphere (Tailleur and Brosgé, 1970; Tailleur, 1973; Patton et al., 1977; Roeder and Mull, 1978; Nelson and Nelson, 1982; Bird et al., 1985).

Rocks in the layered gabbro-peridotite show a progressive gradation from interlayered dunite and pyroxenite, to layered gabbro, and massive hornblende-gabbro. Variations of mineral composition and grain-size repeat within the sequence and comprise layering. The orientation of layering is approximately north-south and near vertical in most areas, probably due to rotation along faults (Harding et al., 1985). The layered gabbro is intruded by coarse-grained hornblende diorite and by plagiogranite at Asik Mountain. Massive and variably-textured intrusive rocks, with complex intrusive relationships, are exposed north of Asik Mountain. Most of these rocks are foliated or lineated and their relation to the undeformed and layered gabbro-peridotite section is not well-understood. Large, fault-bounded blocks of tectonized harzburgite and dunite are also present at Avan Hills.

Metamorphosed sediment and volcanic rock occur along the thrust contact between the ultramafic rocks and the structurally lower mafic volcanic rocks (Zimmerman and Frank, 1982; Curtis et al., 1984; Ellersieck et al., 1984; Boak et al., 1987). Metamorphic rocks, including marble, metapelite, plagioclase-biotite-quartz-garnet schist, amphibole-bearing plagioclase-quartz schist, and amphibolite, range from low to medium grade. The metamorphic rocks typically range from a few meters to tens of meters thick, although as much as 100 meters of metamorphic rock have been reported from Misheguk Mountain.

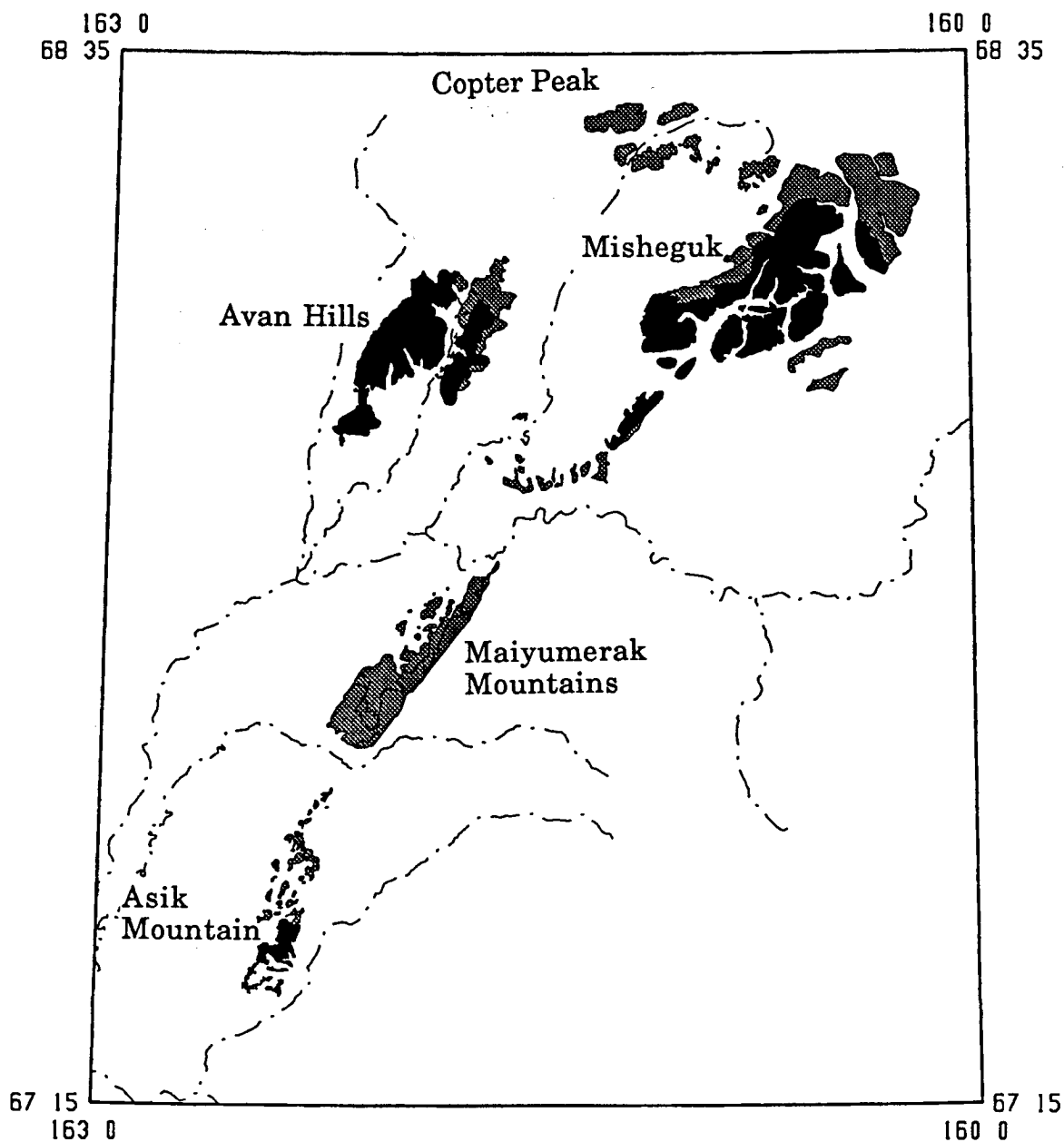


Figure 1. Generalized geologic map of the western Brooks Range ophiolites showing the distribution of peridotite and gabbro (black), and basalt (stippled). Lithologic boundaries are from existing maps (Curtis et al., 1984; Mayfield et al., 1983), field mapping, and from the analysis of Thematic Mapper images.

These metamorphic soles are similar to those recognized in other ophiolite complexes and are probably produced by thrusting of relatively hot peridotite over cooler rock, possibly, with some heat also generated by friction.

Mafic Volcanic Rocks

The Copter Peak igneous sequence was named by Curtis et al. (1982) for exposures of mafic volcanic rock at Copter Peak in the Misheguk Mountain Quadrangle. Volcanic rocks in the western Brooks Range that are correlated with the Copter Peak igneous sequence include rocks at Siniktanneyak Mountain (Nelson and Nelson, 1982), Misheguk Mountain (Curtis et al., 1982, 1984; Ellersieck et al., 1982, 1984), Avan Hills (Curtis et al., 1982, 1983, 1984), Iyikrok Mountain (Mayfield et al., 1983a, b), Asik Mountain (Blanchard et al., unpubl. map of Noatak C-1,2, and D-1,2 Quads.) and rocks along the lower Kivalina River (Mayfield et al., 1987). Less extensive exposures of the sequence occur in the Pupik Hills, at Mount Bastille and near Memorial Creek (Mayfield et al. 1983).

The age of the Copter Peak igneous sequence is not well-determined. Radiolaria from interpillow chert and intercalated chert layers are predominantly Mesozoic (Nelson et al., 1979; Ellersieck et al., 1982). If the mafic volcanics correlate with the mafic and ultramafic rocks in the Misheguk igneous sequence, then they are probably Triassic to Jurassic age (Mayfield et al., 1983, Wirth et al., 1986). Blocks of limestone that yield Devonian to Permian macro-fossils (Nelson et al., 1979; Nelson and Nelson, 1982) are present in some of the volcanics, but are considered to be tectonically incorporated (Ellersieck et al., 1982).

Pillow basalt, diabase, basaltic tuff, and radiolarian chert form a nearly

continuous belt, the Angayucham terrane (Jones et al., 1984), along the southern margin of the Brooks Range (Patton et al., 1977). Hitzman et al. (1982, 1986) divided basalts in the Angayucham Mountains into two different units on the basis of age and metamorphism. Additional work by Pallister and Budahn (in press.) confirmed the division of basalt units. Radiolaria from interlayered cherts within the volcanics are Jurassic and Triassic, although some are Paleozoic (Hitzman et al., 1982; cited in Pallister and Budahn, in press). Major element compositions suggest that the basalts are hypersthene-normative, olivine tholeiites (Pallister and Budahn, in press). Although the two basalt units appear to be the same in the field, geochemical data indicate that they are different. Trace element analyses indicate that the rocks are most similar to recent "within-plate", and oceanic-plateau and island basalts (Pallister and Budahn, in press; Barker, in press).

Mafic volcanic rocks in the central part of the southern Brooks Range, Cathedral and Twelve-Mile Mountains, contain chert layers that yield Carboniferous radiolaria (Bird, 1977; Gottschalk, 1987). Geochemical data from Gottschalk (1987) suggest that the basalts are quartz-normative tholeiites that are similar to present-day mid-ocean ridge basalts.

Maiyumerak Mountains

One of the largest exposures of the Copter Peak igneous sequence is in the Maiyumerak Mountains. Unlike many of the other exposures of the Copter Peak igneous sequence in the western Brooks Range, volcanic rocks in the Maiyumerak Mountains are not overlain by layered gabbro or peridotite. This present structural and topographic relationship might be a function of structural or erosional history. Alternatively, volcanic rocks in the Maiyumerak Mountains might not have been over-thrust by the Misheguk

igneous sequence.

The volcanic rocks are typically massive or pillowed. Individual flows, averaging one to several tens-of-meters thick, are distinguished by brecciated, altered and vesiculated zones that are interpreted as flow tops. The pillowed basalt flows are comprised of individual pillows that average 30 - 200 cm in length, and range from less than 10 cm to over 5 m in length. Lava tubes and flow toes are commonly present. Minor red, green, and grey chert are commonly present between pillows. Basalts in the pillow units are both fine-grained and porphyritic. The margins of pillows are usually vesiculated and are locally fractured and brecciated. The vesicles and fractures are commonly filled with carbonate or silica minerals. The flows of massive basalt are similar, but are generally more coarse-grained and less altered than the pillow basalts.

Small amounts of what might be fragmental volcanic sediment also occur in the Maiyumerak Mountains. These rocks are typically thin-bedded and graded, consisting of silt- to sand-size grains. Layering in their lower portions is often parallel with the highly irregular basal contact of the underlying volcanic rock, but becomes planar at higher stratigraphic levels.

Aphanitic, porphyritic and diabasic dikes occur throughout most of the area we studied, and are particularly well-exposed on the ridge tops in the central and southwestern parts of the range. The dikes are generally tabular and range from 0.5 meters to over 10 meters in width. The thicker dikes might consist of a number of multiply-intruded dikes. There is evidence for multiple intrusion from the relations of chilled zones on the margins of the dikes. Most of the dikes are mafic, and are composed of phenocrysts of plagioclase and pyroxene in a groundmass consisting of plagioclase, \pm pyroxene, chlorite, magnetite and other alteration minerals that might have been volcanic glass; textures range from aphanitic to porphyritic and holocrystalline. One felsic dike

with quartz phenocrysts was also observed.

Harding et al. (1986) and Bird et al. (1987) discriminated basalts in the southern Maiyumerak Mountains on the basis of their spectral reflectance in Landsat Thematic Mapper images, weathering characteristics, and metamorphic mineral assemblages. Basalt in the western and eastern parts of the range have greater band 7 and 5 reflectance relative to basalt in the central part of the range. Basalt in the central part of the range consists of plagioclase, clinopyroxene, and various iron oxide minerals, and weathers red-brown. Basalts in the western and eastern parts of the range consist mostly of plagioclase, actinolite, chlorite, and iron oxides, and weather dark grey. Clinopyroxene apparently does not occur in these basalts.

The average strike of sedimentary and flow layering in the central part of the southern Maiyumerak Mountains is N 27° E, and dips average 72° NW (Figure 2). Dikes in the same area strike approximately N 29° E and dip approximately 37° SE. The angle between layering and tabular dikes is approximately 100°. This angle is near the angle that is predicted by models for the emplacement of sheeted dikes at accreting plate margins. The geometric relationships between layering and dikes in black-weathering basalts in the eastern and western parts of the range are similar, but these rocks appear to have been rotated, relative to the red-weathering basalts.

Asik Mountain

Rocks previously mapped as the Copter Peak igneous sequence, between Asik Mountain and the Eli River have diverse compositions, textures, structures and metamorphic mineral assemblages. In general, the least deformed rocks occur in the northern part of the area, just south of the Eli River. South of the Eli River, near Asik Mountain, rocks are more deformed and metamorphosed.

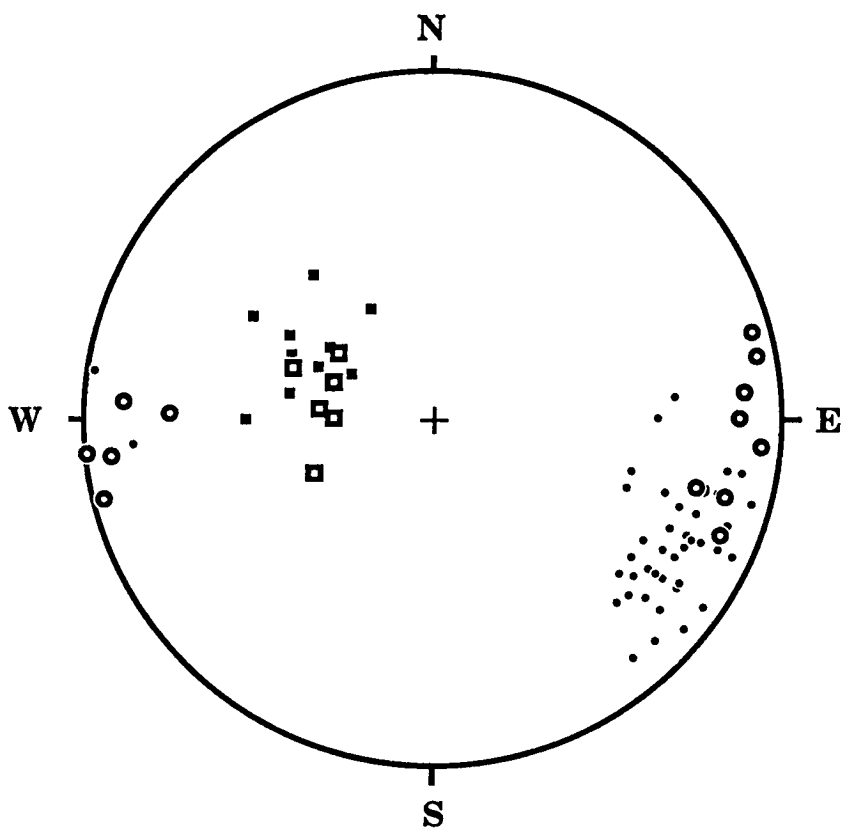


Figure 2. Lower-hemisphere, equal-area stereonet of poles to dikes (small, solid circles) and basalt flows (small, filled squares) in the central part of the Maiyumerak Mountains, and poles to dikes (large, open circles) and basalt flows (large, open squares) in the eastern part of the Maiyumerak Mountains.

The northern exposures are mostly of mafic volcanic flows, and are mostly red-weathering, porphyritic and fine-grained. Pillow structures and flow structures, delineated by vesicles, amygdules and fractures, are sometimes present; interpillow chert is common. Red-weathering, fine-grained sediment that might be interpillow sediment was also observed as float. The origin of fragmental volcanic rock in the area has been obscured by silicification and alteration.

South of the relatively undeformed volcanics, the rocks are characterized by an increase in the grain-size of mica (mostly chlorite) and by an increase in deformation fabric (foliation and lineation). Relict textures and the composition of metamorphic mineral assemblages suggest that these rocks were derived largely from mafic volcanic flows.

Rocks just north of Asik Mountain have a pronounced lineation. The rocks are phaneritic and more coarse-grained, consisting of plagioclase and pyroxene and/or amphibole. Quartz is sometimes present. Rocks exposed in a creek just north of Asik Mountain indicate that the more deformed coarse-grained intrusive and volcanic rocks overlie, and are in fault contact with, the low-grade and weakly deformed volcanic rocks exposed just south of the Eli River. The metamorphic rocks can be distinguished from the less deformed volcanic rocks to the north, on false-color low-altitude aerial photographs and on Landsat Thematic Mapper images.

The features described above indicate that the northern part of Asik Mountain consists of rocks that have different crystallization and deformation histories. Previous maps of the area show that the ultramafic-gabbroic rocks are separated from the mafic volcanic rocks by a single, major thrust fault. Our data, however, indicate that the mafic-volcanic thrust-sheet (Copter Peak Allocthon) might consist of rocks from two or more places that have been

tectonically juxtaposed, implying the presence of several faults. Evidence for this interpretation is based on the diverse lithologies, textures, and structures observed in the region north of Asik Mountain.

Avan Hills

Most of the mafic volcanic rocks that we studied in the Avan Hills are sheared and altered. Some pillow structures were observed, but most of the rocks are too deformed to recognize primary flow structures. The rocks are not foliated, but are cross-cut by closely-spaced fractures that are usually mineralized. Thin-sections show that most of the phenocrysts are plagioclase and clinopyroxene; some altered phenocrysts in the basalts might have been olivine.

Minor amounts of chert and volcanoclastic sediment are also present in the Copter Peak igneous sequence at Avan Hills. The volcanoclastic sediments consist of angular fragments, up to 1 cm in length, in a matrix of fine-grained volcanic fragments. Massive red and green chert is present throughout much of the volcanic section; small masses of layered chert, averaging 1-5 meters thick, are also locally present.

Intermediate to mafic composition intrusive rocks in the lower thrust sheet (Curtis et al., 1984) have textures that range from medium-grained and porphyritic to fine-grained and equigranular. Although the rocks are severely altered, they were classified in the field as gabbro and diorite(?). These rocks occur in close association with each other, and appear to represent a series of small, multiply-intruded bodies in the mafic volcanic section.

Major Element Chemistry

Most of the mafic volcanic rocks of the Copter Peak igneous sequence are classified, on a silica versus total-alkali diagram (Le Maitre, 1984), as basalt, basaltic andesite, and trachyandesite. Some of the rocks have relatively high SiO_2 contents and are classified as andesite, dacite, and rhyolite (Figure 3). With the exception of the one sample of a dike from the Maiyumerak Mountains that contains phenocrysts of quartz (MM-101-85), there is petrographic evidence for andesite, dacite, or rhyolite compositions within the sequence. Petrographic studies of other basalts from ophiolites and oceanic basins, and experimental results, indicate that the concentrations of some of the major elements (eg. Si, Na, K) can be affected by low temperature, submarine hydrothermal processes at the time of their formation (eg. Vallance, 1974). Therefore, although the apparent variation of silica and the total alkalis might, in part, be due to crystal fractionation, the silica and alkali concentrations have probably been modified by hydrothermal processes.

Due to the pervasive affects of metamorphism and alteration in these rocks, attributed to submarine hydrothermal processes, little can be interpreted about their igneous history from their major element compositions. However, a few of the elements appear to behave coherently. The co-variance of TiO_2 with Yb is an expected result of igneous processes, but not of metamorphism and alteration (Figure 4). Volcanic rocks from the Maiyumerak Mountains plot separately from volcanics from the Avan Hills in a diagram of FeO^*/MgO versus TiO_2 (Figure 5). In this diagram, samples from Asik Mountain and the Maiyumerak Mountains can not be distinguished. Samples from the Maiyumerak Mountains are distinguished from the others by their concentrations of FeO^* , MgO and Al_2O_3 .

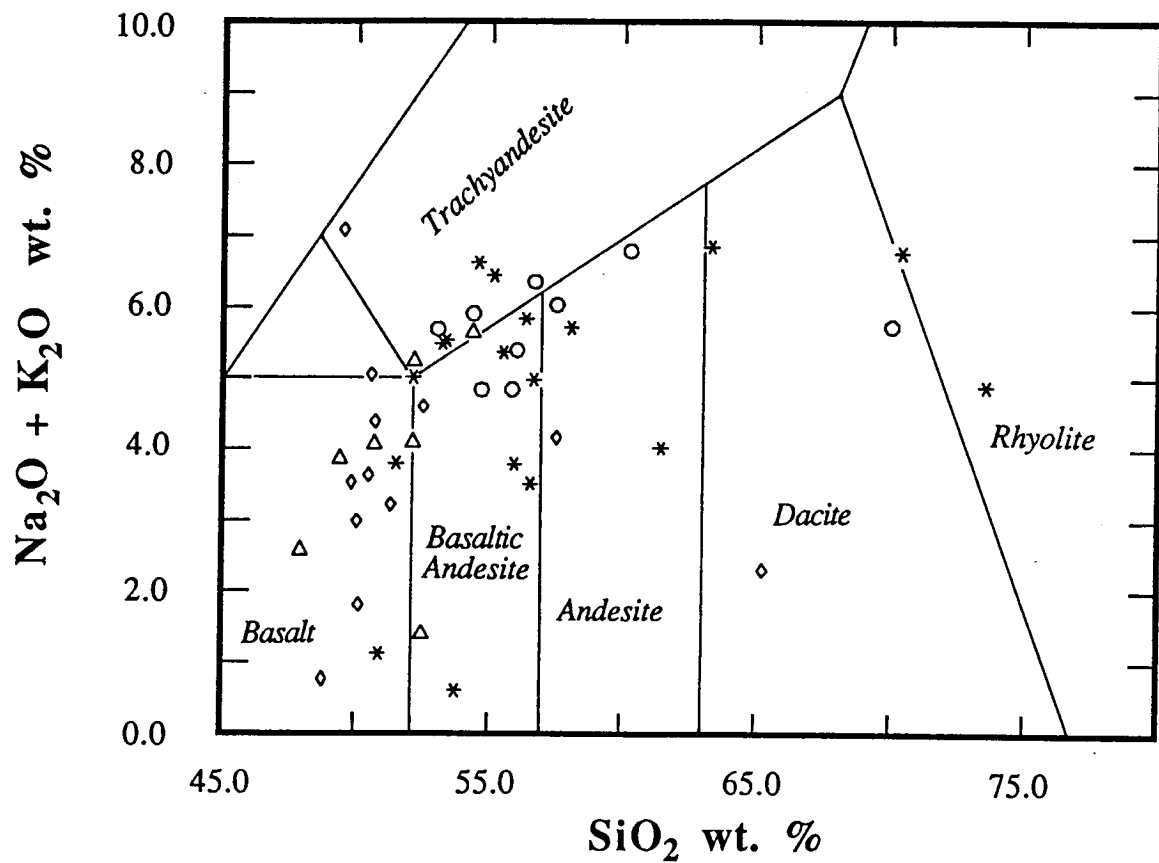


Figure 3. Total alkali versus silica (Le Maitre, 1984) variation of major element compositions of volcanic rocks from the Maiyumerak Mountains (red-weathering basalts - asterisks; black-weathering basalts - circles), Avan Hills (diamonds), and Asik Mountain (triangles).

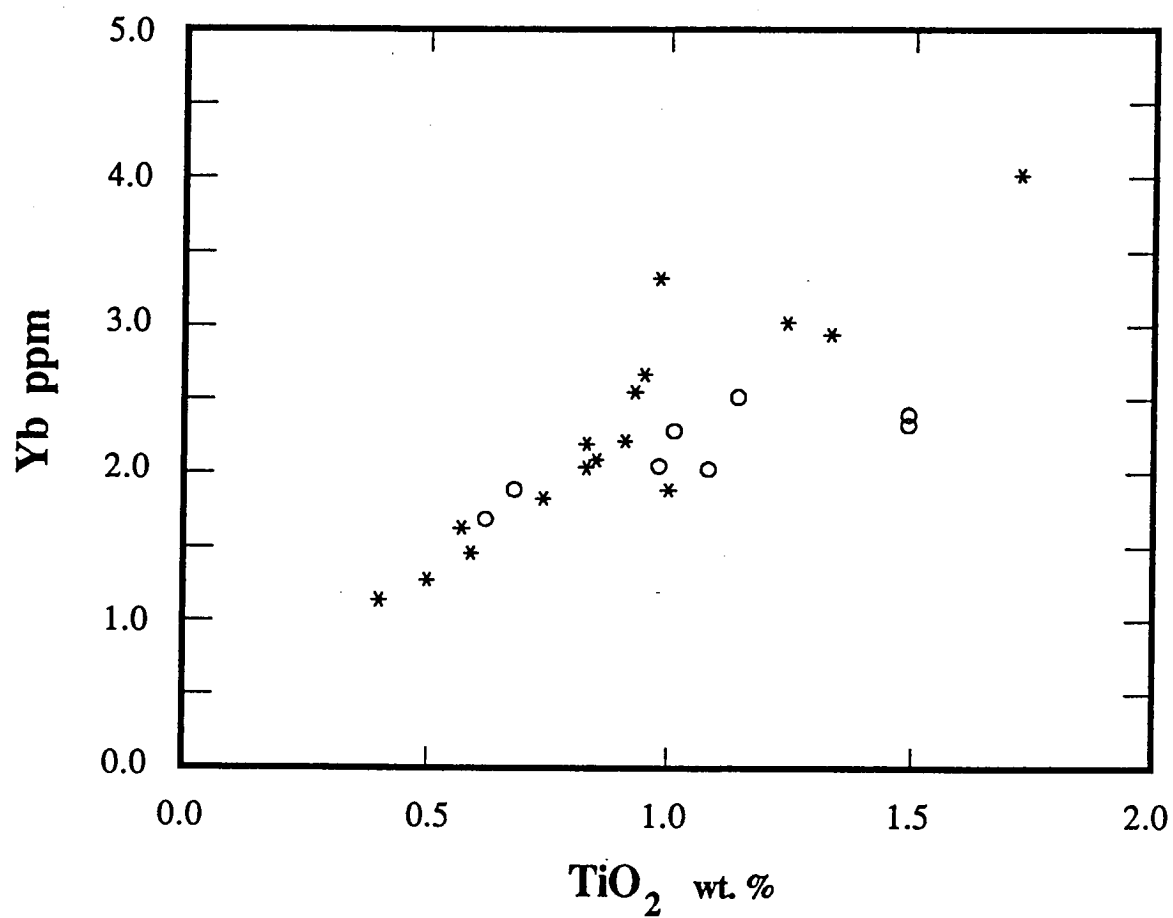


Figure 4. Variation of Yb and TiO_2 in samples from the Maiyumerak Mountains. Symbols as shown in Figure 1.

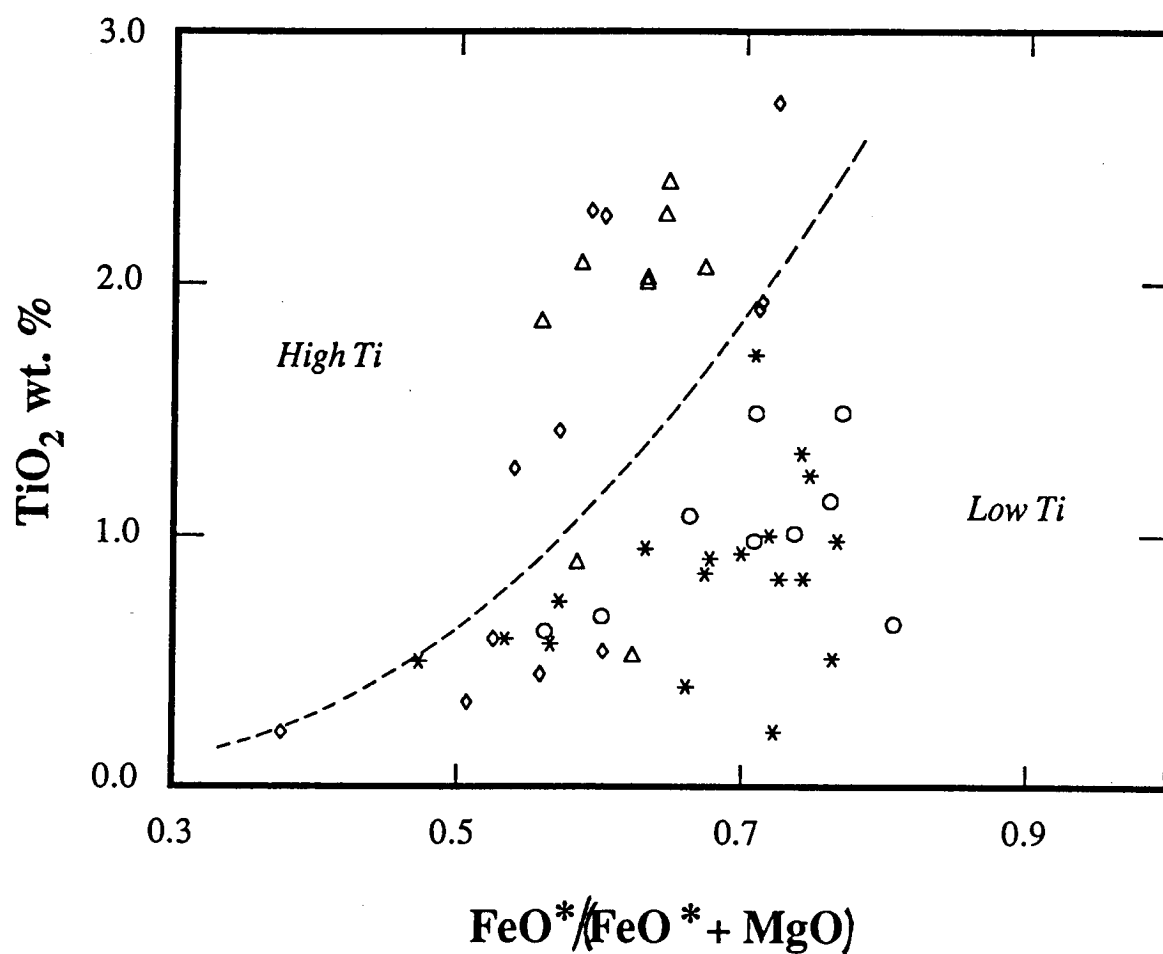


Figure 5. TiO₂ versus $\text{FeO}^*/(\text{FeO}^* + \text{MgO})$ variation of volcanic rocks from the western Brooks Range. Symbols as in Figure 1. Boundaries from Serri (1981).

Trace Element Chemistry

In general, variations in trace elements are more reliable indicators of primary igneous processes than the major elements (eg. Pearce et al., 1984).

The rare-earth element concentrations of volcanic rocks from the western Brooks Range (Figures 6-12) indicate that there are significant chemical differences. Samples from the two basalt units (red- versus black-weathering) in the Maiyumerak Mountains have similar flat REE patterns at about ten times chondritic values. However, there are slight differences in their light-REE (LREE) patterns. The red-weathering basalts in the central portion of the Maiyumerak Mountains have flat, or slightly depleted LREE patterns, whereas the black-weathering basalts have flat or slightly enriched LREE patterns. Samples from Asik Mountain have depleted to enriched LREE patterns (Figures 9-11). The slightly metamorphosed mafic flows have flat or slightly concave-downward REE patterns, whereas the metavolcanics have LREE-enriched or LREE-depleted patterns. Volcanic rocks from Avan Hills have mostly straight and LREE-enriched patterns, although one sample has a LREE-depleted pattern. A sample that might be either a fine-grained volcanic flow or a volcanic sediment has a relatively strongly LREE-enriched pattern; lanthanum is nearly 100 times the chondritic value.

The average concentrations of some trace elements in volcanic rocks from Asik Mountain, Avan Hills, and the Maiyumerak Mountains are shown in Figure 13. The average of incompatible element concentrations of the Avan Hills rocks are 1 to 5 times that of "normal mid-ocean ridge basalt" (N-MORB). The trace element pattern is smooth and it shows the relative enrichment of the more incompatible elements from K to Ce (Figure 13). In contrast, samples

from the Maiyumerak Mountains and Asik Mountain have Ta to Yb concentrations that are similar to N-MORB, and K to Th concentrations that are enriched relative to N-MORB (Figure 13). Trace element patterns of the Maiyumerak Mountain rocks are characterized by depletions of K, Ta, P, Hf, and Ti relative to the other elements plotted. Similar depletions are evident in the trace element pattern of rocks from Asik Mountain, but they are not as pronounced as those from the Maiyumerak Mountains. Trace element patterns for modern basalts from several different tectonic environments are shown in Figure 14 for comparison.

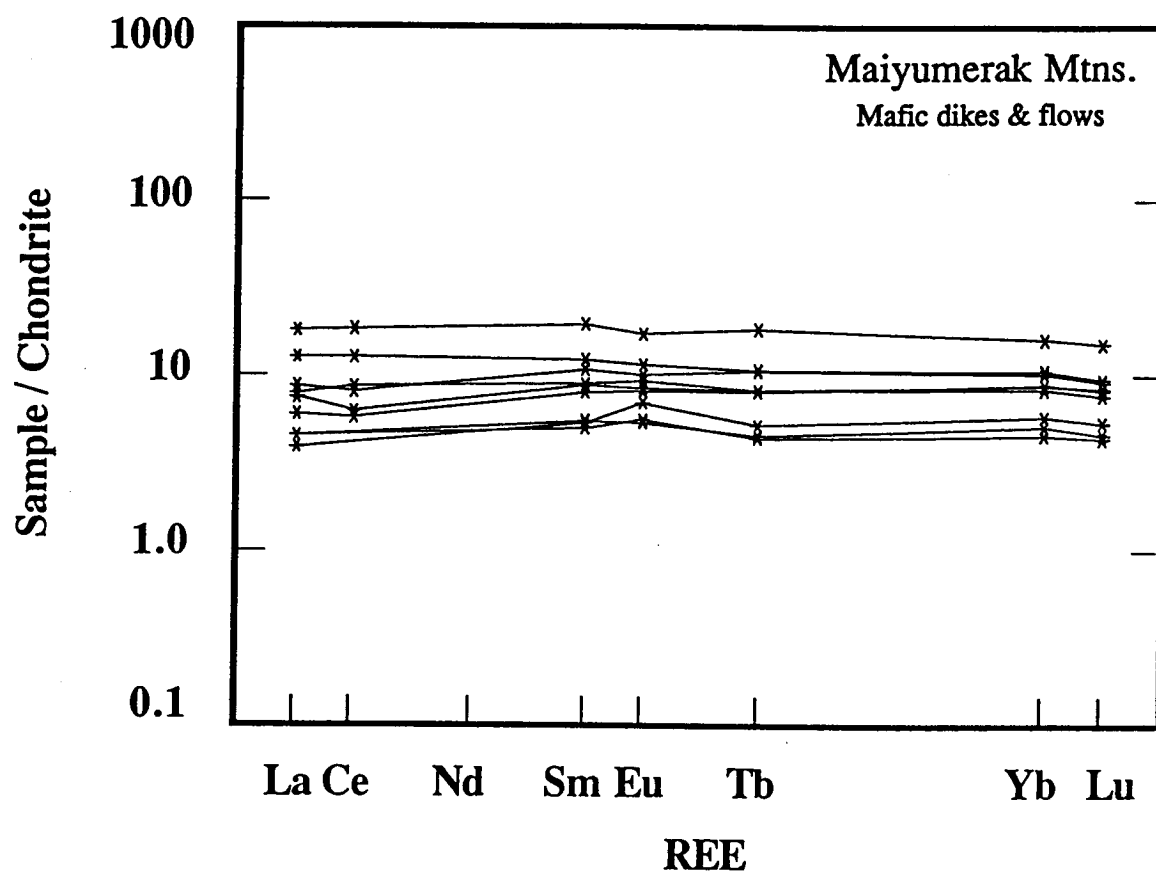


Figure 6. Chondrite normalized rare-earth element plot of red-weathering mafic flows and dikes from the central part of the southern Maiyumerak Mountains.

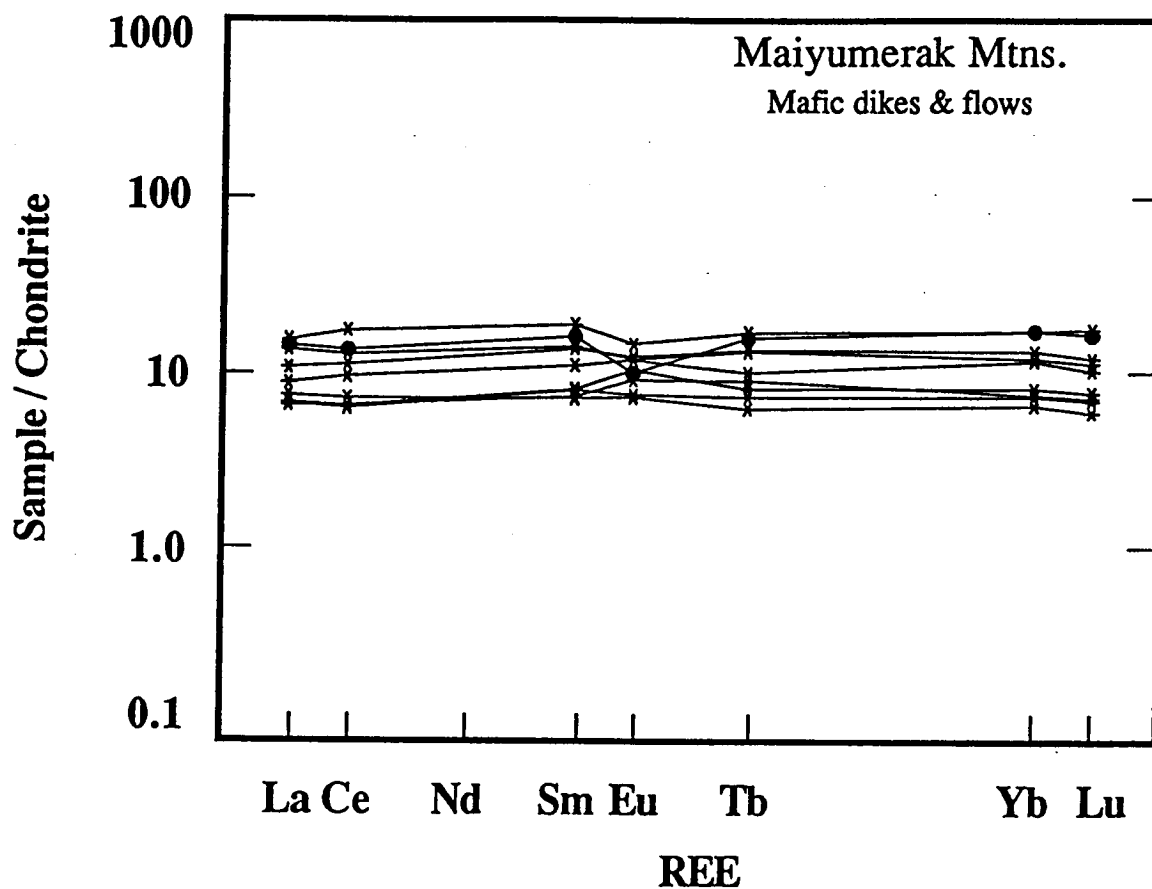


Figure 7. Chondrite normalized rare-earth element plot of red-weathering mafic flows and dikes (x) and a felsic dike (filled circles) from the central part of the southern Maiyumerak Mountains.

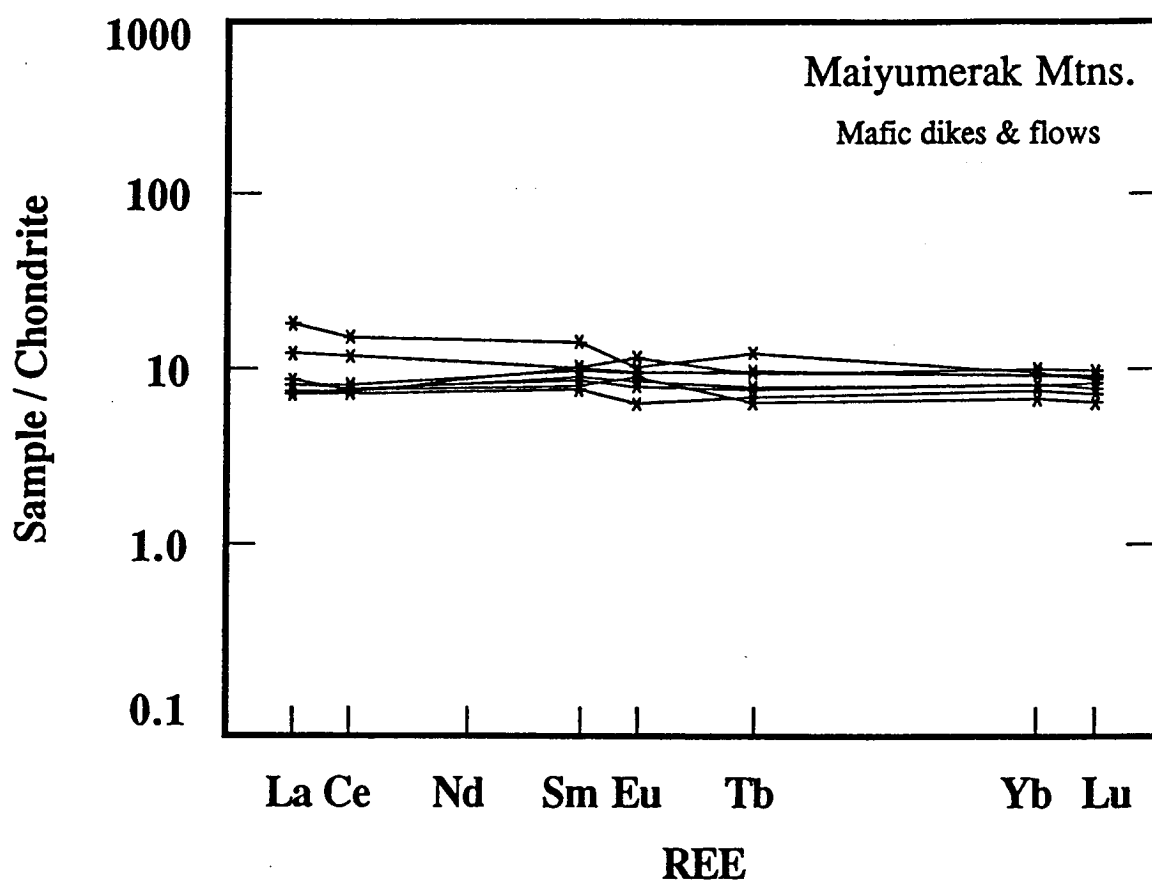


Figure 8. Chondrite normalized rare-earth element plot of black-weathering mafic flows and dikes from the western part of the southern Maiyumerak Mountains.

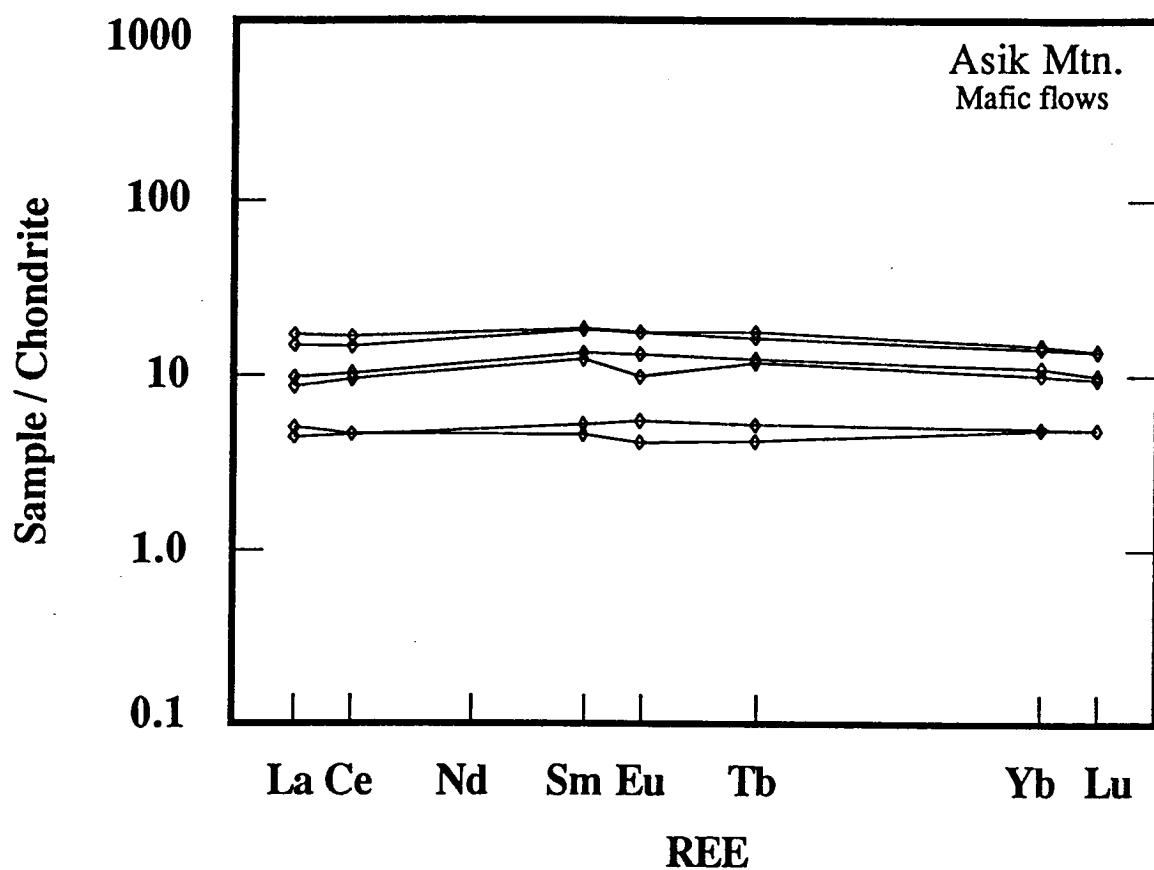


Figure 9. Chondrite normalized rare-earth element plot of mafic flows dikes from north of Asik Mountain.

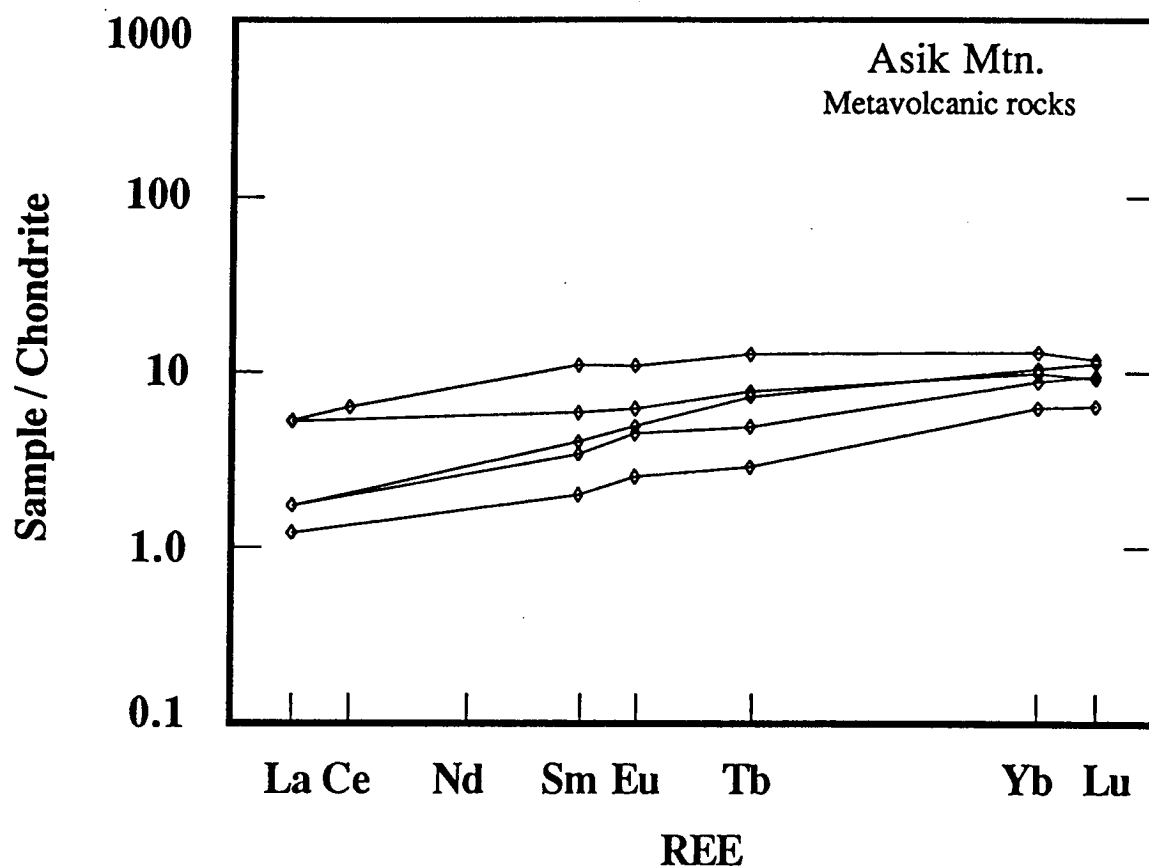


Figure 10. Chondrite normalized rare-earth element plot of metavolcanic rocks from north of Asik Mountain.

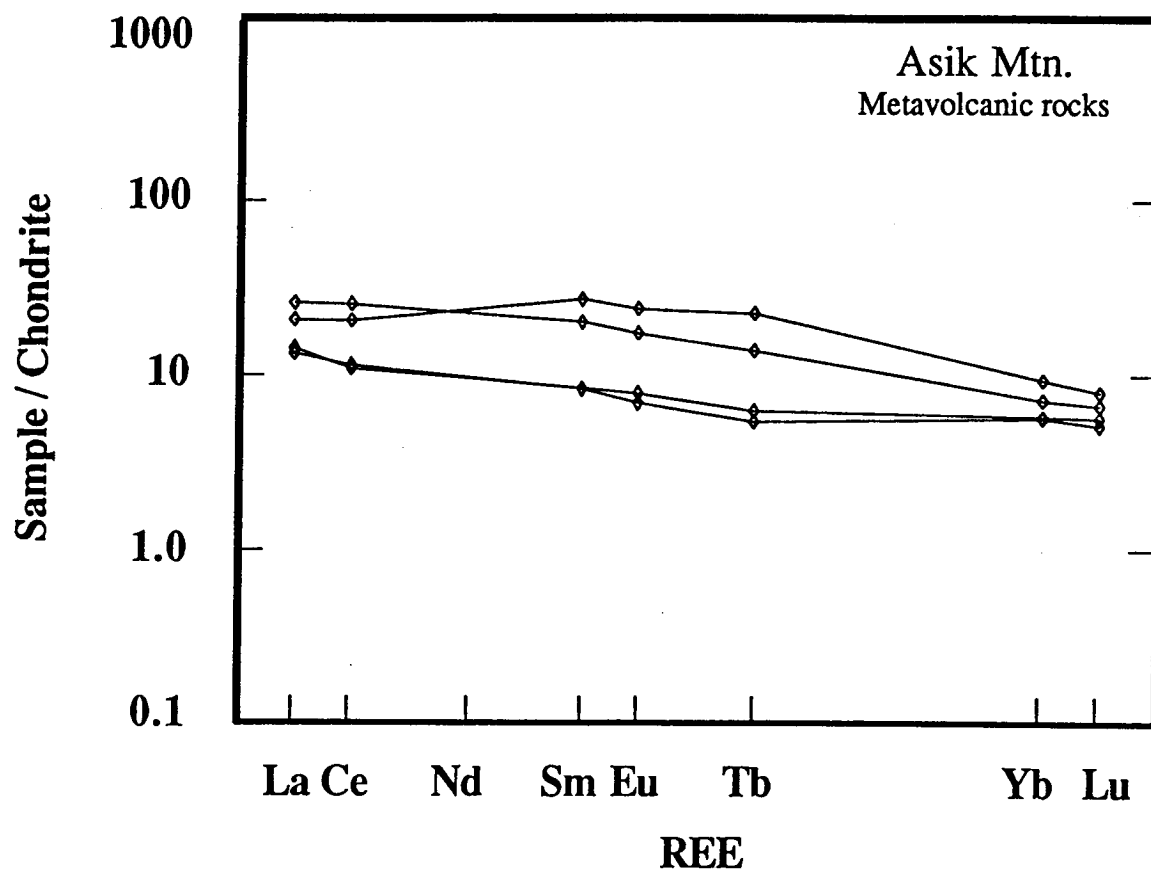


Figure 11. Chondrite normalized rare-earth element plot of metavolcanic rocks from north of Asik Mountain.

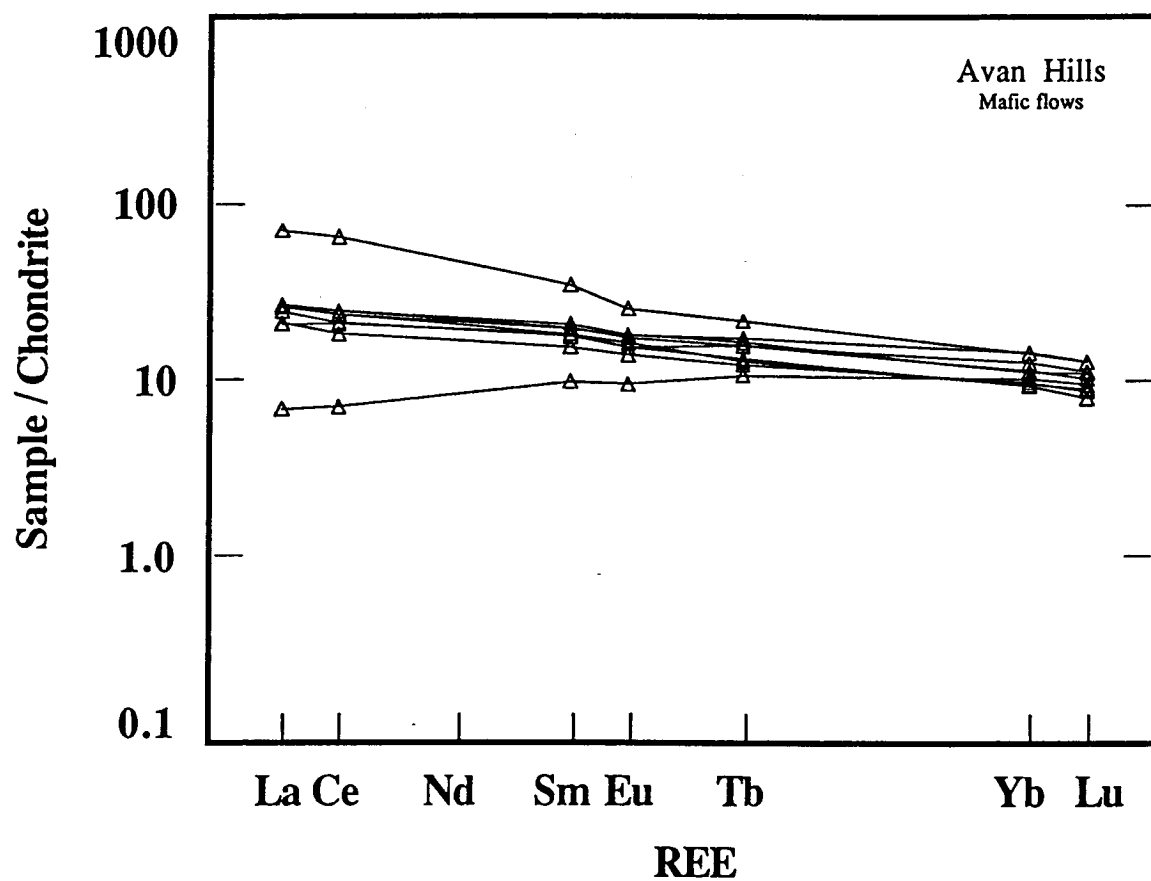


Figure 12. Chondrite normalized rare-earth element plot of mafic flows from the northern and central Avan Hills.

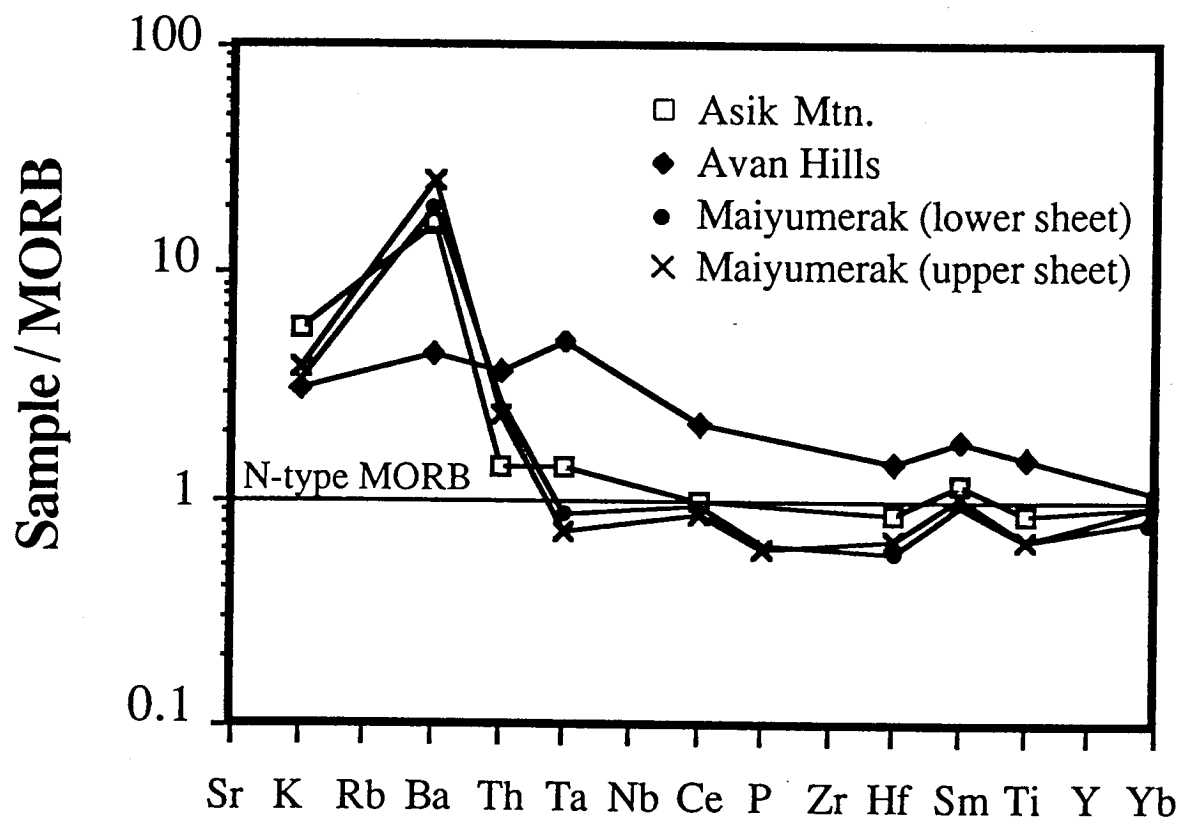


Figure 13. Trace element patterns of mafic volcanic rocks from western Brooks Range ophiolites. Concentrations are normalized to normal mid-ocean ridge basalt (N-MORB) of Tarney et al. (1981).

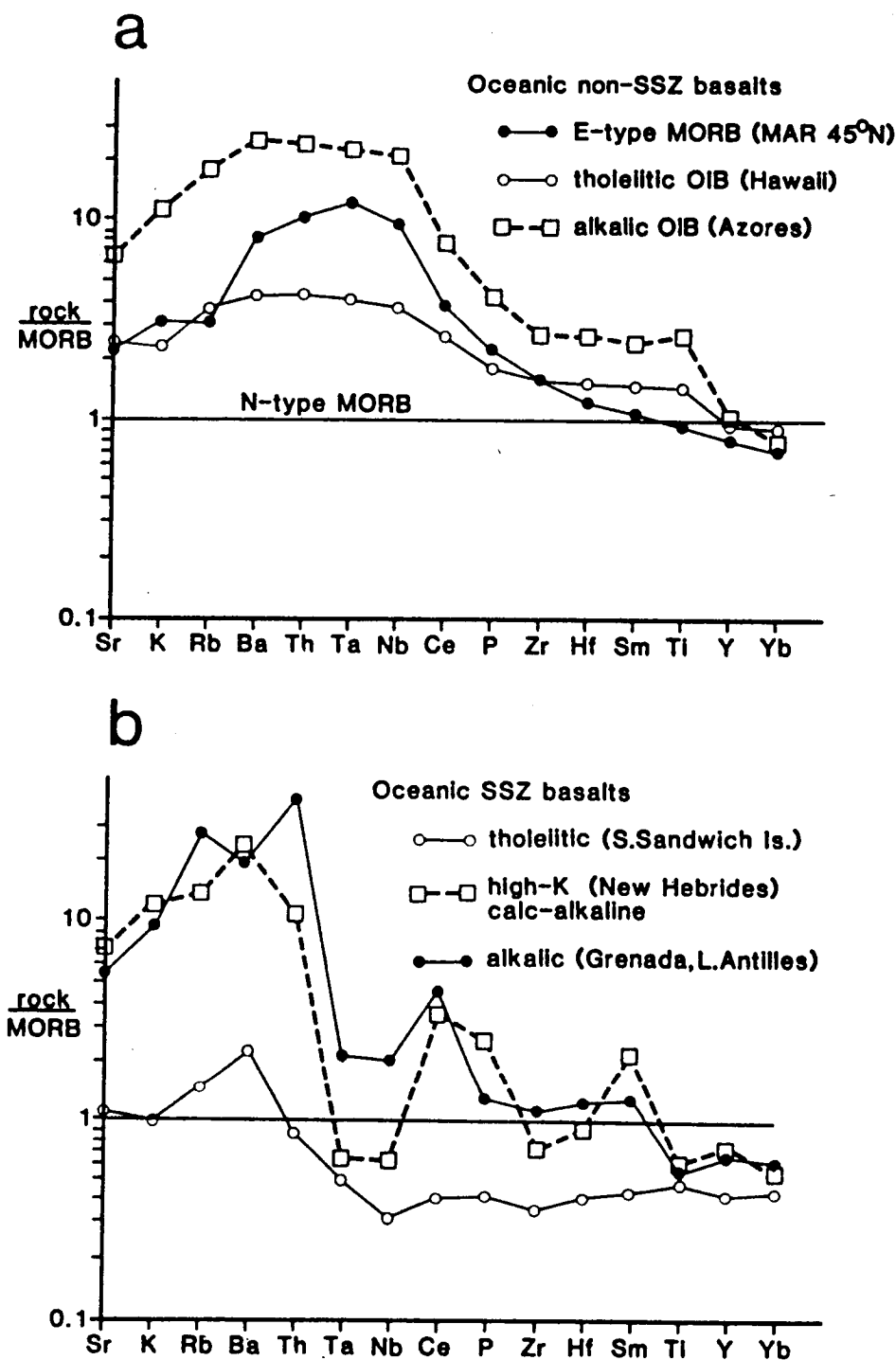


Figure 14. Trace element patterns of oceanic basalts from (a) "non-supra-subduction zone", and (b) "supra-subduction zone" settings (from Pearce et al., 1984).

Geochemical Tectonic-Discriminants

The ratios of isotopes and some trace elements in volcanic rocks are independent of processes of igneous crystallization and reflect the characteristics of their mantle source. In this sense, the chemical "fingerprints" of allocthonous volcanic rocks have been used to infer the tectonic environment of their formation (eg. Pearce and Cann, 1973; Wood et al., 1979; Thompson et al., 1980; Kay 1984; Pearce et al. 1984).

Volcanic rocks from the Maiyumerak Mountains plot in the field of recent volcanic rocks from convergent plate margins in diagrams of TiO_2 - MnO - P_2O_5 , Ti/Cr versus Ni , Hf/3-Th-Ta , and Th/Yb versus Ta/Yb (Figures 15-18). The red-weathering basalts plot consistently in the field of modern island arc tholeiites (IAT) and the black-weathering basalts plot in the fields of calc-alkaline basalt (CAB). This interpretation is further supported by their trace element patterns (Figure 13), and by their distribution on a plot of TiO_2 versus $\text{FeO}^*/(\text{FeO}^* + \text{MgO})$ in which the rocks are classified as low-Ti basalts (Serri, 1981), characteristic of volcanic rocks formed during the initial stages of back-arc basins.

On the same diagrams, samples from the Avan Hills plot in the fields of ocean floor tholeiites (OFT), enriched mid-ocean ridge basalt (E-MORB), and high-Ti basalt. The Hf-Th-Ta ratios of the Avan Hills volcanics indicate that they are distinct from mid-ocean ridge basalt and from low-Ta island arc tholeiite and calc-alkaline basalt, an interpretation supported by the similarity of their trace element patterns with oceanic island basalts (eg. Hawaii).

Trace element data from Asik Mountain do not cluster on the variation diagrams. This is interpreted to be due either to a long and complex magmatic history, or to submarine alteration that affected the concentrations of some of the

trace elements. In general, the trace element ratios of samples from Asik Mountain plot across the field boundaries that separate oceanic basalt from volcanic arc basalt on variation diagrams. Similarly, the REE and trace element patterns of the Asik Mountain samples have the characteristics of basalts from oceanic and volcanic arc settings.

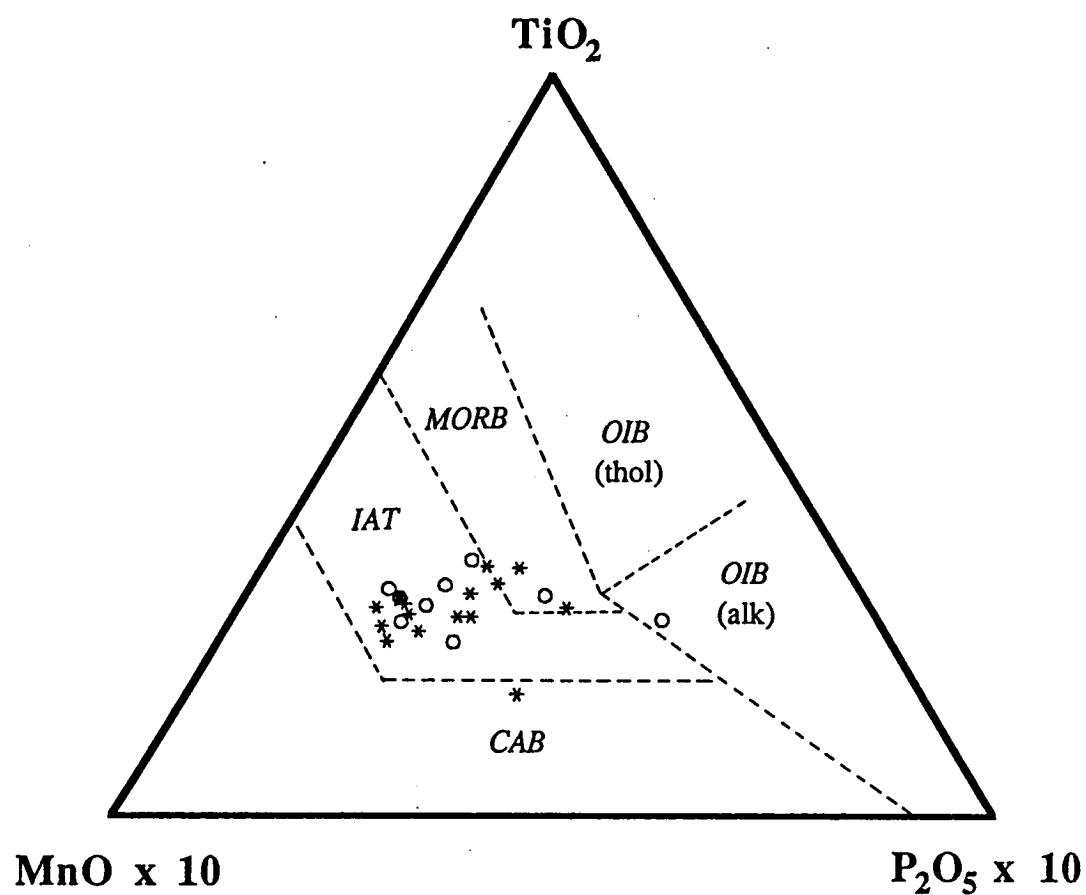


Figure 15. TiO_2 - MnO - P_2O_5 ternary plot of mafic dikes and flows from the central (*) and western (o) parts of the southern Maiyumerak Mountains.

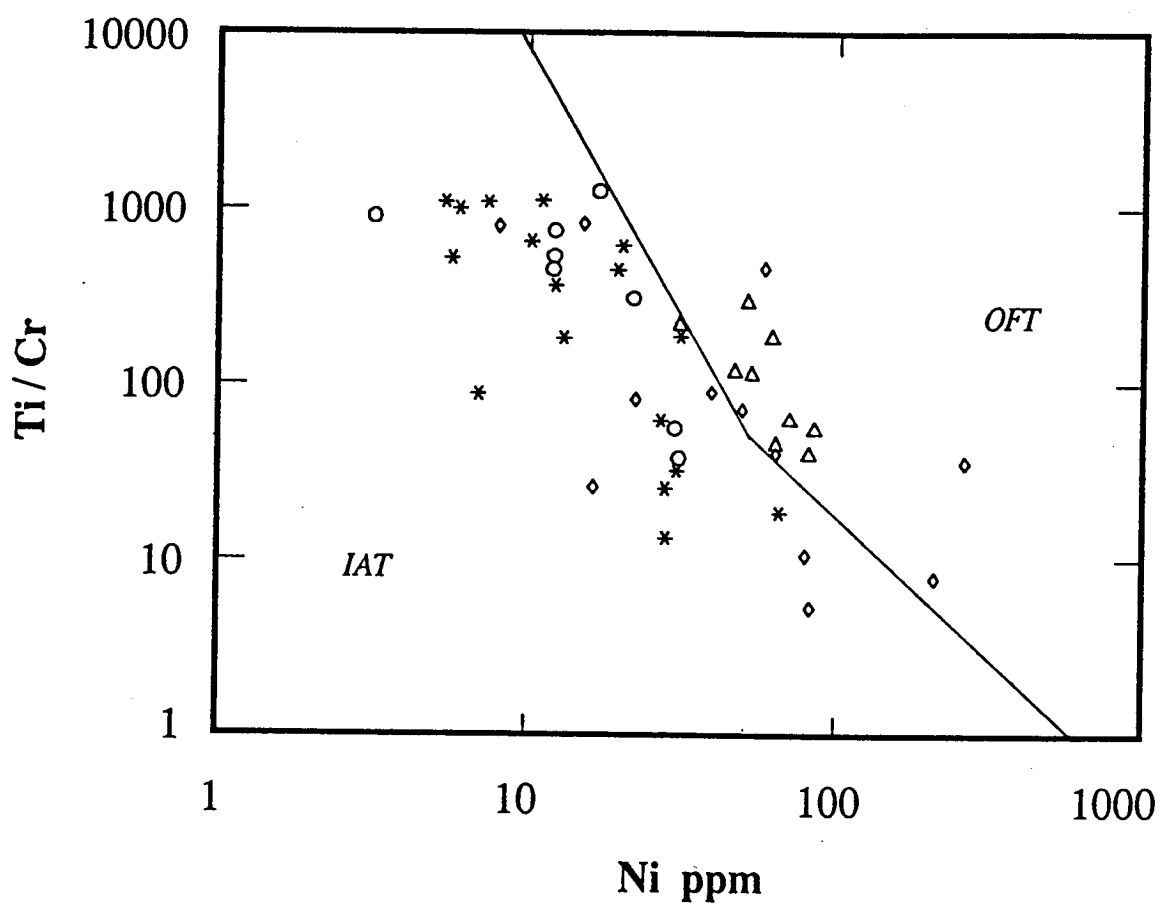


Figure 16. Ti/Cr versus Ni variation of samples from western Brooks Range ophiolites. Symbols as in Figure 1. Boundaries from Beccaluva et al. (1979).

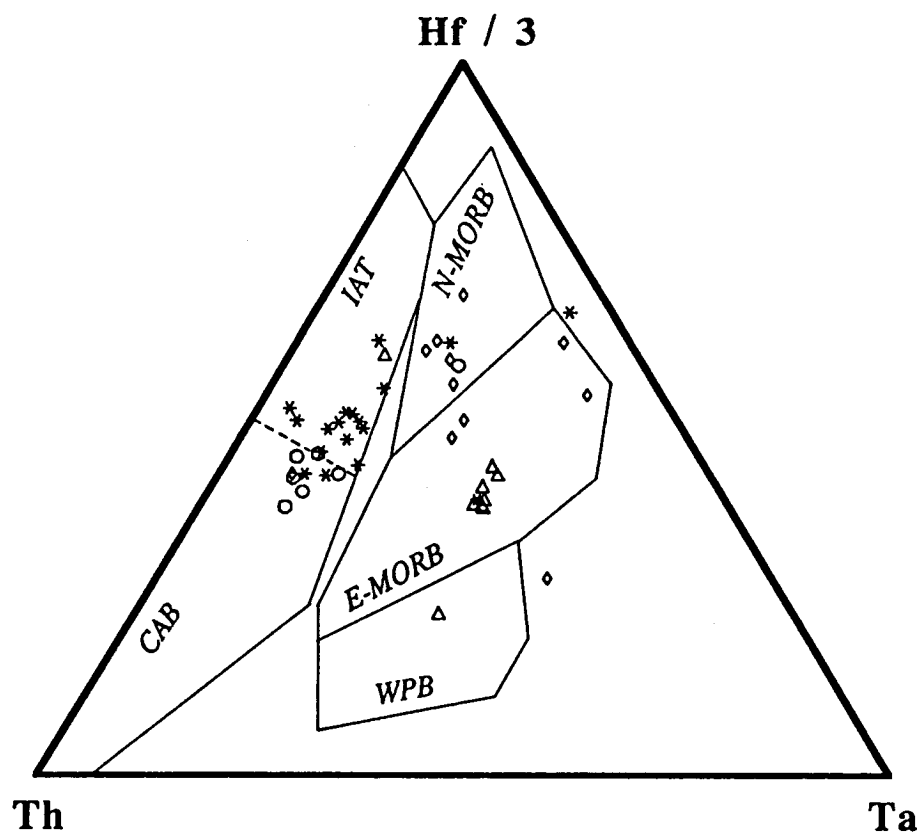


Figure 17. Hf-Th-Ta ternary diagram of mafic volcanic flows and dikes from western Brooks Range ophiolites. Symbols as in Figure 1. Boundaries from Wood (1979).

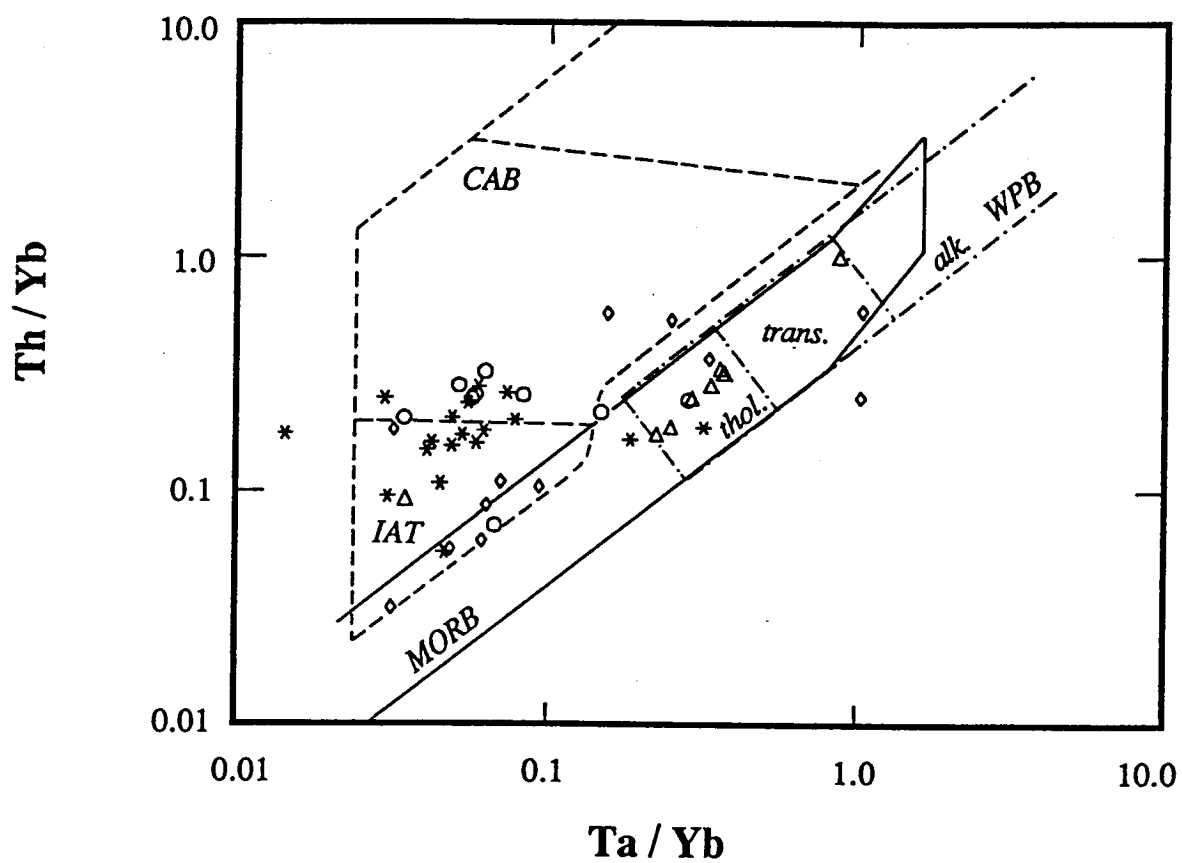


Figure 18. Th/Yb versus Ta/Yb variation of mafic volcanic flows and dikes from western Brooks Range ophiolites. Symbols as in Figure 1. Boundaries from Pearce (1983).

Discussion

We propose, on the basis of the geologic and trace element chemistry data presented, that the Copter Peak igneous sequence is a composite sequence, consisting of volcanic and intrusive rocks from several tectonic settings. Volcanic rocks exposed in the Avan Hills have trace element concentrations similar to basalts in the Angayucham terrane. The rocks have been interpreted to have formed in an oceanic island, a plateau, or a seamount setting (Pallister and Budahn, in press; Barker et al., in press). Volcanic rocks from Asik Mountain are compositionally and texturally heterogeneous, and probably had a complex magmatic and metamorphic history.

In contrast, volcanic rocks in the Maiyumerak Mountains are different from all others in the western Brooks Range, and from those described in the Angayucham terrane. The thick section of sheeted dikes within the section of relatively homogeneous basalt is unique in the Copter Peak igneous sequence. Furthermore, the trace element chemistry is also distinct; the relative Ti and Ta depletion is characteristic of rocks from volcanic arcs. Chemical differences between the two spectrally distinct basalt units in the Maiyumerak Mountains are subtle; basalts from the black-weathering unit plot in the calc-alkaline field and basalts from the red-weathering unit plot in the tholeiitic field of basalts from convergent margins. The combination of trace element data and geologic data indicate that the most likely tectonic setting for the formation of the Maiyumerak Mountain volcanic rocks was a back-arc basin or volcanic arc.

The geologic and geochemical evidence from the western Brooks Range ophiolites show that the Copter Peak igneous sequence includes rocks that originated in diverse tectonic settings; Landsat data were essential for the discrimination of the various volcanic rocks in this remote region.

**Ophiolite Crystallization, Thrusting, and Uplift,
Western Brooks Range, Alaska:
Evidence from $^{40}\text{Ar}/^{39}\text{Ar}$ Dating**

Abstract

$^{40}\text{Ar}/^{39}\text{Ar}$ data from layered mafic rocks in the western Brooks Range, Alaska, are used to study the age of crystallization, thrusting, and uplift of oceanic lithosphere that was obducted during the Late Jurassic-Early Cretaceous Brookian Orogeny. Hornblende from gabbro, diorite, and plagiogranite at Asik Mountain have low potassium concentrations ($\text{K}_2\text{O} = 0.07\text{--}0.2\%$) and complex Ar release spectra. Isochron plots of $^{36}\text{Ar}/^{40}\text{Ar}$ and $^{39}\text{Ar}/^{40}\text{Ar}$ values for hornblende samples from coarse-grained and layered gabbro yields isochron ages of 163.8 ± 9.4 , 179.3 ± 7.2 , and 183.5 ± 7.0 Ma. Hornblende from coarse-grained diorite dikes yield intercept ages of 171.7 ± 10.2 and 193.9 ± 12.0 . Hornblende samples from plagiogranite yield similar intercept ages, but have large errors. Hornblende samples from strongly lineated diorite and amphibolite, structurally below a thrust fault that separates gabbro and peridotite from volcanic and intrusive rocks at Asik Mountain, yield ages of 165.6 ± 2.4 and 169 ± 5.8 Ma. Biotite and hornblende from schist and amphibolite along a thrust fault between upper layered peridotite and gabbro and lower mafic volcanics, at Avan Hills, yield ages of 168 ± 1.0 and 165.4 ± 3.4 Ma, respectively. Biotite and potassium-feldspar from monzonite in the metamorphic sole yield ages of 164.1 ± 1.0 and 146.2 ± 0.8 Ma, respectively.

The mean $^{40}\text{Ar}/^{39}\text{Ar}$ age of hornblende samples from gabbro, diorite, and plagiogranite is 178.7 ± 8.6 Ma and is interpreted to be the minimum age of crystallization. The metamorphic samples are from the structurally highest, and by interpretation, the oldest thrusts in the Brooks Range. The $^{40}\text{Ar}/^{39}\text{Ar}$ ages from the metamorphic sole rocks are interpreted as the minimum age of ophiolite detachment and thrusting (~166 Ma ago), the earliest time for the beginning of "Brookian" deformation. The $^{40}\text{Ar}/^{39}\text{Ar}$ age of potassium-feldspar suggests that the ophiolite cooled and was uplifted approximately 145-150 Ma ago; Ar loss continued until about 110 Ma ago. Ar data from metamorphic hornblende, from below the thrust at Asik Mountain, are interpreted to record a regional deformation and heating event at the time of thrusting.

Although the crystallization age is not well-constrained, the time between crystallization and detachment and/or thrusting is approximately 10 Ma. The age of clastic (flysch) sediments, deposited in a northward migrating foredeep in front of the advancing thrust sheets, constrains the ophiolite emplacement to no later than Tithonian, about 25 Ma after crystallization. The $^{40}\text{Ar}/^{39}\text{Ar}$ data from potassium-feldspar indicate cooling below approximately 150 °C by 145-150 Ma ago, and might indicate that uplift occurred during emplacement. Ar diffusion from the potassium-feldspar occurred until approximately 110 Ma ago, the time of uplift previously interpreted from K-Ar ages from other parts of the Brooks Range.

Introduction

Chronologic studies of Brooks Range ophiolites were done as part of a Landsat Thematic Mapper study of the ophiolites. During our examination and processing of the Thematic mapper data we observed spectral variations among the ophiolitic rocks that might be evidence for several different metamorphic events. The timing of these events, relative to the formation and emplacement of the ophiolites, was not well understood.

We use the $^{40}\text{Ar}/^{39}\text{Ar}$ technique to study crystallization, metamorphism, thrusting, emplacement, and uplift of the ophiolites. The ubiquitous presence of potassium in most common rocks types, and the systematics of the K-Ar system, make this technique useful for studying various rock types over a range of ages. The $^{40}\text{Ar}/^{39}\text{Ar}$ technique of K-Ar dating can also yield information about the thermal history of the materials being dated.

In the conventional K-Ar technique, a mineral or a powdered rock sample is fused. The Ar released during heating is collected and analysed, and an age is calculated from the $^{40}\text{Ar}/^{39}\text{Ar}$ ratio and the amount of potassium in the sample. The interpretation of the calculated age involves several assumptions about the presence of non-radiogenic Ar components and the loss or gain of Ar. Additionally, the concentration of potassium in the sample is usually determined on a separate aliquot of the sample and by a technique other than mass-spectrometry.

In the $^{40}\text{Ar}/^{39}\text{Ar}$ technique, unlike the conventional K-Ar method, the parent/daughter ratio is determined during the same analysis and from the same sample, eliminating the uncertainties of determining potassium and

argon concentrations, and sample inhomogeneity. The $^{40}\text{Ar}/^{39}\text{Ar}$ technique uses step-wise incremental heating of mineral separates. The gas fractions released during each heating increment are analysed, and an age spectrum is calculated. The resulting age spectra are often complex due to partial argon loss, and to the presence of non-radiogenic ^{40}Ar components and excess argon. In rocks that contain excess argon, or that have experienced partial argon loss, the Ar released during the low temperature heating increments often yield "mixing ages" that are difficult to interpret. However, Ar released during the higher temperature increments, is presumably from more retentive sites that are not affected by low-temperature thermal events, often yields ages that plot as plateaus and are more-easily interpreted. The $^{36}\text{Ar}/^{40}\text{Ar}$ and $^{39}\text{Ar}/^{40}\text{Ar}$ ratios of gases released by stepwise heating can yield information about the isotopic composition of trapped Ar component when plotted on an isochron diagram.

Analytical Techniques

Amphibole, mica and feldspar grains, averaging 0.18-0.5 mm in diameter, were separated using heavy liquid and magnetic separation techniques. The mineral separates were further concentrated by hand-picking and were irradiated in a fast neutron beam at the Ford reactor, University of Michigan. The analyses were done using an automated Nuclide 4.5-60-RSS mass spectrometer at the State University of New York at Albany under the direction of M. Harrison and M. Heitzler. The mass spectrometer has a sensitivity of about 2×10^{-15} mol Ar/mv. Ratios used to correct data for the samples were $(^{40}\text{Ar}/^{39}\text{Ar})_{\text{K}} = 0.029$, $(^{36}\text{Ar}/^{37}\text{Ar})_{\text{Ca}} = 0.000222$, and $(^{39}\text{Ar}/^{37}\text{Ar})_{\text{Ca}} = 0.000825$. The specifications of the mass spectrometer, and the analytical techniques used

in this study, were described by Harrison et al., (1986). Mineral ages were calculated using the decay constants and isotope abundances of Steiger and Jäger (1977). $^{36}\text{Ar}/^{40}\text{Ar}$ versus $^{39}\text{Ar}/^{40}\text{Ar}$ isochron ages (Huneke diagrams) were calculated using the regression calculations described by York (1969). Errors reported for ages are one sigma unless otherwise stated. Errors reported for geologic ages include 1% error in the J-factor. K/Ca ratios were calculated from the $^{39}\text{Ar}/^{37}\text{Ar}$ ratios of the samples and flux monitors (0.015), and from the K/Ca ratio of the flux monitor (26.8).

Acknowledgements

We wish to thank Stephen Box, Inyo Ellersieck, Steve Nelson, John Pallister, and Irving Tailleir for their informative and stimulating discussions of Brooks Range ophiolites. Samples for this study were collected during field studies supported by the NASA program "Thematic Mapper Research in the Earth Sciences" (Grant No. NAS5-28739). M. Harrison and M. Heizler provided valuable assistance during $^{40}\text{Ar}/^{39}\text{Ar}$ mass spectrometry. We acknowledge the U.S. Park Service for permitting us to do this study within the Noatak National Preserve.

Geology

The Brooks Range consists of thrust sheets of Cambrian to Early Cretaceous carbonate and clastic sedimentary rocks and minor volcanic and intrusive rocks that were thrust northward and folded during Late Jurassic to Early Cretaceous time (reviewed by Mayfield et al., 1983). Late Precambrian-Permian(?) metamorphic rocks in the southern part of the range are autochthonous or parautochthonous, and might correlate with basement rock in the Colville Basin north of the Brooks Range. Late Jurassic-Upper Cretaceous clastic sediments were transported northward from the evolving Brooks Range into the Colville Basin .

Mafic and ultramafic rocks dip south under the Yukon-Koyukuk Basin along the southern margin of the Brooks Range. These rocks have been interpreted as the "root zone" for the allochthonous mafic and ultramafic rocks in the northern part of the range (Roeder and Mull, 1978). Andesitic volcanic rocks and sediments in the central part of the Yukon-Koyukuk basin might be the remnants of an Early to mid-Cretaceous volcanic arc. These rocks are overlain by clastic sediments that were transported southward from the Brooks Range during Cenozoic time.

Western Brooks Range Ophiolites

Mafic and ultramafic rocks, collectively named the Misheguk igneous sequence, are the structurally highest rocks in the western Brooks Range (Figure 1) and are exposed at Misheguk Mountain, Siniktanneyak Mountain, Avan Hills, Iyikrok Mountain, and Asik Mountain (Mayfield et al., 1983).

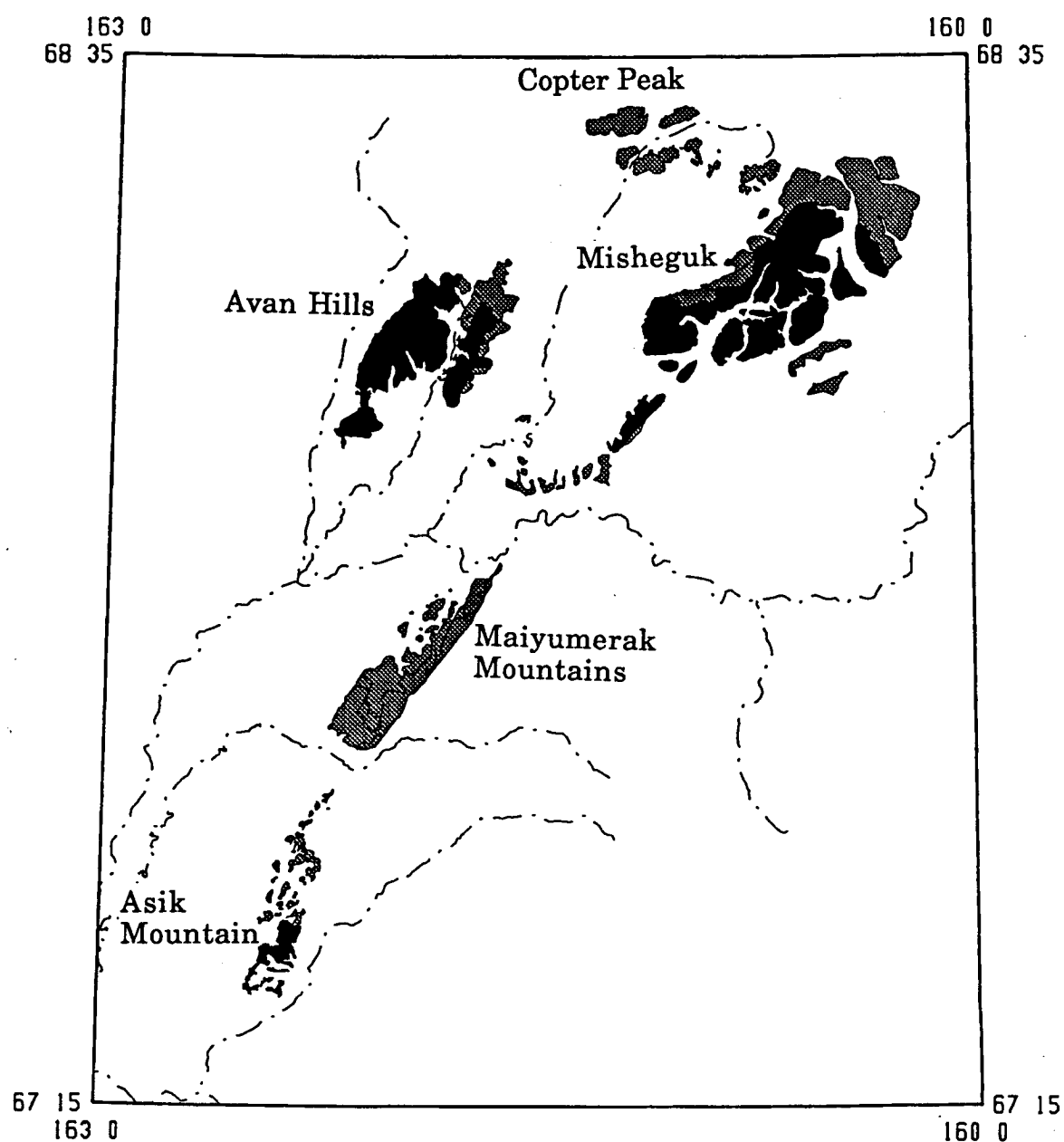


Figure 1. Generalized geologic map of western Brooks Range ophiolites in the Noatak Basin area. Peridotite and gabbro are shown in black, and basalt is shown with a stippled pattern. Lithologic boundaries are from existing maps (Curtis et al., 1984; Mayfield et al., 1983), field mapping, and from the analysis of Thematic Mapper images.

Variations in mineral composition and grain size define layering at Asik Mountain and Avan Hills. The layering is nearly vertical at both places and trends north-south, probably due to rotation along faults. At Asik Mountain, the rocks grade from interlayered dunite and pyroxenite, in the west, to gabbro and massive hornblende gabbro (sample AM-259) in the east. Coarse-grained hornblende gabbro exposed near the top of the layered section has a crescumulate texture (samples AM-260 and 262). At Asik Mountain the layered gabbros are cross-cut by dikes of coarse-grained hornblende diorite (samples AM-39 and 39b) and by plagiogranite (sample AM-95).

North of Asik Mountain, massive and variably-textured gabbro and plagiogranite (sample AM-228) have complex intrusive relationships and are pervasively deformed. The heterogeneous and deformed character of these rocks contrasts with the undeformed and layered gabbroic rocks on Asik Mountain, suggesting that they are separated by a fault. Alternatively, they might be a more heterogeneous continuation of the layered mafic and ultramafic sequence that was subsequently deformed.

Although complex faulting within the Avan Hills massif has disrupted and repeated the layered mafic and ultramafic section, there is a west to east variation of lithology, similar to that at Asik Mountain; the Avan rocks grade from dunite, to dunite with interlayers of pyroxenite and gabbro-norite, to olivine gabbro, and gabbro. Large faulted blocks of tectonized harzburgite and dunite are also present at Avan Hills.

The upper thrust sheets at Asik Mountain and at Avan Hills have layering and compositions that are similar to rocks in the lower parts of ophiolite complexes (Tailleur, 1970, 1973; Patton et al., 1977, Roeder and Mull, 1978; and Mayfield et al., 1983). The ultramafic and mafic rocks of the upper thrust

overlie, and are in thrust-fault contact with mafic volcanic rocks. The rocks, called the Copter Peak igneous sequence (Mayfield et al., 1983), are exposed at Siniktanneyak Mountain, Misheguk Mountain, Copter Peak, Avan Hills Iyikrok Mountain, Asik Mountain, and in the Maiyumerak Mountains. The Copter Peak igneous sequence consists of massive and pillowed metavolcanic flows at Asik Mountain and Avan Hills; minor mafic to intermediate(?) composition intrusive rock are also present. Volcanic rocks in the Maiyumerak Mountains are a thick sequence of layered and pillowed basalt flows. A north-south-trending sheeted dike sequence is exposed across the southern part of the Maiyumerak Mountains. Trace element data and metamorphic mineral assemblages vary among the basalts within the Maiyumerak Mountains suggesting that originated in different tectonic settings (Wirth et al., 1987). The rocks in this thrust sheet are similar to the volcanic rocks of ophiolites. Roeder and Mull (1978) proposed that the two thrust sheets comprise an ophiolite, but that the original sequence of basalt overlying gabbro and peridotite was inverted by thrusting.

Metamorphic rocks occur in many places along the contact of the ultramafic rocks and the structurally lower mafic volcanic rocks (Zimmerman and Frank, 1982; Curtis et al., 1984; Ellersieck et al., 1984; Boak et al., 1987). The metamorphic rocks range from low- to medium-grade, consisting of amphibolite, schist, pelite or marble. Biotite schist, biotite-garnet schist (sample AH-153), amphibolite (sample AH-161), and amphibole-bearing plagioclase-quartz schists are the main rock types present along the thrust fault at Avan Hills and generally range from a few meters to tens of meters thick. As much as 100 meters of metamorphic rock have been reported from Misheguk Mountain (Ellersieck et al., 1984). The amphibole-bearing plagioclase-quartz

schists are folded, and well-layered; the layering might be preserved sedimentary layering. Biotite schist and amphibolite commonly contain angular clasts of foliated minerals in a non-foliated matrix, perhaps because the rocks remained heated after motion ceased along the thrust. Medium-grained and foliated monzonite (sample AH-135) along the thrust in Avan Hills is partly hydrothermally altered to pectolite, chlorite, and sericite.

Zimmerman and Frank (1982) found a cummingtonite, orthopyroxene, and plagioclase assemblage in one sample from the Avan Hills and suggested that the rock formed in the hornblende- to pyroxene-hornfels facies. Boak et al. (1987) studied para-amphibolite, pelite and ortho-amphibolite from exposures west of Iyikrok Mountain. They concluded that the rocks were metamorphosed at temperatures of approximately 560 °C, using a biotite-garnet geothermometer. Metamorphic soles recognized in other ophiolite complexes are probably related to the thrusting of relatively hot peridotite over cooler volcanic rock, with possibly some heat contribution from friction (eg. Malpas, 1979).

Previous Geochronologic Investigations

The results of previous K-Ar studies of ophiolites in the Brooks Range and Yukon-Koyukuk Basin are summarized in Figure 2.

Patton et al. (1977) obtained an age of 384 ± 55 Ma from one sample of hornblende from an amphibolite at Asik Mountain, much older than previous age determinations of ophiolitic rocks from the Brooks Range. The apparently old age of the sample might be due to excess Ar, which is commonly present in the samples that we have studied.

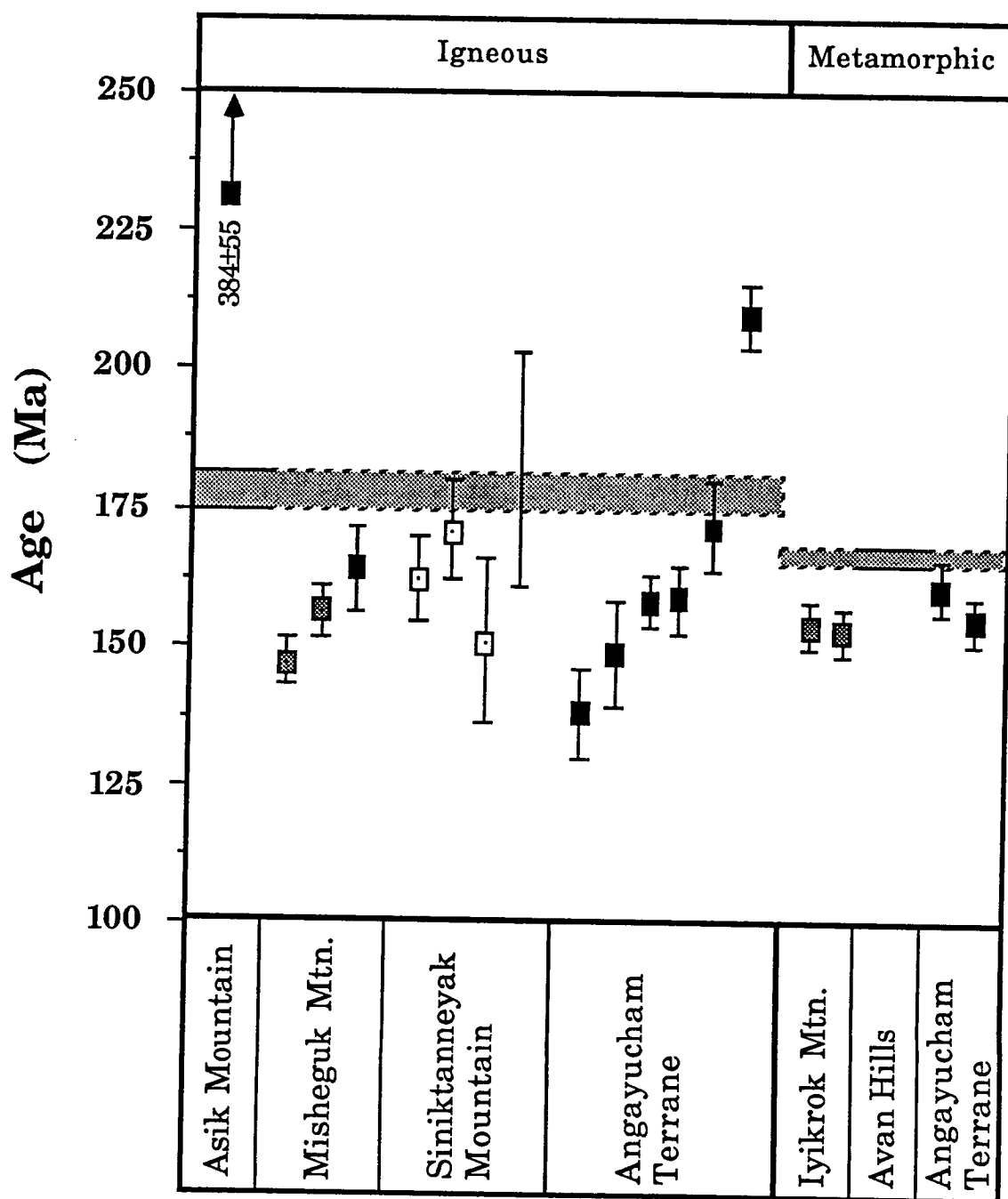


Figure 2. Summary of K-Ar ages determined for northern Alaska ophiolites.

Data are from Patton et al. (1977)(solid symbols), Nelson and Nelson (1983)(unfilled symbols), Boak et al. (1987)(stippled symbols), and Turner (in prep.)(bar showing range of analyses). Also shown are the mean $^{40}\text{Ar}/^{39}\text{Ar}$ ages of crystallization and thrusting determined from this study. All errors are $\pm 1\sigma$.

Although no radiometric ages have been reported for the Avan Hills rocks, there have been several studies of gabbroic and metamorphic rocks from other exposures in the western Brooks Range. Hornblende from a pegmatite that cross-cuts gabbro at Siniktanneyak Mountain, yielded a K-Ar age of 151 ± 15 Ma (Patton et al., 1977). Two other K-Ar ages have been reported for the mafic rocks exposed at Siniktanneyak Mountain. Biotite and hornblende from quartz diorite yield K-Ar ages of 162 ± 8 and 171 ± 9 Ma, respectively (Nelson and Nelson, 1982; S. W. Nelson, written commun., 1985). Five unpublished hornblende K-Ar ages (cited in Boak et al., 1987; Turner et al., in prep) range from 161-202 Ma. Blocks of limestone within mafic volcanic rocks at Siniktanneyak Mountain contain Fasnian (lower Upper Devonian) stromatoporoids and corals; these blocks might have been tectonically incorporated into the volcanic rocks (Ellersieck et al., 1982). Curtis et al. (1984) reported Mesozoic radiolaria from chert within mafic volcanic rocks in the eastern Avan Hills.

Hornblende gabbro at Misheguk Mountain yielded a K-Ar age of 164 ± 7.2 Ma (Patton et al., 1977). Boak et al. (1985, 1987) dated gabbro and diorite from Misheguk Mountain and determined K-Ar ages of 147.2 ± 4.4 and 155.8 ± 4.7 Ma, respectively. They also dated hornblende from amphibolite and garnet-bearing biotite-hornblende gneiss at the base of the mafic and ultramafic complex at Iyikrok Mountain. The mineral separates yielded K-Ar ages of 154.2 ± 4.6 and 153.2 ± 4.6 Ma, and are indistinguishable from the age of igneous rock that they determined. Boak et al. (1985, 1987) suggested that both the igneous and metamorphic ages reflect a thermal metamorphic event that post-dated igneous crystallization. Chert layers within the mafic volcanic section at Misheguk Mountain contain Triassic radiolaria (Ellersieck et al., 1984).

Reiser et al. (1965), Brosgé et al. (1969), and Patton et al. (1977) reported K-

Ar ages for igneous and metamorphic rocks from mafic-ultramafic sequences in the Yukon-Koyuk and Rampart Belts south of the Brooks Range. Eight ages calculated for hornblende and plagioclase separated from layered gabbro and hornblende-bearing dikes, range between 138-210 Ma, with most determinations between 149 and 172 Ma. Metamorphic hornblende from amphibolite at the base of the layered mafic and ultramafic complexes yielded K-Ar ages of 161-155 Ma. The Middle and Late Jurassic ages determined from the igneous and metamorphic minerals are identical within their analytical errors, and are interpreted to record metamorphism during tectonic emplacement of the of the complexes onto continental crust rather than the age of crystallization (Patton et al., 1977). Fossils from chert in the Yukon-Koyukuk and Rampart ophiolite belts range from Mississippian to Permian (Patton et al., 1977; Bird, 1977; Gottschalk, 1987; Pallister, 1985; Pallister and Budahn, in press.)

Turner et al. (1979) reported seventy-six K-Ar ages for non-ophiolitic igneous and metamorphic rocks in the southwestern Brooks Range. Many of the metamorphic biotite and muscovite ages are Early Cretaceous (100-120 Ma) and are interpreted to record the age of cooling below the argon retention temperature for biotite and muscovite after Late Jurassic-Early Cretaceous thrusting.

$^{40}\text{Ar}/^{39}\text{Ar}$ Results

The results of incremental heating experiments on sixteen mineral separates are reported in Table 1. Ar release spectra and isochron diagrams are presented in Figures 3 to 17. The total-gas ages, plateau ages, and isochron ages are summarized in Table 2.

Integrated, or "total-gas", ages for each sample were calculated from the sum of the apparent ages weighted by the moles of ^{39}Ar released during each heating increment. The total-gas age approximates the age that would be obtained if the sample had been degassed in a single heating step, as would be the case in the conventional K-Ar technique. A "plateau" age has been calculated for samples with release spectra that have contiguous gas fractions of similar age. The plateau age corresponds to the age that would be obtained if the "plateau" portion of the release spectra had been outgassed in a single heating step. Plateau ages were calculated from the sum of the apparent ages of the heating steps, weighted by the moles of ^{39}Ar released during each heating increment, included in the plateau. Isochron ages were also calculated from the $^{36}\text{Ar}/^{40}\text{Ar}$ and $^{39}\text{Ar}/^{40}\text{Ar}$ data for gas increments that are included in plateaus. Isochron ages for sample release spectra that lack plateaus were calculated using all the gas fractions, excluding the initial heating increments, which typically are similar to "air" in composition, and the highly anomalous fractions, which usually resulted from the analysis of small amounts of Ar.

Hornblende Gabbro

Sample AM-39 has a complex release spectra (Figure 3); the calculated apparent ages in both the low (650-950 °C) and intermediate (1060-1110 °C) temperature increments are relatively old. Ar released during the last five heating increments yielded similar ages (weighted mean = 201 ± 10.5 Ma). A regression of the $^{36}\text{Ar}/^{40}\text{Ar}$ and $^{39}\text{Ar}/^{40}\text{Ar}$ data for these increments yields a similar age (within 1 sigma error) and confirms that there is a trapped Ar component present that has a composition similar to air. The addition of the 1030 °C increment, also of similar apparent age, does not significantly change the interpretation of the isochron data. The Ar gas released during heating steps below 1030 °C apparently contain excess argon.

Sample AM-39b, collected from the same exposure as for sample AM-39, and of similar composition, yielded a different release spectra (Figure 4). As in the sample AM-39, the low-temperature fractions yielded anomalously old ages, probably due to the presence of excess argon. With the exception of heating step 10, gas fractions released at temperatures above 1090 °C yielded similar ages. Gas fractions released between 1090 and 1400 °C comprise a plateau that has a mean age of 171.7 ± 5.1 Ma. The isochron age of these fractions is similar to the plateau age, within the one sigma errors, and yields a very low $^{36}\text{Ar}/^{40}\text{Ar}$ intercept ($^{40}\text{Ar}/^{36}\text{Ar} = 114 \pm 60$). A regression of all of the heating increments, excluding those below 870 °C and the anomalous 1065 and 1120 °C heating increments, yields a similar age (179.2 ± 31.5 Ma), but has a large error due to the scatter in the points (MSWD=23.5).

Most of the Ar from the pyroxene-hornblende gabbro (sample AM-259) was released between the 1040 and 1080 °C heating increments (Figure 5). The

apparent ages calculated for the two increments are similar (mean age = 168.4 ± 0.5 Ma). A regression of all of the gas fractions on an isochron diagram yields an age of 163.8 ± 4.7 Ma and an $^{40}\text{Ar}/^{36}\text{Ar}$ ratio of 334.7 ± 31.8 (MSWD = 5.66).

Incremental heating of hornblende from pegmatitic hornblendite (sample AM-260) yielded a complex Ar release spectra (Figure 6). Although many of the gas fractions released between 1050 and 1450 °C have large errors, most yielded approximately the same age (mean weighted age = 193.6 ± 7.5 Ma). A regression of the Ar data for the same gas fractions yields an age of 183.5 ± 3.5 Ma and an $^{40}\text{Ar}/^{36}\text{Ar}$ ratio of 326.1 ± 23.4 (MSWD = 9.01). The omission of data from the anomalous gas fractions released during the 1110, 1130, and 1150 °C heating increments does not significantly change the intercepts of the calculated line, but does improve the fit of the line to the data (MSWD = 4.06).

Ar analyses, and replicate analyses, of hornblende from hornblende gabbro (sample AM-262) are similar; total-gas ages are 188.1 and 194.4 Ma, and more than 77% of the Ar released by each sample is of similar age (179.3 ± 3.6 Ma and 180.7 ± 5.1 Ma; Figures 7 and 8). Regression calculations of the data on an isochron diagram yield ages of 154.0 ± 17.4 and 148.8 ± 18.9 Ma, and $^{40}\text{Ar}/^{36}\text{Ar}$ ratios of 448 ± 101 (MSWD = 11.45) and 464 ± 89 (MSWD = 2.12), respectively.

Plagiogranite

Ar data for hornblende from plagiogranite sample AM-95, and its replicate analysis, have "saddle-shaped" release spectra (Figures 9 and 10). The minimum apparent age of both spectra is about 190 Ma, and the total-gas ages of both are approximately 230 Ma. An isochron plot of all the gas fractions, excluding the early gas fractions with "air" compositions and anomalous

fractions, yields an age of 177.4 ± 30.1 and an $^{40}\text{Ar}/^{36}\text{Ar}$ ratio of 409.7 ± 71.4 (MSWD = 5.28). An isochron plot of the replicate analysis, using similar point selection criteria, yields an age of 175.1 ± 19 Ma and an $^{40}\text{Ar}/^{36}\text{Ar}$ ratio of 435.8 ± 52.5 (MSWD = 9.78).

The release spectra of sample AM-228 (Figure 11), also a plagiogranite, is unique for the samples analysed. It does not have the old apparent ages typical for the low temperature steps, and most of the steps have similar apparent ages (168-198 Ma). Apparent ages calculated for the last four steps (1170-1400 °C) form a plateau with an age of 195.1 ± 2.5 Ma. An isochron plot of data for the same gas fractions yields an age of 189.5 ± 41 Ma and an $^{40}\text{Ar}/^{36}\text{Ar}$ ratio of 327 ± 145 (MSWD = 5.1). Regression of data from all of the gas fractions yields an age of 187.2 ± 2.9 Ma and an $^{40}\text{Ar}/^{36}\text{Ar}$ ratio of 302.3 ± 11.3 (MSWD = 17.4).

Metamorphosed Diorite

Most of the Ar released during the incremental heating of metamorphosed diorite sample AM-234 yielded ages that range from 174-187 Ma (Figure 12); the remaining fractions, from the lowest- and highest-temperature heating increments, have older apparent ages. The Ar fractions released during the heating steps between 1020 and 1140 °C yielded similar apparent ages (mean age = 175.0 ± 1.9 Ma). A regression of Ar data from these gas fractions yields an age of 168.0 ± 4.7 Ma and an $^{40}\text{Ar}/^{36}\text{Ar}$ ratio of 391 ± 55 (MSWD = 4.87). A regression of the data for all but the first and last gas heating steps, yields an age of 169.0 ± 2.9 Ma and an $^{40}\text{Ar}/^{36}\text{Ar}$ ratio of 390.9 ± 32.6 (MSWD = 10.0).

Lineated Amphibolite

The Ar release spectra for amphibolite AM-236 is complex (Figure 13), consisting of two "plateau" segments (980-1100 °C and 1150-1240°C) with ages of about 168 Ma and 182 Ma, respectively. A regression of data for the 980-1100 °C heating step yields an age of 165.8 ± 1.0 Ma and an $^{40}\text{Ar}/^{36}\text{Ar}$ ratio of 333.1 ± 20.1 (MSWD = 0.32).

Monzonite

Most of the Ar outgassed by the potassium feldspar from Avan Hills monzonite (AH-135) was released during the 1300 °C heating increment (Figure 14). The apparent ages calculated for the relatively small amounts of gas that were released prior to the 1300 °C heating step do not form a coherent pattern. The apparent age calculated from the 1300 °C heating step, which comprises more than 63% of the total gas released, is 146.2 ± 0.4 Ma, and is similar to the total-gas age (148.6 Ma).

Ar data for biotite, also separated from the monzonite, yielded a total-gas age of 162.9 Ma. $^{40}\text{Ar}/^{39}\text{Ar}$ ages calculated for more than 97% of its release spectra are similar and have a mean age of 164.1 ± 0.5 Ma (Figure 15).

Biotite Schist

Biotite from biotite schist AH-153 yielded a total-gas age of 165.9 Ma and a release spectrum with a somewhat irregular plateau (mean age = 167.9 ± 0.5 Ma) that includes more than 87% of the total gas released (Figure 16).

Ar degassed during the 920 and 1000 °C heating increments yields apparent age that are older than the preceeding and following heating increments. Similar results have been observed for biotite by Berger and York (1981) and by Onstott and Peacock (1987).

Amphibolite

During incremental heating, ferro-hornblende AH-161 released a relatively large amount of gas ($\sim 34 \times 10^{-13}$ moles). Apparent ages calculated from data for the heating steps are similar (Figure 17). Ar degassed during the 1000 and 1050 °C heating increments comprised more than 53% of the total gas released by heating, and has a mean age of 165.4 ± 1.7 Ma. Regression Ar data for the 1000-1160 °C increments, excluding data from the anomalous 1065 °C heating increment, yields an age of 164.6 ± 0.4 Ma and an $^{40}\text{Ar}/^{36}\text{Ar}$ ratio of 276.5 ± 13.4 (MSWD = 2.58).

Table 1. $^{40}\text{Ar}/^{39}\text{Ar}$ incremental release data.

Temp (°C)	$\frac{^{40}\text{Ar}}{^{39}\text{Ar}}$	$\frac{^{37}\text{Ar}}{^{39}\text{Ar}}$	$\frac{^{36}\text{Ar}}{^{39}\text{Ar}}$ (10^{-3})	^{39}Ar (10^{-13}) moles	Cumula- tive % ^{39}Ar	$^{40}\text{Ar}^*$ (%)	$\frac{^{40}\text{Ar}^*}{^{39}\text{Ar}}$ (10^{-4})	$\frac{^{39}\text{Ar}}{^{40}\text{Ar}}$ (10^{-4})	$\frac{^{36}\text{Ar}}{^{40}\text{Ar}}$ (10^{-4})	Apparent Age (Ma)
AM-39-85 hornblende; J = 0.006339										
650	2483	33.62	7816	0.0202	0.39	7.01	180.59	3.92	31.44	1376.6 ± 786.2
750	149.6	10.85	293.6	0.0279	0.92	37.92	64.07	66.28	19.50	614.9 ± 123.7
850	148.3	42.31	319.1	0.0190	1.28	32.50	58.77	65.14	21.02	571.3 ± 145.4
950	42.62	45.49	57.46	0.1309	3.79	61.55	29.66	226.23	11.56	310.8 ± 24.3
1000	27.67	51.68	35.04	0.6490	16.20	72.67	21.56	346.74	8.83	231.1 ± 3.0
1030	23.13	55.05	29.53	1.3888	42.77	76.52	18.80	413.66	7.72	203.2 ± 1.6
1045	25.11	50.73	22.34	0.5828	53.92	83.94	22.72	382.50	4.95	242.7 ± 2.7
1060	30.80	43.92	22.17	0.2422	58.55	82.44	28.08	313.56	4.80	295.5 ± 10.8
1080	38.42	41.51	77.17	0.0690	59.87	40.07	18.93	251.82	18.29	204.4 ± 54.8
1110	57.21	44.87	104.74	0.0579	60.98	44.30	30.26	168.58	16.96	316.5 ± 62.2
1140	23.43	54.22	24.01	0.2677	66.10	78.46	20.75	408.79	6.21	222.9 ± 10.3
1160	24.02	54.45	35.55	0.3863	73.50	67.33	17.82	398.66	10.35	193.1 ± 7.9
1180	28.60	51.99	48.65	0.2859	78.96	57.96	18.35	335.43	13.44	198.6 ± 8.0
1210	32.19	50.67	51.93	0.1868	82.54	57.73	20.98	298.29	13.18	225.2 ± 15.9
1240	29.10	52.76	50.81	0.2608	87.53	56.43	18.27	329.46	13.92	197.7 ± 14.5
1450	76.35	53.25	212.77	0.6520	100.00	21.95	17.68	125.43	26.35	191.7 ± 6.4
	Total			5.2272						

Total Gas Age = 226.5 Ma

Table 1. (continued).

Temp (°C)	$\frac{40\text{Ar}}{39\text{Ar}}$	$\frac{37\text{Ar}}{39\text{Ar}}$	$\frac{36\text{Ar}}{39\text{Ar}}$ (10 ⁻³)	$\frac{39\text{Ar}}{(10^{-13})}$ moles	Cumulative % $\frac{39\text{Ar}}$	$\frac{40\text{Ar}^*}{(%)}$	$\frac{40\text{Ar}^*}{39\text{Ar}}$	$\frac{39\text{Ar}}{40\text{Ar}}$ (10 ⁻⁴)	$\frac{36\text{Ar}}{40\text{Ar}}$ (10 ⁻⁴)	Apparent Age (Ma)
AM-39b-85 hornblende; J = 0.005995										
720	266.26	13.52	753.29	0.0702	1.45	16.63	45.02	37.14	28.18	431.0 ± 18.2
820	71.66	16.57	111.97	0.0495	2.47	53.79	40.18	137.70	15.15	389.3 ± 53.1
870	59.81	30.91	75.04	0.0311	3.12	62.89	40.68	163.00	11.55	393.7 ± 82.2
920	36.53	42.83	75.62	0.0827	4.83	44.95	17.58	264.31	18.25	180.8 ± 30.1
945	29.59	41.97	50.16	0.1049	6.99	57.28	18.12	326.52	14.00	186.1 ± 22.0
965	28.02	40.55	41.08	0.1502	10.10	64.54	19.16	345.25	11.63	196.1 ± 6.2
995	23.02	48.17	27.57	0.5017	20.46	77.54	18.75	417.72	7.45	192.2 ± 3.8
1025	22.32	47.58	34.18	0.5523	31.88	68.05	15.94	430.97	10.68	164.6 ± 4.4
1045	21.77	46.96	29.74	0.3940	40.02	72.80	16.68	442.10	9.02	171.9 ± 6.4
1065	22.36	43.89	40.99	0.2542	45.27	57.57	13.59	431.62	14.13	141.3 ± 8.9
1090	21.28	45.63	26.06	0.2609	50.66	76.36	17.19	452.91	7.72	176.9 ± 6.7
1120	23.40	41.92	38.33	0.1749	54.28	61.72	15.33	413.02	12.61	158.6 ± 12.8
1160	21.19	45.20	27.26	0.3448	61.40	74.81	16.69	454.97	8.31	172.0 ± 5.6
1200	21.47	44.63	28.58	0.4972	71.68	73.48	16.53	449.13	8.82	170.5 ± 2.6
1400	22.11	45.07	28.77	1.3705	100.00	74.54	17.17	436.08	8.54	176.8 ± 1.7
			Total	4.8391						

Total Gas Age = 181.2 Ma

Table 1. (continued).

Temp (°C)	$\frac{^{40}\text{Ar}}{^{39}\text{Ar}}$	$\frac{^{37}\text{Ar}}{^{39}\text{Ar}}$	$\frac{^{36}\text{Ar}}{^{39}\text{Ar}}$ (10 ⁻³)	$\frac{^{39}\text{Ar}}{^{10^{-13}}}$ moles	Cumulative % $\frac{^{39}\text{Ar}}{^{39}\text{Ar}}$	$\frac{^{40}\text{Ar}^*}{^{39}\text{Ar}}$ (%)	$\frac{^{40}\text{Ar}^*}{^{39}\text{Ar}}$ (10 ⁻⁴)	$\frac{^{39}\text{Ar}}{^{40}\text{Ar}}$ (10 ⁻⁴)	$\frac{^{36}\text{Ar}}{^{40}\text{Ar}}$ (10 ⁻⁴)	Apparent Age (Ma)
AM-95-85 hornblende; J = 0.006354										
850	312.49	30.64	816.80	0.1154	2.91	23.07	74.93	31.22	25.93	702.5 ± 71.5
950	46.07	48.60	73.15	0.1492	6.67	55.85	28.72	208.74	13.87	302.4 ± 38.9
1000	26.77	65.21	38.77	0.8960	29.25	71.54	20.63	354.32	9.36	222.2 ± 3.1
1020	22.77	75.27	35.59	0.7908	49.17	73.25	18.24	413.13	8.75	197.9 ± 6.2
1035	35.83	58.25	61.20	0.1265	52.36	54.10	22.57	266.28	14.14	241.8 ± 13.4
1050	45.79	37.89	157.07	0.0386	53.34	3.11	1.88	211.88	32.89	21.45 ± 96.6
1070	51.39	40.58	92.90	0.0348	54.21	40.40	27.46	188.35	16.94	290.1 ± 86.0
1100	46.22	66.36	46.04	0.0537	55.57	66.48	38.99	205.00	8.08	399.3 ± 23.3
1140	25.42	71.56	40.24	0.5088	68.39	68.85	19.28	371.25	10.09	208.5 ± 2.6
1180	29.07	66.83	49.51	0.4550	79.85	62.24	19.84	325.91	12.32	214.2 ± 11.8
1220	48.99	52.58	99.57	0.0741	81.72	41.22	23.99	195.63	18.40	255.9 ± 48.8
1260	31.89	62.85	58.48	0.2459	87.92	55.09	19.68	298.02	14.45	212.6 ± 8.7
1450	86.86	68.05	242.31	0.4795	100.00	22.39	20.81	108.89	26.20	224.1 ± 8.1
			Total	3.9638						

Total Gas Age = 233.6 Ma

Table 1. (continued).

Temp (°C)	$\frac{40\text{Ar}}{39\text{Ar}}$	$\frac{37\text{Ar}}{39\text{Ar}}$	$\frac{36\text{Ar}}{39\text{Ar}}$ (10 ⁻³)	$\frac{39\text{Ar}}{(10^{-13})}$ moles	Cumula- tive % $\frac{39\text{Ar}}{39\text{Ar}}$	$\frac{40\text{Ar}^*}{39\text{Ar}}$ (%)	$\frac{40\text{Ar}^*}{39\text{Ar}}$ (10 ⁻⁴)	$\frac{39\text{Ar}}{40\text{Ar}}$ (10 ⁻⁴)	$\frac{36\text{Ar}}{40\text{Ar}}$ (10 ⁻⁴)	Apparent Age (Ma)
AM-95-85 (replicate) hornblende; J = 0.006017										
720	373.23	22.42	1087	0.0759	1.84	14.25	54.39	26.30	29.00	510.8 ± 35.0
820	95.90	28.30	174.69	0.0543	3.16	47.17	47.21	101.87	17.59	451.1 ± 43.6
870	52.06	11.37	70.12	0.0929	5.41	60.33	32.36	190.38	13.01	321.0 ± 14.1
910	49.02	17.29	81.39	0.0655	7.00	51.58	26.45	201.23	15.88	266.4 ± 26.9
950	45.54	26.98	64.48	0.0938	9.27	60.57	28.87	214.83	12.92	289.0 ± 22.3
990	30.97	50.18	41.53	0.3147	16.90	70.19	22.91	309.82	9.91	232.9 ± 8.5
1020	33.16	38.09	34.20	0.0946	19.20	74.60	26.36	292.30	8.01	265.6 ± 15.2
1060	29.02	59.54	44.18	0.2142	24.39	67.30	20.87	327.96	10.84	213.4 ± 3.4
1100	24.92	62.41	38.87	0.4955	34.41	69.66	18.45	381.03	10.14	189.9 ± 4.0
1140	26.01	63.64	41.18	0.4686	47.77	68.60	18.99	364.63	10.50	195.2 ± 3.2
1180	26.10	60.92	35.48	0.8935	69.44	74.71	20.62	364.30	8.48	211.0 ± 2.3
1220	41.49	28.52	90.35	0.0865	71.53	39.00	17.03	235.52	20.33	176.0 ± 23.9
1260	27.23	56.11	35.28	0.8398	91.90	74.80	21.45	350.63	8.44	219.0 ± 2.2
1450	34.65	41.43	53.11	0.3341	100.00	61.93	22.41	278.96	12.73	228.2 ± 3.5
			Total	4.1239						

Total Gas Age = 225.9 Ma

Table 1. (continued).

Temp (°C)	$\frac{40\text{Ar}}{39\text{Ar}}$	$\frac{37\text{Ar}}{39\text{Ar}}$	$\frac{36\text{Ar}}{39\text{Ar}}$ (10 ⁻³)	$\frac{39\text{Ar}}{(10^{-13})}$ moles	Cumulative % $\frac{39\text{Ar}}$	$\frac{40\text{Ar}^*}{(\%)}$	$\frac{40\text{Ar}^*}{39\text{Ar}}$	$\frac{39\text{Ar}}{40\text{Ar}}$ (10 ⁻⁴)	$\frac{36\text{Ar}}{40\text{Ar}}$ (10 ⁻⁴)	Apparent Age (Ma)
AM-228-85 hornblende; J = 0.006021										
720	58.76	6.77	135.49	0.5364	7.83	32.46	19.24	169.33	22.82	197.8 ± 3.4
820	27.17	6.54	38.46	0.2556	11.57	58.80	16.30	366.42	13.65	168.9 ± 11.7
870	26.22	83.77	32.79	0.1885	14.32	63.74	17.17	379.13	11.85	177.5 ± 7.2
920	26.63	19.14	32.25	0.1781	16.92	67.40	18.62	369.95	10.61	191.7 ± 9.6
960	25.49	29.52	29.54	0.4169	23.01	72.55	19.13	383.18	9.10	196.7 ± 5.2
985	21.47	33.85	24.37	0.5831	31.52	76.06	16.93	453.33	7.94	175.2 ± 2.3
1020	25.09	29.53	32.94	0.2006	34.45	67.47	17.70	389.27	10.66	182.7 ± 6.5
1050	21.87	31.77	22.66	0.4321	40.76	77.96	17.70	445.75	7.25	182.9 ± 2.6
1090*	-----	33.78	22.01	0.9207	54.21	77.74	-----	-----	-----	(>164.9 ± 2.7)
1130	23.34	36.11	30.12	0.3864	59.85	71.10	17.29	416.19	9.58	178.7 ± 2.3
1170	21.74	34.74	18.38	0.6061	68.70	84.73	19.11	447.36	5.02	196.5 ± 3.3
1210	21.89	33.19	18.09	0.7085	79.05	84.84	19.22	444.94	4.99	197.5 ± 2.5
1250	21.78	34.14	19.85	0.8460	91.40	82.77	18.65	446.77	5.71	192.0 ± 1.4
1400	23.20	32.99	23.29	0.5889	100.00	78.97	18.97	419.75	6.96	195.2 ± 3.3
			Total	6.8479						

* ^{40}Ar peak saturated filament 1090 °C heating increment.

Total Gas Age = 189.3 Ma

Table 1. (continued).

Temp (°C)	$\frac{^{40}\text{Ar}}{^{39}\text{Ar}}$	$\frac{^{37}\text{Ar}}{^{39}\text{Ar}}$	$\frac{^{36}\text{Ar}}{^{39}\text{Ar}}$ (10 ⁻³)	$\frac{^{39}\text{Ar}}{^{10-13}}$ moles	Cumulative % $\frac{^{39}\text{Ar}}$	$\frac{^{40}\text{Ar}^*}{^{39}\text{Ar}}$ (%)	$\frac{^{40}\text{Ar}^*}{^{39}\text{Ar}}$ (10 ⁻⁴)	$\frac{^{36}\text{Ar}}{^{40}\text{Ar}}$ (10 ⁻⁴)	Apparent Age (Ma)
AM-234-85 hornblende; J = 0.006017									
720	199.45	9.54	528.17	0.3116	2.57	22.00	44.32	26.38	426.5 ± 17.1
820	42.47	7.27	78.35	0.1977	4.19	45.98	19.88	18.09	203.8 ± 7.6
870	37.49	7.15	55.24	0.1708	5.60	56.74	21.73	14.34	221.7 ± 11.5
910	36.96	11.33	50.02	0.1384	6.74	60.75	23.11	12.89	234.9 ± 13.4
950	25.59	13.22	36.67	0.2687	8.95	60.06	15.77	13.23	163.5 ± 7.0
980	23.51	12.88	19.28	0.3965	12.21	78.40	18.83	7.04	193.7 ± 4.5
1020	19.92	13.60	13.98	0.9529	20.06	83.16	16.84	5.55	174.1 ± 1.8
1060	22.00	12.88	19.42	0.2705	22.29	76.35	17.26	7.61	178.3 ± 5.2
1100	18.48	13.66	9.19	3.3059	49.50	89.85	16.82	3.35	173.9 ± 0.5
1140	19.76	13.66	12.08	2.4351	69.55	86.15	17.25	4.60	178.2 ± 0.8
1170	20.40	13.50	11.81	1.5114	81.99	86.81	17.96	4.35	185.2 ± 1.5
1210	20.11	13.21	11.60	1.3197	92.85	86.80	17.71	4.35	182.7 ± 1.4
1250	21.14	13.33	13.34	0.5777	97.61	84.65	18.24	4.98	187.9 ± 3.5
1400	26.98	12.60	24.51	0.2903	100.00	75.15	20.75	8.11	212.2 ± 9.4
			Total	12.1472					

Total Gas Age = 187.6 Ma

Table 1. (continued).

Temp (°C)	$\frac{40\text{Ar}}{39\text{Ar}}$	$\frac{37\text{Ar}}{39\text{Ar}}$	$\frac{36\text{Ar}}{39\text{Ar}}$ (10 ⁻³)	$\frac{39\text{Ar}}{(10^{-13})}$ moles	Cumula- tive % $\frac{39\text{Ar}}$	$\frac{40\text{Ar}^*}{39\text{Ar}}$ (%)	$\frac{40\text{Ar}^*}{39\text{Ar}}$	$\frac{39\text{Ar}}{40\text{Ar}}$ (10 ⁻⁴)	$\frac{36\text{Ar}}{40\text{Ar}}$ (10 ⁻⁴)	Apparent Age (Ma)
AM-236-85 hornblende; J = 0.006200										
700	235.87	9.80	721.01	0.4590	3.44	9.93	23.61	42.07	30.05	246.5 ± 9.5
750	28.39	5.72	213.67	0.1796	4.78	77.78	22.53	350.90	7.12	235.9 ± 19.5
800	23.27	6.65	24.64	0.1672	6.04	69.05	16.48	427.94	10.01	175.6 ± 14.9
850	2.49	0.749	2.08	1.3412	16.09	74.48	1.90	405.68	7.83	21.12 ± 3.2
900	19.82	7.99	38.76	0.1546	17.24	43.58	8.92	501.97	18.73	97.1 ± 11.0
950	22.30	14.37	18.38	0.2072	18.80	78.38	17.99	443.78	6.92	190.8 ± 6.5
980	21.42	15.16	22.81	0.3157	21.16	72.19	15.84	461.64	9.15	169.0 ± 9.7
1010	18.47	15.40	12.19	0.9168	28.03	85.40	16.04	53.55	4.81	171.1 ± 2.3
1040	16.69	16.04	75.51	3.6652	55.49	92.64	15.69	592.20	2.42	167.4 ± 0.8
1070	17.36	15.05	9.47	0.6661	60.48	88.79	15.71	569.86	3.62	167.7 ± 3.6
1100	21.21	15.47	22.63	0.2388	62.27	71.98	15.70	466.18	9.15	167.6 ± 15.4
1150	18.90	16.77	9.56	2.0767	77.83	90.54	17.38	522.59	3.13	184.7 ± 0.9
1200	18.79	15.75	10.81	2.7827	98.67	88.21	16.81	526.22	3.92	178.9 ± 1.3
1240	26.23	13.95	32.78	0.1655	99.91	65.25	17.62	377.38	11.39	187.1 ± 13.1
1400	114.11	0.999	91.40	0.0115	100.00	71.98	87.21	87.59	8.00	779.8 ± 147.6
			Total	13.3478						

Total Gas Age = 162.2 Ma

Table 1. (continued).

Temp (°C)	$\frac{40\text{Ar}}{39\text{Ar}}$	$\frac{37\text{Ar}}{39\text{Ar}}$	$\frac{36\text{Ar}}{39\text{Ar}}$ (10^{-3})	$\frac{39\text{Ar}}{(10^{-13})}$ moles	Cumulative % $\frac{39\text{Ar}}{39\text{Ar}}$	$\frac{40\text{Ar}^*}{(%)}$	$\frac{40\text{Ar}^*}{39\text{Ar}}$ (10^{-4})	$\frac{39\text{Ar}}{40\text{Ar}}$ (10^{-4})	$\frac{36\text{Ar}}{40\text{Ar}}$ (10^{-4})	Apparent Age (Ma)
AM-259-85 hornblende; J = 0.006045										
820	74.31	6.43	205.83	0.0134	0.23	16.98	13.96	133.91	27.54	146.1 ± 270.4
920	60.20	24.47	135.55	0.0234	0.64	33.69	22.17	162.84	21.71	226.9 ± 89.5
980	32.49	34.50	53.78	0.0703	1.87	55.53	19.39	299.26	14.40	199.9 ± 19.9
1040	20.14	27.35	19.93	2.3668	43.12	79.35	16.38	486.08	6.91	170.4 ± 0.5
1080	19.04	25.59	16.70	2.7956	91.86	82.60	16.10	514.82	5.81	167.5 ± 0.6
1120	25.52	20.36	33.12	0.1328	94.17	64.86	17.33	385.73	11.35	179.7 ± 12.6
1160	21.88	26.96	33.60	0.1907	97.50	61.11	14.00	447.53	12.78	146.6 ± 7.3
1200*	40.60	26.80	93.56	<u>0.1436</u>	100.00	35.56	15.02	241.00	21.63	156.8 ± 14.3
			Total	5.7365						

* Crucible cracked

Total Gas Age = 168.6 Ma

Table 1. (continued).

Temp (°C)	$\frac{^{40}\text{Ar}}{^{39}\text{Ar}}$	$\frac{^{37}\text{Ar}}{^{39}\text{Ar}}$	$\frac{^{36}\text{Ar}}{^{39}\text{Ar}}$ (10 ⁻³)	^{39}Ar (10 ⁻¹³) moles	Cumulative % ^{39}Ar	$\frac{^{40}\text{Ar}^*}{^{39}\text{Ar}}$ (%)	$\frac{^{40}\text{Ar}^*}{^{39}\text{Ar}}$	$\frac{^{39}\text{Ar}}{^{40}\text{Ar}}$ (10 ⁻⁴)	$\frac{^{36}\text{Ar}}{^{40}\text{Ar}}$ (10 ⁻⁴)	Apparent Age (Ma)
AM-260-85 hornblende; J = 0.006170										
850	275.70	25.32	764.8	0.1362	1.90	18.38	52.41	35.54	27.54	505.5 ± 35.6
950	50.56	41.66	74.98	0.1685	4.26	58.10	32.17	191.30	13.23	326.6 ± 23.3
1000	30.75	37.10	27.44	0.2577	7.85	76.60	25.81	315.78	6.78	266.6 ± 10.2
1020	26.19	38.43	25.42	0.3682	13.00	76.82	21.83	370.48	6.97	228.0 ± 5.6
1050	20.80	39.21	19.08	1.5258	34.31	83.76	18.27	466.28	5.24	192.7 ± 3.5
1080	18.79	36.17	13.69	1.5329	55.71	89.36	17.59	517.38	3.35	185.9 ± 2.0
1110	23.06	35.17	23.26	0.2959	59.85	74.58	18.99	421.87	7.39	199.9 ± 2.0
1130	23.98	38.21	24.26	0.4490	66.12	76.83	19.88	404.75	7.08	208.8 ± 6.5
1150	22.83	38.86	24.17	0.5903	74.36	76.86	18.78	424.92	7.24	197.8 ± 4.8
1180	21.62	37.87	25.09	0.8785	86.63	75.06	17.17	449.05	8.02	181.7 ± 2.8
1210	27.77	37.04	43.80	0.3509	91.53	58.99	17.74	349.78	13.13	187.4 ± 9.9
1240	26.83	38.24	39.77	0.2561	95.11	60.98	18.10	361.66	12.13	191.0 ± 11.4
1450	65.69	41.32	169.4	0.3502	100.00	27.28	18.94	147.26	24.44	199.3 ± 14.4
			Total	7.1602						

Total Gas Age = 205.2 Ma

Table 1. (continued).

Temp (°C)	$\frac{^{40}\text{Ar}}{^{39}\text{Ar}}$	$\frac{^{37}\text{Ar}}{^{39}\text{Ar}}$	$\frac{^{36}\text{Ar}}{^{39}\text{Ar}}$ (10^{-3})	$\frac{^{39}\text{Ar}}{(10^{-13})}$ moles	Cumulative % $\frac{^{39}\text{Ar}}{^{39}\text{Ar}}$	$\frac{^{40}\text{Ar}^*}{(\%)}$	$\frac{^{40}\text{Ar}^*}{^{39}\text{Ar}}$	$\frac{^{39}\text{Ar}}{^{40}\text{Ar}}$ (10^{-4})	$\frac{^{36}\text{Ar}}{^{40}\text{Ar}}$ (10^{-4})	Apparent Age (Ma)
AM-262-85 hornblende; J = 0.0062114										
650	676.3	21.17	21.79	0.0668	0.96	4.93	34.31	14.54	32.15	348.6 ± 94.7
750	319.9	18.68	802.0	0.0296	1.38	24.98	85.44	30.79	24.95	768.0 ± 146.4
850	53.26	8.33	38.52	0.0669	2.34	69.81	42.68	186.59	7.03	424.3 ± 41.6
900	43.63	12.64	52.82	0.0477	3.02	53.27	29.12	227.00	11.73	299.9 ± 15.2
950	48.10	24.03	87.25	0.0488	3.72	40.90	24.33	204.00	17.36	253.9 ± 59.4
980	49.18	26.41	78.01	0.0573	4.54	48.06	28.43	199.15	15.01	293.3 ± 40.4
1000	33.58	33.23	50.39	0.0680	5.52	50.90	21.41	290.08	13.55	225.2 ± 24.1
1020	26.39	36.00	38.40	0.1511	7.68	58.47	17.88	368.43	12.23	190.0 ± 27.6
1040	22.18	38.75	20.76	0.5252	15.20	80.20	19.15	437.29	6.02	202.7 ± 4.1
1060	17.95	39.12	16.06	1.1818	32.13	85.64	16.24	540.45	4.53	173.4 ± 2.85
1090	17.55	38.66	16.86	1.5604	54.49	84.31	15.54	553.09	5.04	166.3 ± 2.1
1120	21.79	37.99	19.61	0.3721	59.82	79.76	19.03	445.47	5.88	201.6 ± 5.4
1140	22.95	38.74	32.45	0.4749	66.62	66.10	16.37	422.70	10.79	174.7 ± 4.6
1160	20.91	39.54	24.93	0.7725	77.69	74.69	16.63	463.64	8.09	177.3 ± 4.2
1190	19.76	39.43	20.32	1.0155	92.23	80.51	16.84	490.65	6.22	179.5 ± 2.2
1220	27.95	37.52	62.56	0.1873	94.92	38.82	12.25	347.40	19.81	132.3 ± 10.1
1250	29.30	39.08	24.41	0.1897	97.63	77.08	25.41	330.87	6.18	264.4 ± 12.0
1450	78.77	37.64	222.64	<u>0.1651</u>	100.00	18.84	15.89	123.17	27.26	169.8 ± 28.1
			Total	6.9807						

Total Gas Age = 188.1 Ma

Table 1. (continued).

Temp (°C)	$\frac{40\text{Ar}}{39\text{Ar}}$	$\frac{37\text{Ar}}{39\text{Ar}}$	$\frac{36\text{Ar}}{39\text{Ar}}$ (10 ⁻³)	$\frac{39\text{Ar}}{(10^{-13})}$ moles	Cumulative % $\frac{39\text{Ar}}$	$\frac{40\text{Ar}^*}{(\%)}$	$\frac{40\text{Ar}^*}{39\text{Ar}}$	$\frac{39\text{Ar}}{(10^{-4})}$	$\frac{36\text{Ar}}{40\text{Ar}}$ (10 ⁻⁴)	Apparent Age (Ma)
AM-262-85 (replicate) hornblende; J = 0.006051										
820	165.81	7.12	333.01	0.0363	1.13	40.25	68.25	59.97	19.99	623.6 ± 92.8
880	50.08	7.89	770.09	0.0460	2.56	53.23	28.00	198.48	15.07	282.3 ± 31.4
940	49.74	10.96	56.51	0.0371	3.71	64.34	34.04	199.33	10.94	337.9 ± 40.1
1000	34.81	28.85	50.75	0.0814	6.24	60.15	22.20	28.07	12.89	227.4 ± 17.0
1040	24.87	32.90	21.25	0.1482	10.84	81.11	21.30	391.55	5.90	218.7 ± 10.0
1080	19.65	36.19	20.67	0.6461	30.91	80.21	16.37	494.50	6.54	170.4 ± 2.2
1120	20.30	35.40	21.82	0.6392	50.77	78.93	16.63	478.96	6.98	173.0 ± 2.5
1150	21.87	34.42	23.07	0.2861	59.66	77.78	17.79	444.77	7.23	184.4 ± 6.8
1180	21.11	34.94	20.69	0.4421	73.39	80.89	17.77	460.71	6.27	184.2 ± 4.9
1210	24.12	30.88	29.45	0.3621	84.64	71.37	17.87	404.54	9.47	185.2 ± 5.8
1250	23.09	33.41	28.65	0.1782	90.17	70.97	17.26	421.57	9.41	179.2 ± 5.9
1400	34.56	22.64	47.05	0.3163	100.00	63.40	22.53	284.21	12.20	230.6 ± 4.9
	Total			3.2191						

Total Gas Age = 194.4 Ma

Table 1. (continued).

Temp (°C)	$\frac{40\text{Ar}}{39\text{Ar}}$	$\frac{37\text{Ar}}{39\text{Ar}}$	$\frac{36\text{Ar}}{39\text{Ar}}$ (10 ⁻³)	$\frac{39\text{Ar}}{(10^{-13})}$ moles	Cumulative % $\frac{39\text{Ar}}$	$\frac{40\text{Ar}^*}{39\text{Ar}}$ (%)	$\frac{40\text{Ar}^*}{39\text{Ar}}$	$\frac{39\text{Ar}}{(10^{-4})}$	$\frac{36\text{Ar}}{40\text{Ar}}$ (10 ⁻⁴)	Apparent Age (Ma)
AH - 135 - 85 feldspar; J = 0.006330										
500	71.85	0.243	132.4	2.6337	3.03	45.52	32.74	139.20	18.42	339.8 ± 2.3
550	14.43	0.091	13.03	2.3145	5.68	73.00	10.56	694.30	9.03	116.7 ± 1.5
580	15.79	0.055	8.83	0.7301	6.52	82.76	13.16	634.18	5.60	144.4 ± 6.8
610	17.83	0.137	6.53	0.2274	6.78	87.30	15.87	561.71	3.67	172.7 ± 13.0
640	16.57	0.081	10.83	0.8568	7.77	80.12	13.35	604.26	6.53	146.4 ± 2.6
670	18.22	0.173	15.20	0.7559	8.68	74.84	13.72	559.51	8.33	150.2 ± 2.6
710	14.99	0.244	7.44	0.3524	9.04	83.99	12.78	668.25	4.94	140.4 ± 9.4
740	13.46	0.504	7.03	0.8778	10.10	84.06	11.40	743.92	5.15	125.7 ± 5.1
780	12.85	1.35	4.97	1.7053	12.00	89.16	11.51	778.81	3.51	126.9 ± 1.6
830	12.72	0.462	0.482	1.5404	13.80	98.52	12.59	787.52	0.32	138.3 ± 2.9
880	12.78	0.226	2.36	1.4745	15.47	94.07	12.08	783.63	1.81	132.9 ± 3.1
930	12.54	0.149	1.79	2.7976	18.68	95.45	12.00	798.96	1.40	132.1 ± 0.8
980	12.85	0.142	17.04	1.5167	20.42	99.12	12.79	779.91	0.11	140.4 ± 1.6
1030	12.82	0.152	4.17	1.5673	22.22	89.91	11.57	781.61	3.23	127.5 ± 1.5
1080	12.73	0.090	2.33	2.2356	24.79	94.17	12.03	786.81	1.82	132.4 ± 2.3
1120	13.10	0.089	2.22	3.5003	28.81	94.68	12.43	764.76	1.68	136.6 ± 1.9
1150	14.00	0.102	4.54	2.4400	31.62	90.07	12.64	715.57	3.23	138.9 ± 1.6
1180	14.50	0.054	3.69	2.0138	33.93	92.07	13.39	690.86	2.54	146.7 ± 1.7
1220	14.74	0.046	5.75	1.0654	35.15	87.87	13.02	679.33	3.90	142.9 ± 4.1
1300	14.31	0.018	3.25	55.0491	98.36	93.11	13.33	699.89	2.27	146.2 ± 0.4
1430	118.3	0.108	354.8	1.4192	100.00	11.38	13.48	84.51	29.99	147.7 ± 7.2
			Total	87.0745						

Total Gas Age = 148.6 Ma

Table 1. (continued).

Temp (°C)	$\frac{40\text{Ar}}{39\text{Ar}}$	$\frac{37\text{Ar}}{39\text{Ar}}$	$\frac{36\text{Ar}}{39\text{Ar}}$ (10 ⁻³)	$\frac{39\text{Ar}}{(10^{-13})}$ moles	Cumulative % $\frac{39\text{Ar}}$	$\frac{40\text{Ar}^*}{39\text{Ar}}$ (%)	$\frac{40\text{Ar}^*}{39\text{Ar}}$ (10 ⁻⁴)	$\frac{39\text{Ar}}{40\text{Ar}}$ (10 ⁻⁴)	$\frac{36\text{Ar}}{40\text{Ar}}$ (10 ⁻⁴)	Apparent Age (Ma)
AH - 135 - 85 biotite; J = 0.006205										
600	18.43	0.201	37.46	1.7352	1.58	39.26	7.35	543.23	20.32	80.5 ± 1.5
660	16.24	0.043	2.84	5.5521	6.64	94.18	15.38	616.61	1.74	164.5 ± 0.8
720	15.69	0.131	0.764	13.0770	18.55	98.22	15.45	638.24	0.47	165.2 ± 0.3
770	15.40	0.141	0.379	12.6813	30.10	98.92	15.27	650.47	0.23	163.3 ± 0.3
840	15.61	0.246	0.827	5.6230	35.23	97.82	15.36	641.68	0.50	164.2 ± 0.7
920	15.75	0.147	0.682	6.6929	41.32	98.16	15.53	635.98	0.42	166.0 ± 1.7
1000	15.68	0.038	0.437	16.6760	56.52	98.84	15.52	638.93	0.27	165.9 ± 0.3
1050	15.40	0.026	0.370	17.2613	72.24	98.95	15.27	650.39	0.24	163.3 ± 0.5
1100	15.41	0.043	0.630	18.6920	89.27	98.48	15.20	649.95	0.40	162.6 ± 0.3
1150	15.53	0.111	0.592	10.9100	99.21	98.47	15.34	644.73	0.37	164.1 ± 0.5
1200	17.75	0.904	2.926	0.4477	99.61	89.68	16.93	563.74	1.60	180.2 ± 3.4
1250	27.48	0.623	42.20	0.1888	99.79	49.88	15.03	364.05	15.33	160.9 ± 21.8
1400	181.9	0.625	569.1	0.2341	100.00	7.48	13.78	54.95	31.28	148.0 ± 41.6
			Total	109.7714						

Total Gas Age = 162.9 Ma

Table 1. (continued).

Temp (°C)	$\frac{40}{39}\text{Ar}$	$\frac{37}{39}\text{Ar}$	$\frac{36}{39}\text{Ar}$ (10 ⁻³)	$\frac{39}{\text{Ar}}$ (10 ⁻¹³) moles	Cumula- tive % $\frac{39}{\text{Ar}}$	$\frac{40}{\text{Ar}}^*$ (%)	$\frac{40}{39}\text{Ar}^*$	$\frac{39}{40}\text{Ar}$ (10 ⁻⁴)	$\frac{36}{40}\text{Ar}$ (10 ⁻⁴)	Apparent Age (Ma)
AH - 153 - 85 biotite; J = 0.006290										
600	14.27	0.135	16.06	4.5340	5.33	66.10	9.50	702.16	11.26	104.7 ± 0.4
660	15.89	0.021	0.912	8.6635	15.51	97.80	15.60	630.32	0.573	168.8 ± 0.6
720	15.90	13.42	0.381	11.005	28.44	98.99	15.79	629.86	0.193	170.8 ± 0.3
770	15.58	0.017	0.255	10.919	41.27	99.07	15.48	642.93	0.162	167.6 ± 0.6
840	15.60	0.039	0.745	5.7427	48.01	97.90	15.36	642.13	0.475	166.3 ± 0.6
920	15.93	0.849	0.972	3.7279	52.39	98.87	15.88	628.66	0.006	171.8 ± 0.3
1000	17.39	0.120	1.624	5.8642	59.29	96.67	16.89	575.88	0.923	182.2 ± 0.8
1070	15.87	0.043	0.891	16.512	78.69	98.01	15.58	631.21	0.557	168.7 ± 0.4
1130	15.37	0.033	0.759	15.603	97.02	98.19	15.12	651.70	0.490	163.9 ± 0.6
1180	16.11	0.117	2.848	2.1270	99.52	93.34	15.26	621.60	1.750	165.3 ± 0.5
1250	27.12	0.739	32.96	0.2006	99.76	58.76	17.41	368.90	12.12	187.5 ± 13.4
1400	223.9	0.838	630.4	0.2070	100.00	16.63	37.66	44.642	28.15	383.6 ± 45.4
			Total	85.1039						

Total Gas Age = 165.9 Ma

Table 1. (continued).

Temp (°C)	$\frac{^{40}\text{Ar}}{^{39}\text{Ar}}$	$\frac{^{37}\text{Ar}}{^{39}\text{Ar}}$	$\frac{^{36}\text{Ar}}{^{39}\text{Ar}}$ (10 ⁻³)	$\frac{^{39}\text{Ar}}{^{39}\text{Ar}}$ (10 ⁻¹³) moles	Cumulative % $\frac{^{40}\text{Ar}}{^{39}\text{Ar}}$	$\frac{^{40}\text{Ar}}{^{39}\text{Ar}}$ (%)	$\frac{^{40}\text{Ar}}{^{39}\text{Ar}}$ (10 ⁻⁴)	$\frac{^{36}\text{Ar}}{^{40}\text{Ar}}$ (10 ⁻⁴)	Apparent Age (Ma)
AH - 161 - 85 hornblende; J = 0.006177									
850	30.95	1.87	0.482	4.7654	13.98	54.15	16.84	322.88	178.5 ± 0.9
940	18.48	4.36	8.979	4.7287	27.84	86.56	16.15	539.90	171.5 ± 1.1
1000	16.06	7.56	3.745	10.921	59.87	95.75	15.52	619.88	165.1 ± 0.5
1020	15.78	7.34	3.142	5.1294	74.91	96.40	15.40	630.85	163.9 ± 0.6
1035	16.07	6.99	3.571	1.4929	79.29	94.14	15.47	622.21	164.7 ± 1.4
1050	16.80	7.48	5.351	0.8478	81.78	90.18	15.77	592.71	167.7 ± 3.7
1065	17.12	8.13	11.06	1.0958	84.99	81.68	14.45	581.29	154.2 ± 2.2
1085	18.04	7.84	10.09	0.9460	87.77	83.72	15.65	551.53	166.4 ± 3.8
1115	17.87	6.28	10.69	2.8233	96.05	83.65	15.17	557.70	161.6 ± 1.1
1140	20.22	5.39	18.35	1.0880	99.24	73.14	15.19	493.10	161.8 ± 2.0
1160	25.64	7.92	31.53	0.1631	99.71	58.58	16.92	387.87	179.4 ± 18.4
1180	26.71	8.60	55.50	0.0373	99.82	27.02	10.92	372.20	117.8 ± 19.6
1220	53.40	11.55	81.62	0.0162	99.87	35.60	30.28	185.70	309.3 ± 180.3
1450	340.7	34.22	1110	0.0440	100.00	4.16	15.07	285.49	160.6 ± 123.2
			Total	34.0984					

Total Gas Age = 167.1 Ma

Table 1. (continued).

Temp (°C)	$\frac{^{40}\text{Ar}}{^{39}\text{Ar}}$	$\frac{^{37}\text{Ar}}{^{39}\text{Ar}}$	$\frac{^{36}\text{Ar}}{^{39}\text{Ar}}$ (10^{-3})	^{39}Ar (10^{-13}) moles	Cumula- tive % ^{39}Ar	$\frac{^{40}\text{Ar}^*}{^{39}\text{Ar}}$ (%)	$\frac{^{39}\text{Ar}}{^{40}\text{Ar}}$ (10^{-4})	$\frac{^{36}\text{Ar}}{^{40}\text{Ar}}$ (10^{-4})	Apparent Age (Ma)
AM-177 - 85 biotite; J = 0.006016									
600	18.5	0.5932	50.76	2.14	6.53	18.8	541.13	27.41	37.7 ± 1.4
660	6.63	0.3153	7.427	3.98	18.7	66.0	1514.2	11.15	47.4 ± 0.5
700	12.39	0.2371	8.184	3.10	28.2	79.7	808.99	6.58	105.0 ± 0.7
750	17.05	0.2352	3.526	3.63	39.3	93.4	587.46	2.04	165.8 ± 0.5
800	16.14	0.2511	3.675	3.48	49.9	92.7	620.53	2.25	156.3 ± 0.7
850	16.45	0.3490	2.499	3.96	62.0	95.0	608.80	1.48	162.9 ± 0.7
900	17.31	0.3124	2.314	3.96	74.1	95.6	578.41	1.30	172.0 ± 0.6
950	17.83	0.2511	3.276	2.40	81.5	93.8	561.61	1.81	174.2 ± 0.9
1000	18.60	0.2024	3.087	1.91	87.3	94.2	538.25	1.64	182.3 ± 1.0
1050	20.36	0.2137	7.140	0.752	89.6	87.8	491.83	3.49	187.8 ± 1.6
1100	18.36	0.1380	2.197	0.882	92.3	94.6	545.36	1.19	182.5 ± 1.2
1150	18.25	0.1432	1.746	0.366	93.4	95.6	548.60	0.946	182.8 ± 2.4
1200	17.32	0.3287	5.380	0.615	95.3	88.3	578.14	3.08	163.1 ± 2.2
1270	17.74	1.226	7.078	0.214	95.9	82.0	563.89	3.90	163.0 ± 5.1
1400	20.67	0.6513	14.47	1.33	100.0	78.5	484.22	6.94	169.9 ± 0.6

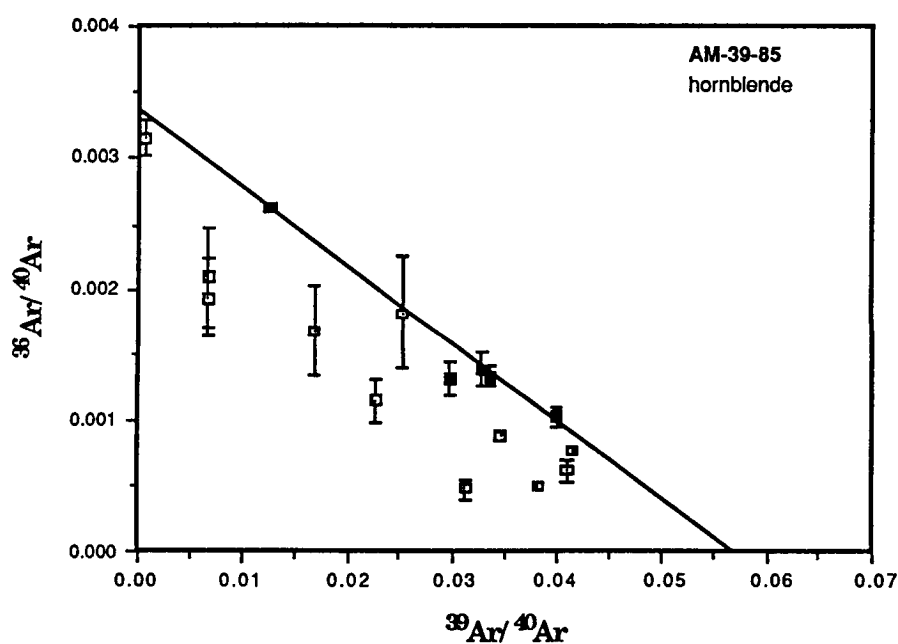
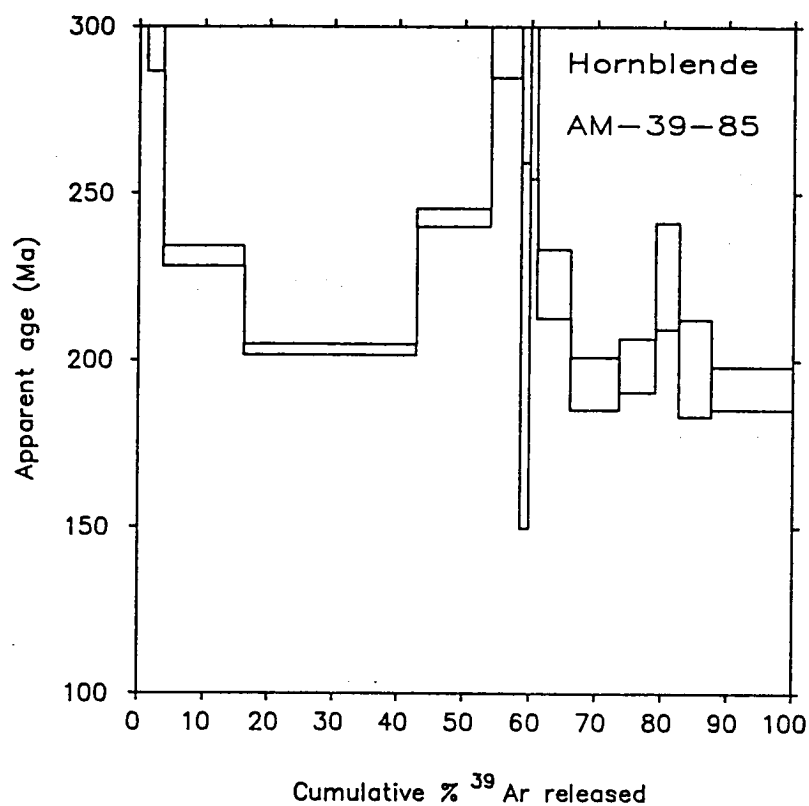


Figure 3. $^{40}\text{Ar}/^{39}\text{Ar}$ age spectrum (upper diagram) and $^{36}\text{Ar}/^{40}\text{Ar}$ versus $^{39}\text{Ar}/^{40}\text{Ar}$ plot (lower diagram) for hornblende sample AM-39. Heating steps included in the regression calculation are shown with filled symbols in the isochron plot.

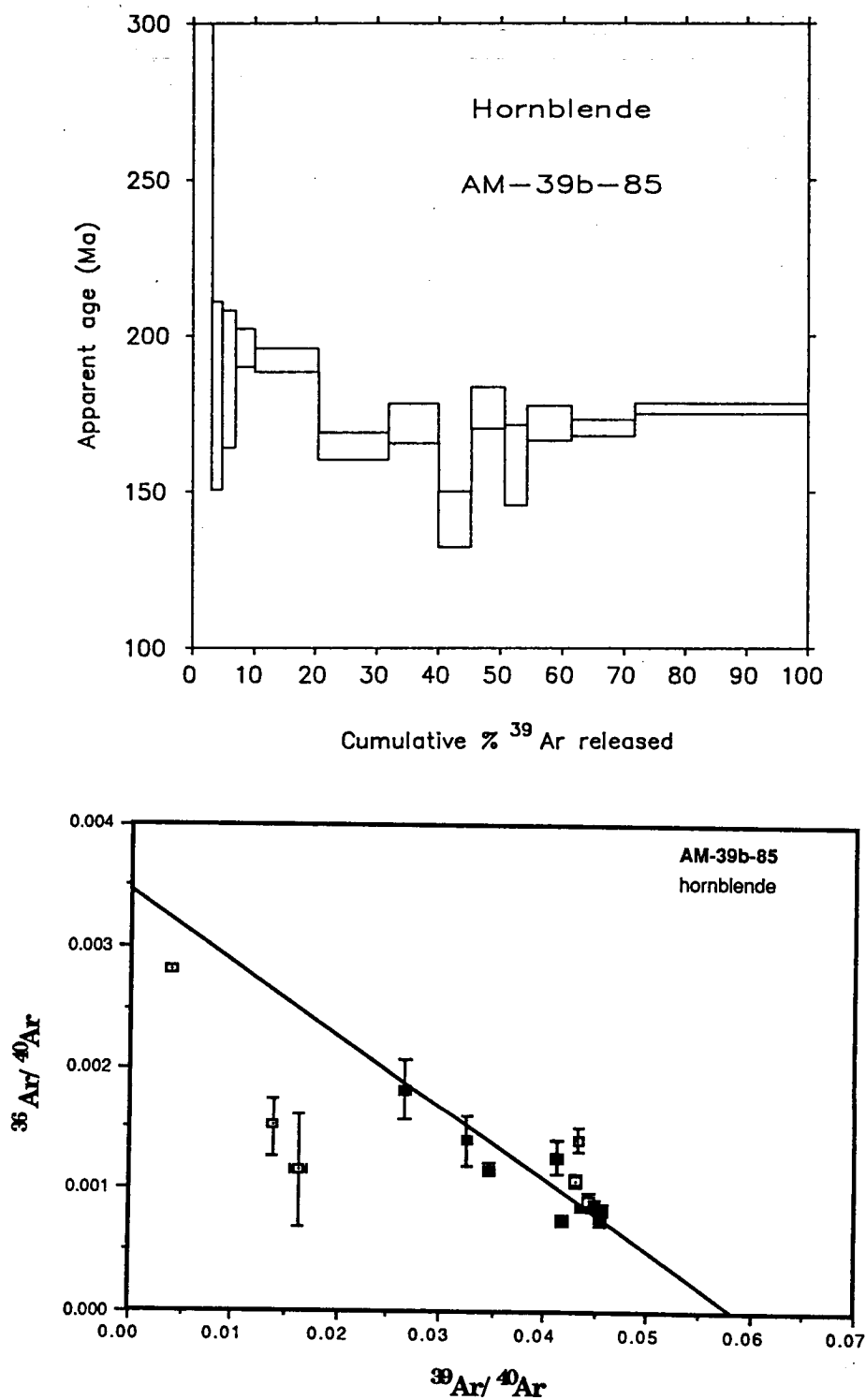


Figure 4. $^{40}\text{Ar}/^{39}\text{Ar}$ age spectrum (upper diagram) and $^{36}\text{Ar}/^{40}\text{Ar}$ versus $^{39}\text{Ar}/^{40}\text{Ar}$ plot (lower diagram) for hornblende sample AM-39b. Heating steps included in the regression calculation are shown with filled symbols in the isochron plot.

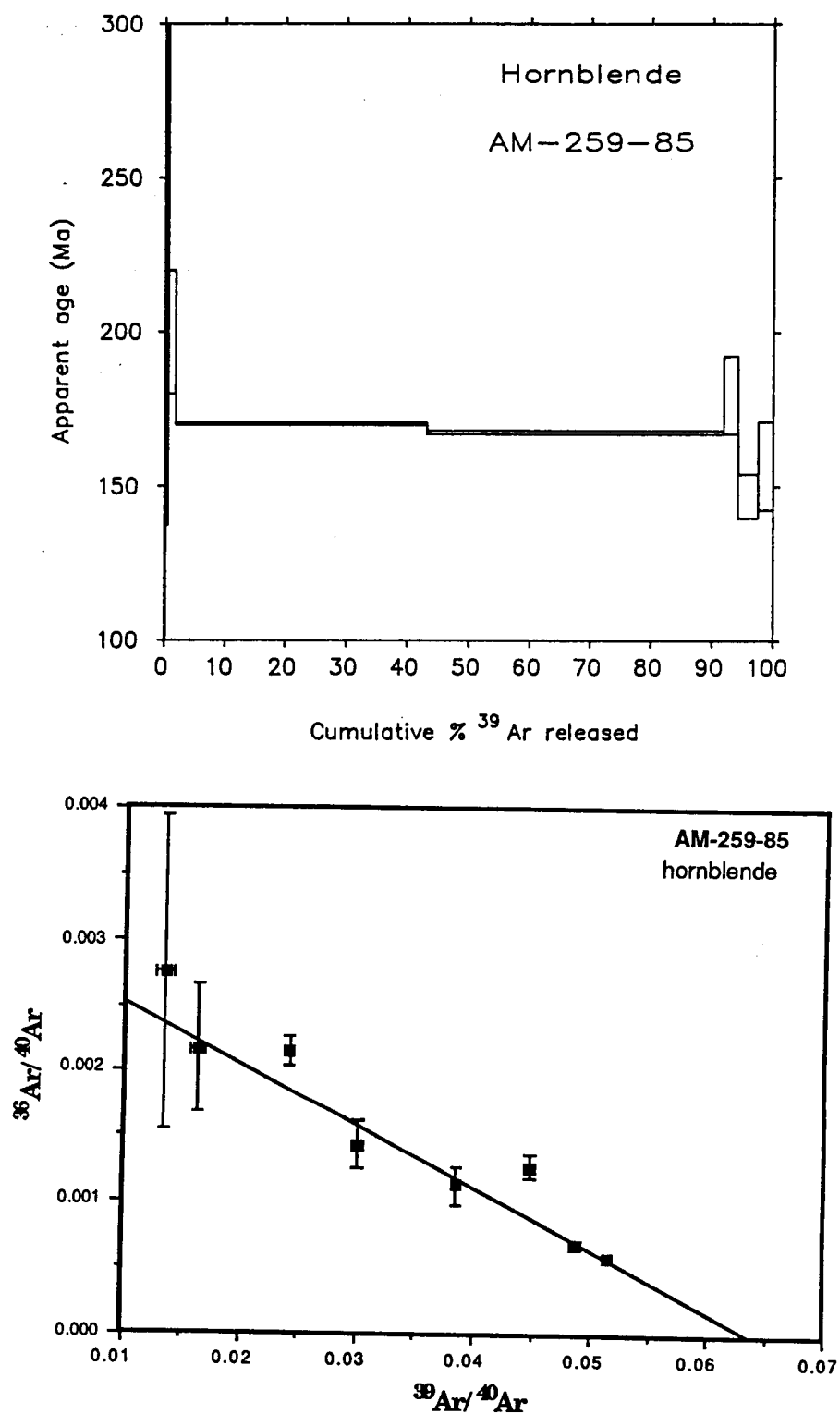


Figure 5. $^{40}\text{Ar}/^{39}\text{Ar}$ age spectrum (upper diagram) and $^{36}\text{Ar}/^{40}\text{Ar}$ versus $^{39}\text{Ar}/^{40}\text{Ar}$ plot (lower diagram) for hornblende sample AM-259. Heating steps included in the regression calculation are shown with filled symbols in the isochron plot.

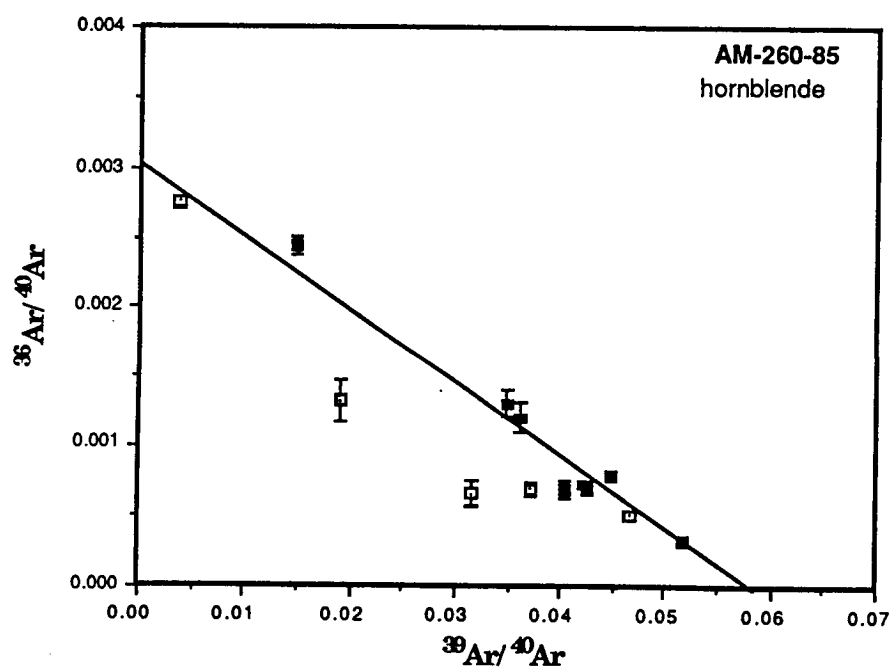
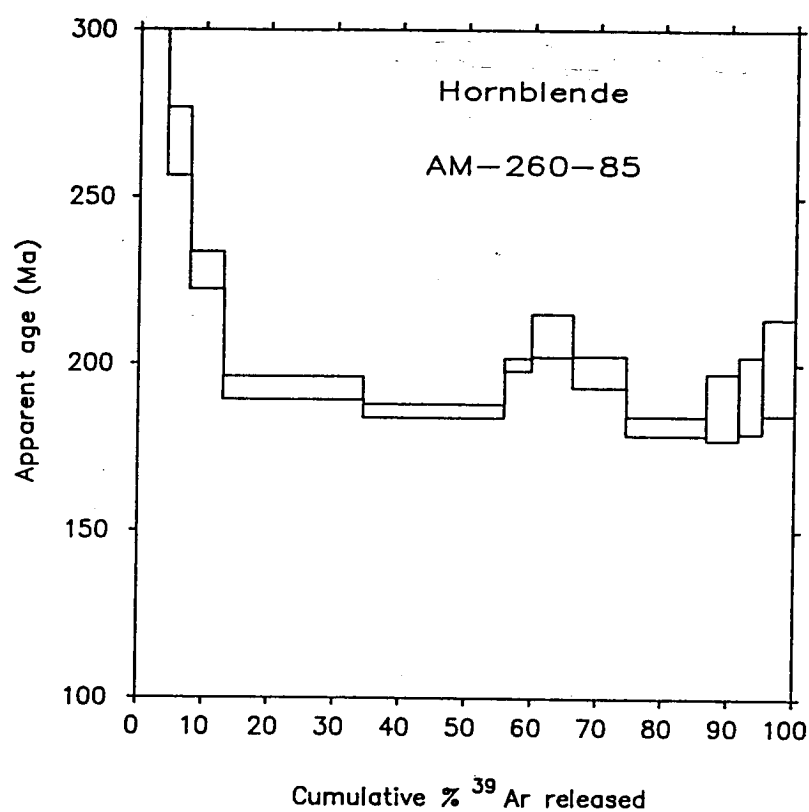


Figure 6. $^{40}\text{Ar}/^{39}\text{Ar}$ age spectrum (upper diagram) and $^{36}\text{Ar}/^{40}\text{Ar}$ versus $^{39}\text{Ar}/^{40}\text{Ar}$ plot (lower diagram) for hornblende sample AM-260. Heating steps included in the regression calculation are shown with filled symbols in the isochron plot.

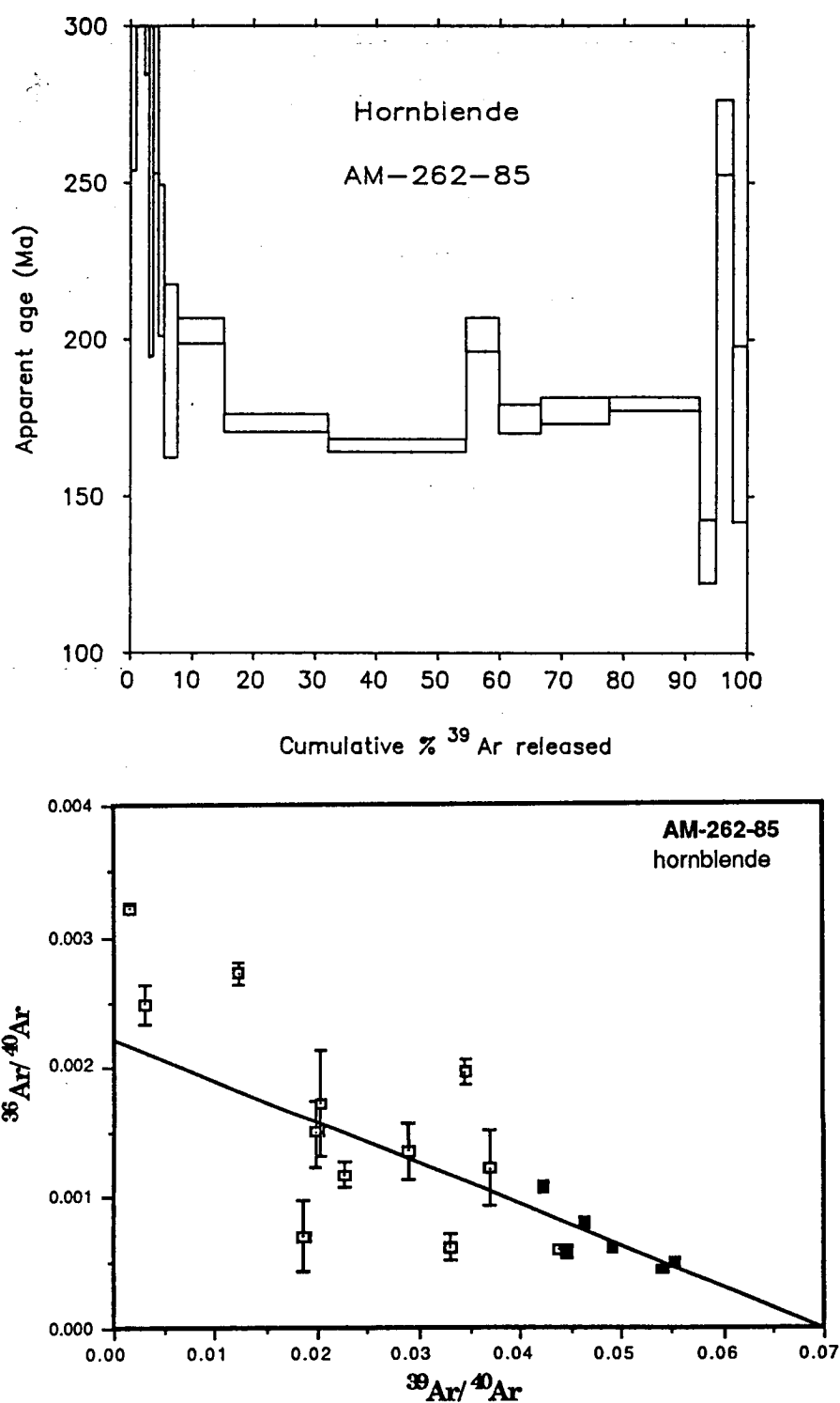


Figure 7. $^{40}\text{Ar}/^{39}\text{Ar}$ age spectrum (upper diagram) and $^{36}\text{Ar}/^{40}\text{Ar}$ versus $^{39}\text{Ar}/^{40}\text{Ar}$ plot (lower diagram) for hornblende sample AM-262. Heating steps included in the regression calculation are shown with filled symbols in the isochron plot.

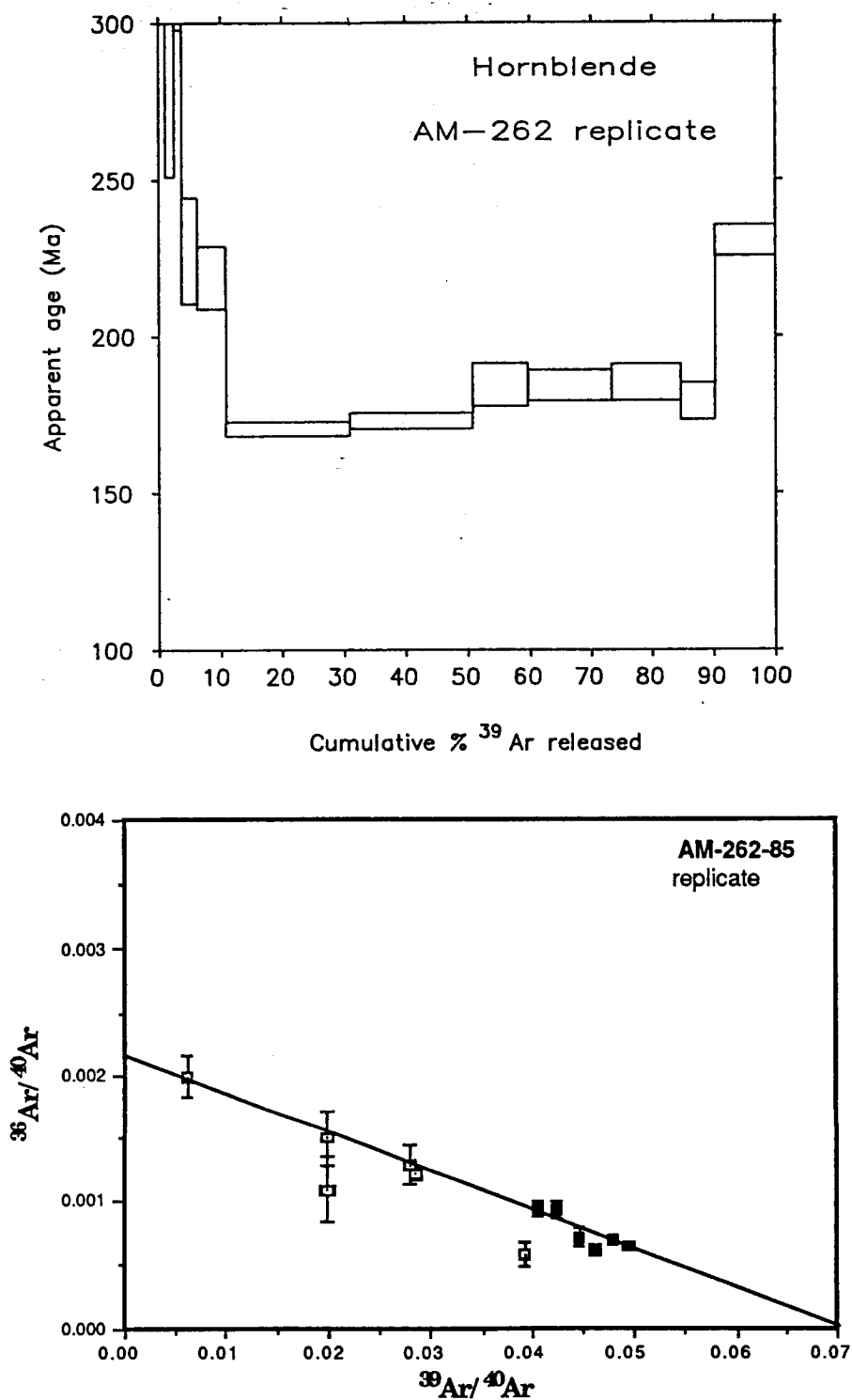


Figure 8. $^{40}\text{Ar}/^{39}\text{Ar}$ age spectrum (upper diagram) and $^{36}\text{Ar}/^{40}\text{Ar}$ versus $^{39}\text{Ar}/^{40}\text{Ar}$ plot (lower diagram) for the replicate analysis of hornblende sample AM-262. Heating steps included in the regression calculation are shown with filled symbols in the isochron plot.

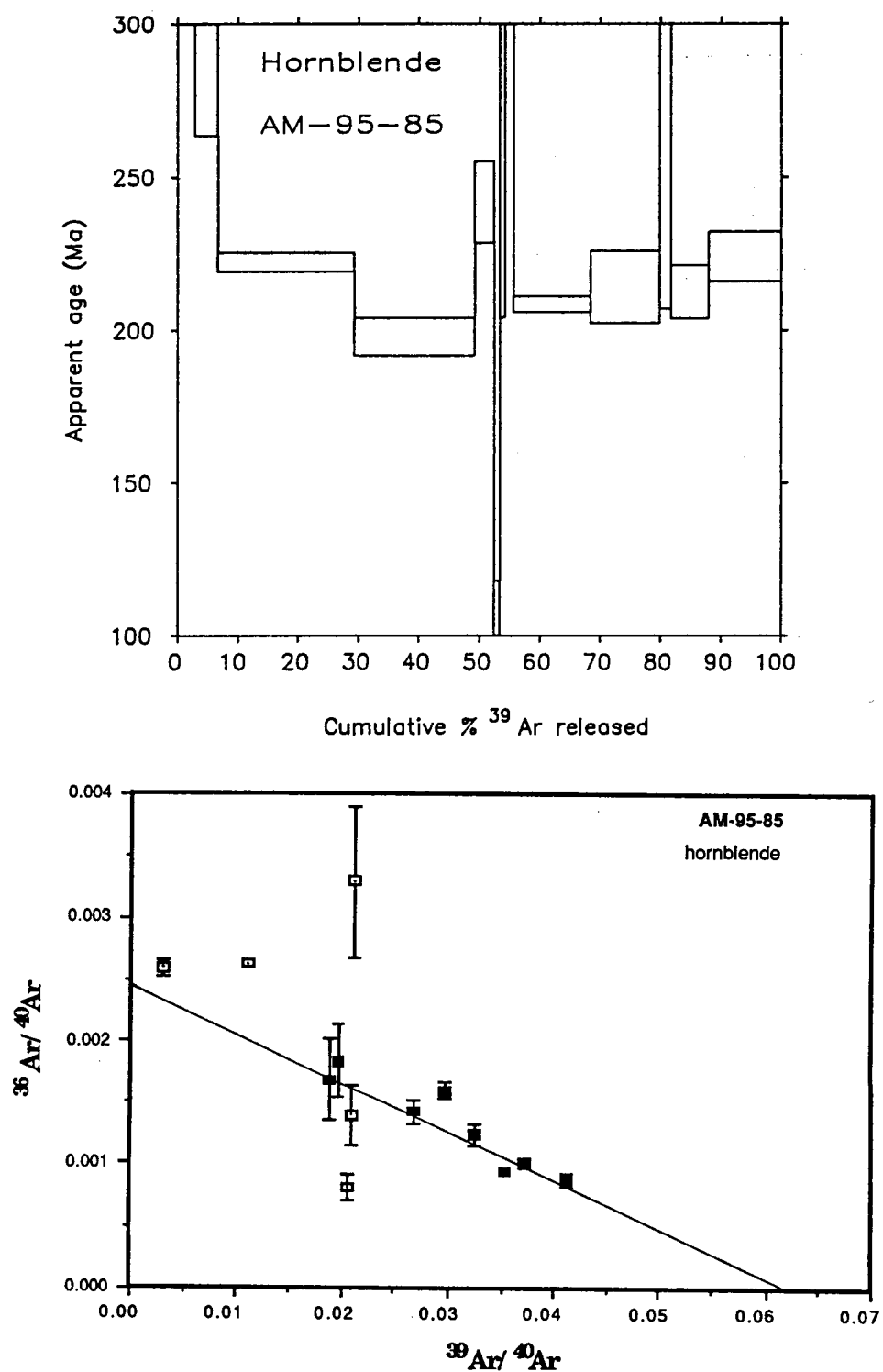


Figure 9. $^{40}\text{Ar}/^{39}\text{Ar}$ age spectrum (upper diagram) and $^{36}\text{Ar}/^{40}\text{Ar}$ versus $^{39}\text{Ar}/^{40}\text{Ar}$ plot (lower diagram) for hornblende sample AM-95. Heating steps included in the regression calculation are shown with filled symbols in the isochron plot.

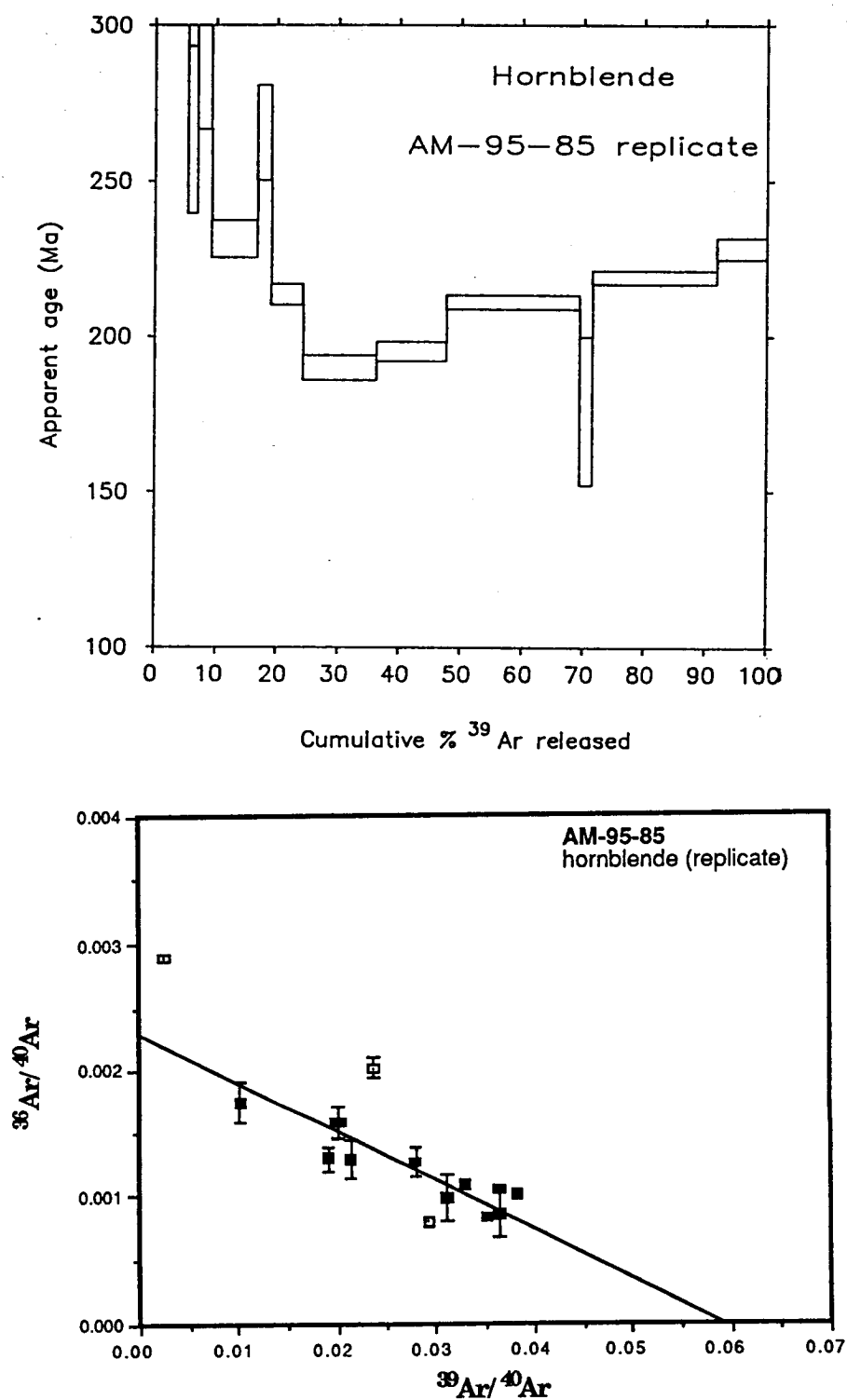


Figure 10. $^{40}\text{Ar}/^{39}\text{Ar}$ age spectrum (upper diagram) and $^{36}\text{Ar}/^{40}\text{Ar}$ versus $^{39}\text{Ar}/^{40}\text{Ar}$ plot (lower diagram) for the replicate analysis of hornblende sample AM-95. Heating steps included in the regression calculation are shown with filled symbols in the isochron plot.

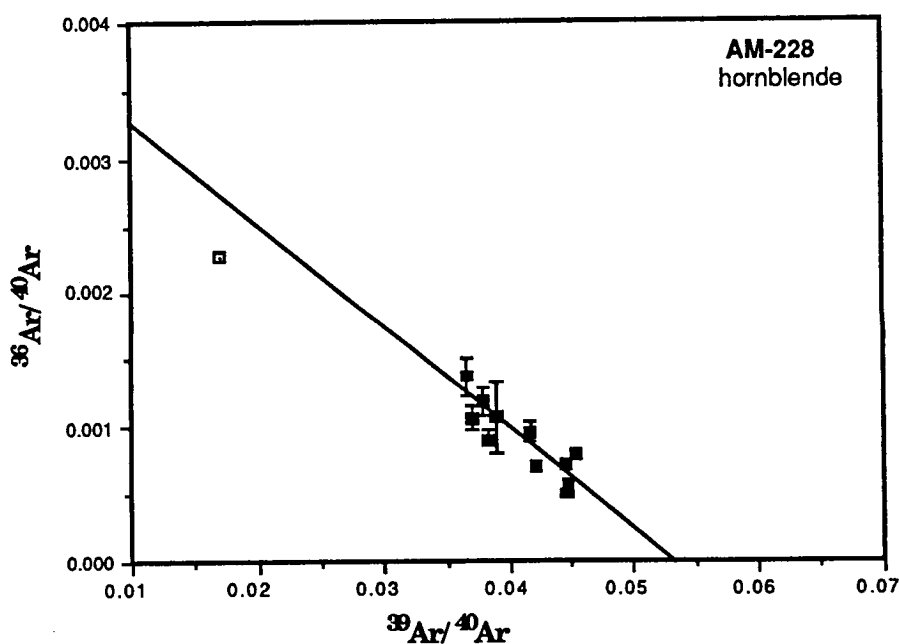
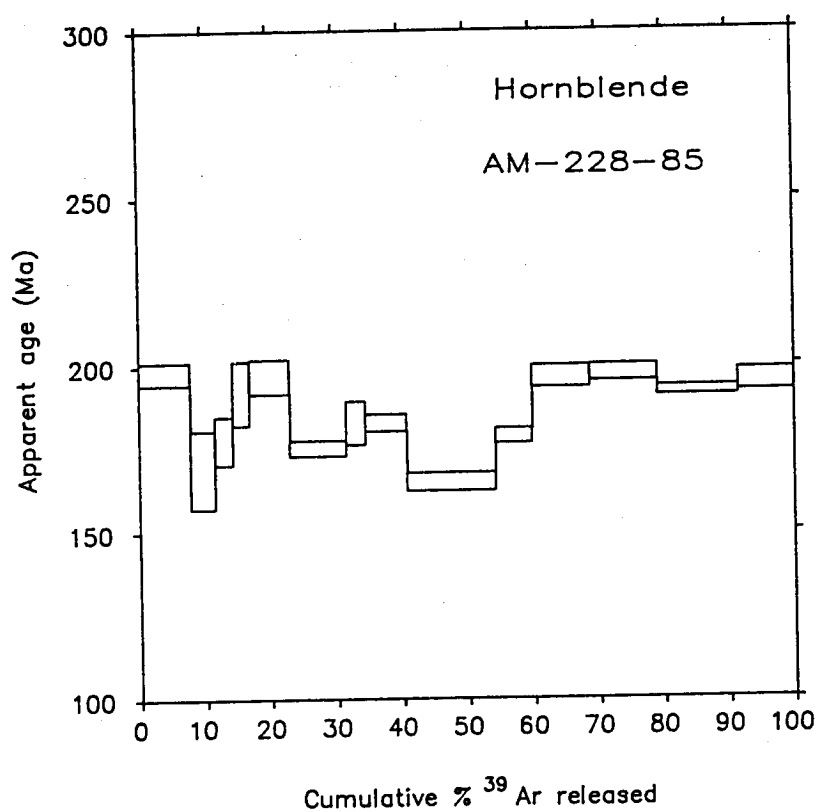


Figure 11. $^{40}\text{Ar}/^{39}\text{Ar}$ age spectrum (upper diagram) and $^{36}\text{Ar}/^{40}\text{Ar}$ versus $^{39}\text{Ar}/^{40}\text{Ar}$ plot (lower diagram) for hornblende sample AM-228. Heating steps included in the regression calculation are shown with filled symbols in the isochron plot.

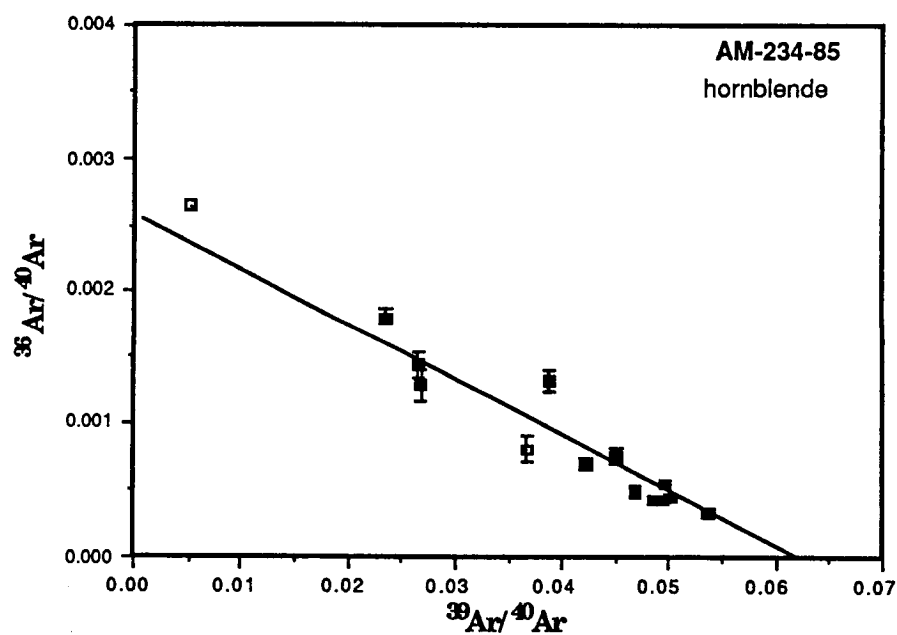
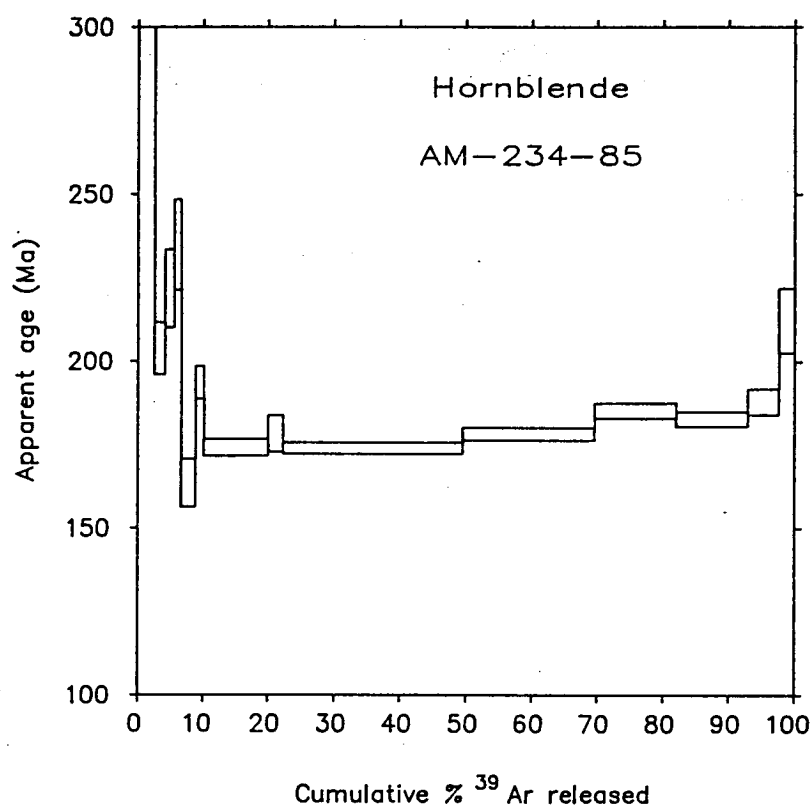


Figure 12. $^{40}\text{Ar}/^{39}\text{Ar}$ age spectrum (upper diagram) and $^{36}\text{Ar}/^{40}\text{Ar}$ versus $^{39}\text{Ar}/^{40}\text{Ar}$ plot (lower diagram) for hornblende sample AM-234. Heating steps included in the regression calculation are shown with filled symbols in the isochron plot.

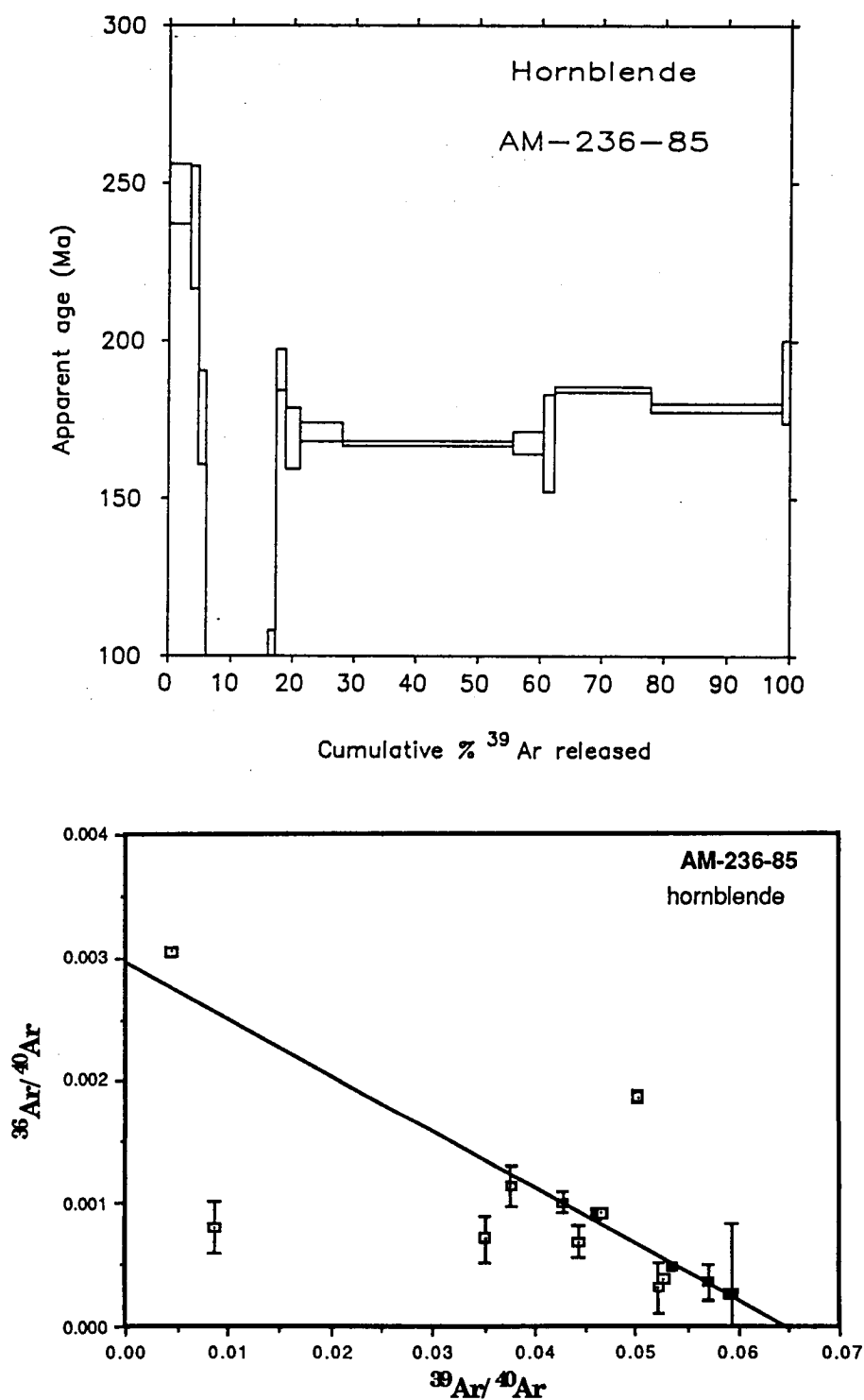


Figure 13. $^{40}\text{Ar}/^{39}\text{Ar}$ age spectrum (upper diagram) and $^{36}\text{Ar}/^{40}\text{Ar}$ versus $^{39}\text{Ar}/^{40}\text{Ar}$ plot (lower diagram) for hornblende sample AM-236. Heating steps included in the regression calculation are shown with filled symbols in the isochron plot.

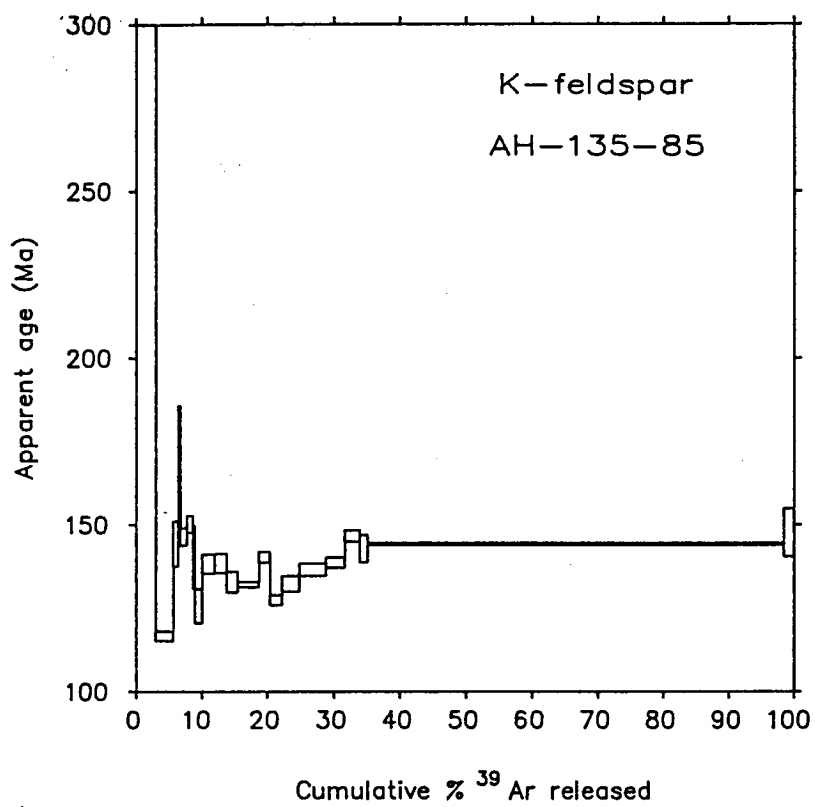


Figure 14. $^{40}\text{Ar}/^{39}\text{Ar}$ age spectrum for potassium feldspar sample AH-135.

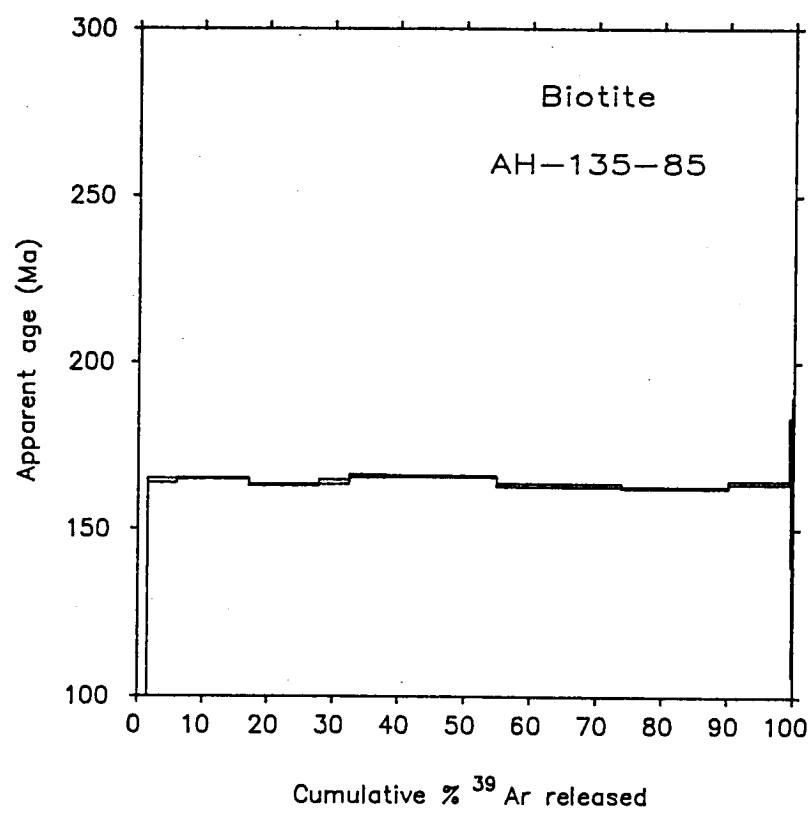


Figure 15. $^{40}\text{Ar}/^{39}\text{Ar}$ age spectrum for biotite sample AH-135.

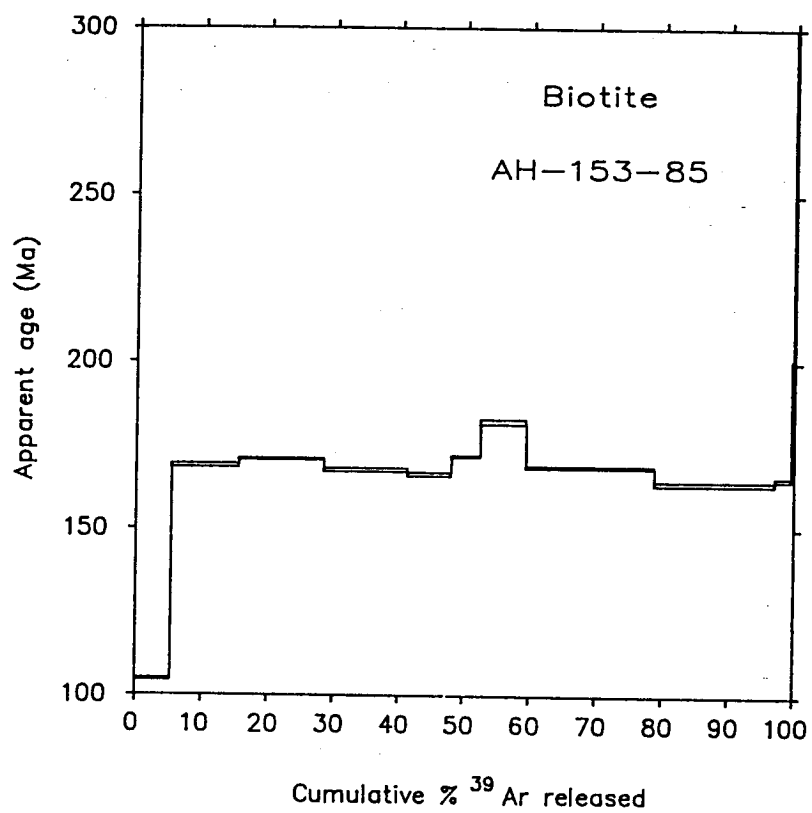


Figure 16. $^{40}\text{Ar}/^{39}\text{Ar}$ age spectrum for biotite sample AH-153.

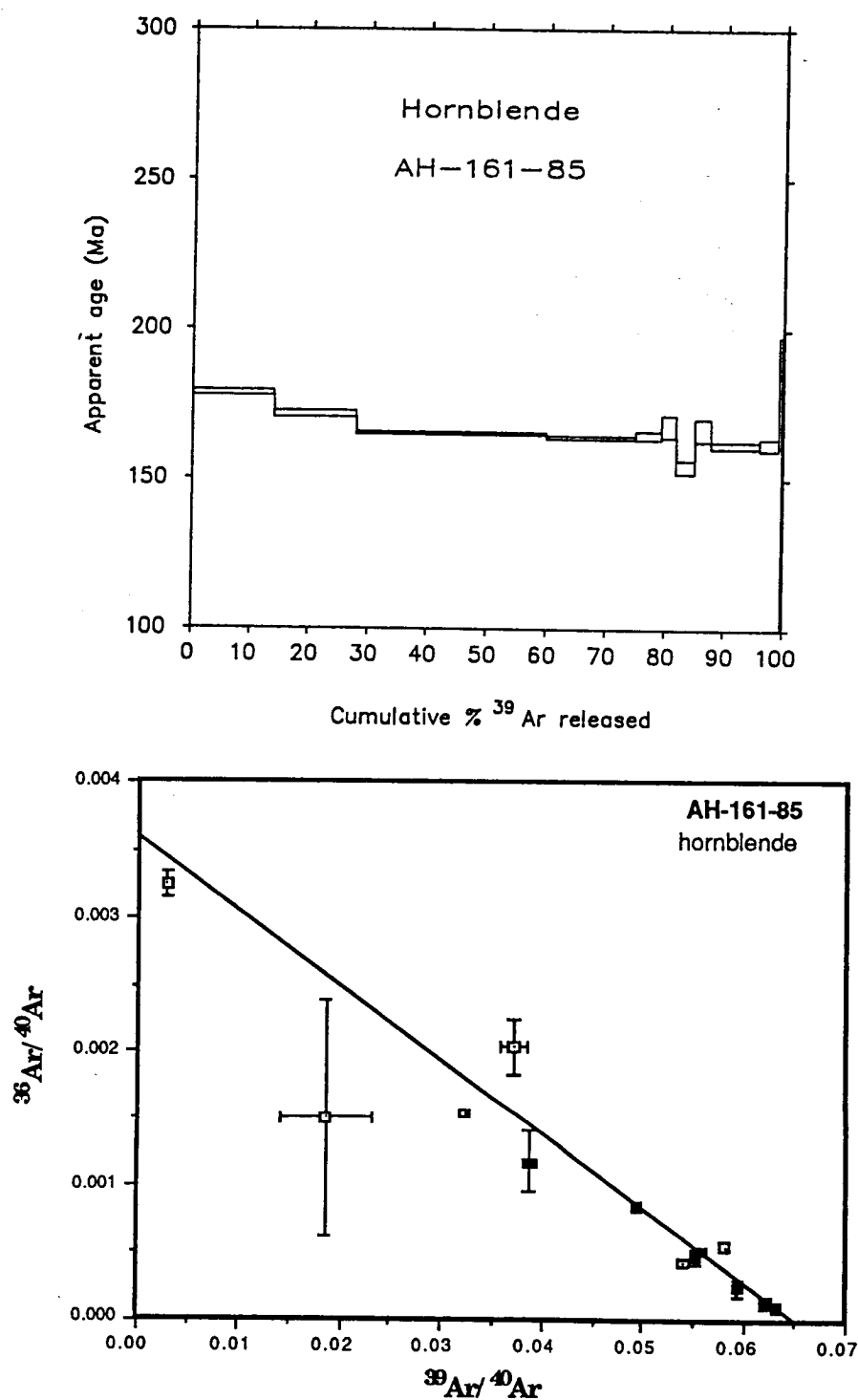


Figure 13. $^{40}\text{Ar}/^{39}\text{Ar}$ age spectrum (upper diagram) and $^{36}\text{Ar}/^{40}\text{Ar}$ versus $^{39}\text{Ar}/^{40}\text{Ar}$ plot (lower diagram) for hornblende sample AH-161. Heating steps included in the regression calculation are shown with filled symbols in the isochron plot.

Table 2. Summary of $^{40}\text{Ar}/^{39}\text{Ar}$ ages from western Brooks Range ophiolites.

Sample	Mineral	Total Gas ¹ Age (Ma)	Plateau ² Age (Ma)	Isochron ³ Age (Ma)	$^{40}\text{Ar}/^{36}\text{Ar}$ ⁴ Component	Interpreted ⁵ Geologic Age
Gabbro dike (AM-39)	hornblende	226.5	201.0 ± 10.5	193.9 ± 6.0 (1.54)	294.6 ± 4.4	193.9 ± 7.9
Gabbro dike (AM-39b)	hornblende	181.2	171.7 ± 5.1	179.2 ± 31.5 (23.5)	289.8 ± 92.2	171.7 ± 6.8
Plagiogranite (AM-95)	hornblende	233.6	233.5 ± 16.0	177.4 ± 30.1 (5.28)	409.7 ± 71.4	177.4 ± 31.9
replicate (AM-95)	hornblende	225.9	215.4 ± 4.3	175.1 ± 19.0 (9.78)	435.8 ± 52.5	175.1 ± 20.8
Plagiogranite (AM-228)	hornblende	189.3	195.1 ± 2.6	195.3 ± 11.1 (5.28)	248.2 ± 53.8	189.5 ± 42.9
Lineated diorite (AM-234)	hornblende	187.6	175.0 ± 1.9	169.0 ± 2.9 (10.0)	390.9 ± 32.6	169.0 ± 4.5
Amphibolite (AM-236)	hornblende	162.2	168.3 ± 3.2	165.6 ± 1.2 (.385)	338.4 ± 24.0	165.6 ± 2.8
Gabbro (AM-259)	hornblende	168.6	168.4 ± 0.6	163.8 ± 4.7 (5.66)	334.7 ± 31.8	163.8 ± 6.3
Gabbro (AM-260)	hornblende	205.2	193.6 ± 7.5	183.5 ± 3.5 (9.01)	326.1 ± 23.4	183.5 ± 5.3
Hornblende (AM-262)	hornblende	188.1	179.3 ± 3.6	154.0 ± 17.4 (11.5)	448 ± 101	179.3 ± 5.4
replicate (AM-262)	hornblende	194.4	180.7 ± 5.1	148.8 ± 18.9 (2.12)	463 ± 89	180.7 ± 6.9
Monzonite (AH135)	k-feldspar	148.6	146.2 ± 0.4	----	----	146.2 ± 1.9
Monzonite (AH-135)	biotite	162.9	164.1 ± 0.5	----	----	164.1 ± 2.1
Schist (AH-153)	biotite	165.9	168.8 ± 0.5	----	----	168.8 ± 2.2
Amphibolite (AH-161)	hornblende	167.1	165.4 ± 1.7	164.6 ± 0.4 (2.58)	276.5 ± 13.4	165.4 ± 3.4

1 Mean of all increments weighted by percent of gas released.

2 Mean gas fractions included within the plateau and weighted by moles ^{39}Ar released.

3 Numbers in parentheses are mean-square weighted deviations (MSWD) for the regression.

4 Inverse of $^{36}\text{Ar}/^{40}\text{Ar}$ intercept on isochron diagram, and one sigma error from regression.

5 Interpreted geologic age and 2 sigma error of sample, including error in estimation of J-factor.

Discussion

Hornblende samples from hornblende gabbro (samples AM-39, 39b, 259, and 260), plagiogranite (samples AM-95 and 228) and hornblendite (sample AM-262) contained small amounts of potassium and radiogenic Ar. Thus the release spectra are complex and the apparent ages calculated from data for some heating steps have large analytical errors. Despite this, the release spectra and results of the isochron plots for the replicate analyses of samples AM-95 and AM-262 are similar for each sample indicating that the Ar analyses are reproducible.

Closure Temperatures

Mineral ages calculated from $^{40}\text{Ar}/^{39}\text{Ar}$ data are the amount of time elapsed since a particular mineral has last cooled through its "closure temperature", the temperature below which radiogenic Ar does not escape the mineral by diffusion (Dodson, 1973). The temperature at which argon loss effectively ceases can be changed by cooling rate, bulk composition, and structural inhomogeneities. Closure temperatures have been determined for various minerals using different techniques (see eg. Dodson, 1973; Foland, 1974; Harrison et al., 1979; Harrison, 1980; Berger and York, 1981; Harrison, 1981; Harrison et al., 1985). Closure temperatures of 530 ± 40 °C (Harrison, 1981), 280 ± 40 °C (Harrison et al., 1985) and 150 ± 30 °C (Harrison et al., 1979) for hornblende, biotite, and potassium feldspar, respectively, are used in this study.

Time of Crystallization

Gabbro, diorite, and plagiogranite at Asik Mountain contain coarse-grained, subhedral to euhedral, green hornblende. Although some hornblende contains a few small inclusions of other minerals, most have not been altered, suggesting that the hornblendes are igneous and have not been affected by younger thermal events.

The ages determined for the gabbro and plagiogranite samples are summarized in Figures 18 and 19. Although there is variation in the ages, most of the ages are not significantly different at the 95% confidence level (± 2 sigma errors). The age variations might indicate that the hornblendes cooled through their closure temperatures at different times throughout the ophiolite. Such a variation could be attributed to steep thermal gradients in oceanic lithosphere at accreting plate margins. Alternatively, the ophiolites might have cooled nearly simultaneously, with the scatter in ages indicating variations in the Ar closure temperature in different hornblende samples.

The mean age of the samples (178.7 ± 8.6 Ma), weighted by the square of the inverse of their variance, is interpreted to be the "best-estimate" for the minimum age of crystallization (Figure 18). The mean $^{40}\text{Ar}/^{39}\text{Ar}$ age is approximately 10-15 Ma older than previous estimates from K-Ar dating.

Some of the igneous hornblende samples from Asik Mountain contain excess argon. The evidence for this excess is from both the anomalously older apparent ages calculated from the low-temperature heating increments, and from the $^{36}\text{Ar}/^{40}\text{Ar}$ intercept on the isochron diagrams.

A possible source for the excess argon might have been the magmas that crystallized to form the layered cumulate rocks. It is generally assumed in most

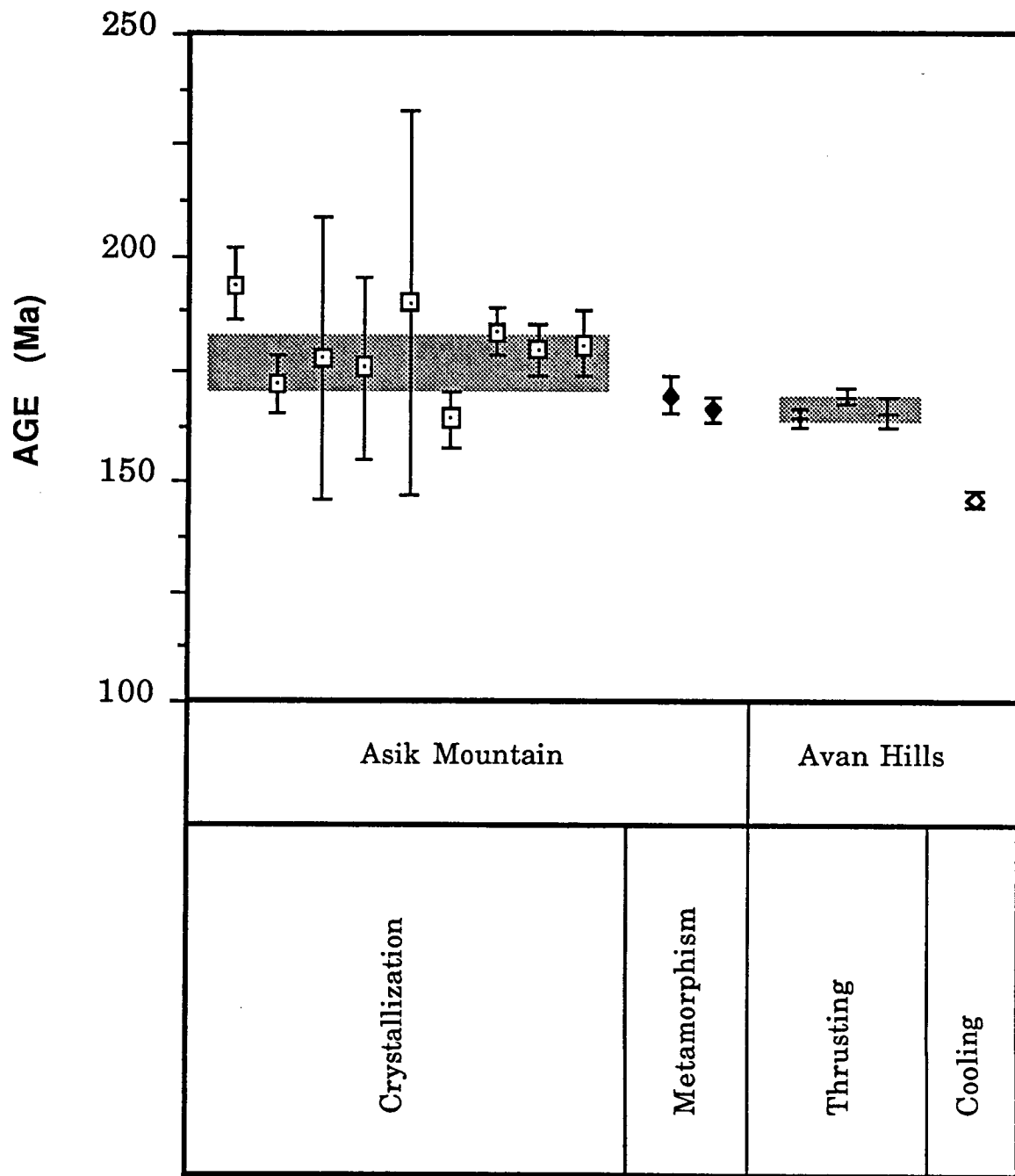


Figure 18. Summary diagram of ages determined from western Brooks Range ophiolites.

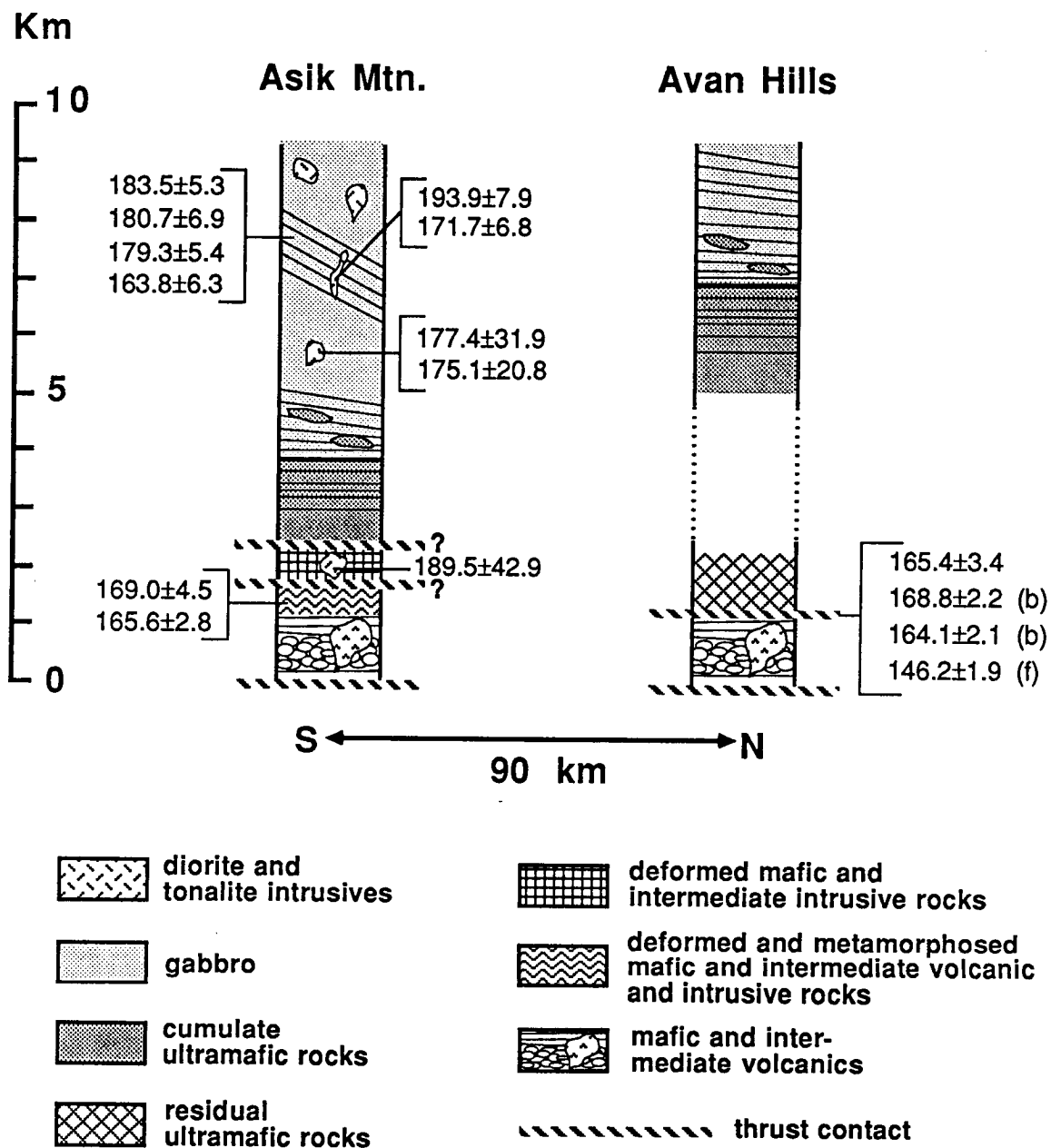


Figure 19. Stratigraphic columns of the Asik Mountain and Avan Hills ophiolites showing the locations and ages of samples.

isotopic dating techniques that the isotopic "clock" starts at the time of crystallization. In the K-Ar system, the "clock" will not be reset at the time of crystallization if radiogenic Ar, which is continually generated by the decay of ^{40}K , is not lost at the time of melting or magma transport. Several studies have demonstrated that "zero-age" submarine volcanic rocks can have apparently old K-Ar ages due to the presence of excess Ar (Funkhouser et al., 1968; Noble and Naughton, 1968; Dalrymple and Moore, 1968; Fisher, 1972).

The excess argon in the ophiolites results in "total-gas" ages that are older than the plateau or isochron ages for a given sample. This might explain the anomalously old age (384 ± 55 Ma) reported for the hornblende at Asik Mountain (Patton et al., 1977) which can not be reconciled with the results of this study. The igneous hornblendes from Asik Mountain have low amounts of potassium, possibly, also causing the error of the K-Ar age.

Time of Thrusting

Two samples of biotite and one sample of hornblende from the metamorphic sole at Avan Hills yielded ages ranging from 164-168 Ma (Figure 19). The samples are from foliated metamorphic rocks exposed within five meters of the thrust surface. The time of their Ar closure is interpreted to record post-metamorphic cooling following heating during thrusting. The ages, therefore, are the "minimum" time since thrusting.

The AH-161 hornblende, and the AH-135 biotite samples have nearly identical ages, 165.4 ± 1.7 and 164.1 ± 0.5 Ma, respectively. The age of biotite AH-153 (168.8 ± 2.2 Ma) is slightly older than these two metamorphic ages, possibly due to either variable rates of cooling along the metamorphic sole, or to

variations in closure temperature.

The mean age for the three samples is 166 ± 2 Ma, approximately 10 Ma older than K-Ar ages determined from similar rock types in the Brooks Range (eg. Boak et al., 1987). The difference in the calculated ages might indicate that the ophiolites were thrust at different times in different part of the Brooks Range, or the difference might be the result of differences in analytical technique.

Time of Metamorphism

Ar data for lineated diorite (AM-234) and amphibolite (AM-236) from Asik Mountain yield ages of 169.0 ± 2.9 and 165.8 ± 1.0 Ma, respectively. The ages of the two samples are similar and are significantly younger than the mean age of hornblende samples from gabbro, diorite and plagiogranite. The amphiboles from both samples are lineated and appear to have recrystallized a regional, rather than local, deformation event. The results of $^{40}\text{Ar}/^{39}\text{Ar}$ dating indicate that the regional structures developed contemporaneously with the more localized thermal contact metamorphic rocks exposed along the thrust faults at the base of peridotite. The deformation-produced lineations might have formed in a tectonic setting different from the layered part of the ophiolite, or they might be due to a different stress regime within the same tectonic setting.

Hornblende AM-236 also contains evidence for an older thermal event. Ar data from the plateau formed by the 1150-1240 °C increments yields a mean age of ~182 Ma, similar to mean age of igneous hornblende ages that are interpreted to record the time since crystallization.

Time of Uplift

The $^{40}\text{Ar}/^{39}\text{Ar}$ age of potassium feldspar AH-135 is 146.2 ± 1.9 Ma; approximately 30 Ma younger than the time of crystallization and 20 Ma younger than the time of thrusting. The age of the rock implies that it was at a temperature greater than 150 ± 30 °C prior to about 146 Ma ago.

Presently, about 1000-2000 meters of layered mafic and ultramafic rock overlie the metamorphic sole. At reasonable geothermal gradients, a depth of 1–2 km is well above the depth at which Ar closure occurs in potassium feldspar (estimated to be at 4-7 km assuming 25-30°C/km). In this model, the age of the potassium feldspar would record the time at which the monzonite was overlain by less than about four kilometers of rock. These relations imply that the feldspar was overlain by a thick section of rock, and that at least 2 kilometers of rock has been removed by erosion or tectonism.

It is also possible that the residual heat of the gabbro and peridotite thrust sheet kept the underlying metamorphic sole at elevated temperatures. However, model calculations for the cooling of oceanic lithosphere suggest that most of the residual heat in an initially hot (~1000 °C) mafic and ultramafic thrust sheet would dissipate within a relatively short time (~2-5 Ma). The same models predict that rocks at about 2.5 kilometers depth in oceanic lithosphere are cooled below 100°C by about 10 Ma after their formation at an accreting plate boundary. However, the relatively long span of time between Ar closure in the amphiboles (~500°C) and in the potassium feldspar (~150°C) suggests that the age of the potassium feldspar is not simply a result of conductive cooling to thermal equilibrium. Rather, the Ar closure age of the feldspar might record a tectonic or thermal event that allowed the "warm" (>150°C) ophiolite to undergo further

cooling. Possibly, rocks in the ophiolite and in the metamorphic sole were kept at elevated temperatures due to either a steepened geothermal gradient, such as might occur in an ocean basin, or due to burial during tectonism, or both.

The $^{40}\text{Ar}/^{39}\text{Ar}$ age of the potassium feldspar agrees with the age of ophiolite emplacement, onto the continental margin, that has been interpreted from stratigraphic relations and fossil ages. The youngest sediments deposited prior to overthrusting by the ophiolites, are Bajocian chert, dated radiolaria and pelecypods (Mull et al., 1982; Maiyfield et al., 1983). Allocthonous flysch and olistostromes structurally overlying the Bajocian cherts, and overthrust by the ophiolites, contain ophiolitic clasts. The oldest fossils reported from these sediments are pelecypods of Tithonian age (Curtis et al., 1982), indicating that sediments were being derived from ophiolitic rocks and deposited on continental crust by Tithonian time. These relations suggest that the ophiolites were emplaced onto the continental margin by the Tithonian.. The Ar closure age of the feldspar might record uplift of the ophiolite during emplacement.

The Ar diffusion history of a mineral, interpreted from its release spectra, can sometimes be modelled if the thermal history of the mineral has been relatively simple since the time of closure. Although the low temperature portion of the release spectrum of potassium feldspar AH-135 is complex, its shape is approximately that of an Ar loss profile, perhaps complicated by the presence of excess Ar. If the profile is due to diffusion, then it suggests that Ar diffusion occurred until about 110 Ma ago. This is similar to the age of post-metamorphic cooling and uplift interpreted from K-Ar data in the southern Brooks Range (Turner et al., 1979).

Implications for Ophiolite Obduction

The $^{40}\text{Ar}/^{39}\text{Ar}$ results constrain models for the thermal history of the ophiolites from the time of crystallization to uplift (Figure 20). The minimum age of ophiolite gabbro crystallization is about 178 ± 9 Ma ago. Prior to that time, the rate of cooling in the ophiolite was probably fast, as suggested by thermal models for the conductive cooling of oceanic lithosphere. Sedimentary and volcanic rocks, originally in the upper part of Copter Peak volcanic sequence, were overthrust, metamorphosed, and cooled below 300-500 °C by 166 ± 3 Ma ago. The $^{40}\text{Ar}/^{39}\text{Ar}$ age interpreted for potassium feldspar in the metamorphic sole indicates that the metamorphic rocks, and possibly the rest of the ophiolite, cooled slowly to about 150 °C by 146 Ma ago, and to approximately 100 °C by about 110 Ma. These data are interpreted to indicate a maximum of 5-15 Ma between crystallization and detachment, and maximum of 20 Ma between the time of detachment and obduction onto continental crust. Studies of other ophiolites indicate similarly short times between crystallization and detachment. If convergence occurred throughout the time between crystallization and emplacement, then the long time between the crystallization and emplacement of the Brooks Range ophiolites implies that the ophiolites originated in a setting far from the margin onto which they were obducted.

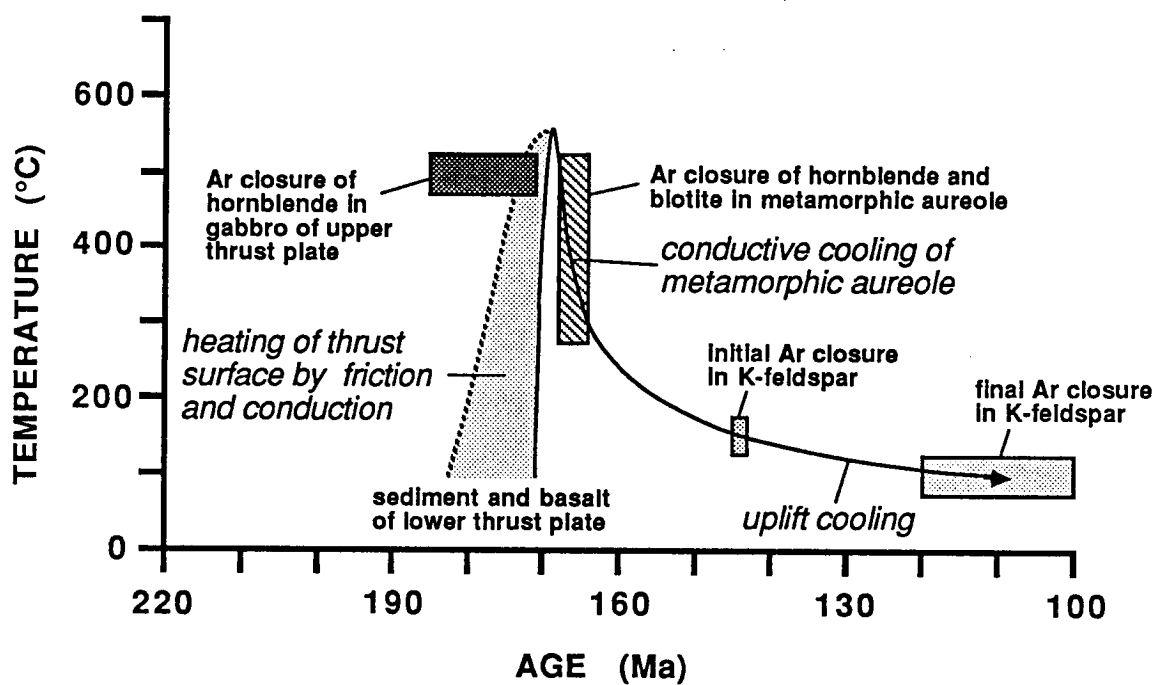


Figure 20. Time versus temperature diagram of hornblende, biotite, and potassium feldspar from western Brooks Range ophiolites. The solid black curve is a likely time versus temperature curve for sediments in the lower thrust sheet.

Regional Cross-Section of the Eastern Brooks Range, Northern Alaska

Introduction

The NASA project involves study of the regional tectonics of Alaska, using TM and other data. As part of this project, regional shortening in the Brooks Range/Colville Basin couple has been evaluated. Regional shortening in an orogenic belt in general increases towards the interior of the orogen. Balanced cross-sections are used to obtain regional shortening estimates for orogenic belts. A balanced cross-section and reconstruction for the eastern Brooks Range and Colville Basin, Northern Alaska, show that the regional shortening is not evenly distributed. The following is a report on work in progress. The change in structural style and the uneven shortening distribution in the Brooks Range and the Colville Basin are discussed, and the mechanical properties of the Colville Basin are analyzed in terms of the wedge models of Davis, Suppe, and Dahlen (1983).

Regional Setting and Geology of the Brooks Range

The Brooks Range, which trends east-west across northern Alaska, is thought to have formed northward of a south-dipping subduction zone during the Late Jurassic and Early Cretaceous. The Range is bordered on the north by the Colville Basin, a peripheral foreland basin filled with Cretaceous and younger sediments eroded from the developing Brooks Range. The southern margin of the Brooks Range is bordered by the Yukon-Koyukuk Basin. The

basin contains a thick section of Cretaceous and younger sediments on oceanic crust; the sediments are derived from both southern and northern sources. Figure 1 is a map showing the major physiographic provinces of Northern Alaska and the line of cross-section.

Rocks of northern Alaska have been divided into three stratigraphic sequences, each separated by major unconformities. The lowermost, Proterozoic to Middle Devonian Franklinian sequence consists mostly of argillite and volcanic-arc deposits (Brosge et al., 1962). Ellesmerian rocks, overlying the Franklinian sequence, are Mississippian to Early Cretaceous in age and consist almost entirely of sediments deposited on a stable continental platform, from a northern cratonic source. The Cretaceous and Tertiary Brookian sediments were deposited northward from the Brooks Range, recording a reversal in direction of sediment transport.

Stratigraphic and isotopic evidence indicates that the Brookian deformational event began in Mid-Jurassic time, ~170-150 Ma (Tailleur and Brosge, 1970; Wirth et al., 1986), with northward thrusting from a south-dipping subduction zone (Mayfield et al., 1983; Tailleur and Snelson, 1969). The cessation of thrusting is dated as Early Cretaceous (Albian, ~112-96 Ma), by fossils found in the Fortress Mountain Formation, the oldest rock unit in the Brooks Range that postdates significant thrust transport (Mull, 1982; Mayfield et al., 1983).

The tectonic events that formed the Brooks Range are not well understood. Models of the tectonic evolution of the Brooks Range include:

- 1) The Northern Alaska terrane rotated counterclockwise away from the Canadian Arctic Archipelago, with a pole of rotation located approximately in the Mackenzie Delta. (Carey, 1958; Tailleur and Snelson, 1969; Tailleur and Brosge, 1970; Tailleur, 1973).

- 2) The Northern Alaska terrane was north of its present position

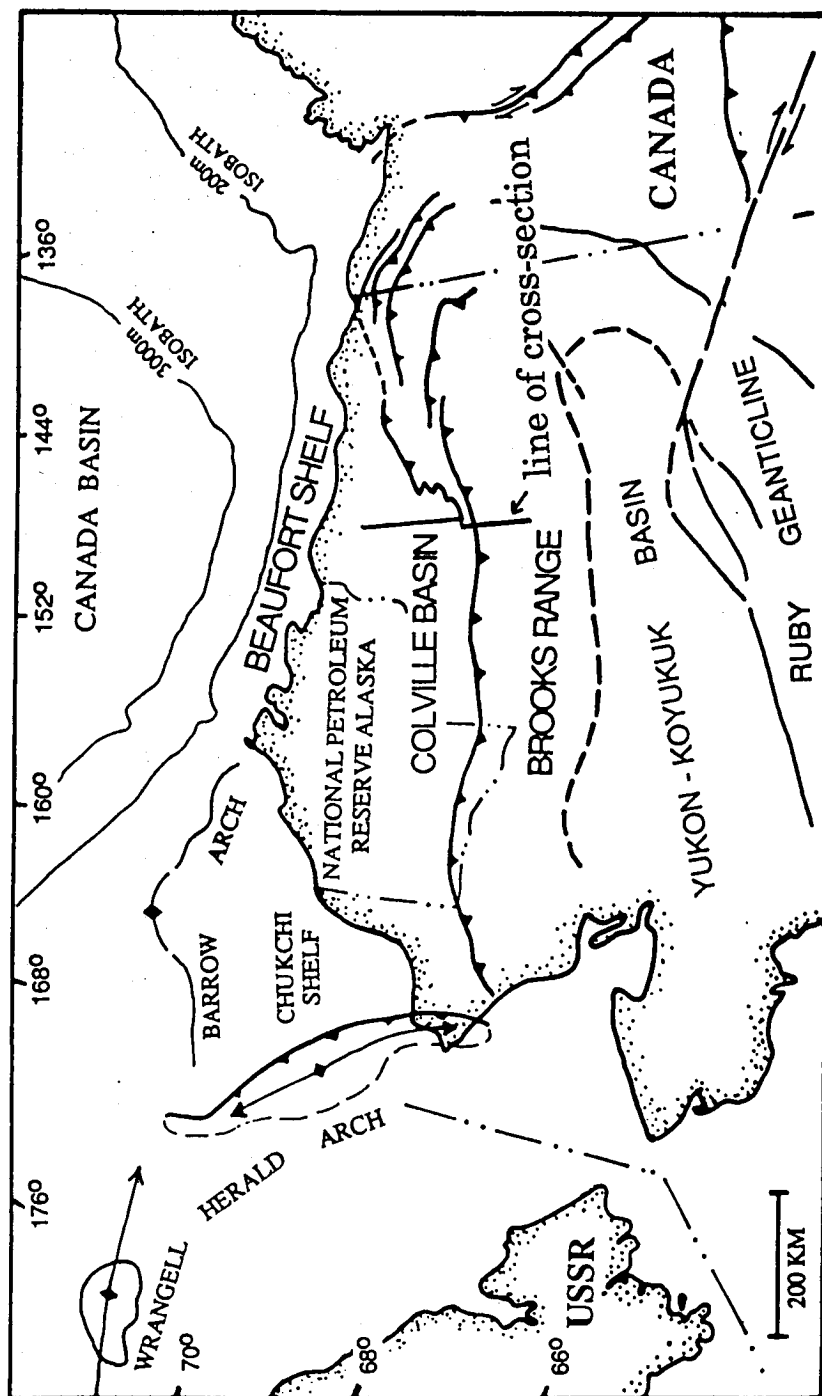


Figure 1: Map of Northern Alaska, showing the line of cross-section.

and moved southward along a strike-slip fault bordering the Canadian Arctic Archipelago (Nilsen, 1980; Oldow et al., 1987).

3) The Northern Alaska terrane has remained essentially "in place" relative to North America (Herron, Dewey, and Pittman, 1974; Churkin and Trexler, 1980).

Balanced Cross-Section Construction

A balanced cross-section is a geologic cross-section of deformed rock that can be restored to its original, undeformed condition by a series of geometrically possible and geologically reasonable steps. During the restoration, the entire cross-sectional area of rock is conserved (Dahlstrom, 1969). The construction of balanced cross-sections has been improved by the development of techniques based on the geometries of fault-bend folds (Suppe, 1983), and fault-propagation folds (Suppe and Medwedeff, 1984). Fault-bend folds form over non-planar fault surfaces (e.g. ramps) and fault-propagation folds over the tips of upward-propagating faults. The major assumption made in using these techniques for balancing a cross-section is that thrust fault ramps form at a constant angle (referred to as the fundamental cutoff-angle) within a coherent rock sequence. A dip spectrum, which is developed from this angle, predicts the dip angles encountered in a cross-section based on the number of imbricate ramps beneath each structure. Analysis of the dip spectrum (Suppe, 1983) involves plotting a histogram of the frequency of occurrence versus dip angle of all known dips from one structural province. The fundamental cutoff-angle, and dip of the "basement" or decollement sole, are determined by comparing the observed dip spectrum with theoretically predicted spectra for different fundamental cutoff angles and basement dips. Successions of modes (peaks) in the dip spectrum

are dip orders; each dip order corresponds to the number of thrust-fault ramps beneath the dipping surface. These techniques provide important constraints for subsurface structural/geometric configurations based on available surface data.

Data for Cross-Section

The data used to construct the cross-section (Figure 2) includes:

1. regional mapping (USGS and Alaskan Survey)
2. seismic reflection profiles
3. line drawing of proprietary seismic data (Hawk, 1985)
4. gravity and magnetic data

Thematic Mapper data were evaluated for use in the balanced cross-section construction. It was determined that the spatial resolution of the TM data is not sufficient for an accurate analysis of fault and bedding plane dips.

A fundamental cutoff angle of 10° was used, based on the distribution of dip values for the Brooks Range. A ramp angle of 26° was used for fault-propagation folds; this value was selected from analysis of the geometries of selected folds in the Colville Basin.

Discussion of the Cross-Section

The cross-section is shown in Figure 2. The configuration of the cross-section shows that there is a pronounced difference in structural style of the Brooks Range and Colville Basin. The Brooks Range is interpreted to be dominated by fault-bend folding with a few fault-propagation folds exposed at the surface. Two duplex structures are shown, one beneath the Fortress Mountain

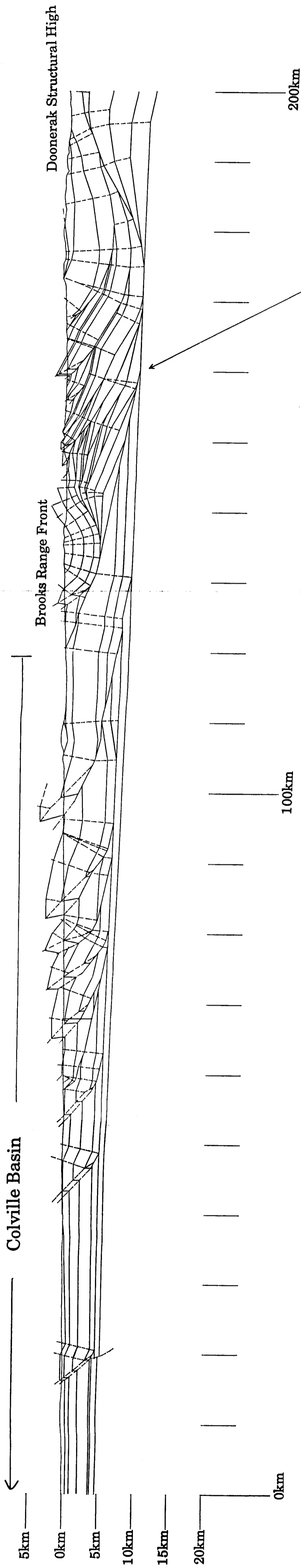
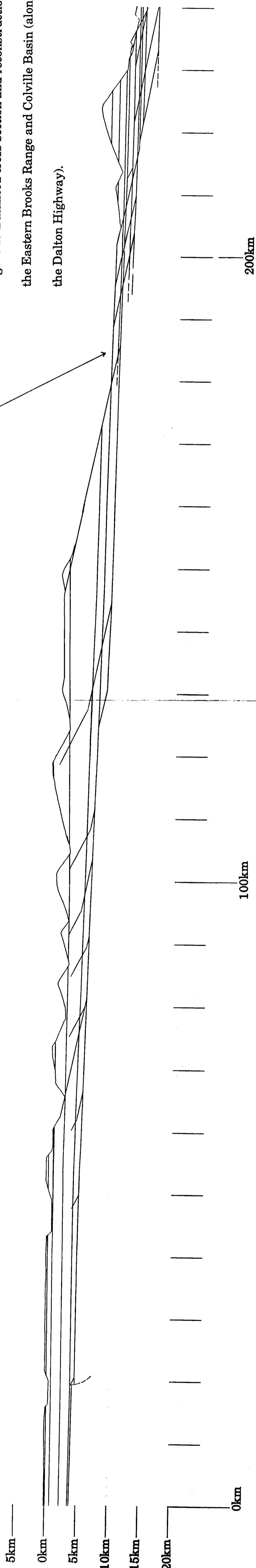


Figure 2: Balanced cross-section and reconstruction of the Eastern Brooks Range and Colville Basin (along the Dalton Highway).



FOLDDOUT FRAME

2 FOLDDOUT FRAME

3 FOLDDOUT FRAME

4 FOLDDOUT FRAME

Syncline at the Brooks Range Front, and one beneath the Doonerak Structural High. The structural reconstructions for the Brooks Range indicate that shortening of 50-60% has occurred.

The Colville Basin is interpreted to be dominated by fault-propagation folding. Tertiary strata within the forelimb of the northernmost fold constitute evidence that deformation continued into the Tertiary. Structural reconstructions of the Colville Basin indicate that shortening of 15% occurred.

Comparison with the Wedge Model

Using various estimates of angular relationships from the balanced cross-section, properties that affect the mechanical behavior of the Colville Basin sediments at the time of deformation can be evaluated in terms of the Davis, Suppe, and Dahlen (1983) wedge model.

In 1978, Chapple proposed that evolving accretionary prisms and mountain belts are analogous to the wedge of sand or snow that forms in front of a moving bulldozer or snowplow. The premise of this model is that the wedge shape or 'critical taper' (the angular relationship between the topographic slope and basal decollement) is maintained as the wedge increases in size. The critical taper of a wedge is maintained by deformation within the wedge; a wedge of sediment or rock at critical taper will slide stably along the basal decollement.

In 1983, Davis, Suppe, and Dahlen published the first of three papers ("Wedge I, II, and III") in which they developed equations for the critical taper of mountain belts and accretionary prisms by treating the deformation as governed by pressure-dependent, time-independent Coulomb behavior. Their wedge equations have three variables:

- 1) the critical taper

- 2) the fluid pressure ratio
- 3) the coefficient of internal friction.

Figure 3 plots data from active accretionary prisms and mountain belts. Calculated fluid-pressure ratios for some active accretionary prisms and mountain belts are shown in rectangles. The rectangles with heavy lines represent mountain belts and accretionary prisms with measured fluid pressure ratios; the theoretically predicted values agree well with the measured values.

Assuming that no erosion occurred in the Colville Basin as folds formed, a topographic slope of 2° is estimated by projecting the existing structures above the present-day erosional surface (see Figure 4). This value is considered a maximum for the slope; the assumption that no erosion occurred is probably incorrect. Any erosion would have reduced the topographic slope to less than 2° . The basal decollement dip is estimated to be $\sim 2^\circ$. Combined, these data suggest a maximum critical taper of 4° for the Colville Basin during deformation. This value is low in comparison with values observed in active mountain belts and accretionary prisms. In Figure 5, the critical taper interpreted for the Colville Basin is plotted as a black dot against the data from active accretionary prisms and mountain belts. If this interpretation of the critical taper is correct, the Davis et al. (1983) wedge model predicts that the fluid-pressure ratio for the basin was extremely high ($>.9$) at the time of deformation.

The Taiwan data of a known moderate fluid-pressure ratio and known critical taper of 9° , was chosen for comparison of the low taper in the Colville Basin. Using the critical taper in Taiwan as a reference, a topographic slope of 7° is plotted for the Colville Basin transect. According to the Davis et al. (1983) model, a moderate fluid-pressure ratio for the Colville Basin during deformation indicates that more than 8 km of uplift and erosion must have occurred in the southern Colville Basin since the end of deformation.

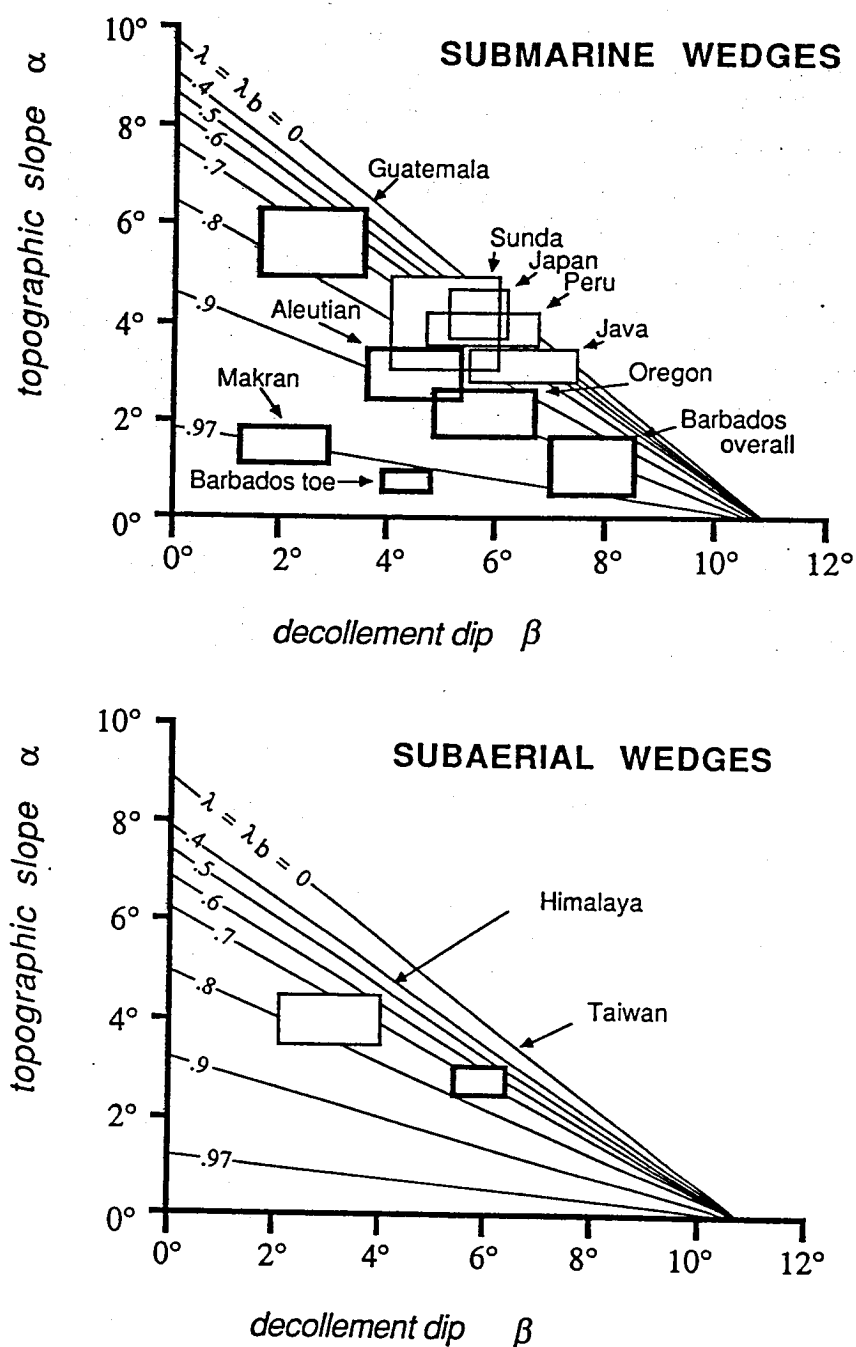


Figure 3: Plots of topographic slope versus dip of the basal decollement for active accretionary prisms and mountain belts, shown in rectangles. Lines represent theoretically calculated fluid pressure ratios (from Davis, Suppe, and Dahlen, 1983).

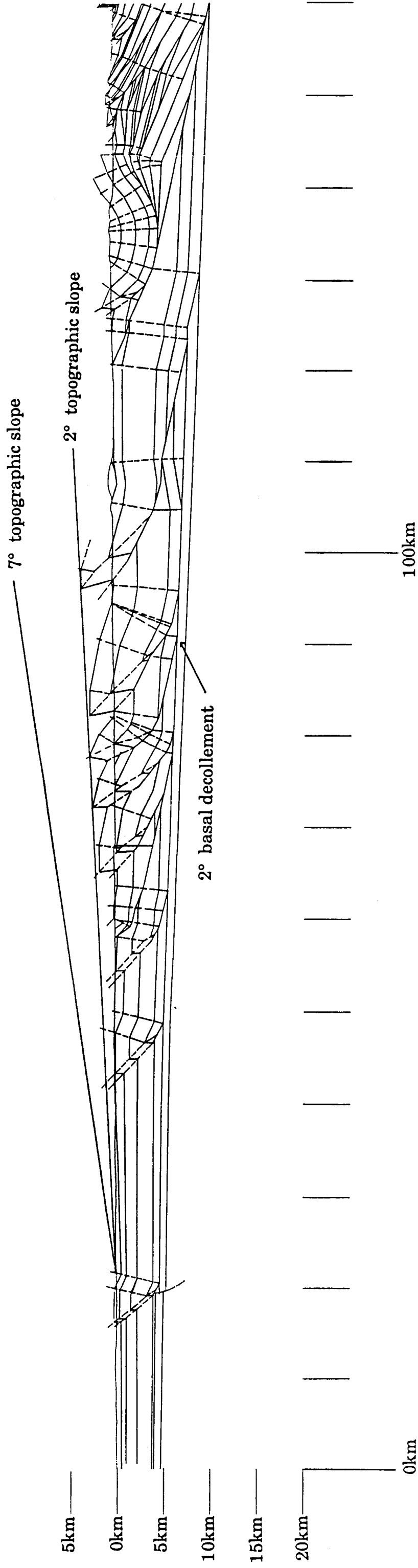


Figure 4: The lower line, drawn above the topographic surface of the cross-section, plots the maximum topographic slope (2°) for structures in the Colville Basin. The basal decollement is interpreted to be 2°; this suggests that the maximum critical taper in the Colville Basin during deformation was 4°. The upper line indicates the topographic slope for a wedge with a critical taper of 9°, such as that observed in Taiwan.

EOLDOUT FRAME

EOLDOUT FRAME

EOLDOUT FRAME

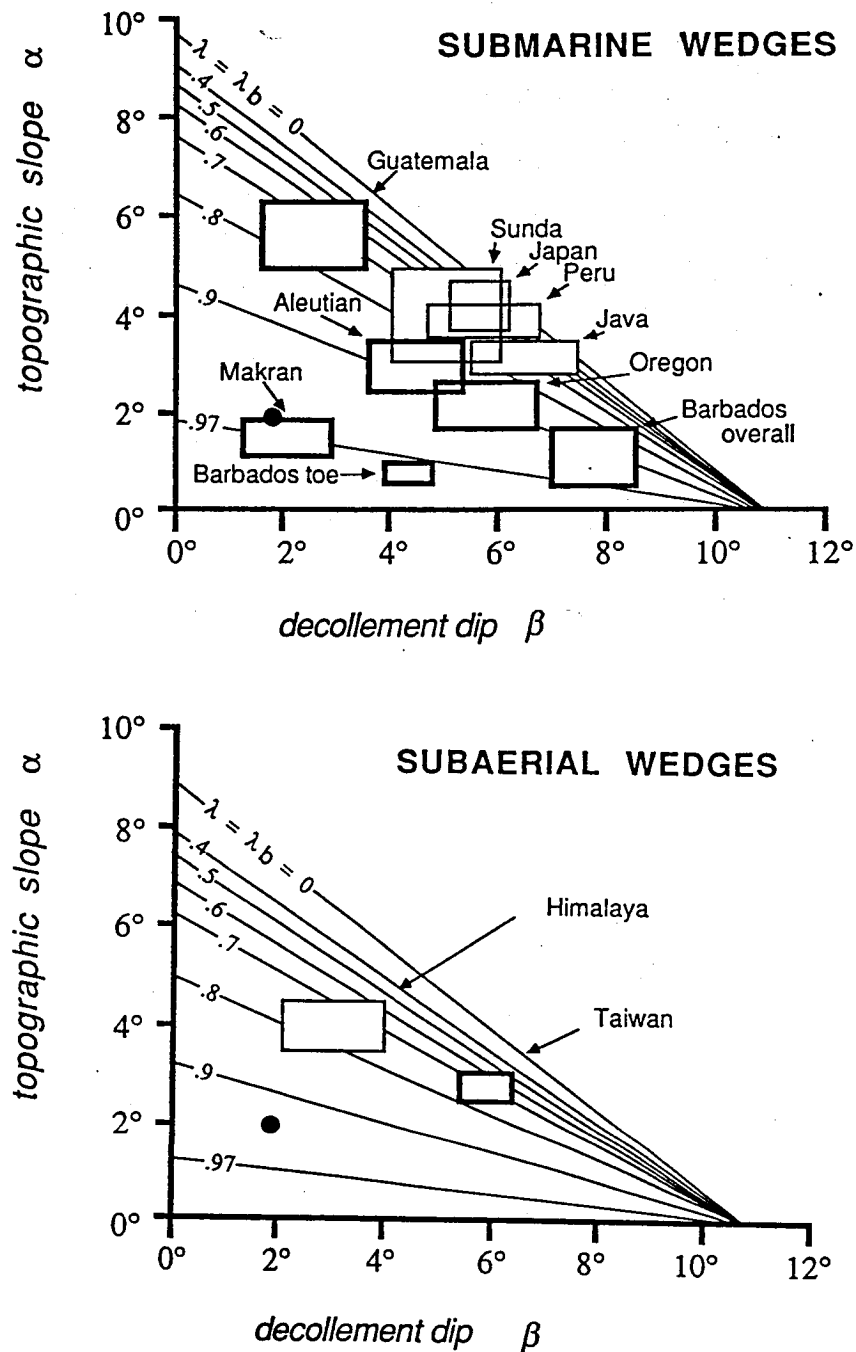


Figure 5: Plots of topographic slope versus dip of the basal decollement for active accretionary prisms and mountain belts, shown in rectangles. Lines represent theoretically calculated fluid pressure ratios (from Davis, Suppe, and Dahlen, 1983). The black dot represents the dip of the basal decollement and the maximum topographic slope calculated for structures in the Colville Basin.

Conclusion

The Brooks Range and Colville Basin have very different structural styles. The Brooks Range structures are dominantly fault-bend folds; those in the Colville Basin are fault-propagation folds. The difference of structural style between the Colville Basin and Brooks Range may be related to a difference in the mechanical properties of the rocks in these two regions during deformation. Analysis of the Colville Basin critical taper using the Davis et al. (1983) wedge model indicates that the fluid-pressure ratio in the Colville Basin was extremely high during deformation. The Brooks Range rocks are Jurassic-and-older and were probably well-lithified during the Jurassic-Cretaceous deformation. Rocks in the Colville Basin are the same age as the deformation; presumably these were not well-lithified during deformation. A high fluid-pressure ratio would be expected within the evolving Colville Basin sediments. Fission-track and $^{40}\text{Ar}/^{39}\text{Ar}$ data may provide additional information into the mechanical properties of the Brooks Range and Colville Basin as they underwent deformation.

Analysis of Digital Aeromagnetic and Topographic Data from the Josephine Peridotite, Southwestern Oregon

As a part of this NASA project, we proposed to incorporate digital aeromagnetic data in our remote sensing study of ophiolites. High-resolution aeromagnetic data was not available for northern Alaskan ophiolites, but was available for the Josephine peridotite in southwestern Oregon. We used the digital aeromagnetic data, in combination with digital topographic data, to test the utility of these data in determining fault geometries and the distribution of serpentinite in ultramafic rock exposures. We had previously documented the distribution of faults and serpentinite within the Josephine peridotite from field studies during last ten years, and by interpretation of false-color infrared aerial photographs and Landsat Multispectral Scanner images (Harding and Bird, 1984). This section is included in the report to illustrate that image processing of geophysical data can also enhance remote sensing studies.

The Josephine peridotite, one of the largest exposures of ultramafic rock in North America, is located in southwestern Oregon and northwestern California (Figure 1.1). The "Josephine peridotite" is dominantly harzburgite, with small amounts of dunite and pyroxenite, all of which have been variably serpentinized. The peridotite is the mantle portion of the Josephine ophiolite. The ophiolite is oceanic lithosphere thought to have formed in a marginal basin

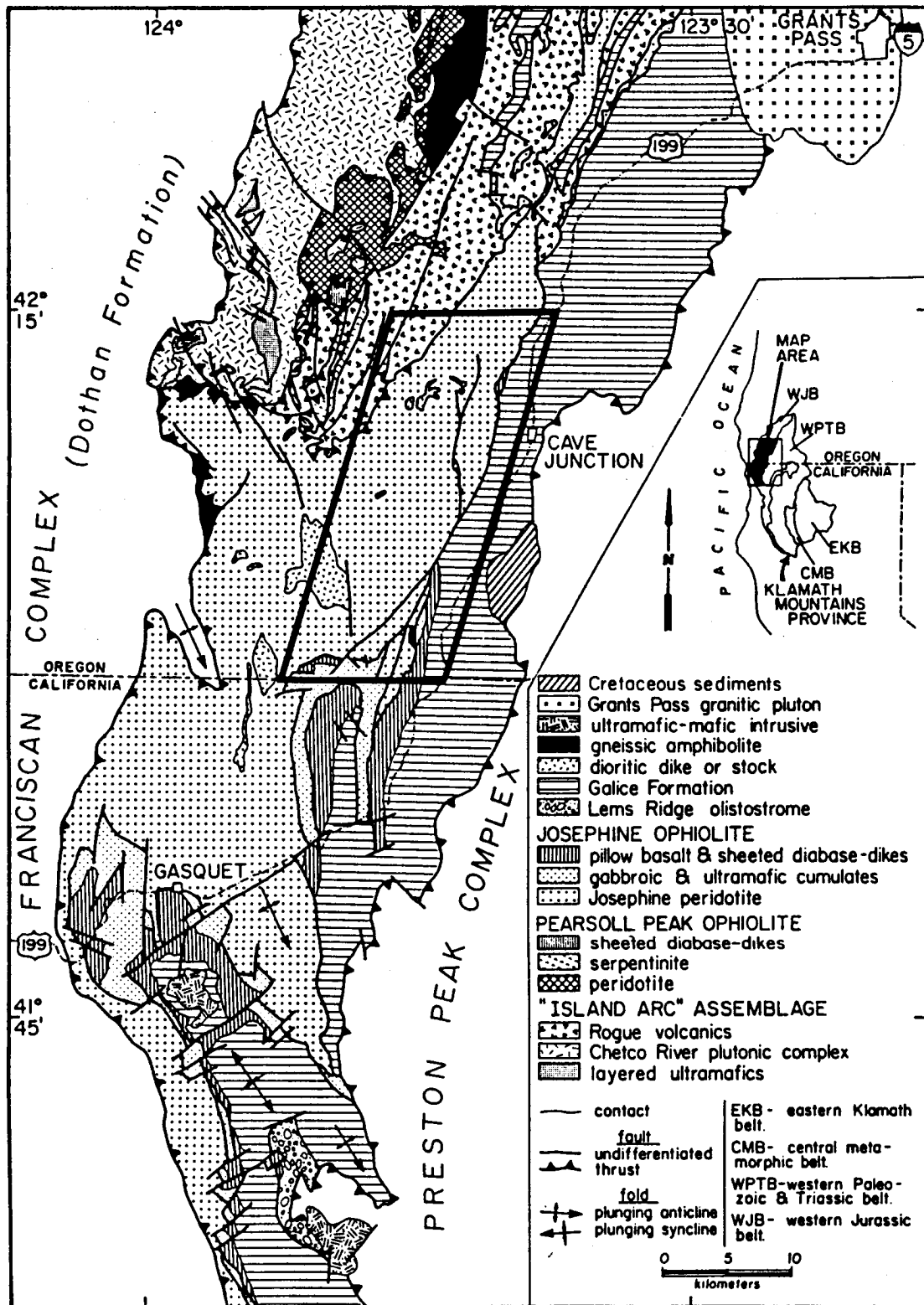


Figure 1.1 Bedrock geology of the central part of the Western Jurassic Belt. Area of study is outlined by the black polygon.

during Mid- to Late Jurassic time and been obducted during the Nevadan orogeny. The distribution of serpentinite, and of faults both within and bounding the peridotite have been mapped by us in the northeastern quarter of the peridotite (Figure 2.6). The ultramafic rocks of the peridotite exhibit a variation in the intensity of serpentinization; "unserpentinized" peridotite of Figure 2.6 corresponds to rocks containing 10 to 50% serpentine, whereas "serpentinized" peridotite is 50 to 100% serpentinized, based on thin-section observations. "Serpentinized" peridotite is local, occurring along the thrust at the base of the peridotite and along high-angle faults. Digital aeromagnetic and topographic data were used to determine the subsurface geometry of faults shown in Figure 2.6, to determine if this data could be used to map the distribution of serpentinite, and to investigate the source of anomolous aeromagnetic highs. This work was part of D. Harding's Ph.D. research, and the following is extracted from Harding's doctoral dissertation (Harding, 1988).

The geometric relations of the faults on the cross-sections in Figure 2.6 have been constrained by digital, total-field aeromagnetic data combined with digital topographic data. The aeromagnetic data is shown in Figure 2.8, in which bright areas correspond to high aeromagnetic intensity. The superimposed lines are geologic boundaries from Figure 1.1 which have been registered to the aeromagnetic data. The white boundary outlines the area studied. The digital data was provided by Dr. Richard Blakely of the United States Geological Survey. The digitization and processing performed by

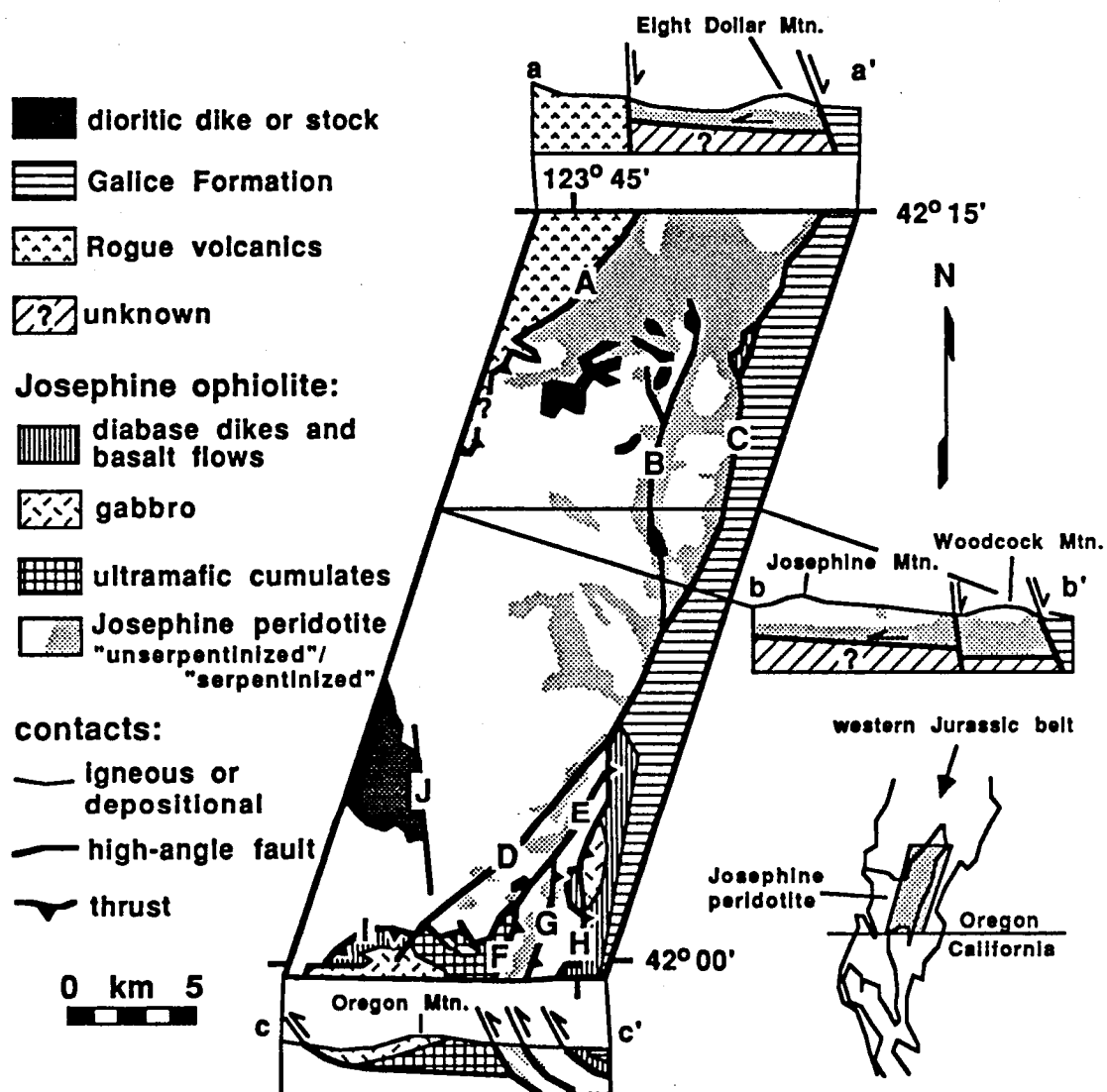


Figure 2.6 Bedrock geology and cross-sections of the study area.

original in color

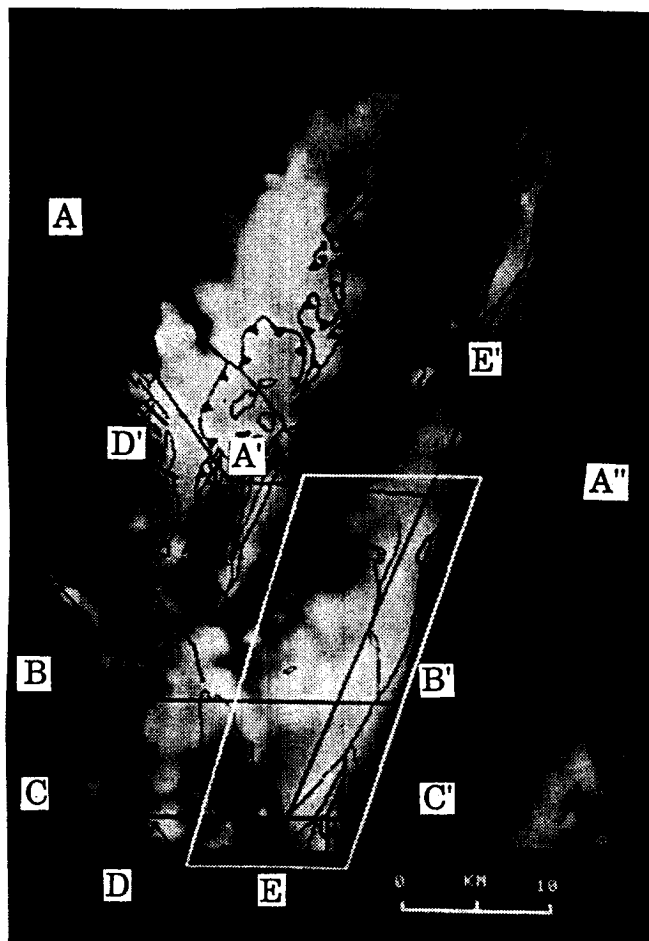


Figure 2.8 Image of digital, total-field aeromagnetic data for the northern part of the Josphine peridotite and adjacent rocks. Dark areas correspond to regions of low aeromagnetic intensity and bright areas correspond to regions of high aeromagnetic intensity. Geologic boundaries from Figure 1.1 and profile lines are superimposed. The polygon outlined in white corresponds to the area shown in Figure 2.6. The figure is aligned vertically north-south.

R. Blakely is described in Table 2.1. The data provided by R. Blakely has been aurally enlarged by a factor of three by interpolation, for Figure 2.8.

Table 2.1 Sources of digital data

<u>Aeromagnetics</u>	<u>Topography</u>
1950 total-field aerial survey, east-west flight lines, 1370 m flight altitude (barometric), 0.8 km avg. flightline spacing, regional field removed, if any, unknown, hand contoured, Balsley et al. (1960)	
↓	
hand digitized along flight lines, 1750 gamma constant subtracted	
↓	
interpolated to match topography, 0.25 minute grid spacing, 120 samples x 120 lines	National Cartographic Information Center digital topography subaveraged to 0.25 minute grid spacing, 120 samples x 120 lines
↓	↓
transformed to Mercator projection by interpolation	

The Josephine peridotite is has high aeromagnetic intensity, as compared to the surrounding regions of sedimentary rock (Dothan and Galice Formations) and the Rouge volcanics. Because the contrast between the peridotite and surrounding rocks is large, the aeromagnetic data can be used to

constrain the attitudes of the faults bounding the peridotite. Five profiles of total-field aeromagnetic intensity (solid line) and elevation above sea-level (dashed line) are shown in Figure 2.9. The locations of the profiles are indicated in Figure 2.8. The vertical exaggeration of the topography is 10:1. The rock types occurring along the line of the profiles are shown at the top of each profile. The margins of the Josephine peridotite are indicated by the dotted vertical lines. Because the data is in digital form, it was possible to interactively examine a large number of profiles. The profiles in Figure 2.9 are representative of the peridotite.

The aeromagnetic profiles over the Josephine peridotite are characterized by high amplitude, short wavelength anomalies. Some of the anomalies correlate with topography, but many do not. The magnetic anomalies that do not correlate with topography are probably produced by local variations of the degree of serpentinization and/or by the strength, direction and polarity of the peridotite's natural remnant magnetic field. Barnard et al. (1981) have shown that the magnetic susceptibility of samples from the Josephine peridotite vary by nearly two orders of magnitude, depending on the degree of serpentinization. (The strength of the magnetic anomaly induced in a rock by the earth's magnetic field depends directly on the rock's magnetic susceptibility.) The magnetic susceptibility varies from 0.0002 to 0.008 emu for rocks ranging from unserpentinized peridotite to serpentinite, respectively. The magnetic susceptibility increases with increasing degree of serpentinization, due to

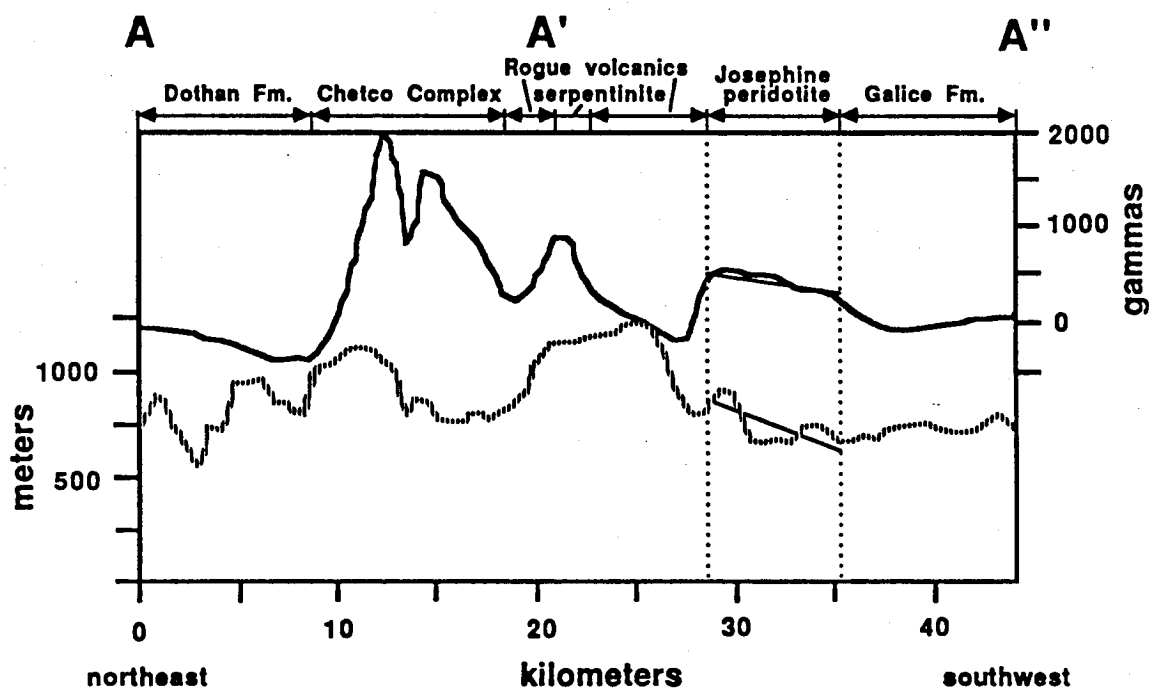


Figure 2.9 Profiles of total-field aeromagnetic intensity in gammas (solid curve) and elevation above sea-level in meters (dashed curve) for the northern part of the Josephine peridotite and adjacent rocks. The topography is vertically exaggerated by a factor of ten. Dotted vertical lines mark the margins of the peridotite. Thin solid lines plot regional aeromagnetic and topographic gradients over the peridotite. The locations of the profiles are shown on Figure 2.8.

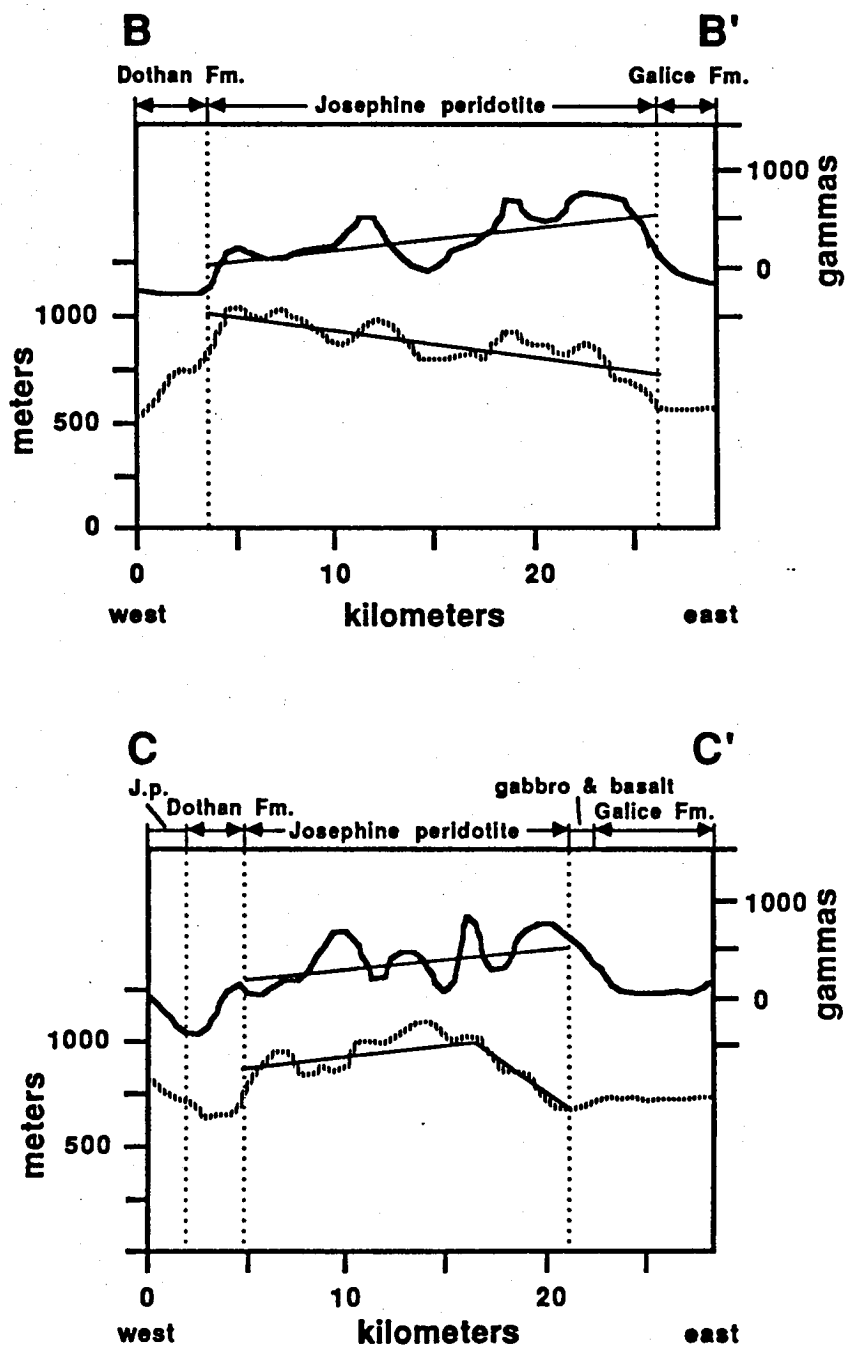


Figure 2.9 Continued.

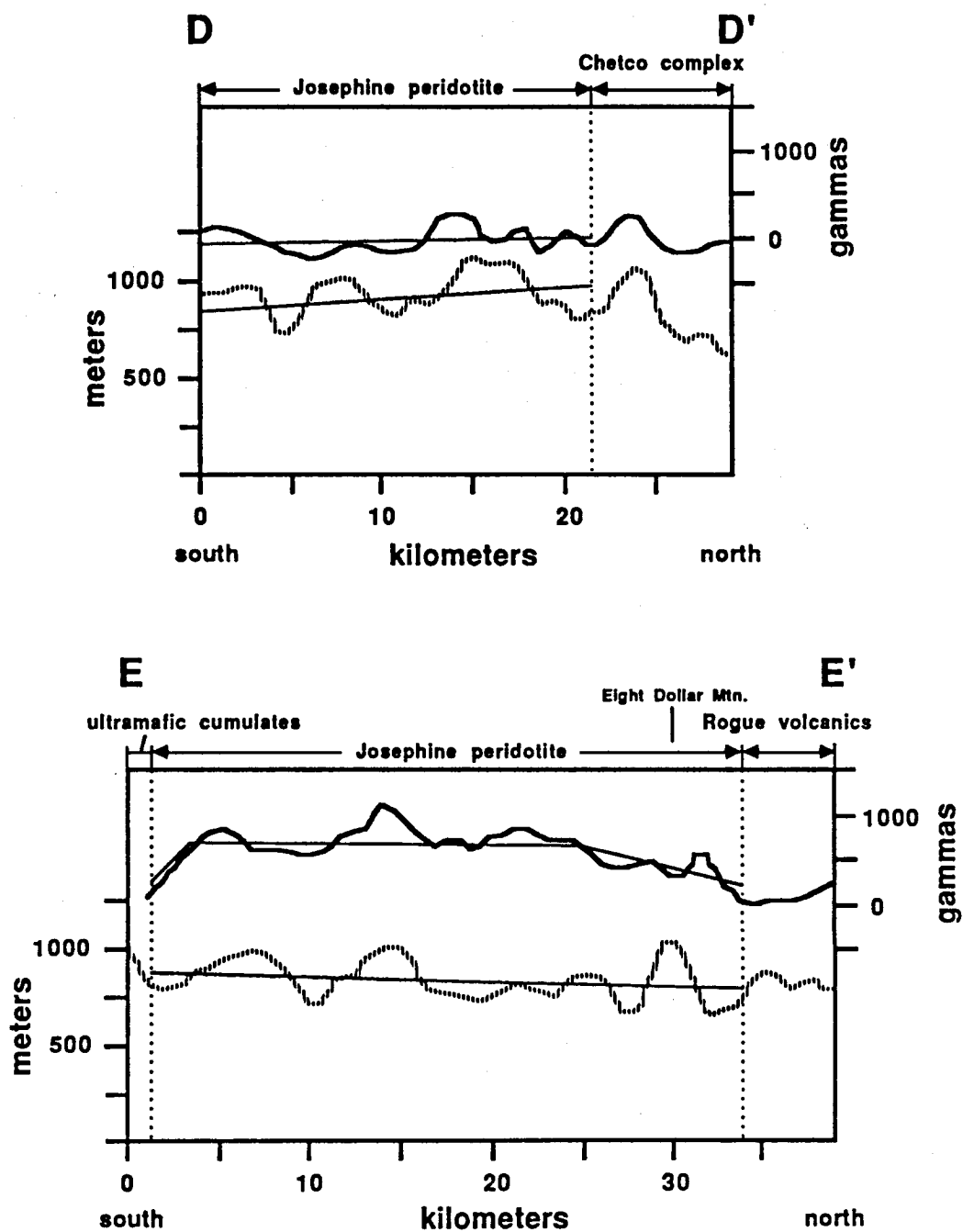


Figure 2.9 Continued.

the formation of magnetite. The total magnetic anomaly produced by a rock is the vector summation of the induced field and the natural remnant magnetism. For most rocks, remnant magnetism is normally small as compared to the induced field, and, therefore, remnant magnetism can be ignored in the interpretation of aeromagnetic data. However, Blakely and Page (1980) have shown for samples of the Josephine peridotite that, on average, the strength of the remnant magnetism is 1.8 times that of the induced field. Because the remnant magnetism is the dominant component of the magnetic anomaly produced by the Josephine peridotite, the spatial variation of the remnant magnetism's strength, direction and polarity must be known to quantitatively model the geometry of the peridotite at depth. None of these parameters are known. Also, the spatial variation in degree of serpentinization, which controls the strength of the induced field, is not known, especially at depth.

Although the unknown parameters are limitations that preclude quantitative modelling of the aeromagnetic data, the general character of the magnetic anomaly produced by the Josephine peridotite can be used to qualitatively describe the geometric relations of the peridotite' mass. Lines are plotted on the profiles to show the regional gradients of the aeromagnetic data and the topography. Assuming that the local variations in the magnetic field (those producing the short wavelength anomalies) average out on a regional scale, the separation between the gradient lines for the magnetics and the

topography is a qualitative estimate of the thickness of the peridotite. The variations of estimated thickness can be used to evaluate the orientation of the basal thrust of the peridotite. For example, profile B-B' shows a divergence of the gradient lines from west to east (the magnetic intensity increases as the elevation decreases), indicating that the peridotite thickens to the east and that the basal thrust therefore dips to the east. This is a general feature of the peridotite, as can be seen in the aeromagnetic image in Figure 2.8. The basal thrust of the peridotite is therefore interpreted to dip to the east, as shown in the cross sections of Figure 2.6. The aeromagnetic survey published by Balsley et al. (1960) did not indicate if any regional gradient in the earth's magnetic field was removed from the data. The regional magnetic gradient in southwestern Oregon increases to the northeast at a rate of approximately 10 gammas per kilometer. This gradient could produce an increase in the aeromagnetic measurements, from west to east across the peridotite, of approximately 100 gammas, accounting for a significant portion of the increase observed in the magnetic profiles B-B' and C-C'. However, the northeast-directed regional gradient should produce a similar increase from south-to-north. No such increase was observed in south-north profiles, such as D-D' and C-C'. Therefore, it was assumed that the regional gradient has been removed from the Balsley survey and that the west-to-east increase of aeromagnetic values across the peridotite is due to thickening.

The depth to the basal thrust of the peridotite cannot be determined from the aeromagnetic data because of the lack of constraints on the magnetic field strength and orientation. Modelling by Blakely et al. (1983) yielded a thickness for the peridotite of approximately one kilometer in the vicinity of the 10 km point on profile B-B', but they assumed that the remnant field strength is negligible and that the magnetic susceptibility of the peridotite is a constant 0.0093 emu. Neither assumption is valid, as was discussed above.

The basal thrust of the peridotite is shown as being planar (not faulted or folded) on the cross-sections a-a' and b-b' because no abrupt changes were apparent in the separation between the magnetic and topographic gradients in these areas. However, profile C-C' shows an abrupt divergence of the gradients along the eastern margin of the peridotite, in the southern part of the area studied (the magnetic gradient continues to rise as the elevation markedly decreases). This divergence may be due to increased serpentinization along faults D, E, G, and H, causing a local increase in the magnetic field strength. Alternatively, the divergence may be caused by thickening of the peridotite due to down-on-the-east displacement on fault D. This displacement is consistent with fault D being a continuation of fault C, which must have down-on-the-east displacement.

Along the northern portion of profile E-E', in the vicinity of Eight Dollar Mountain, the magnetic and elevation gradients converge due to a gradual

decrease in the aeromagnetic intensity. This observation suggests that the peridotite thrust-sheet is thinner in this area, which is consistent with the interpretation presented in Section 2.2 that the basal thrust is shallower, revealing the extensive exposure of pseudomorphous serpentinite at low elevation. The alternative explanation, that the exposure is due to thickening of the serpentinitized sole-rocks, would yield an increase in aeromagnetic intensity. Accordingly, the peridotite thrust sheet is shown as being thinner in cross-section a-a' than in cross-section b-b'.

A magnetic feature that is outside of the area studied occurs along profile B-B' on the western margin of the peridotite, where an abrupt decrease in the aeromagnetic intensity marks the position of a north-south trending, trough-like, magnetic low (Figure 2.8). Profile D-D' is along the axis of the magnetic low. The close spacing of the gradient lines in D-D', that indicate the peridotite sheet is thin, contrasts markedly with the wide spacing of the gradient lines on profile E-E', located along the eastern, presumably thicker, margin of the peridotite. The abrupt decrease in magnetic intensity on the eastern edge of the trough-like low might be produced by thinning of the peridotite by high-angle faulting, as suggested by Blakely et al. (1983). The magnetic high, paralleling the thrust contact of the peridotite along the western edge of the trough-like low, may be due to exposure of serpentinite along the thrust.

In addition to providing information about the subsurface geometry of the basal thrust, the aeromagnetic data constrains the attitude of the faults that bound the peridotite. Along the eastern margin, the magnetic anomaly produced by the peridotite decreases gradually to the lower value of the Galice Formation (profiles A-A'', B-B', and C-C'). Also, the anomaly extends to the east beyond the surface exposure of the peridotite. This relation is in contrast to the relations of the anomaly at the vertical fault contact of the peridotite with the Rogue volcanics (profile A-A'') and the east-dipping thrust contact with the Dothan Formation (profile B-B'). The decrease in aeromagnetic intensity at these faults is abrupt and coincides with the surface expressions of the contacts. The eastward extension of the anomaly beyond the eastern margin of the peridotite suggests that highly magnetic, ultramafic rock extends beneath the rocks to the east, producing the gradual fall-off of magnetic intensity. The eastern bounding faults C and H are, accordingly, shown as east-dipping in the cross sections in Figure 2.6.

The character of the magnetic anomaly along the contact with the Rogue volcanics (fault A) changes along strike. In the north, where the trace across the topography indicates that the fault is near-vertical, the eastward increase in magnetic intensity is abrupt and coincident with the the fault contact (profile A-A''). To the south, where the re-entrants in the contact indicate that the fault is low-angle, the increase in magnetic intensity is gradual (no profile is presented for this contact, but the gradual increase can be observed in the

aeromagnetic image in Figure 2.8). This gradual increase in aeromagnetic intensity suggests that the low-magnetic susceptibility rocks of the Rogue volcanics extend eastward beneath the peridotite, consistent with the interpretation that the southern portion of fault A is a low-angle thrust.

Another anomaly of low aeromagnetic intensity is in the area of a large diorite intrusive in the southwest part of the study area. However, this anomaly is displaced several kilometers to the south-southeast of the surface exposure of the diorite (Figure 2.8). This displacement cannot be accounted for by the inclination of the magnetic field induced in the diorite. The Earth's field in this area is inclined 65° to the north-northeast, so at the flight line altitude, approximately 500 m above the average ground elevation, the induced field associated with a body will be displaced only 235 m ($500 \text{ m} \times \tan 25^\circ$). Also, with this inclination of the earth's field, the displacement of the induced anomaly would be to the south-southwest rather than south-southeast, as observed for the intrusive. Several explanations for the observed displacement are possible: 1) the Buckskin Peak intrusive is a pluton that at depth extends to the south-southeast, beneath the peridotite, 2) the surface expression of the intrusive is a thin sill that extends north-northwest from a root at depth that is centered on the magnetic low, or 3) the strong remnant magnetic field in the surrounding peridotite has normal polarity and is shallowly inclined to the north-northwest. Such a shallow inclination would cause the magnetic high associated with the peridotite to be displaced significantly to the south-southeast, at the elevation of the flight lines, with the intrusive, in effect,

causing a "shadow-zone" that produces a displaced low. This third possibility is unlikely, because it would also cause the fall-off in magnetic intensity at the margins of the peridotite to be significantly displaced south-southeast from the mapped contacts. Such an effect is not observed.

In addition to constraining the geometry of the contacts that bound the Josephine peridotite, the aeromagnetic data was used to evaluate mineralogic variations occurring within the peridotite. The aeromagnetic signature of the peridotite includes large-amplitude, short-wavelength anomalies, not correlated with topography. Such anomalies might indicate the presence of anomalously magnetic lithologies, such as serpentinite or massive chromite deposits.. Aeromagnetic anomalies over the Josephine peridotite that are not correlated with topography were determined by means of a principal components transformation. Figure 2.10 shows the effect of a principal components transformation. The white features in Figure 2.10a are histograms of the frequency of occurrence of aeromagnetic intensity values between -675 and 2485 gammas (X-axis), and of elevation between 25 and 1490 meters (Y-axis). The plotted field is a two-dimensional histogram. The field is the distribution of points produced by plotting the aeromagnetic intensity versus elevation for each location that is within the boundaries of the peridotite. Locations for rocks other than the peridotite were excluded. The line through the two-dimensional histogram labelled PC1 is the first principal component axis, the axis of maximum variance for the data. It represents the

correlation between the elevation and magnetics. The data has a slightly positive correlation, with the magnetics increasing as elevation increases. The intersection between a given elevation and the axis of maximum variance yields the expected magnetic intensity, based on the correlation of the data set as a whole. The second principal component axis, PC2, is oriented perpendicular to PC1. The result of the principal components operation is shown in Figure 2.10b. The shaded region corresponds to the two-dimensional histogram field of Figure 2.10a. The operation transforms the original aeromagnetic-intensity versus elevation-values into PC1 versus PC2 values. The origin for the PC axes is positioned so that all the values in the transformed data set are positive. The PC axes increase in the direction of the arrows. The equations yielding the principal component values for a transformed data point are shown in Figure 2.10.

The second principal component indicates the divergence of a point away from the correlation line, and is, therefore, a measure of aeromagnetic intensity that is not correlated with topography. This can be seen by reference to point A in Figure 2.10b, which represents a location that has an elevation of Y_A and an aeromagnetic intensity of X_A . The location has a positive aeromagnetic anomaly because X_A is greater than X_{cor} , the expected intensity based on the correlation in the data. In the transformed coordinates, point A has values of $PC1_A$ and $PC2_A$. The second principal component value of point A is greater than $PC2_{cor}$, the value for points occurring along the line of correlation.

Locations with a negative aeromagnetic anomaly, such as represented by point B, will have second principal component values less than $PC2_{cor}$. All locations that have an aeromagnetic anomaly of the same magnitude and sign will have the same second principal component value. For example, point C, although it occurs at a lower elevation than point A, has an equal positive magnetic anomaly and, therefore, the same $PC2_A$ value.

The linear correlation between aeromagnetism and topography is approximate because the intensity of a magnetic field decreases with the square of the distance away from a magnetized object. Positive magnetic anomalies at high elevation, that approach the elevation of the flight lines, will, therefore, be undercorrected by the linear principal-component transformation. The determination of an exact correction for the topographic effects on total-field aeromagnetic data is a very complex problem that was not undertaken.

The analysis of the uncorrelated aeromagnetic anomalies is predicated on the assumption that the orientation of the total magnetic field (remnant + induced) for the Josephine peridotite is steeply inclined. With a steep inclination, aeromagnetic anomalies will not be significantly displaced from their associated topographic features at the elevation of the flight lines. If the total field were shallowly inclined, large displacements would result and the plot of aeromagnetic intensity versus elevation in Figure 2.10 would be meaningless. However, the lack of significant displacements between the

faults that bound the peridotite and the associated increases in aeromagnetic intensity indicates that the total field is steeply inclined. This is clear along the northern portion of fault A, which is known to be near-vertical.

Figure 2.11 depicts the second principal component of the transformed elevation and aeromagnetic data for the Josephine peridotite. The transformation was computed and the image displayed using the Cornell Geological Sciences image processing facility. The transformation was computed using only the data for the Josephine peridotite. Data for other lithologies was excluded. The values of the second principal component are shaded black for small PC2 values (magnetic intensity lower than that expected based on correlation between magnetics and elevation), grey for intermediate PC2 values (magnetic intensity equal to that expected based on correlation), and white for large PC2 values (magnetic intensity greater than that expected, based on correlation). The image shows the same general features as previously discussed, such as the increase in aeromagnetic intensity from west to east, and the trough-like magnetic low along the west margin of the peridotite. Several other features are also apparent. The linear zones of uncorrelated magnetic highs (white) occurring around the western base of Eight Dollar Mountain, along Josephine Creek, and along the southeast margin of the peridotite, were not apparent in the image of the original magnetic data (Figure 2.8). There is a linear aeromagnetic high, apparent in the original magnetic data, that is located along the eastern margin of the

ORIGINAL PAGE IS
OF POOR QUALITY

original in color

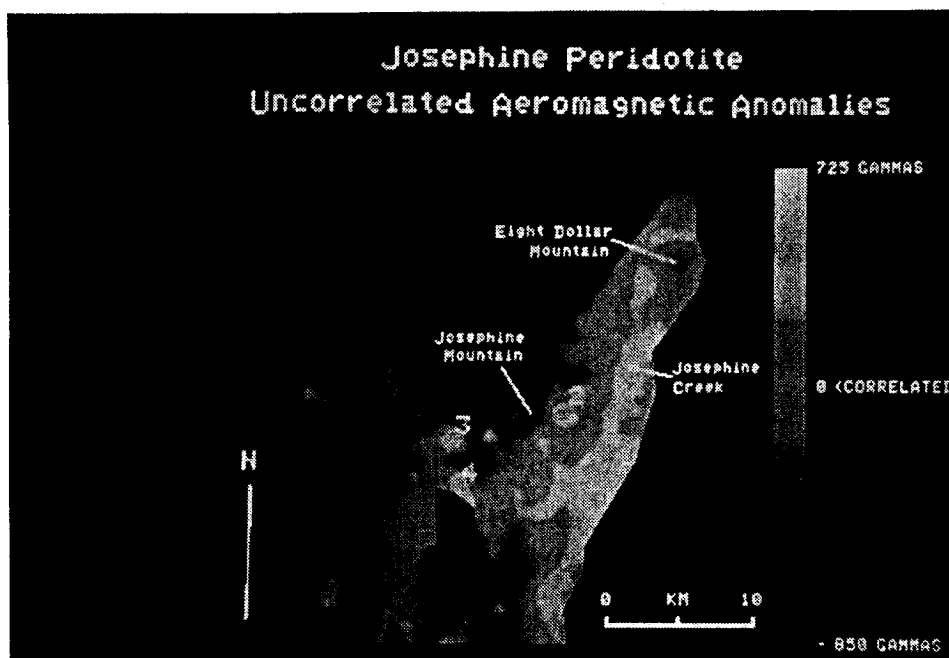


Figure 2.11 Image of the second principal component of the transformed aeromagnetic and elevation data for the northern part of the Josephine peridotite (see text for explanation).

peridotite. This high is located along a north-south ridge (Woodcock Mountain) and is probably caused by the high topography. The linear uncorrelated magnetic high in the principal component image are located along topographic lows coincident with exposures of serpentinite along faults. In addition to the linear magnetic highs, several very large amplitude, uncorrelated, high magnetic anomalies are apparent in the transformed data. These anomalies are numbered 1-4. Anomalies 2, 3, and 4 correspond to locations having very high aeromagnetic intensity which are apparent in the original data (Figure 2.8). These anomalies are each crossed by several flight lines, so they are probably not due to incorrect data in the original aerial survey. The magnitudes of the uncorrelated anomalies (the difference between the observed aeromagnetic intensity and that expected based on the linear correlation between elevation and aeromagnetic intensity) are 691, 723, and 525 gammas, respectively, for anomalies 2, 3, and 4. Anomaly 1 corresponds to a broad, low-amplitude magnetic high associated with a topographic low that is not apparent in the image of the original magnetic data (Figure 2.8). The magnitude of the uncorrelated anomaly is 657 gammas.

After recognizing these anomalous highs in the aeromagnetic data, localities 2 and 3 were examined in the field to determine the source of the magnetic anomalies. Locality 2 occurs where a broad region of pseudomorphous serpentinite, localized around a hornblende diorite dike, crosses a high ridge extending to the east of Josephine Mountain. Locality 3 also occurs

on a high ridge, where a serpentized shear zone crosses the ridge. The very large positive anomalies at these two localities are probably in part due to the undercorrection applied to anomalies at high elevation, caused by the assumption of a linear relationship between aeromagnetism and elevation, rather than a square of the distance relationship. Anomaly 1 corresponds to a broad region of serpentization, recognized in Landsat images, located in the Mendenhall and Woodcock Creek drainages at the intersection of faults B and C. The cause of anomaly 4 is not known.

These results demonstrate that digital aeromagnetic and topographic data, when integrated using standard image processing techniques, are useful in differentiating between topographic and mineralogic contributions to aeromagnetic intensity.

Appendix I

TM data received at Cornell University -- NASA Project NAS5-28739

(X) = provided by NASA (E) = provided by EOSAT (-) = not requested

<u>PATH-ROW</u>	<u>SCENE ID</u>	<u>DATE</u>	<u>QUADS</u>				<u>TRANSPARENCY</u>
			<u>1</u>	<u>2</u>	<u>3</u>	<u>4</u>	<u>band 7</u>

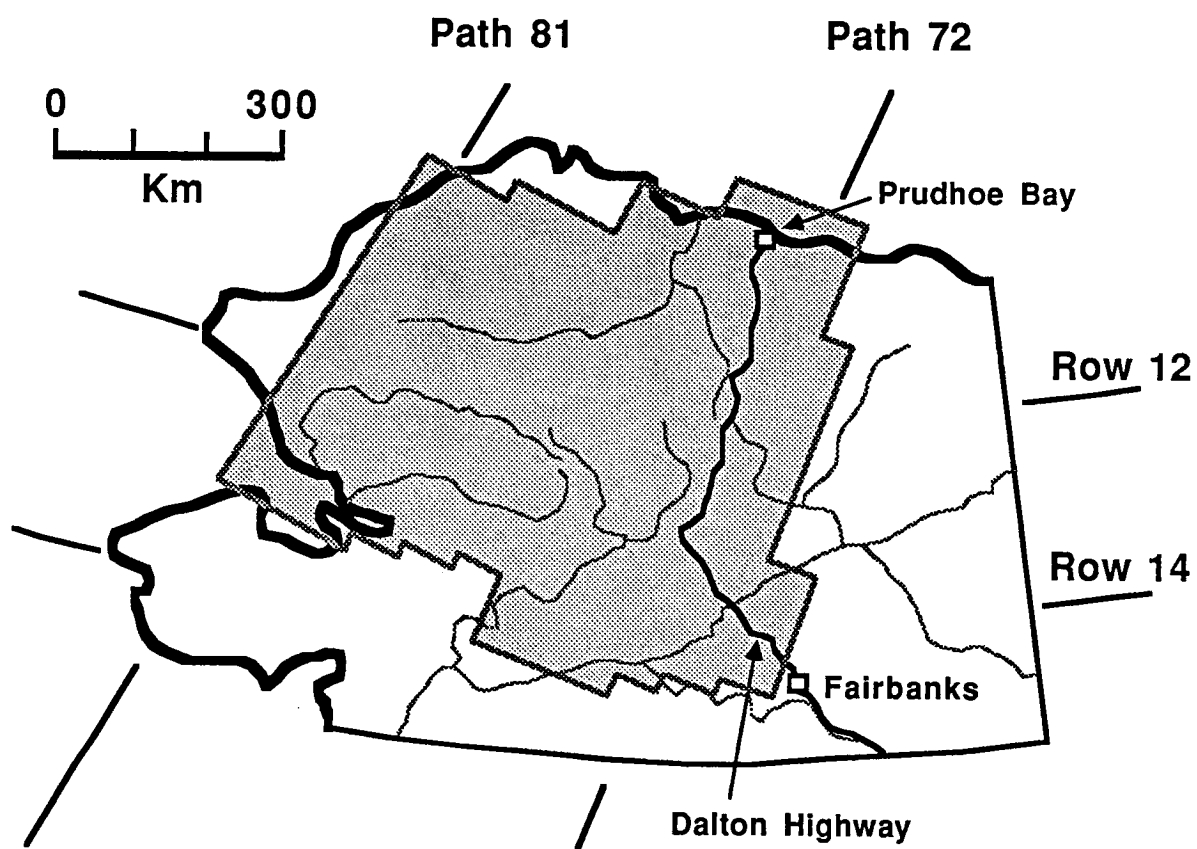
Original Request

005-026	50045-14090	840415	X	-	X	-	X
046-031	50156018264	840804	X	X	-	-	X
071-014	50507-20545	850721	E	E	E	E	E
072-012							
072-013	50466-21005	850610	X	X	X	X	X
072-014							
073-012	50521-21061	850804	X	X	X	X	X
	50505-21062	850719					X
073-013	50505-21065	850719	E	E	E	E	X
073-014	50521-21070	850804	X	X	X	X	
	50505-21071	850719					X
074-012	50512-21123	850726	X	X	X	X	X
074-013	50512-21125	857026	X	X	X	X	X
074-014	50512-21132	850726	X	X	X	X	X
075-012	50503-21184	850717					X
075-013	50503-21191	850717	X	X	X	X	X
076-012							
076-013							
077-012							
077-013	50517-21312	850731	X	X	X	X	X
078-012	50492-21372	850706	X	X	X	X	X
078-013	50492-21374	850707	X	X	X	X	X
079-012							
079-013	50499-21435	850713	X	X	X	X	X
080-012	50506-21494	850720	X	X	X	X	X
080-013	50506-21500	850720	X	X	X	X	X
081-012							
081-013							
155-232 night	50536-07004	850819	X	X	X	X	X

Additional Scene Allotment

073-011	50857-20591	860706	E	E	E	E	E
075-011	50519-21181	850802	E	E	E	E	E
078-011	50492-21370	850706	E	E	E	E	E
080-011	50858-21422	860707	E	E	E	E	E

Northern Alaska



 Area covered by Thematic Mapper Scenes at Cornell University

Appendix II

1985 Field Studies and Rock Samples Collected

As a part of the "Thematic Mapper Study of Alaska Ophiolites" we examined three western Brooks Range ophiolites in the field. The primary objectives of the field studies were to map the distribution of rocks in three representative ophiolites, and to evaluate the affects of vegetation, lichen cover and weathering for the TM studies. In addition, rock samples were collected for petrographic, geochemical, geochronologic and spectral reflectance studies.

The 1985 field studies were conducted between July 21 and August 31 at Asik Mountain, in the southern Maiyumerak Mountains, and in the eastern Avan Hills. Asik Mountain was selected for study because of its accessibility and because of its extensive exposure of gabbro. At Asik Mountain the distribution of rocks was mapped, sections in several layered portions of the ophiolite were measured, and the structural relations between the ophiolite and the surrounding sedimentary rocks were studied.

The Maiyumerak Mountains were studied in order to evaluate the lithologic variation within volcanic rocks. Sheeted dikes, a major component of ophiolites not previously recognized in the Brooks Range, were mapped here by us during this field season.

The Avan Hills ophiolite was studied because of its extensive exposure of ultramafic rock and metamorphic rock. Sections of layered ultramafic cumulates and gabbros were measured in order to compare them with the sections measured at Asik Mountain.

GEOLOGIC SAMPLE DATA

Listed in this Appendix, from left to right, are the Cornell sample number, U.S. Park Service sample number, lithology, geologic unit, latitude and longitude of sample location, and a brief description of the sample location.

Cornell Samples are labeled with a two letter location code, a sample number, and the year collected. Sample location abbreviations are: Avan Hills=AH, Asik Mountain=AM, and Maiyumerak Mountains=MM. If two different samples were collected from the same location, then an "a,b, c,d..." is added to the sample number. U.S. Park Service sample numbers consist of an accession number and a sample number. All the samples have been labeled consecutively in this system.

Rock names in the Appendix are based solely on field classification. Whenever possible, the geologic unit that the rock was collected from is also given. Map units given in the Appendix are the same as those used by Curtis et al. (1983), Gottschalk (1987), and Mull (1985). Abbreviations for the map units are given below:

<u>Unit</u>	<u>Formation/Age</u>	<u>Unit</u>	<u>Formation/Age</u>
QTb	Quaternary-Tertiary Basalt	MDk	Kanayut Conglomerate
Kg	Cretaceous Granite	Mke	" " (Ear Peak Member)
Ko	Okpikruak Formation	Dn	Noatak Sandstone
Kn	Nanushuk Group	Dhcp	Beaucoup Formation
Kfm	Fortress Mtn. Formation	Dhf	Hunt Fork Shale
Kpc	Prince Creek Formation	Dg	Devonian(?) Gabbro
Ksc	Albian-Cenamon. Congl. (sed. clasts)	Dgr	Dev.(?) Granite Gneiss
Kic	Albian Conglomerate (ign. clasts)	Dms	Dev.(?) Metasediments
Jg	Jurassic Gabbro (ophiolitic)	Dwfv	Whiteface Volcanics
Ju	Jurassic Ultramafic Rocks (ophiolitic)	Pzg	Paleozoic(?) Gabbro
JPm	Ipsnavik Diabase Dikes and Sills	Pze	Paleozoic(?) Eclogite
MzPzv	Mesozoic-Paleozoic Basalts	PzPr	Paleo-PreC(?) Meta.
Mk	Kayak Shale	PzPqs	Paleo.-PreC(?) Schist
MDl	Mississippian-Devonian Limestone		

The latitude and longitude of the sample locations were determined by digitizing sample locations from U.S.G.S. 15' and 2° topographic maps. The locations are reported in decimal fractions of degrees.

Sample #	USPS #	Lithology	Unit	Lat. (°)	Long. (°)	Location
AH-1-85	#25-401	alt. vein in gab.	Jg	68.2521	161.6839	NE Avan Hills
AH-2-85	#25-402	alt. vein in gab.	Jg	68.2522	161.6839	NE Avan Hills
AH-3-85	#25-403	gabbro	Jg	68.2522	161.6839	NE Avan Hills
AH-4-85	#25-404	gabbro	Jg	68.2521	161.6839	NE Avan Hills
AH-5-85	#25-405	sheared gabbro	Jg	68.2521	161.6839	NE Avan Hills
AH-6-85	#25-406	gabbro	Jg	68.2533	161.6829	NE Avan Hills
AH-7-85	#25-407	leuco gabbro	Jg	68.2533	161.6829	NE Avan Hills
AH-8-85	#25-408	red gabbro	Jg	68.2533	161.6829	NE Avan Hills
AH-9-85	#25-409	melano gabbro	Jg	68.2532	161.6830	NE Avan Hills
AH-10-85	#25-410	anorthosite dike	Jg	68.2532	161.6830	NE Avan Hills
AH-11-85	#25-411	anorthosite dike	Jg	68.2532	161.6830	NE Avan Hills
AH-12-85	#25-412	ol-clinopyroxenite	Jg	68.2550	161.6942	NE Avan Hills
AH-13-85	#25-413	ol-gabbro	Jg	68.2549	161.6942	NE Avan Hills
AH-14-85	#25-414	lineated ol-gabbro	Jg	68.2549	161.6942	NE Avan Hills
AH-15-85	#25-415	lin. ol-clinopyrox.	Jg	68.2549	161.6949	NE Avan Hills
AH-16-85	#25-416	cpx vein in dunite	Jg	68.2548	161.6965	NE Avan Hills
AH-17-85	#25-417	wehrlite	Jg	68.2548	161.6965	NE Avan Hills
AH-18-85	#25-418	lineated wehrlite	Jg	68.2548	161.6965	NE Avan Hills
AH-19-85	#25-419	foliated wehrlite	Jg	68.2548	161.6965	NE Avan Hills
AH-20-85	#25-420	wehrlite	Jg	68.2548	161.6967	NE Avan Hills
AH-21-85	#25-421	troctolite	Jg	68.2549	161.6965	NE Avan Hills
AH-21a-85	#25-422	gabbro	Jg	68.2565	161.6956	NE Avan Hills
AH-22-85	#25-423	gabbo	Jg	68.2565	161.6952	NE Avan Hills
AH-23-85	#25-424	lineated pyrox.	Jg	68.2565	161.6949	NE Avan Hills
AH-24-85	#25-425	clinopyroxenite	Jg	68.2549	161.7012	NE Avan Hills
AH-25-85	#25-426	dunite-wehrlite	Jg	68.2549	161.7012	NE Avan Hills
AH-26-85	#25-427	gabbro	Jg	68.2549	161.7012	NE Avan Hills
AH-27-85	#25-428	dunite-wehrlite	Jg	68.2541	161.7053	NE Avan Hills
AH-28-85	#25-429	coarse basalt	MzPzv	68.2659	161.7688	NE Avan Hills
AH-29-85	#25-430	fine basalt	MzPzv	68.2659	161.7691	NE Avan Hills
AH-30-85	#25-431	veined basalt	MzPzv	68.2659	161.7691	NE Avan Hills
AH-31-85	#25-432	coarse basalt	MzPzv	68.2658	161.7691	NE Avan Hills
AH-32-85	#25-433	meta basalt	MzPzv	68.2658	161.7694	NE Avan Hills
AH-33-85	#25-434	veined dunite	Ju	68.2658	161.7694	NE Avan Hills
AH-34-85	#25-435	sheared basalt	MzPzv	68.2636	161.7628	NE Avan Hills
AH-35-85	#25-436	carbonate		68.2636	161.7630	NE Avan Hills
AH-36-85	#25-437	basalt	MzPzv	68.2636	161.7630	NE Avan Hills
AH-37-85	#25-438	carbonate		68.2636	161.7630	NE Avan Hills
AH-38-85	#25-439	carbonate/phyllite		68.2636	161.7630	NE Avan Hills
AH-39-85	#25-440	carbonate/phyllite		68.2636	161.7631	NE Avan Hills
AH-40-85	#25-441	carbonate/phyllite		68.2635	161.7631	NE Avan Hills
AH-41-85	#25-442	phyllite		68.2635	161.7630	NE Avan Hills
AH-42-85	#25-443	basalt	MzPzv	68.2635	161.7631	NE Avan Hills
AH-43-85	#25-444	carbonate/phyllite		68.2636	161.7631	NE Avan Hills
AH-44-85	#25-445	basalt	MzPzv	68.2635	161.7631	NE Avan Hills

Sample #	USPS #	Lithology	Unit	Lat. (°)	Long. (°)	Location
AH-45-85	#25-446	basalt	MzPzv	68.2627	161.7597	NE Avan Hills
AH-46-85	#25-447	basalt	MzPzv	68.2627	161.7597	NE Avan Hills
AH-47-85	#25-448	carbonate		68.2627	161.7597	NE Avan Hills
AH-48-85	#25-449	basalt	MzPzv	68.2628	161.7597	NE Avan Hills
AH-49-85	#25-450	chert	MzPzv	68.2628	161.7597	NE Avan Hills
AH-50-85	#25-451	basalt	MzPzv	68.2628	161.7597	NE Avan Hills
AH-51-85	#25-452	basalt	MzPzv	68.2628	161.7598	NE Avan Hills
AH-52-85	#25-453	basalt	MzPzv	68.2629	161.7598	NE Avan Hills
AH-53-85	#25-454	basalt	MzPzv	68.2629	161.7598	NE Avan Hills
AH-54-85	#25-455	basalt	MzPzv	68.2629	161.7598	NE Avan Hills
AH-55-85	#25-456	chert	MzPzv	68.2602	161.7474	NE Avan Hills
AH-56-85	#25-457	basalt	MzPzv	68.2602	161.7474	NE Avan Hills
AH-57-85	#25-458	basalt	MzPzv	68.2602	161.7474	NE Avan Hills
AH-58-85	#25-459	basalt	MzPzv	68.2602	161.7472	NE Avan Hills
AH-59-85	#25-460	basalt	MzPzv	68.2602	161.7472	NE Avan Hills
AH-60-85	#25-461	basalt	MzPzv	68.2602	161.7472	NE Avan Hills
AH-61-85	#25-462	basalt	MzPzv	68.2602	161.7474	NE Avan Hills
AH-62-85	#25-463	basalt	MzPzv	68.2602	161.7474	NE Avan Hills
AH-63-85	#25-464	foliated basalt	MzPzv	68.2602	161.7476	NE Avan Hills
AH-64-85	#25-465	basalt	MzPzv	68.2602	161.7474	NE Avan Hills
AH-65-85	#25-466	basalt	MzPzv	68.2633	161.7459	NE Avan Hills
AH-66-85	#25-467	basalt	MzPzv	68.2633	161.7459	NE Avan Hills
AH-67-85	#25-468	basalt	MzPzv	68.2633	161.7459	NE Avan Hills
AH-68-85	#25-469	basalt	MzPzv	68.2633	161.7459	NE Avan Hills
AH-69-85	#25-470	basalt	MzPzv	68.2633	161.7459	NE Avan Hills
AH-70-85	#25-471	veined serpentinite	Ju	68.2652	161.7353	NE Avan Hills
AH-71-85	#25-472	spinel layer	Ju	68.2672	161.7384	NE Avan Hills
AH-72-85	#25-473	basalt	MzPzv	68.2672	161.7382	NE Avan Hills
AH-73-85	#25-474	metasediment	MzPzv	68.2672	161.7382	NE Avan Hills
AH-74a-85	#25-475	metasediment	MzPzv	68.2672	161.7382	NE Avan Hills
AH-74b-85	#25-476	metasediment	MzPzv	68.2686	161.7333	NE Avan Hills
AH-75-85	#25-477	serp. dunite	Ju	68.2686	161.7333	NE Avan Hills
AH-76-85	#25-478	serpentinite	Ju	68.2686	161.7333	NE Avan Hills
AH-77-85	#25-479	serpentinite	Ju	68.2686	161.7333	NE Avan Hills
AH-78-85	#25-480	serpentinite	Ju	68.2686	161.7333	NE Avan Hills
AH-79-85	#25-481	basalt	MzPzv	68.2686	161.7333	NE Avan Hills
AH-80-85	#25-482	basalt	MzPzv	68.2687	161.7333	NE Avan Hills
AH-81-85	#25-483	basalt	MzPzv	68.2686	161.7333	NE Avan Hills
AH-82-85	#25-484	veined basalt	MzPzv	68.2695	161.7365	NE Avan Hills
AH-83-85	#25-485	vesicular basalt	MzPzv	68.2696	161.7362	NE Avan Hills
AH-84-85	#25-486	basalt	MzPzv	68.2696	161.7362	NE Avan Hills
AH-85-85	#25-487	basalt	MzPzv	68.2692	161.7452	NE Avan Hills
AH-86-85	#25-488	gabbro	Jg	68.2692	161.7466	NE Avan Hills
AH-87-85	#25-489	basalt	MzPzv	68.2690	161.7487	NE Avan Hills
AH-88-85	#25-490	basalt	MzPzv	68.2688	161.7499	NE Avan Hills
AH-89-85	#25-491	diabase	MzPzv	68.2685	161.7520	NE Avan Hills
AH-90-85	#25-492	diabase	MzPzv	68.2682	161.7541	NE Avan Hills

Sample #	USPS #	Lithology	Unit	Lat. (°)	Long. (°)	Location
AH-91-85	#25-493	diabase	MzPzv	68.2677	161.7555	NE Avan Hills
AH-92-85	#25-494	diorite	MzPzv	68.2672	161.7571	NE Avan Hills
AH-93-85	#25-495	leuco diorite	MzPzv	68.2667	161.7577	NE Avan Hills
AH-94-85	#25-496	diorite	MzPzv	68.2663	161.7583	NE Avan Hills
AH-95-85	#25-497	diorite	MzPzv	68.2658	161.7584	NE Avan Hills
AH-96-85	#25-498	diorite	MzPzv	68.2599	161.7445	NE Avan Hills
AH-97-85	#25-499	dunite	Ju	68.2595	161.7396	NE Avan Hills
AH-98-85	#25-501	dunite	Ju	68.2595	161.7396	NE Avan Hills
AH-99-85	#25-502	veined dun.-spin.	Ju	68.2595	161.7399	NE Avan Hills
AH-100-85	#25-503	sheared clinopyrox	Ju	68.2593	161.7330	NE Avan Hills
AH-101-85	#25-504	sheared clinopyrox	Ju	68.2594	161.7330	NE Avan Hills
AH-102-85	#25-505	veined serp.	Ju	68.2593	161.7330	NE Avan Hills
AH-103-85	#25-506	clinopyroxenite	Ju	68.2598	161.7225	NE Avan Hills
AH-104-85	#25-507	wehrlite	Ju	68.2599	161.7224	NE Avan Hills
AH-105-85	#25-508	dunite	Ju	68.2599	161.7224	NE Avan Hills
AH-106-85	#25-509	clinopyroxenite	Ju	68.2512	161.7428	NE Avan Hills
AH-107-85	#25-510	clinopyroxenite	Ju	68.2512	161.7428	NE Avan Hills
AH-108-85	#25-511	dunite	Ju	68.2512	161.7430	NE Avan Hills
AH-109-85	#25-512	basalt	MzPzv	68.2514	161.7512	NE Avan Hills
AH-110-85	#25-513	basalt	MzPzv	68.2514	161.7512	NE Avan Hills
AH-111-85	#25-514	basalt	MzPzv	68.2514	161.7512	NE Avan Hills
AH-112-85	#25-515	carbonate		68.2534	161.7589	NE Avan Hills
AH-113-85	#25-516	basalt	MzPzv	68.2535	161.7589	NE Avan Hills
AH-114-85	#25-517	foliated basalt	MzPzv	68.2535	161.7589	NE Avan Hills
AH-115-85	#25-518	carbonate		68.2535	161.7592	NE Avan Hills
AH-116-85	#25-519	carbonate		68.2535	161.7592	NE Avan Hills
AH-117-85	#25-520	carbonate		68.2535	161.7592	NE Avan Hills
AH-118-85	#25-521	wacke	Ko	68.2724	161.7964	Upper Avan River
AH-119-85	#25-522	wacke	Ko	68.2724	161.7964	Upper Avan River
AH-120-85	#25-523	chert	MzPzv	68.2750	161.7995	Upper Avan River
AH-121-85	#25-524	biotite schist	MzPzv	68.2764	161.8058	Upper Avan River
AH-122-85	#25-525	biotite schist	MzPzv	68.2764	161.8055	Upper Avan River
AH-123-85	#25-526	biotite schist	MzPzv	68.2764	161.8057	Upper Avan River
AH-124-85	#25-527	biotite schist	MzPzv	68.2764	161.8057	Upper Avan River
AH-125-85	#25-528	biotite schist	MzPzv	68.2764	161.8057	Upper Avan River
AH-126-85	#25-529	biotite schist	MzPzv	68.2764	161.8057	Upper Avan River
AH-127-85	#25-530	biotite schist	MzPzv	68.2764	161.8057	Upper Avan River
AH-128-85	#25-531	biotite schist	MzPzv	68.2764	161.8057	Upper Avan River
AH-129-85	#25-532	biotite schist	MzPzv	68.2764	161.8057	Upper Avan River
AH-130-85	#25-533	layered metased.	MzPzv	68.2765	161.8057	Upper Avan River
AH-131-85	#25-534	layered metased.	MzPzv	68.2764	161.8057	Upper Avan River
AH-132-85	#25-535	layered metased.	MzPzv	68.2764	161.8057	Upper Avan River
AH-133-85	#25-536	layered metased.	MzPzv	68.2764	161.8057	Upper Avan River
AH-134-85	#25-537	layered metased.	MzPzv	68.2764	161.8057	Upper Avan River
AH-135-85	#25-538	biotite monzodior.	MzPzv	68.2764	161.8057	Upper Avan River
AH-136-85	#25-539	serpentinite	MzPzv	68.2765	161.8057	Upper Avan River

Sample #	USPS #	Lithology	Unit	Lat. (°)	Long. (°)	Location
AH-137-85	#25-540	melano gabbro	Jg	68.2718	161.8104	Upper Avan River
AH-138-85	#25-541	melano gabbro	Jg	68.2718	161.8105	Upper Avan River
AH-139-85	#25-542	gabbro	Jg	68.2718	161.8105	Upper Avan River
AH-140-85	#25-543	leuco gabbro	Jg	68.2718	161.8105	Upper Avan River
AH-141-85	#25-544	gabbro	Jg	68.2718	161.8105	Upper Avan River
AH-142-85	#25-545	diorite ?	Jg	68.2718	161.8105	Upper Avan River
AH-143-85	#25-546	gabbro	Jg	68.2718	161.8105	Upper Avan River
AH-144-85	#25-547	gabbro	Jg	68.2718	161.8105	Upper Avan River
AH-145-85	#25-548	anorthosite	Jg	68.2568	161.7889	N-central Avan Hills
AH-146-85	#25-549	basalt	MzPzv	68.2575	161.7941	N-central Avan Hills
AH-147-85	#25-550	basalt	MzPzv	68.2421	161.8275	N-central Avan Hills
AH-148-85	#25-551	basalt	MzPzv	68.2421	273.0000	N-central Avan Hills
AH-149-85	#25-552	basalt	MzPzv	68.2421	161.8273	N-central Avan Hills
AH-150-85	#25-553	metasediment	MzPzv	68.2362	161.8277	N-central Avan Hills
AH-151-85	#25-554	biotite schist	MzPzv	68.2363	161.8277	N-central Avan Hills
AH-152-85	#25-555	biotite schist	MzPzv	68.2363	161.8277	N-central Avan Hills
AH-153-85	#25-556	biotite schist	MzPzv	68.2363	161.8277	N-central Avan Hills
AH-154-85	#25-557	biotite schist	MzPzv	68.2363	161.8277	N-central Avan Hills
AH-155-85	#25-558	metasediment	MzPzv	68.2363	161.8277	N-central Avan Hills
AH-156-85	#25-559	foliated basalt	MzPzv	68.2363	161.8277	N-central Avan Hills
AH-157-85	#25-560	biotite schist	MzPzv	68.2363	161.8275	N-central Avan Hills
AH-158-85	#25-561	biotite schist	MzPzv	68.2363	161.8275	N-central Avan Hills
AH-159-85	#25-562	biotite schist	MzPzv	68.2363	161.8275	N-central Avan Hills
AH-160-85	#25-563	biotite schist	MzPzv	68.2363	161.8277	N-central Avan Hills
AH-161-85	#25-564	bio. schist breccia	MzPzv	68.2363	161.8275	N-central Avan Hills
AH-162-85	#25-565	anatectic? dike	MzPzv	68.2363	161.8277	N-central Avan Hills
AH-163-85	#25-566	veined dunite	Ju	68.2363	161.8277	N-central Avan Hills
AH-164-85	#25-567	gab. breccia float	Jg	68.2363	161.8277	N-central Avan Hills
AH-164a-85	#25-568	biotite schist	MzPzv	68.2363	161.8483	N-central Avan Hills
AH-166-85	#25-569	dunite	Ju	68.2383	161.8481	N-central Avan Hills
AH-167-85	#25-570	serp w/ spinel	Ju	68.2383	161.8481	N-central Avan Hills
AH-168-85	#25-571	harzburgite?	Ju	68.2383	161.8481	N-central Avan Hills
AH-169-85	#25-572	dunite	Ju	68.2383	161.8481	N-central Avan Hills
AH-170-85	#25-573	dunite	Ju	68.2286	161.8495	N-central Avan Hills
AH-171-85	#25-574	dunite	Ju	68.2286	161.8493	N-central Avan Hills
AH-172-85	#25-575	dunite w/ spinel	Ju	68.2286	161.8493	N-central Avan Hills
AH-173-85	#25-576	serpentine	Ju	68.2487	161.8037	N-central Avan Hills
AH-174-85	#25-577	dunite w/ spinel	Ju	68.2518	161.7283	NE Avan Hills
AH-175-85	#25-578	dunite	Ju	68.2518	161.7283	NE Avan Hills
AH-176-85	#25-579	dunite	Ju	68.2518	161.7284	NE Avan Hills
AH-177-85	#25-580	dun w/ cpx vein	Ju	68.2517	161.7255	NE Avan Hills
AH-178-85	#25-581	clinopyroxenite	Ju	68.2517	161.7255	NE Avan Hills
AH-179-85	#25-582	clinopyroxenite	Ju	68.2517	161.7255	NE Avan Hills
AH-180-85	#25-583	dunite	Ju	68.2517	161.7258	NE Avan Hills
AH-181-85	#25-584	dunite	Ju	68.2516	161.7228	NE Avan Hills

Sample #	USPS #	Lithology	Unit	Lat. (°)	Long. (°)	Location
AH-182-85	#25-585	spinel layer	Ju	68.2516	161.7228	NE Avan Hills
AH-183-85	#25-586	dunite w/ spinel	Ju	68.2498	161.7242	NE Avan Hills
AH-184-85	#25-587	clinopyroxenite	Ju	68.2499	161.7242	NE Avan Hills
AH-185-85	#25-588	wehrlite	Ju	68.2498	161.7244	NE Avan Hills
AH-186-85	#25-589	dunite	Ju	68.2489	161.7242	NE Avan Hills
AH-187-85	#25-590	clinopyroxenite	Ju	68.2489	161.7238	NE Avan Hills
AH-188-85	#25-591	clinopyroxenite	Ju	68.2489	161.7238	NE Avan Hills
AH-189-85	#25-592	clinopyroxenite	Ju	68.2489	161.7238	NE Avan Hills
AH-190-85	#25-593	clinopyroxenite	Ju	68.2489	161.7238	NE Avan Hills
AH-191-85	#25-594	clinopyroxenite	Ju	68.2489	161.7236	NE Avan Hills
AH-192-85	#25-595	clinopyroxenite	Ju	68.2489	161.7238	NE Avan Hills
AH-193-85	#25-596	clinopyroxenite	Ju	68.2456	161.7330	NE Avan Hills
AH-194-85	#25-597	wehlite	Ju	68.2456	161.7330	NE Avan Hills
AH-195-85	#25-598	dunite	Ju	68.2456	161.7330	NE Avan Hills
AH-196-85	#25-599	dunite	Ju	68.2456	161.7330	NE Avan Hills
AH-197-85	#25-601	dunite	Ju	68.2456	161.7330	NE Avan Hills
AH-198-85	#25-602	clinopyroxenite	Ju	68.2439	161.7429	NE Avan Hills
AH-199-85	#25-603	dunite	Ju	68.2439	161.7429	NE Avan Hills
AH-200-85	#25-604	dunite	Ju	68.2439	161.7429	NE Avan Hills
AH-201-85	#25-605	troctolite	Ju	68.2439	161.7429	NE Avan Hills
AH-202-85	#25-606	dunite	Ju	68.2439	161.7429	NE Avan Hills
AH-203-85	#25-607	zeolites?	Ju	68.2459	161.7513	NE Avan Hills
AH-204-85	#25-608	dunnite w/ spinel	Ju	68.2459	161.7513	NE Avan Hills
AH-205-85	#25-609	spinel layer	Ju	68.2459	161.7513	NE Avan Hills
AH-206-85	#25-610	dunite w/ spinel	Ju	68.2469	161.7542	NE Avan Hills
AH-207-85	#25-611	serpentinite	Ju	68.2470	161.7543	NE Avan Hills
AH-208-85	#25-612	serpentinite	Ju	68.2470	161.7546	NE Avan Hills
AH-209-85	#25-613	serpentinite	Ju	68.2470	161.7546	NE Avan Hills
AH-210-85	#25-614	serpentinite	Ju	68.2470	161.7550	NE Avan Hills
AH-211-85	#25-615	serpentinite	Ju	68.2470	161.7553	NE Avan Hills
AH-212-85	#25-616	metasediment	MzPzv	68.2471	161.7555	NE Avan Hills
AH-213-85	#25-617	gabbro	Jg	68.2471	161.7557	NE Avan Hills
AH-214-85	#25-618	gabbro	Jg	68.2471	161.7557	NE Avan Hills
AH-215-85	#25-619	foliated gabbro	Jg	68.2472	161.7561	NE Avan Hills
AH-216-85	#25-620	biotite schist	MzPzv	68.2472	161.7563	NE Avan Hills
AH-217-85	#25-621	biotite schist	MzPzv	68.2473	161.7565	NE Avan Hills
AH-218-85	#25-622	biotite schist	MzPzv	68.2473	161.7567	NE Avan Hills
AH-219-85	#25-623	biotite schist	MzPzv	68.2473	161.7569	NE Avan Hills
AH-220-85	#25-624	metasediment	MzPzv	68.2474	161.7569	NE Avan Hills
AH-221-85	#25-625	metasediment	MzPzv	68.2474	161.7571	NE Avan Hills
AH-222-85	#25-626	metasediment	MzPzv	68.2475	161.7573	NE Avan Hills
AH-223-85	#25-627	biotite schist	MzPzv	68.2475	161.7575	NE Avan Hills
AH-224-85	#25-628	biotite schist	MzPzv	68.2476	161.7576	NE Avan Hills
AH-225-85	#25-629	metasediment	MzPzv	68.2476	161.7576	NE Avan Hills
AH-226-85	#25-630	biotite schist	MzPzv	68.2476	161.7580	NE Avan Hills

Sample #	USPS #	Lithology	Unit	Lat. (°)	Long. (°)	Location
AM-1-85	#25-659	melano gabbro	Jg	67.4685	162.3168	East Asik Mtn
AM-2-85	#25-660	gabbro	Jg	67.4684	162.3168	East Asik Mtn
AM-3-85	#25-661	tect. gabbro	Jg	67.4685	162.3168	East Asik Mtn
AM-4-85	#25-662	fine gr. gabbro	Jg	67.4685	162.3168	East Asik Mtn
AM-5-85	#25-663	coarse gabbro	Jg	67.4685	162.3168	East Asik Mtn
AM-6-85	#25-664	foliated gabbro	Jg	67.4685	162.3168	East Asik Mtn
AM-7-85	#25-665	wehrlite	Jg	67.4688	162.3189	East Asik Mtn
AM-8-85	#25-666	foliated gabbro	Jg	67.4688	162.3191	East Asik Mtn
AM-9-85	#25-667	fol. leuco gabbro	Jg	67.4685	162.3216	East Asik Mtn
AM-10-85	#25-668	2?-pyx. gabbro	Jg	67.4667	162.3342	Asik Mtn.
AM-11-85	#25-669	2?-pyx. gabbro	Jg	67.4668	162.3345	Asik Mtn.
AM-12-85	#25-670	gabbro	Jg	67.4667	162.3416	Asik Mtn.
AM-13-85	#25-671	horn. in mylonite	Jg	67.4667	162.3416	Asik Mtn.
AM-14-85	#25-672	anorthosite	Jg	67.4662	162.3442	Asik Mtn.
AM-15-85	#25-673	2?-pyx. gabbro	Jg	67.4662	162.3442	Asik Mtn.
AM-16-85	#25-674	gabbro	Jg	67.4663	162.3469	Asik Mtn.
AM-17-85	#25-675	2?-pyx. gabbro	Jg	67.4664	162.3482	Asik Mtn.
AM-18-85	#25-676	layered gabbro	Jg	67.4679	162.3543	Asik Mtn.
AM-19-85	#25-677	gabbro	Jg	67.4709	162.3576	Asik Mtn.
AM-20-85	#25-678	ol-clinopyroxenite	Jg	67.4697	162.3235	East Asik Mtn.
AM-21-85	#25-679	coarse gabbro	Jg	67.4697	162.3232	East Asik Mtn.
AM-22-85	#25-680	olivine gabbro	Jg	67.4637	162.3622	Asik Mtn.
AM-23-85	#25-681	wehrlite	Jg	67.4643	162.3599	Asik Mtn.
AM-24-85	#25-682	leuco gabbro	Jg	67.4617	162.3561	Asik Mtn.
AM-25-85	#25-683	chert	JPm	67.4569	162.1590	East Asik Mtn.
AM-26-85	#25-684	chert	JPm	67.4556	162.3120	East Asik Mtn.
AM-27-85	#25-685	chert	JPm	67.4540	162.3115	East Asik Mtn.
AM-28-85	#25-686	diabase	JPm	67.4560	162.2991	Asik Mtn-Agie R.
AM-29-85	#25-687	diabase	JPm	67.4604	162.3031	Asik Mtn-Agie R.
AM-30-85	#25-688	diabase	JPm	67.4626	162.3000	Asik Mtn-Agie R.
AM-31-85	#25-689	diabase	JPm	67.4626	162.2998	Asik Mtn-Agie R.
AM-32-85	#25-690	diabase	JPm	67.4660	162.2995	Asik Mtn-Agie R.
AM-33-85	#25-691	carbonate		67.4550	162.2945	Asik Mtn-Agie R.
AM-34-85	#25-692	carbonate		67.4493	162.2910	Asik Mtn-Agie R.
AM-35-85	#25-693	carbonate		67.4462	162.2857	Asik Mtn-Agie R.
AM-36-85	#25-694	siltstone		67.4462	162.2857	Asik Mtn-Agie R.
AM-37-85	#25-695	fossil. carbonate		67.4463	162.2857	Asik Mtn-Agie R.
AM-38-85	#25-696	carbonate		67.4574	162.2708	Asik Mtn-Agie R.
AM-39-85	#25-697	horn. gabbro dike	Jg	67.4599	162.3502	Asik Mtn.
AM-40-85	#25-698	wehrlite	Jg	67.4599	162.3504	Asik Mtn.
AM-41-85	#25-699	wehrlite	Jg	67.4599	162.3502	Asik Mtn.
AM-42-85	#25-701	troctolite	Jg	67.4591	162.3544	Asik Mtn.
AM-43-85	#25-702	gabbro	Jg	67.4591	162.3544	Asik Mtn.
AM-44-85	#25-703	gabbro	Jg	67.4592	162.3544	Asik Mtn.
AM-45-85	#25-704	gabbro	Jg	67.4591	162.3544	Asik Mtn.

Sample #	USPS #	Lithology	Unit	Lat. (°)	Long. (°)	Location
AM-46-85	#25-705	gabbro	Hg	67.4591	162.3544	Asik Mtn.
AM-47-85	#25-706	layered gabbro	Jg	67.4605	162.3603	Asik Mtn.
AM-48-85	#25-707	layered gabbro	Jg	67.4605	162.3601	Asik Mtn.
AM-49-85	#25-708	layered gabbro	Jg	67.4605	162.3603	Asik Mtn.
AM-50-85	#25-709	mafic dike	Jg	67.4605	162.3603	Asik Mtn.
AM-51a-85	#25-710	gabbro	Jg	67.4608	162.3643	Asik Mtn.
AM-51b-85	#25-711	layered gabbro	Jg	67.4608	162.3639	Asik Mtn.
AM-52a-85	#25-712	layered gabbro	Jg	67.4608	162.3639	Asik Mtn.
AM-52b-85	#25-713	layered gabbro	Jg	67.4608	162.3639	Asik Mtn.
AM-53a-85	#25-714	layered gabbro	Jg	67.4608	162.3639	Asik Mtn.
AM-53b-85	#25-715	layered gabbro	Jg	67.4608	162.3639	Asik Mtn.
AM-54-85	#25-716	leuco gabbro	Jg	67.4657	162.3629	Asik Mtn.
AM-55-85	#25-717	leuco gabbro	Jg	67.4657	162.3629	Asik Mtn.
AM-58-85	#25-718	chert	JPm	67.4713	162.3015	NE Asik Mtn.
AM-59-85	#25-719	diabase	JPm	67.4713	162.3015	NE Asik Mtn.
AM-60-85	#25-720	chert	JPm	67.4713	162.3015	NE Asik Mtn.
AM-61-85	#25-721	chert	JPm	67.4700	162.3040	NE Asik Mtn.
AM-68-85	#25-722	chert	JPm	67.4776	162.3040	NE Asik Mtn.
AM-69-85	#25-723	sheared metavolc.	MzPzv	67.4776	162.3040	NE Asik Mtn.
AM-70-85	#25-724	sheared metased.	MzPzv	67.4800	162.3107	NE Asik Mtn.
AM-71-85	#25-725	sheared gabbro	Jg	67.4864	162.3090	NE Asik Mtn.
AM-72-85	#25-726	chert	JPm	67.4861	162.3075	NE Asik Mtn.
AM-73-85	#25-727	chert	JPm	67.4858	162.3064	NE Asik Mtn.
AM-74-85	#25-728	mafic schist	JPm	67.4852	162.3047	NE Asik Mtn.
AM-75-85	#25-729	diabase	JPm	67.4850	162.3032	NE Asik Mtn.
AM-76-85	#25-730	foliated diabase	JPm	67.4846	162.3015	NE Asik Mtn.
AM-77-85	#25-731	carbonate		67.4872	162.2907	NE Asik Mtn.
AM-78-85	#25-732	carbonate		67.4872	162.2907	NE Asik Mtn.
AM-79-85	#25-733	wacke	Ko	67.4872	162.2907	NE Asik Mtn.
AM-80-85	#25-734	wacke	Ko	67.4872	162.2905	NE Asik Mtn.
AM-81-85	#25-735	carbonate		67.4874	162.2784	NE Asik Mtn.
AM-82-85	#25-736	chert	JPm	67.4700	162.3098	NE Asik Mtn.
AM-83-85	#25-737	diabase	JPm	67.4721	162.3057	NE Asik Mtn.
AM-84-85	#25-738	foliated diabase	JPm	67.4728	162.3050	NE Asik Mtn.
AM-85-85	#25-739	foliated diabase	JPm	67.4728	162.3051	NE Asik Mtn.
AM-86-85	#25-740	foliated diabase	JPm	67.4727	162.3066	NE Asik Mtn.
AM-87-85	#25-741	foliated diabase	JPm	67.4726	162.3069	NE Asik Mtn.
AM-88-85	#25-742	chert	JPm	67.4751	162.3045	NE Asik Mtn.
AM-89-85	#25-743	chert	JPm	67.4751	162.3045	NE Asik Mtn.
AM-90a-85	#25-744	lin. & fol. gab.	Jg	67.4742	162.3056	NE Asik Mtn.
AM-90b-85	#25-745	lin. & fol. gab.	Jg	67.4742	162.3056	NE Asik Mtn.
AM-90c-85	#25-746	lin. & fol. gab.	Jg	67.4742	162.3056	NE Asik Mtn.
AM-91-85	#25-747	plagiogranite	Jg	67.4470	162.3632	SW Asik Mtn.
AM-92-85	#25-748	fol. plagiogranite	Jg	67.4470	162.3634	SW Asik Mtn.
AM-93-85	#25-749	fol. plagiogranite	Jg	67.4470	162.3634	SW Asik Mtn.

Sample #	USPS #	Lithology	Unit	Lat. (°)	Long. (°)	Location
AM-94-85	#25-750	sandstone boulder		67.4452	162.3915	SW Asik Mtn.
AM-95-85	#25-751	horn. plagiogranite	Jg	67.4452	162.3913	SW Asik Mtn.
AM-96-85	#25-752	gabbro	Jg	67.4378	162.4432	SW Asik Mtn.
AM-97-85	#25-753	troctolite	Jg	67.4378	162.4430	SW Asik Mtn.
AM-98-85	#25-754	gabbro	Jg	67.4394	162.4474	SW Asik Mtn.
AM-99-85	#25-755	wehrlite	Jg	67.4428	162.4411	SW Asik Mtn.
AM-100-85	#25-756	dunite	Jg	67.4428	162.4411	SW Asik Mtn.
AM-101-85	#25-757	dunite	Jg	67.4428	162.4411	SW Asik Mtn.
AM-102-85	#25-758	gabbro	Jg	67.4457	162.4444	SW Asik Mtn.
AM-103-85	#25-759	gabbro	Jg	67.4457	162.4445	SW Asik Mtn.
AM-104-85	#25-760	clinopyroxenite	Jg	67.4470	162.4402	SW Asik Mtn.
AM-105-85	#25-761	clinopyroxenite	Jg	67.4469	162.4402	SW Asik Mtn.
AM-106-85	#25-762	gabbro	Jg	67.4520	162.4160	SW Asik Mtn.
AM-107-85	#25-763	gabbro	Jg	67.4520	162.4160	SW Asik Mtn.
AM-108-85	#25-764	qtzte. boulder	Jg	67.4519	162.3999	SW Asik Mtn.
AM-109-85	#25-765	gabbro	Jg	67.4525	162.3867	SW Asik Mtn.
AM-110-85	#25-766	gabbro	Jg	67.4317	162.4562	SW of Asik Mtn.
AM-111-85	#25-767	gabbro	Jg	67.4317	162.4560	SW of Asik Mtn.
AM-112-85	#25-768	gabbro	Jg	67.4317	162.4560	SW of Asik Mtn.
AM-113-85	#25-769	clinopyroxenite	Ju	67.4265	162.6580	SW of Asik Mtn.
AM-114-85	#25-770	clinopyroxenite	Ju	67.4265	162.4658	SW of Asik Mtn.
AM-115-85	#25-771	clinopyroxenite	Ju	67.4265	162.4658	SW of Asik Mtn.
AM-116-85	#25-772	serp. dunite	Ju	67.4242	162.4678	SW of Asik Mtn.
AM-117-85	#25-773	dunite w/ spinel	Ju	67.4243	162.4674	SW of Asik Mtn.
AM-118-85	#25-774	clinopyroxenite	Ju	67.4242	162.4674	SW of Asik Mtn.
AM-119-85	#25-775	dunite	Ju	67.4224	162.4694	SW of Asik Mtn.
AM-120-85	#25-776	wehrlite	Ju	67.4225	162.4692	SW of Asik Mtn.
AM-121-85	#25-777	dunite	Ju	67.4210	162.4730	SW of Asik Mtn.
AM-122-85	#25-778	clinopyroxenite	Ju	67.4211	162.4730	SW of Asik Mtn.
AM-123-85	#25-779	clinopyroxenite	Ju	67.4193	162.4774	SW of Asik Mtn.
AM-124-85	#25-780	wehrlite	Ju	67.4193	162.4776	SW of Asik Mtn.
AM-125-85	#25-781	layered gabbro	Ju	67.4171	162.4786	SW of Asik Mtn.
AM-126-85	#25-782	troctolite	Ju	67.4153	162.4838	SW of Asik Mtn.
AM-127-85	#25-783	dunite	Ju	67.4110	162.4821	SW of Asik Mtn.
AM-128-85	#25-784	layered gabbro	Ju	67.4038	162.4823	SW of Asik Mtn.
AM-129-85	#25-785	clinopyroxenite	Ju	67.4036	162.4853	SW of Asik Mtn.
AM-130-85	#25-786	clinopyroxenite	Ju	67.4032	162.4891	SW of Asik Mtn.
AM-131-85	#25-787	wehrlite	Ju	67.4021	162.4854	SW of Asik Mtn.
AM-132-85	#25-788	clinopyroxenite	Ju	67.4021	162.4854	SW of Asik Mtn.
AM-133-85	#25-789	clinopyroxenite	Ju	67.4224	162.4726	SW of Asik Mtn.
AM-134-85	#25-790	dunite	Ju	67.4224	162.4726	SW of Asik Mtn.
AM-135-85	#25-791	clinopyroxenite	Ju	67.4225	162.4755	SW of Asik Mtn.
AM-144-85	#25-792	leuco gabbro	Jg	67.3987	162.4669	SW of Asik Mtn.
AM-145-85	#25-793	dunite	Ju	67.3990	162.4750	SW of Asik Mtn.
AM-147-85	#25-794	dunite	Ju	67.3920	162.4669	SW of Asik Mtn.

Sample #	USPS #	Lithology	Unit	Lat. (°)	Long. (°)	Location
AM-148-85	#25-795	clinopyroxenite	Ju	67.3934	162.4724	SW of Asik Mtn.
AM-149-85	#25-796	dunite w/ spinel	Ju	67.4014	162.4766	SW of Asik Mtn.
AM-150a-85	#25-797	clinopyroxenite	Ju	67.4016	162.4863	SW of Asik Mtn.
AM-150b-85	#25-798	serp. dunite	Ju	67.4016	162.4976	SW of Asik Mtn.
AM-150c-85	#25-799	clinopyroxenite	Ju	67.4017	162.4971	SW of Asik Mtn.
AM-150d-85	#25-801	dunite	Ju	67.4012	162.4847	SW of Asik Mtn.
AM-151-85	#25-802	clinopyroxenite	Ju	67.4010	162.3828	SW of Asik Mtn.
AM-152-85	#25-803	dunite-clinopyrox.	Ju	67.4010	162.4828	SW of Asik Mtn.
AM-153-85	#25-804	dunite	Ju	67.3973	162.4794	SW of Asik Mtn.
AM-154-85	#25-805	wehrlite	Ju	67.3973	162.4794	SW of Asik Mtn.
AM-155-85	#25-806	clinopyroxenite	Ju	67.3973	162.4794	SW of Asik Mtn.
AM-156-85	#25-807	clinopyroxenite	Ju	67.3973	162.4794	SW of Asik Mtn.
AM-157-85	#25-808	dunite	Ju	67.3973	162.4796	SW of Asik Mtn.
AM-158-85	#25-809	ol-clinopyroxenite	Ju	67.3974	162.4794	SW of Asik Mtn.
AM-159-85	#25-810	ol-clinopyroxenite	Ju	67.3973	162.4794	SW of Asik Mtn.
AM-160-85	#25-811	dunite	Ju	67.3974	162.4796	SW of Asik Mtn.
AM-161-85	#25-812	clinopyroxenite	Ju	67.3974	162.4796	SW of Asik Mtn.
AM-162-85	#25-813	dunite	Ju	67.3974	162.4796	SW of Asik Mtn.
AM-163-85	#25-814	dunite	Ju	67.3974	162.4796	SW of Asik Mtn.
AM-164-85	#25-815	dunite	Ju	67.3975	162.4796	SW of Asik Mtn.
AM-165-85	#25-816	wehrlite	Ju	67.3974	162.4792	SW of Asik Mtn.
AM-166-85	#25-817	dunite	Ju	67.3975	162.4796	SW of Asik Mtn.
AM-167-85	#25-818	clinopyroxenite	Ju	67.3974	162.4792	SW of Asik Mtn.
AM-168-85	#25-819	coarse clinopyrox.	Ju	67.4018	162.4616	SW of Asik Mtn.
AM-169-85	#25-820	gabbro	Ju	67.3993	162.4626	SW of Asik Mtn.
AM-170-85	#25-821	gabbro	Ju	67.4002	162.4695	SW of Asik Mtn.
AM-171-85	#25-822	dunite	Ju	67.4000	162.4727	SW of Asik Mtn.
AM-172-85	#25-823	dunite	Ju	67.4000	162.4727	SW of Asik Mtn.
AM-173-85	#25-824	gabbro	Jg	67.4494	162.3947	SW of Asik Mtn.
AM-174-85	#25-825	lin. leuco gabbro	Jg	67.4863	162.3354	NE Asik Mtn.
AM-175-85	#25-826	lin. melano gab.	Jg	67.4897	162.3290	NE Asik Mtn.
AM-176-85	#25-827	lineated gabbro	Jg	67.4953	162.3228	NE Asik Mtn.
AM-177-85	#25-828	fol. plagiogranite	Jg	67.4953	162.3226	NE Asik Mtn.
AM-178-85	#25-829	qtz. vein in gabbro	Jg	67.4952	162.3226	NE Asik Mtn.
AM-179-85	#25-830	fol. plagiogranite?	Jg	67.4943	162.3177	NE Asik Mtn.
AM-180-85	#25-831	fol. plagiogranite?	Jg	67.4930	162.3166	NE Asik Mtn.
AM-181-85	#25-832	tect. diorite	Jg	67.4930	162.3166	NE Asik Mtn.
AM-182-85	#25-833	fine gabbro	Jg	67.4930	162.3166	NE Asik Mtn.
AM-183-85	#25-834	leuco gabbro	Jg	67.4930	162.3166	NE Asik Mtn.
AM-184-85	#25-835	metased mylonite	MzPzv	67.4947	162.3136	NE Asik Mtn.
AM-185-85	#25-836	mafic schist	MzPzv	67.4962	162.3140	NE Asik Mtn.
AM-186-85	#25-837	mafic schist	MzPzv	67.4972	162.3155	NE Asik Mtn.
AM-187-85	#25-838	sheared metased.	MzPzv	67.4972	162.3155	NE Asik Mtn.
AM-188-85	#25-839	mafic schist	MzPzv	67.4972	162.3155	NE Asik Mtn.
AM-189-85	#25-840	sheared metased.	MzPzv	67.4984	162.3092	NE Asik Mtn.

Sample #	USPS #	Lithology	Unit	Lat. (°)	Long. (°)	Location
AM-190-85	#25-841	sheared metavol.	MzPzv	67.4984	162.3092	NE Asik Mtn.
AM-191-85	#25-842	foliated basalt	MzPzv	67.4984	162.3092	NE Asik Mtn.
AM-192-85	#25-843	meta chert	JPm	67.5005	162.3052	NE Asik Mtn.
AM-193-85	#25-844	meta chert	JPm	67.5006	162.3052	NE of Asik Mtn.
AM-194-85	#25-845	sheared intrusive ?	MzPzv	67.5358	162.3197	NE of Asik Mtn.
AM-195-85	#25-846	mafic volcanic	MzPzv	67.5358	162.3199	NE of Asik Mtn.
AM-196-85	#25-847	mafic schist	MzPzv	67.5379	162.3153	NE of Asik Mtn.
AM-197-85	#25-848	basalt	MzPzv	67.5390	162.3118	NE of Asik Mtn.
AM-198-85	#25-849	basalt	MzPzv	67.5390	162.3118	NE of Asik Mtn.
AM-199-85	#25-850	basalt	MzPzv	67.5412	162.3072	NE of Asik Mtn.
AM-200-85	#25-851	basalt	MzPzv	67.5412	162.3072	NE of Asik Mtn.
AM-201-85	#25-852	basalt	MzPzv	67.5426	162.3038	NE of Asik Mtn.
AM-202-85	#25-853	volc. sediment	MzPzv	67.5451	162.2963	NE of Asik Mtn.
AM-203-85	#25-854	vol. sediment	MzPzv	67.5462	162.2942	NE of Asik Mtn.
AM-204-85	#25-855	chert	MzPzv	67.5462	162.2942	NE of Asik Mtn.
AM-205-85	#25-856	basalt	MzPzv	67.5462	162.2942	NE of Asik Mtn.
AM-206-85	#25-857	volcaniclastic	MzPzv	67.5473	162.2927	NE of Asik Mtn.
AM-207-85	#25-858	volcaniclastic	MzPzv	67.5473	162.2927	NE of Asik Mtn.
AM-208-85	#25-859	volcaniclastic	MzPzv	67.5473	162.2927	NE of Asik Mtn.
AM-209-85	#25-860	volcaniclastic	MzPzv	67.5473	162.2927	NE of Asik Mtn.
AM-210-85	#25-861	volcaniclastic	MzPzv	67.5474	162.2927	NE of Asik Mtn.
AM-211-85	#25-862	pillow basalt	MzPzv	67.5490	162.2943	NE of Asik Mtn.
AM-212-85	#25-863	foliated basalt	MzPzv	67.5490	162.2943	NE of Asik Mtn.
AM-213-85	#25-864	foliated basalt	MzPzv	67.5490	162.2943	NE of Asik Mtn.
AM-214-85	#25-865	basalt	MzPzv	67.5500	162.2935	NE of Asik Mtn.
AM-215-85	#25-867	volcaniclastic	MzPzv	67.5500	162.2935	NE of Asik Mtn.
AM-216-85	#25-868	meta basalt	MzPzv	67.5525	162.2834	NE of Asik Mtn.
AM-217-85	#25-869	chlorite schist	MzPzv	67.5541	162.2752	NE of Asik Mtn.
AM-218-85	#25-870	chlorite schist	MzPzv	67.5542	162.2754	NE of Asik Mtn.
AM-219-85	#25-871	chlorite schist	MzPzv	67.5542	162.2752	NE of Asik Mtn.
AM-220-85	#25-872	metabasalt	MzPzv	67.5588	162.2618	NE of Asik Mtn.
AM-221-85	#25-873	metabasalt	MzPzv	67.5588	162.2618	NE of Asik Mtn.
AM-222-85	#25-874	fol. metavolcanic	MzPzv	67.5621	162.2541	NE of Asik Mtn.
AM-223-85	#25-875	black slate		67.5629	162.2467	NE of Asik Mtn.
AM-224-85	#25-876	carbonate		67.5631	162.2449	NE of Asik Mtn.
AM-225-85	#25-877	grey slate		67.5658	162.2364	NE of Asik Mtn.
AM-225a-85	#25-878	fossil. carbonate		67.5658	162.2362	NE of Asik Mtn.
AM-226-85	#25-879	fol. metavolcanic	MzPzv	67.5405	162.2805	NE of Asik Mtn.
AM-226a-85	#25-880	fol. metavolcanic	MzPzv	67.5407	162.3806	NE of Asik Mtn.
AM-227-85	#25-881	foliated gabbro	Jg	67.4958	162.3389	NW Asik Mtn.
AM-228-85	#25-882	plagiogranite	MzPzv	67.4936	162.3539	NW Asik Mtn.
AM-229-85	#25-883	fol. metavolcanic	MzPzv	67.5023	162.3686	NW of Asik Mtn.
AM-230-85	#25-884	fol. metavolcanic	MzPzv	67.5022	162.3686	NW of Asik Mtn.
AM-231-85	#25-885	fol. metavolcanic	MzPzv	67.5036	162.3741	NW of Asik Mtn.
AM-232-85	#25-886	fol. metavolcanic	MzPzv	67.5039	162.3787	NW of Asik Mtn.

Sample #	USPS #	Lithology	Unit	Lat. (°)	Long. (°)	Location
MM-1-85	#25-915	pillow basalt	MzPzv	67.7701	162.0571	Central Maiyumeraks
MM-2-85	#25-916	greenchert	MzPzv	67.7721	162.0585	Central Maiyumeraks
MM-3-85	#25-917	basalt	MzPzv	67.7721	162.0585	Central Maiyumeraks
MM-4-85	#25-918	altered basalt	MzPzv	67.7721	162.0585	Central Maiyumeraks
MM-5-85	#25-919	amygdular basalt	MzPzv	67.7754	162.0640	Central Maiyumeraks
MM-6-85	#25-920	mineralized basalt	MzPzv	67.7754	162.0464	Central Maiyumeraks
MM-7-85	#25-921	basalt	MzPzv	67.7617	162.0657	Central Maiyumeraks
MM-8-85	#25-922	basalt	MzPzv	67.7617	162.0660	Central Maiyumeraks
MM-9-85	#25-923	basalt	MzPzv	67.7617	162.0657	Central Maiyumeraks
MM-10-85	#25-924	basalt	MzPzv	67.7617	162.0657	Central Maiyumeraks
MM-11-85	#25-925	basalt	MzPzv	67.7619	162.0717	Central Maiyumeraks
MM-12-85	#25-926	basalt	MzPzv	67.7619	162.1072	Central Maiyumeraks
MM-13-85	#25-927	basalt	MzPzv	67.7592	162.1080	Central Maiyumeraks
MM-14-85	#25-928	basalt	MzPzv	67.7575	162.1272	W-central Maiyumeraks
MM-15-85	#25-929	basalt	MzPzv	67.7648	162.0464	Central Maiyumeraks
MM-16-85	#25-930	basalt	MzPzv	67.7648	162.0462	Central Maiyumeraks
MM-17-85	#25-931	chert	MzPzv	67.7647	162.0439	Central Maiyumeraks
MM-18-85	#25-932	mafic volcanic	MzPzv	67.7656	162.0521	Central Maiyumeraks
MM-19-85	#25-933	volcanic sediment?	MzPzv	67.7511	162.1055	S-central Maiyumeraks
MM-20-85	#25-934	volcanic breccia	MzPzv	67.7513	162.1055	S-central Maiyumeraks
MM-21-85	#25-935	diorite dike	MzPzv	67.7512	162.1055	S-central Maiyumeraks
MM-22-85	#25-936	layered volcanic	MzPzv	67.7512	162.1006	S-central Maiyumeraks
MM-23-85	#25-937	amyg. basalt	MzPzv	67.7512	162.1006	S-central Maiyumeraks
MM-24-85	#25-938	basaltic dike	MzPzv	67.7537	162.0959	S-central Maiyumeraks
MM-25-85	#25-939	basalt	MzPzv	67.7537	162.0961	S-central Maiyumeraks
MM-26-85	#25-940	layered basalt	MzPzv	67.7537	162.0961	S-central Maiyumeraks
MM-27-85	#25-941	amyg. basalt	MzPzv	67.7537	162.0961	S-central Maiyumeraks
MM-28-85	#25-942	basaltic dike	MzPzv	67.7460	162.1138	S-central Maiyumeraks
MM-29-85	#25-943	amyg. basalt	MzPzv	67.7460	162.1138	S-central Maiyumeraks
MM-30-85	#25-944	basalt	MzPzv	67.7460	162.1138	S-central Maiyumeraks
MM-31-85	#25-945	pillow margin	MzPzv	67.7460	162.1138	S-central Maiyumeraks
MM-32-85	#25-946	basaltic dike	MzPzv	67.7458	162.1123	S-central Maiyumeraks
MM-33-85	#25-947	quartz vein	MzPzv	67.7458	162.1123	S-central Maiyumeraks
MM-34-85	#25-948	dike margin	MzPzv	67.7458	162.1123	S-central Maiyumeraks
MM-35-85	#25-949	basaltic dike	MzPzv	67.7458	162.1138	S-central Maiyumeraks
MM-36-85	#25-950	basaltic dike	MzPzv	67.7458	162.1135	S-central Maiyumeraks
MM-37-85	#25-951	pillow basalt	MzPzv	67.7458	162.1135	S-central Maiyumeraks
MM-38-85	#25-952	basaltic dike	MzPzv	67.7458	162.1135	S-central Maiyumeraks
MM-39-85	#25-953	basaltic dike	MzPzv	67.7458	162.1135	S-central Maiyumeraks
MM-40-85	#25-954	pillow basalt	MzPzv	67.7458	162.1135	S-central Maiyumeraks
MM-41-85	#25-955	basaltic dike	MzPzv	67.7458	162.1133	S-central Maiyumeraks
MM-42-85	#25-956	basaltic sed.?	MzPzv	67.7461	162.1106	S-central Maiyumeraks
MM-43-85	#25-957	basalt agglom.?	MzPzv	67.7461	162.1104	S-central Maiyumeraks
MM-44-85	#25-958	basalt	MzPzv	67.7461	162.1103	S-central Maiyumeraks
MM-45-85	#25-959	basaltic sediment	MzPzv	67.7523	162.1017	S-central Maiyumeraks

Sample #	USPS #	Lithology	Unit	Lat. (°)	Long. (°)	Location
MM-46-85	#25-960	basalt	MzPzv	67.7523	162.0996	S-central Maiyumeraks
MM-47-85	#25-961	basalt	MzPzv	67.7461	162.1135	S-central Maiyumeraks
MM-48-85	#25-962	pillow basalt	MzPzv	67.7500	162.0910	S-central Maiyumeraks
MM-49-85	#25-963	basaltic dike	MzPzv	67.7496	162.0895	S-central Maiyumeraks
MM-50-85	#25-964	pyritic bas. dike	MzPzv	67.7497	162.0893	S-central Maiyumeraks
MM-51-85	#25-965	basalt	MzPzv	67.7486	162.0894	S-central Maiyumeraks
MM-52-85	#25-966	diorite dike	MzPzv	67.7483	162.0894	S-central Maiyumeraks
MM-53-85	#25-967	basalt	MzPzv	67.7483	162.0894	S-central Maiyumeraks
MM-54-85	#25-968	black basalt	MzPzv	67.7483	162.0894	S-central Maiyumeraks
MM-55-85	#25-969	pillow basalt	MzPzv	67.7483	162.0894	S-central Maiyumeraks
MM-56-85	#25-970	black basalt	MzPzv	67.7483	162.0894	S-central Maiyumeraks
MM-57-85	#25-971	basalt	MzPzv	67.7483	162.0894	S-central Maiyumeraks
MM-58-85	#25-972	diorite dike	MzPzv	67.7455	162.0918	E-central Maiyumeraks
MM-59-85	#25-973	basalt	MzPzv	67.7442	162.0911	E-central Maiyumeraks
MM-60-85	#25-974	basaltic dike	MzPzv	67.7442	162.0911	E-central Maiyumeraks
MM-61-85	#25-975	basalt	MzPzv	67.7442	162.0911	E-central Maiyumeraks
MM-62-85	#25-976	dike margin	MzPzv	67.7442	162.0911	E-central Maiyumeraks
MM-63-85	#25-977	diorite dike	MzPzv	67.7442	162.0911	E-central Maiyumeraks
MM-64-85	#25-978	diabase	MzPzv	67.7436	162.0892	E-central Maiyumeraks
MM-65-85	#25-979	diabase	MzPzv	67.7425	162.0897	E-central Maiyumeraks
MM-66-85	#25-980	basaltic dike	MzPzv	67.7437	162.0934	E-central Maiyumeraks
MM-67-85	#25-981	basalt	MzPzv	67.7437	162.0934	E-central Maiyumeraks
MM-68-85	#25-982	basalt	MzPzv	67.7437	162.0934	E-central Maiyumeraks
MM-69-85	#25-983	basalt	MzPzv	67.7452	162.0966	E-central Maiyumeraks
MM-70-85	#25-984	basaltic dike	MzPzv	67.7486	162.0851	E-central Maiyumeraks
MM-71-85	#25-985	basalt	MzPzv	67.7486	162.0851	E-central Maiyumeraks
MM-72-85	#25-986	basalt	MzPzv	67.7486	162.0851	E-central Maiyumeraks
MM-74-85	#25-987	basaltic dike	MzPzv	67.7494	162.0829	E-central Maiyumeraks
MM-75-85	#25-988	pillow basalt	MzPzv	67.7495	162.0829	E-central Maiyumeraks
MM-76-85	#25-989	basaltic dike	MzPzv	67.7482	162.0810	E-central Maiyumeraks
MM-77-85	#25-990	basalt	MzPzv	67.7482	162.0810	E-central Maiyumeraks
MM-78-85	#25-991	basaltic dike	MzPzv	67.7468	162.0889	E-central Maiyumeraks
MM-79-85	#25-992	basalt	MzPzv	67.7468	162.0889	E-central Maiyumeraks
MM-80-85	#25-993	bas. dike marg.	MzPzv	67.7454	162.1156	E-central Maiyumeraks
MM-81-85	#25-994	amyg. basalt	MzPzv	67.7454	162.1156	E-central Maiyumeraks
MM-82-85	#25-995	basaltic dike	MzPzv	67.7454	162.1156	E-central Maiyumeraks
MM-83-85	#25-996	basaltic dike	MzPzv	67.7454	162.1154	E-central Maiyumeraks
MM-84-85	#25-997	basaltic dike	MzPzv	67.7454	162.1154	E-central Maiyumeraks
MM-85-85	#25-998	basaltic dike	MzPzv	67.7454	162.1154	E-central Maiyumeraks
MM-86-85	#25-999	amyg. basalt	MzPzv	67.7449	162.1143	E-central Maiyumeraks
MM-87-85	#25-1000	pyritic basalt	MzPzv	67.7449	162.1143	E-central Maiyumeraks
MM-88-85	#25-1001	basaltic dike	MzPzv	67.7449	162.1143	E-central Maiyumeraks
MM-89-85	#25-1002	basaltic dike	MzPzv	67.7430	162.1174	E-central Maiyumeraks
MM-90-85	#25-1003	pillow basalt	MzPzv	67.7430	162.1178	E-central Maiyumeraks
MM-91-85	#25-1004	basaltic dike	MzPzv	67.7429	162.1189	E-central Maiyumeraks

Sample #	USPS #	Lithology	Unit	Lat. (°)	Long. (°)	Location
MM-92-85	#25-1005	bas. dike marg.	MzPzv	67.7429	162.1195	E-central Maiyumeraks
MM-93-85	#25-1006	pyritic dike	MzPzv	67.7428	162.1203	E-central Maiyumeraks
MM-94-85	#25-1007	basaltic dike	MzPzv	67.7427	162.1212	E-central Maiyumeraks
MM-95-85	#25-1008	basaltic dike	MzPzv	67.7427	162.1220	E-central Maiyumeraks
MM-96-85	#25-1009	pillow basalt	MzPzv	67.7427	162.1226	E-central Maiyumeraks
MM-97-85	#25-1010	basaltic dike	MzPzv	67.7427	162.1231	E-central Maiyumeraks
MM-98-85	#25-1011	pillow basalt	MzPzv	67.7427	162.1233	E-central Maiyumeraks
MM-99-85	#25-1012	basaltic dike	MzPzv	67.7427	162.1239	E-central Maiyumeraks
MM-100-85	#25-1013	dioritic dike	MzPzv	67.7429	162.1248	E-central Maiyumeraks
MM-101-85	#25-1014	dacite dike	MzPzv	67.7430	162.1256	E-central Maiyumeraks
MM-102-85	#25-1015	basaltic dike	MzPzv	67.7430	162.1263	E-central Maiyumeraks
MM-103-85	#25-1016	basaltic dike	MzPzv	67.7431	162.1267	E-central Maiyumeraks
MM-104-85	#25-1017	dioritic dike	MzPzv	67.7432	162.1277	E-central Maiyumeraks
MM-105-85	#25-1018	basaltic dike	MzPzv	67.7432	162.1284	E-central Maiyumeraks
MM-106-85	#25-1019	basaltic dike	MzPzv	67.7435	162.1290	E-central Maiyumeraks
MM-107-85	#25-1020	basaltic sediment	MzPzv	67.7440	162.1297	E-central Maiyumeraks
MM-108-85	#25-1021	basaltic dike	MzPzv	67.7441	162.1301	E-central Maiyumeraks
MM-109-85	#25-1022	basaltic dike	MzPzv	67.7442	162.1303	E-central Maiyumeraks
MM-110-85	#25-1023	basaltic dike	MzPzv	67.7442	162.1303	E-central Maiyumeraks
MM-111-85	#25-1024	basaltic dike	MzPzv	67.7443	162.1303	E-central Maiyumeraks
MM-112-85	#25-1025	basaltic dike	MzPzv	67.7443	162.1307	E-central Maiyumeraks
MM-113-85	#25-1026	basaltic dike	MzPzv	67.7443	162.1307	E-central Maiyumeraks
MM-114-85	#25-1027	basaltic dike	MzPzv	67.7444	162.1308	E-central Maiyumeraks
MM-115-85	#25-1028	basalt dike margin	MzPzv	67.7444	162.1307	E-central Maiyumeraks
MM-116-85	#25-1029	basaltic dike	MzPzv	67.7445	162.1308	E-central Maiyumeraks
MM-117-85	#25-1030	basaltic dike	MzPzv	67.7445	162.1308	E-central Maiyumeraks
MM-118-85	#25-1031	basaltic dike	MzPzv	67.7445	162.1308	E-central Maiyumeraks
MM-119-85	#25-1032	porph. bas. float	MzPzv	67.7597	162.1388	W-central Maiyumeraks
MM-120-85	#25-1033	basalt	MzPzv	67.7597	162.1388	W-central Maiyumeraks
MM-121-85	#25-1034	basalt	MzPzv	67.7613	162.1412	W-central Maiyumeraks
MM-122-85	#25-1035	basalt	MzPzv	67.7621	162.1463	W-central Maiyumeraks
MM-123-85	#25-1036	pillow basalt	MzPzv	67.7617	162.1473	W-central Maiyumeraks
MM-124-85	#25-1037	vesicular basalt	MzPzv	67.7613	162.1639	W-central Maiyumeraks
MM-125-85	#25-1038	basalt	MzPzv	67.7607	162.1631	W-central Maiyumeraks
MM-126-85	#25-1039	chert	MzPzv	67.7594	162.1489	W-central Maiyumeraks
MM-127-85	#25-1040	chert	MzPzv	67.7594	162.1489	W-central Maiyumeraks
MM-128-85	#25-1041	chert	MzPzv	67.7602	162.1470	W-central Maiyumeraks
MM-129-85	#25-1042	overlying basalt	MzPzv	67.7602	162.1472	W-central Maiyumeraks
MM-130-85	#25-1043	chert	MzPzv	67.7645	162.1387	W-central Maiyumeraks
MM-131-85	#25-1044	chert	MzPzv	67.7645	162.1387	W-central Maiyumeraks
MM-132-85	#25-1045	underly. min. bas.	MzPzv	67.7644	162.1387	W-central Maiyumeraks
MM-133-85	#25-1046	underly. min. bas.	MzPzv	67.7644	162.1387	W-central Maiyumeraks
MM-134-85	#25-1047	vesicular basalt	MzPzv	67.7658	162.1369	W-central Maiyumeraks
MM-135-85	#25-1048	mineral. basalt	MzPzv	67.7679	162.1320	W-central Maiyumeraks
MM-136-85	#25-1049	basaltic dike	MzPzv	67.7745	162.1308	E-central Maiyumeraks

[illegible]

Appendix III

1987 Field Studies and Rock Samples Collected

The primary objective of the 1987 field study was to examine ophiolite exposures within which we observed unexplained spectral variations in the Thematic Mapper images.

Rock composition, metamorphic grade, and deformation fabrics were studied in volcanic rocks north of Asik Mountain to determine if these aspects of the rock correlate with spectral variations. Samples were also collected for the laboratory determination of spectral reflectance values.

In the Maiyumerak Mountains, we studied the relationship between spectral variations, metamorphic and hydrothermal alteration. We examined areas that we had not previously studied in the field, but had mapped using Thematic Mapper images, in order to evaluate the quality of the remote sensing mapping. Samples were collected for laboratory determination of spectral reflectance values and chemistry.

Ultramafic rocks in the Avan Hills have large TM spectral reflectance variations. These rocks were studied to evaluate the affects of serpentinization, weathering, lichen cover, and mineral composition on reflectance. Samples were collected for laboratory determination of spectral reflectance values.

Other exposures of mafic volcanic rock were studied along the Noatak River and the Dalton Highway for comparison with the rocks described above. Samples were collected for geochemical and spectral analysis (Figure III-1). Because of logistical convenience, and in consideration of future research (Surface Expression of Lithosphere Dynamics, Northern Alaska, submitted to NASA, April, 1987), samples that are suitable for studies of uplift were also collected along the Noatak River and Dalton Highway.

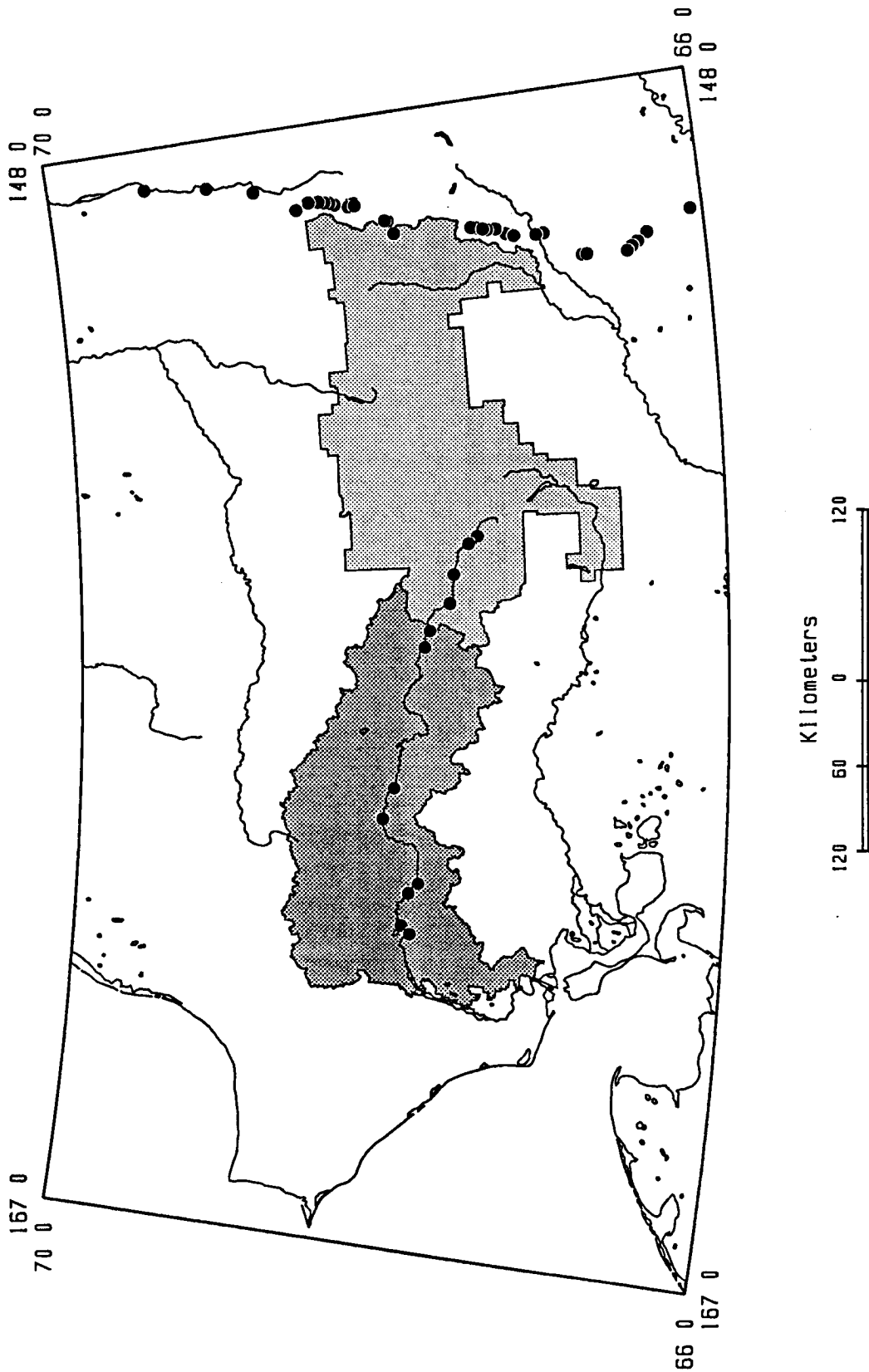


Figure III-1. Map of sample locations in the central and eastern part of the Brooks Range. Also shown are the areas included in the Noatak National Preserve (dark gray shading) and the Gates of the Arctic National Park (light gray shading).

GEOLOGIC SAMPLE DATA

Listed in this Appendix, from left to right, are the Cornell sample number, U.S. Park Service sample number, lithology, geologic unit, latitude and longitude of sample location, and a brief description of the sample location.

Cornell Samples are labeled with a two letter location code, a sample number, and the year collected. Sample location abbreviations are: Avan Hills=AH, Asik Mountain=AM, and Maiyumerak Mountains=MM. If two different samples were collected from the same location, then an "a,b, c,d..." is added to the sample number. U.S. Park Service sample numbers consist of an accession number and a sample number. All the samples have been labeled consecutively in this system.

Rock names in the Appendix are based solely on field classification. Whenever possible, the geologic unit that the rock was collected from is also given. Map units given in the Appendix are the same as those used by Curtis et al. (1983), Gottschalk (1987), and Mull (1985). Abbreviations for the map units are given below:

Unit	Formation/Age	Unit	Formation/Age
QTb	Quaternary-Tertiary Basalt	MDk	Kanayut Conglomerate
Kg	Cretaceous Granite	Mke	" " (Ear Peak Member)
Ko	Okpikruak Formation	Dn	Noatak Sandstone
Kn	Nanushuk Group	Dbcp	Beaucoup Formation
Kfm	Fortress Mtn. Formation	Dhf	Hunt Fork Shale
Kpc	Prince Creek Formation	Dg	Devonian(?) Gabbro
Ksc	Albian-Cenamon. Congl. (sed. clasts)	Dgr	Dev.(?) Granite Gneiss
Kic	Albian Conglomerate (ign. clasts)	Dms	Dev.(?) Metasediments
Jg	Jurassic Gabbro (ophiolitic)	Dwfv	Whiteface Volcanics
Ju	Jurassic Ultramafic Rocks (ophiolitic)	Pzg	Paleozoic(?) Gabbro
Jpm	Iqnavik Diabase Dikes and Sills	Pze	Paleozoic(?) Eclogite
MzPzv	Mesozoic-Paleozoic Basalts	PzPr	Paleo-PreC(?) Meta.
Mk	Kayak Shale	PzPqs	Paleo.-PreC(?) Schist
MDl	Mississippian-Devonian Limestone		

The latitude and longitude of the sample locations were determined by digitizing sample locations from U.S.G.S. 15' and 2° topographic maps. The locations are reported in decimal fractions of degrees.

Sample #	USPS #	Lithology	Unit	Lat. (°)	Long. (°)	Location
AH-1-87	#33-1055	dunite	Ju	68.2696	161.9046	NW Avan Hills
AH-2a-87	#33-1056	dunite	Ju	68.2748	161.9573	NW Avan Hills
AH-2b-87	#33-1057	wehrlite	Ju	68.2748	161.9573	NW Avan Hills
AH-3a-87	#33-1058	dunite	Ju	68.2747	161.9507	NW Avan Hills
AH-3b-87	#33-1059	serpentine	Ju	68.2747	161.9509	NW Avan Hills
AH-3c-87	#33-1060	dunite	Ju	68.2747	161.9507	NW Avan Hills
AH-3d-87	#33-1061	dunite	Ju	68.2747	161.9507	NW Avan Hills
AH-3e-87	#33-1062	harzburgite	Ju	68.2747	161.9507	NW Avan Hills
AH-4-87	#33-1063	dunite w/ spinel	Ju	68.2749	161.9456	NW Avan Hills
AH-5-87	#33-1064	foliated dunite	Ju	68.2752	161.9421	NW Avan Hills
AH-6-87	#33-1065	pyroxenite vein	Ju	68.2764	161.9369	NW Avan Hills
AH-7-87	#33-1066	veined dunite	Ju	68.2750	161.9348	NW Avan Hills
AH-8a-87	#33-1067	pyroxenite vein	Ju	68.2744	161.9330	NW Avan Hills
AH-8b-87	#33-1068	troctolite boulder	Ju	68.2744	161.9327	NW Avan Hills
AH-9a-87	#33-1069	spinel in dunite	Ju	68.2738	161.9300	NW Avan Hills
AH-9b-87	#33-1070	dunite	Ju	68.2738	161.9300	NW Avan Hills
AH-9c-87	#33-1071	troctolite boulder	Ju	68.2738	161.9300	NW Avan Hills
AH-10a-87	#33-1072	basalt	MzPzm	68.2743	161.9678	NW Avan Hills
AH-10b-87	#33-1073	basalt	MzPzm	68.2743	161.9678	NW Avan Hills
AH-10c-87	#33-1074	calcite veined bas	MzPzm	68.2743	161.9678	NW Avan Hills
AH-10d-87	#33-1075	serpentine	Ju	68.2743	161.9678	NW Avan Hills
AH-11a-87	#33-1076	gabbro	Ju	68.2849	161.8871	NW Avan Hills
AH-11b-87	#33-1077	troctolite float	Ju	68.2849	161.8871	NW Avan Hills
AH-11c-87	#33-1078	troctolite	Ju	68.2849	161.8871	NW Avan Hills
AH-11d-87	#33-1079	wehrlite	Ju	68.2849	161.8871	NW Avan Hills
AH-12a-87	#33-1080	wehrlite	Ju	68.2894	161.8925	NW Avan Hills
AH-12b-87	#33-1081	dunite	Ju	68.2894	161.8925	NW Avan Hills
AH-13a-87	#33-1082	leuco gabbro	Jg	68.2892	161.8640	NW Avan Hills
AH-13b-87	#33-1083	leuco gabbro	Jg	68.2892	161.8640	NW Avan Hills
AH-14a-87	#33-1084	troctolite in gabbro	Jg	68.2892	161.8652	NW Avan Hills
AH-14b-87	#33-1085	troctolite in gabbro	Jg	68.2892	161.8652	NW Avan Hills
AH-15a-87	#33-1086	gabbro	Jg	68.2892	161.8661	NW Avan Hills
AH-15b-87	#33-1087	gabbro	Jg	68.2892	161.8661	NW Avan Hills
AH-16a-87	#33-1088	red gabbro	Jg	68.2890	161.8675	NW Avan Hills
AH-16b-87	#33-1089	leuco gabbro	Jg	68.2890	161.8675	NW Avan Hills
AH-16c-87	#33-1090	olivine gabbro	Jg	68.2890	161.8675	NW Avan Hills
AH-17a-87	#33-1091	gabbro	Jg	68.2889	161.8694	NW Avan Hills
AH-17b-87	#33-1092	gabbro	Jg	68.2889	161.8694	NW Avan Hills
AH-18a-87	#33-1093	gabbro	Jg	68.2889	161.8708	NW Avan Hills
AH-18b-87	#33-1094	gabbro	Jg	68.2889	161.8708	NW Avan Hills
AH-19a-87	#33-1095	gabbro	Jg	68.2889	161.8724	NW Avan Hills
AH-19b-87	#33-1096	gabbro peg.	Jg	68.2889	161.8724	NW Avan Hills
AH-19c-87	#33-1097	gabbro peg.	Jg	68.2889	161.8724	NW Avan Hills
AH-20a-87	#33-1098	pyroxenite	Ju	68.2889	161.8741	NW Avan Hills
AH-20b-87	#33-1099	pyrox-dunite	Ju	68.2889	161.8741	NW Avan Hills

Sample #	USPS #	Lithology	Unit	Lat. (°)	Long. (°)	Location
AH-21-87	#33-1101	pyroxenite	Ju	68.2889	161.8749	NW Avan Hills
AH-22a-87	#33-1102	coarse pyroxenite	Ju	68.2890	161.8757	NW Avan Hills
AH-22b-87	#33-1103	gabbro	Ju	68.2890	161.8757	NW Avan Hills
AH-23-87	#33-1104	wehrlite	Ju	68.2890	161.8782	NW Avan Hills
AH-24-87	#33-1105	dunite w/ spinel	Ju	68.2890	161.8792	NW Avan Hills
AH-25a-87	#33-1106	clinopyroxenite	Ju	68.2890	161.8808	NW Avan Hills
AH-25b-87	#33-1107	dunite	Ju	68.2890	161.8808	NW Avan Hills
AH-26-87	#33-1108	wehrlite	Ju	68.2891	161.8827	NW Avan Hills
AH-27-87	#33-1109	pyroxenite	Ju	68.2891	161.8874	NW Avan Hills
AH-28a-87	#33-1110	melano gabbro	Jg	68.2590	161.9055	NW Avan Hills
AH-28b-87	#33-1111	leuco gabbro	Jg	68.2590	161.9055	NW Avan Hills
AH-28c-87	#33-1112	pyroxenite	Ju	68.2590	161.9055	NW Avan Hills
AH-28d-87	#33-1113	dunite	Ju	68.2590	161.9055	NW Avan Hills
AH-28e-87	#33-1114	wehrlite	Ju	68.2590	161.9055	NW Avan Hills
AH-29a-87	#33-1115	wehrlite	Ju	68.2577	161.9092	NW Avan Hills
AH-29b-87	#33-1116	dunite	Ju	68.2577	161.9092	NW Avan Hills
AH-29c-87	#33-1117	ol-clinopyroxenite	Ju	68.2577	161.9092	NW Avan Hills
AH-29d-87	#33-1118	dunite	Ju	68.2577	161.9092	NW Avan Hills
AH-29e-87	#33-1119	serpentinite	Ju	68.2577	161.9092	NW Avan Hills
AH-29f-87	#33-1120	pink pyroxenite	Ju	68.2577	161.9092	NW Avan Hills
AH-29g-87	#33-1121	green pyroxenite	Ju	68.2577	161.9092	NW Avan Hills
AH-30a-87	#33-1122	dunite	Ju	68.2549	161.9173	NW Avan Hills
AH-30b-87	#33-1123	dunite	Ju	68.2549	161.9173	NW Avan Hills
AH-30c-87	#33-1124	dunite	Ju	68.2549	161.9173	NW Avan Hills
AH-30d-87	#33-1125	serpentinite	Ju	68.2549	161.9173	NW Avan Hills
AH-31a-87	#33-1126	dunite	Ju	68.2538	161.9206	NW Avan Hills
AH-31b-87	#33-1127	dunite	Ju	68.2538	161.9206	NW Avan Hills
AH-31c-87	#33-1128	dunite	Ju	68.2538	161.9206	NW Avan Hills
AH-31d-87	#33-1129	dunite	Ju	68.2538	161.9206	NW Avan Hills
AH-31e-87	#33-1130	dunite	Ju	68.2538	161.9206	NW Avan Hills
AH-32a-87	#33-1131	ol-clinopyroxenite	Ju	68.2550	161.9441	NW Avan Hills
AH-32b-87	#33-1132	dunite	Ju	68.2550	161.9441	NW Avan Hills
AH-32c-87	#33-1133	dunite	Ju	68.2550	161.9441	NW Avan Hills
AH-32d-87	#33-1134	spinel in dunite	Ju	68.2550	161.9441	NW Avan Hills
AH-33a-87	#33-1135	dunite	Ju	68.2459	161.9602	NW Avan Hills
AH-33b-87	#33-1136	wehrlite	Ju	68.2459	161.9602	NW Avan Hills
AH-33c-87	#33-1137	wehrlite	Ju	68.2459	161.9602	NW Avan Hills
AH-33d-87	#33-1138	wehrlite	Ju	68.2459	161.9602	NW Avan Hills
AH-33e-87	#33-1139	wehrlite	Ju	68.2456	161.9602	NW Avan Hills
AH-33f-87	#33-1140	wehrlite	Ju	68.2459	161.9602	NW Avan Hills
AH-34-87	#33-1141	dunite cr. sand	Ju	68.2734	161.9284	NW Avan Hills
AH-35-87	#33-1142	laterite	Ju	68.2734	161.9284	NW Avan Hills
AH-36-87	#33-1143	dunite	Ju	68.2734	161.9283	NW Avan Hills
AH-37-87	#33-1144	veined dunite	Ju	68.2727	161.9236	NW Avan Hills
AH-38a-87	#33-1145	dunite w/ spinel	Ju	68.2727	161.9207	NW Avan Hills

Sample #	USPS #	Lithology	Unit	Lat. (°)	Long. (°)	Location
AH-38b-87	#33-1146	pyroxenite vein	Ju	68.2727	161.9207	NW Avan Hills
AH-39a-87	#33-1147	dunite	Ju	68.2725	161.9195	NW Avan Hills
AH-39b-87	#33-1148	pink pyroxenite	Ju	68.2724	161.9195	NW Avan Hills
AH-39c-87	#33-1149	wehrlite	Ju	68.2725	161.9195	NW Avan Hills
AH-39d-87	#33-1150	coarse pyroxenite	Ju	68.2725	161.9195	NW Avan Hills
AH-40-87	#33-1151	dunite	Ju	68.2719	161.9185	NW Avan Hills
AH-41a-87	#33-1152	pyroxenite	Ju	68.2711	161.9134	NW Avan Hills
AH-41b-87	#33-1153	clinopyroxenite	Ju	68.2711	161.9134	NW Avan Hills
AH-41c-87	#33-1154	dunite	Ju	68.2711	161.9134	NW Avan Hills
AH-42-87	#33-1155	pyroxenite	Ju	68.2706	161.9093	NW Avan Hills
AH-43-87	#33-1156	granite	Jg	68.3030	161.8419	NW Avan Hills
AH-43a-87	#33-1157			68.3030	161.8419	NW Avan Hills
AH-43b-87	#33-1158	gabbro	Jg	68.3030	161.8419	NW Avan Hills
AH-43c-87	#33-1159	granite dike	Jg	68.3030	161.8419	NW Avan Hills
AH-43d-87	#33-1160	dunite	Jg	68.3030	161.8419	NW Avan Hills
AH-43e-87	#33-1161	olivine gabbro	Jg	68.3030	161.8419	NW Avan Hills
AH-44a-87	#33-1162	foliated gabbro	Jg	68.3036	161.8347	NW Avan Hills
AH-44b-87	#33-1163	fol. ol. gabbro	Jg	68.3036	161.8347	NW Avan Hills
AH-44c-87	#33-1164	deformed gabbro	Jg	68.3036	161.8347	NW Avan Hills
AH-44d-87	#33-1165	lineated gabbro	Jg	68.3036	161.8347	NW Avan Hills
AH-44e-87	#33-1166	pyroxenite	Jg	68.3036	161.8347	NW Avan Hills
AH-44f-87	#33-1167	granite	Jg	68.3036	161.8347	NW Avan Hills
AH-44g-87	#33-1168	lineated gabbro	Jg	68.3036	161.8347	NW Avan Hills
AH-45a-87	#33-1169	meta basalt	MzPzm	68.1878	161.7371	SE Avan Hills
AH-45b-87	#33-1170	red chert	MzPzm	68.1876	161.7371	SE Avan Hills
AH-45c-87	#33-1171	fine-gr. basalt	MzPzm	68.1876	161.7371	SE Avan Hills
AH-45d-87	#33-1172	diabase	MzPzm	68.1874	161.7372	SE Avan Hills
AH-45e-87	#33-1173	med-gr. basalt	MzPzm	68.1873	161.7373	SE Avan Hills
AH-45f-87	#33-1174	vesicular basalt	MzPzm	68.1871	161.7373	SE Avan Hills
AH-45g-87	#33-1175	basalt	MzPzm	68.1870	161.7371	SE Avan Hills
AH-45h-87	#33-1176	basalt	MzPzm	68.1868	161.7373	SE Avan Hills
AH-45i-87	#33-1177	red & green chert	MzPzm	68.1868	161.7373	SE Avan Hills
AH-45j-87	#33-1178	diabase	MzPzm	68.1866	161.7371	SE Avan Hills
AH-45k-87	#33-1179	fine-gr. basalt	MzPzm	68.1866	161.7371	SE Avan Hills
AH-46a-87	#33-1180	horn veins in gab.	Jg	68.1912	161.7472	SE Avan Hills
AH-46b-87	#33-1181	antigorite	Jg	68.1909	161.7476	SE Avan Hills
AH-46c-87	#33-1182	chrysotile	Jg	68.1909	161.7478	SE Avan Hills
AH-46d-87	#33-1183	black serpentine	Jg	68.1908	161.7482	SE Avan Hills
AH-46e-87	#33-1184	white alt. vein	Jg	68.1907	161.7484	SE Avan Hills
AH-46f-87	#33-1185	vesicular basalt	MzPzm	68.1905	161.7488	SE Avan Hills
AH-47a-87	#33-1186	limestone		68.1890	161.7518	SE Avan Hills
AH-47b-87	#33-1187	green chert		68.1892	161.7521	SE Avan Hills
AH-47c-87	#33-1188	basalt	MzPzm	68.1930	161.7525	SE Avan Hills
AH-47d-87	#33-1189	basalt	MzPzm	68.1894	161.7527	SE Avan Hills
AH-47e-87	#33-1190	chert or sediment		68.1894	161.7529	SE Avan Hills

Sample #	USPS #	Lithology	Unit	Lat. (°)	Long. (°)	Location
AH-47f-87	#33-1191	serpentine	Jg	68.1960	161.7533	SE Avan Hills
AH-48a-87	#33-1192	serpent. wehrlite	Jg	68.1873	161.7567	SE Avan Hills
AH-48b-87	#33-1193	serpentinite	Jg	68.1871	161.7577	SE Avan Hills
AH-48c-87	#33-1194	gabbro	Jg	68.1871	161.7581	SE Avan Hills
AH-48d-87	#33-1195	serpentinite	Jg	68.1871	161.7583	SE Avan Hills
AH-48e-87	#33-1196	gabbro	Jg	68.1870	161.7585	SE Avan Hills
AH-48f-87	#33-1197	gabbro	Jg	68.1868	161.7589	SE Avan Hills
AH-48g-87	#33-1198	gabbro	Jg	68.1866	161.7597	SE Avan Hills
AH-48h-87	#33-1199	gabbro	Jg	68.1865	161.7603	SE Avan Hills
AH-48i-87	#33-1201	gabbro	Jg	68.1865	161.7310	SE Avan Hills
AH-48j-87	#33-1202	gabbro	Jg	68.1863	161.7618	SE Avan Hills
AH-49a-87	#33-1203	gabbro	Jg	68.1875	161.7653	SE Avan Hills
AH-49b-87	#33-1204	troctolite	Jg	68.1875	161.7653	SE Avan Hills
AH-49c-87	#33-1205	gabbro	Jg	68.1871	161.7617	SE Avan Hills
AH-49d-87	#33-1206	med-gr. gabbro	Jg	68.1875	161.7653	SE Avan Hills
AH-49e-87	#33-1207	gabbro	Jg	68.1888	161.7685	SE Avan Hills
AH-49f-87	#33-1208	troctolite	Jg	68.1887	161.7687	SE Avan Hills
AH-49g-87	#33-1209	troctolite	Jg	68.1887	161.7685	SE Avan Hills
AH-49h-87	#33-1210	gabbro	Jg	68.1887	161.7685	SE Avan Hills
AH-50a-87	#33-1211	olivine-plag peg.	Jg	68.1892	161.7560	SE Avan Hills
AH-50b-87	#33-1212	wehrlite	Jg	68.1892	161.7560	SE Avan Hills
AH-50c-87	#33-1213	olivine-plag peg.	Jg	68.1892	161.7560	SE Avan Hills
AH-50d-87	#33-1214	wehrlite	Jg	68.1892	161.7560	SE Avan Hills
AH-50e-87	#33-1215	wehrlite pegmatite	Jg	68.1892	161.7560	SE Avan Hills
AH-50f-87	#33-1216	plag-pyx	Jg	68.1892	161.7560	SE Avan Hills
AH-50g-87	#33-1217	dunite	Jg	68.1892	161.7560	SE Avan Hills
AH-75a-87	#33-1218	dunite	Jg	68.1107	161.1789	SW Avan Hills
AH-75b-87	#33-1219	harzburgite	Ju	68.1107	161.1789	SW Avan Hills
AH-75c-87	#33-1220	harzburgite	Ju	68.1107	161.1789	SW Avan Hills
AH-75d-87	#33-1221	harzburgite	Ju	68.1107	161.1789	SW Avan Hills
AH-75e-87	#33-1222	dunite	Ju	68.1107	161.1789	SW Avan Hills
AH-75f-87	#33-1223	dunite	Ju	68.1107	161.1789	SW Avan Hills
AH-76a-87	#33-1224	harzburgite	Ju	68.1683	161.1683	SW Avan Hills
AH-76b-87	#33-1225	harzburgite	Ju	68.1683	161.1683	SW Avan Hills
AH-76c-87	#33-1226	dunite	Ju	68.1683	161.1683	SW Avan Hills
AH-76d-87	#33-1227	harzburgite	Ju	68.1683	161.1683	SW Avan Hills
AH-77a-87	#33-1228	gabbro	Jg	68.1159	161.1599	SW Avan Hills
AH-77b-87	#33-1229	gabbro	Jg	68.1159	161.1599	SW Avan Hills
AH-78a-87	#33-1230	gabbro	Jg	68.1200	161.1578	SW Avan Hills
AH-78b-87	#33-1231	leuco gabbro	Jg	68.1200	161.1578	SW Avan Hills
AH-79a-87	#33-1232	dunite	Ju	68.1265	161.1478	SW Avan Hills
AH-79b-87	#33-1233	dunite	Ju	68.1265	161.1478	SW Avan Hills
AH-80a-87	#33-1234	serpent. harzburg.	Ju	68.1372	161.1458	SW Avan Hills
AH-80b-87	#33-1235	serpent. harzburg.	Ju	68.1372	161.1458	SW Avan Hills
AH-80c-87	#33-1236	soil from serp.	Ju	68.1372	161.1327	SW Avan Hills

[illegible]

Sample #	USPS #	Lithology	Unit	Lat. (°)	Long. (°)	Location
AM-1-87	#33-1271	basalt	MzPzv	67.6504	162.2186	S. of Eli River
AM-2-87	#33-1272	basalt	MzPzv	67.6483	162.2218	S. of Eli River
AM-3-87	#33-1273	diabase	MzPzv	67.6472	162.2281	S. of Eli River
AM-4-87	#33-1274	basalt	MzPzv	67.6461	162.2345	S. of Eli River
AM-5a-87	#33-1275	diabase	MzPzv	67.6445	162.2370	S. of Eli River
AM-5b-87	#33-1276	basalt	MzPzv	67.6445	162.2372	S. of Eli River
AM-6-87	#33-1277	basalt	MzPzv	67.6393	162.2362	S. of Eli River
AM-7a-87	#33-1278	basalt	MzPzv	67.6405	162.2435	S. of Eli River
AM-7b-87	#33-1279	basalt	MzPzv	67.6405	162.2435	S. of Eli River
AM-8a-87	#33-1280	basalt	MzPzv	67.6401	162.2399	S. of Eli River
AM-8b-87	#33-1281	basalt	MzPzv	67.6401	162.2401	S. of Eli River
AM-9-87	#33-1282	limestone		67.6361	162.2265	S. of Eli River
AM-10-87	#33-1283	basalt	MzPzv	67.6310	162.2310	S. of Eli River
AM-11-87	#33-1284	basalt	MzPzv	67.6337	162.2581	S. of Eli River
AM-12-87	#33-1285	basalt	MzPzv	67.6333	162.2674	S. of Eli River
AM-13-87	#33-1286	basalt	MzPzv	67.6298	162.2676	S. of Eli River
AM-14-87	#33-1287	basalt	MzPzv	67.6230	162.2876	S. of Eli River
AM-15-87	#33-1288	basalt	MzPzv	67.6134	162.3071	S. of Eli River
AM-16-87	#33-1289	basalt	MzPzv	67.6120	162.3108	S. of Eli River
AM-17-87	#33-1290	basalt	MzPzv	67.6062	162.3075	S. of Eli River
AM-18a-87	#33-1291	basalt	MzPzv	67.5967	162.3132	S. of Eli River
AM-18b-87	#33-1292	lithophasae?	MzPzv	67.5967	162.3132	S. of Eli River
AM-19a-87	#33-1293	basalt	MzPzv	67.5829	162.3111	S. of Eli River
AM-19b-87	#33-1294	basalt	MzPzv	67.5829	162.3113	S. of Eli River
AM-19c-87	#33-1295	basalt	MzPzv	67.5829	162.3111	S. of Eli River
AM-20a-87	#33-1296	basalt	MzPzv	67.5841	162.3096	S. of Eli River
AM-20b-87	#33-1297	basalt	MzPzv	67.5841	162.3096	S. of Eli River
AM-20c-87	#33-1298	basalt	MzPzv	67.5841	162.3096	S. of Eli River
AM-21-87	#33-1299	basalt	MzPzv	67.5794	162.3102	S. of Eli River
AM-22-87	#33-1300	basalt	MzPzv	67.5731	162.3166	S. of Eli River
AM-23-87	#33-1301	basalt	MzPzv	67.5719	162.3199	S. of Eli River
AM-24-87	#33-1302	basalt	MzPzv	67.5694	162.3263	S. of Eli River
AM-25a-87	#33-1303	altered basalt	MzPzv	67.5643	162.3359	S. of Eli River
AM-25b-87	#33-1304	greenschist	MzPzv	67.5642	162.3400	S. of Eli River
AM-25c-87	#33-1305	greenschist	MzPzv	67.5639	162.3430	S. of Eli River
AM-25d-87	#33-1306	greenschist	MzPzv	67.5632	162.3466	S. of Eli River
AM-26-87	#33-1307	greenschist	MzPzv	67.5565	162.3927	S. of Eli River
AM-27-87	#33-1308	greenschist	MzPzv	67.5535	162.3967	S. of Eli River
AM-28-87	#33-1309	greenschist	MzPzv	67.5410	162.4034	S. of Eli River
AM-29-87	#33-1310	greenschist	MzPzv	67.5376	162.4095	S. of Eli River
AM-30-87	#33-1311	amphibolite	MzPzv	67.5215	162.4116	S. of Eli River
AM-31-87	#33-1312	fol. greenschist	MzPzv	67.5037	162.3791	North Asik Mtn.
AM-32-87	#33-1313	layered gabbro	MzPzv	67.5080	162.3828	North Asik Mtn.
AM-33-87	#33-1314	melano gabbro	MzPzv	67.5080	162.3828	North Asik Mtn.
AM-34-87	#33-1315	mafic volcanic	MzPzv	67.5107	162.3815	North Asik Mtn.

Sample #	USPS #	Lithology	Unit	Lat. (°)	Long. (°)	Location
AM-35-87	#33-1316	lineated gabbo	MzPzv	67.5107	162.3815	North Asik Mtn.
AM-36-87	#33-1317	lineated intrusive	MzPzv	67.5107	162.3815	North Asik Mtn.
AM-37-87	#33-1318	mafic volcanic	MzPzv	67.5151	162.3786	North Asik Mtn.
AM-38a-87	#33-1319	mafic volcanic	MzPzv	67.5151	162.3786	North Asik Mtn.
AM-38b-87	#33-1320	foliated volcanic	MzPzv	67.5150	162.3786	North Asik Mtn.
AM-39-87	#33-1321	felsic volcanic	MzPzv	67.5156	162.3801	North Asik Mtn.
AM-40-87	#33-1322	mafic volcanic	MzPzv	67.5156	162.3801	North Asik Mtn.
AM-41-87	#33-1323	mafic volcanic	MzPzv	67.5156	162.3801	North Asik Mtn.
AM-42-87	#33-1324	amphibolite	MzPzv	67.4959	162.3149	North Asik Mtn.
AM-43-87	#33-1325	inter. intrusive	MzPzv	67.4959	162.3151	North Asik Mtn.
AM-44-87	#33-1326	metavolcanic	MzPzv	67.4963	162.3128	North Asik Mtn.
AM-45-87	#33-1327	metavolcanic	MzPzv	67.4964	162.3128	North Asik Mtn.
AM-46-87	#33-1328	diabase	JPm	67.4964	162.3130	North Asik Mtn.
AM-47-87	#33-1329	diabase	JPm	67.4861	162.3080	North Asik Mtn.
AM-48-87	#33-1330	diabase	JPm	67.4861	162.3080	North Asik Mtn.
AM-49-87	#33-1331	diabase	JPm	67.4849	162.3024	North Asik Mtn.
AM-50-87	#33-1332	wacke	Ko	67.4920	162.2734	North Asik Mtn.
AM-51-87	#33-1333	wacke	Ko	67.4975	162.2789	North Asik Mtn.
AM-52a-87	#33-1334	gabbro	Jg	67.4935	162.3528	North Asik Mtn.
AM-52b-87	#33-1335	plagiogr. dike	Jg	67.4936	162.3528	North Asik Mtn.
AM-53-87	#33-1336	plagiogranite	Jg	67.4926	162.3516	North Asik Mtn.
AM-54a-87	#33-1337	horn. gabbro	Jg	67.4868	162.3516	North Asik Mtn.
AM-54b-87	#33-1338	horn. gabbro	Jg	67.4868	162.3518	North Asik Mtn.
AM-55-87	#33-1339	horn. gabbro	Jg	67.4862	162.3622	North Asik Mtn.
AM-56-87	#33-1340	horn. gabbro	Jg	67.4853	162.3595	North Asik Mtn.
AM-57-87	#33-1341	horn. gabbro	Jg	67.4839	162.3545	North Asik Mtn.
AM-58-87	#33-1342	epidote-qtz vein	Jg	67.4831	162.3544	North Asik Mtn.
AM-59-87	#33-1343	lin. leuco gabbro	Jg	67.4826	162.3549	North Asik Mtn.
AM-60a-87	#33-1344	gabbro	Jg	67.4798	162.3562	North Asik Mtn.
AM-60b-87	#33-1345	horn. gabbro peg.	Jg	67.4798	162.3562	North Asik Mtn.
AM-60c-87	#33-1346	pyroxenite	Jg	67.4798	162.3562	North Asik Mtn.
AM-61a-87	#33-1347	fine gr. gabbro	Jg	67.4795	162.3501	North Asik Mtn.
AM-61b-87	#33-1348	med. gabbro	Jg	67.4795	162.3501	North Asik Mtn.
AM-61c-87	#33-1349	coarse gabbro	Jg	67.4795	162.3501	North Asik Mtn.
AM-61d-87	#33-1350	horn-pyx gabbro	Jg	67.4795	162.3501	North Asik Mtn.
AM-62a-87	#33-1351	melano gabbro	Jg	67.4818	162.3424	North Asik Mtn.
AM-62b-87	#33-1352	gabbro	Jg	67.4818	162.3424	North Asik Mtn.
AM-62c-87	#33-1353	leuco gabbro	Jg	67.4818	162.3424	North Asik Mtn.
AM-62d-87	#33-1354	coarse gabbro	Jg	67.4818	162.3424	North Asik Mtn.
AM-62e-87	#33-1355	fine gabbro	Jg	67.4818	162.3424	North Asik Mtn.
AM-63a-87	#33-1356	foliated gabbro	MzPzv	67.4965	162.3767	North Asik Mtn.
AM-63b-87	#33-1357	foliated gabbro	MzPzv	67.4965	162.3767	North Asik Mtn.
AM-63c-87	#33-1358	foliated gabbro	MzPzv	67.4965	162.3767	North Asik Mtn.
AM-63d-87	#33-1359	foliated gabbro	MzPzv	67.4965	162.3767	North Asik Mtn.
AM-64-87	#33-1360	cataclast. gabbro	MzPzv	67.4932	162.3725	North Asik Mtn.

[illegible]

Sample #	USPS #	Lithology	Unit	Lat. (°)	Long. (°)	Location
MM-1a-87	#33-1400	basaltic dike	MzPzv	67.7396	162.0992	SW Maiyumerak Mtns.
MM-1b-87	#33-1401	basaltic dike	MzPzv	67.7396	162.0992	SW Maiyumerak Mtns.
MM-1c-87	#33-1402	basaltic dike	MzPzv	67.7396	162.0992	SW Maiyumerak Mtns.
MM-1d-87	#33-1403	basaltic dike	MzPzv	67.7396	162.0992	SW Maiyumerak Mtns.
MM-1e-87	#33-1404	basaltic dike	MzPzv	67.7396	162.0992	SW Maiyumerak Mtns.
MM-1f-87	#33-1405	basaltic dike	MzPzv	67.7396	162.0992	SW Maiyumerak Mtns.
MM-1g-87	#33-1406	basaltic dike	MzPzv	67.7396	162.0992	SW Maiyumerak Mtns.
MM-1h-87	#33-1407	basaltic dike	MzPzv	67.7396	162.0992	SW Maiyumerak Mtns.
MM-2a-87	#33-1408	basaltic dike	MzPzv	67.7414	162.1037	SW Maiyumerak Mtns.
MM-2b-87	#33-1409	basaltic dike	MzPzv	67.7414	162.1037	SW Maiyumerak Mtns.
MM-2c-87	#33-1410	basaltic dike	MzPzv	67.7414	162.1037	SW Maiyumerak Mtns.
MM-2d-87	#33-1411	basaltic dike	MzPzv	67.7414	162.1037	SW Maiyumerak Mtns.
MM-2e-87	#33-1412	basaltic dike	MzPzv	67.7414	162.1037	SW Maiyumerak Mtns.
MM-2f-87	#33-1413	basaltic dike	MzPzv	67.7414	162.1037	SW Maiyumerak Mtns.
MM-2g-87	#33-1414	basaltic dike	MzPzv	67.7414	162.1037	SW Maiyumerak Mtns.
MM-2h-87	#33-1415	basaltic dike	MzPzv	67.7414	162.1037	SW Maiyumerak Mtns.
MM-3a-87	#33-1416	basaltic dike	MzPzv	67.7422	162.1078	SW Maiyumerak Mtns.
MM-3b-87	#33-1417	basaltic dike	MzPzv	67.7422	162.1078	SW Maiyumerak Mtns.
MM-3c-87	#33-1418	basaltic dike	MzPzv	67.7422	162.1078	SW Maiyumerak Mtns.
MM-3d-87	#33-1419	basaltic dike	MzPzv	67.7422	162.1078	SW Maiyumerak Mtns.
MM-3e-87	#33-1420	basaltic dike	MzPzv	67.7422	162.1078	SW Maiyumerak Mtns.
MM-3f-87	#33-1421	basaltic dike	MzPzv	67.7422	162.1078	SW Maiyumerak Mtns.
MM-3g-87	#33-1422	basaltic dike	MzPzv	67.7422	162.1078	SW Maiyumerak Mtns.
MM-3h-87	#33-1423	basaltic dike	MzPzv	67.7422	162.1078	SW Maiyumerak Mtns.
MM-4a-87	#33-1424	basaltic dike	MzPzv	67.7426	162.1220	SW Maiyumerak Mtns.
MM-4b-87	#33-1425	basaltic dike	MzPzv	67.7426	162.1220	SW Maiyumerak Mtns.
MM-4c-87	#33-1426	basaltic dike	MzPzv	67.7426	162.1220	SW Maiyumerak Mtns.
MM-4d-87	#33-1427	basaltic dike	MzPzv	67.7426	162.1220	SW Maiyumerak Mtns.
MM-4e-87	#33-1428	basaltic dike	MzPzv	67.7426	162.1220	SW Maiyumerak Mtns.
MM-4f-87	#33-1429	basaltic dike	MzPzv	67.7426	162.1220	SW Maiyumerak Mtns.
MM-4g-87	#33-1430	basaltic dike	MzPzv	67.7426	162.1220	SW Maiyumerak Mtns.
MM-4h-87	#33-1431	basaltic dike	MzPzv	67.7426	162.1220	SW Maiyumerak Mtns.
MM-5a-87	#33-1432	basaltic dike	MzPzv	67.7429	162.1264	SW Maiyumerak Mtns.
MM-5b-87	#33-1433	basaltic dike	MzPzv	67.7429	162.1264	SW Maiyumerak Mtns.
MM-5c-87	#33-1434	basaltic dike	MzPzv	67.7429	162.1264	SW Maiyumerak Mtns.
MM-5d-87	#33-1435	basaltic dike	MzPzv	67.7429	162.1264	SW Maiyumerak Mtns.
MM-5e-87	#33-1436	basaltic dike	MzPzv	67.7429	162.1264	SW Maiyumerak Mtns.
MM-5f-87	#33-1437	basaltic dike	MzPzv	67.7429	162.1264	SW Maiyumerak Mtns.
MM-5g-87	#33-1438	basaltic dike	MzPzv	67.7429	162.1264	SW Maiyumerak Mtns.
MM-5h-87	#33-1439	basaltic dike	MzPzv	67.7429	162.1264	SW Maiyumerak Mtns.
MM-6a-87	#33-1440	basalt	MzPzv	67.7524	162.1276	SW Maiyumerak Mtns.
MM-6b-87	#33-1441	basalt	MzPzv	67.7524	162.1276	SW Maiyumerak Mtns.
MM-7a-87	#33-1442	basaltic dike	MzPzv	67.7506	162.1961	SW Maiyumerak Mtns.
MM-7b-87	#33-1443	basalt	MzPzv	67.7506	162.1961	SW Maiyumerak Mtns.
MM-8-87	#33-1444	basalt	MzPzv	67.7514	162.1873	SW Maiyumerak Mtns.

Sample #	USPS #	Lithology	Unit	Lat. (°)	Long. (°)	Location
MM-9a-87	#33-1445	basaltic dike	MzPzv	67.7525	162.1761	SW Maiyumerak Mtns.
MM-9b-87	#33-1446	dike margin	MzPzv	67.7525	162.1761	SW Maiyumerak Mtns.
MM-9c-87	#33-1447	pillow basalt	MzPzv	67.7525	162.1761	SW Maiyumerak Mtns.
MM-10a-87	#33-1448	basaltic dike	MzPzv	67.7522	162.1695	SW Maiyumerak Mtns.
MM-10b-87	#33-1449	pillow basalt	MzPzv	67.7522	162.1695	SW Maiyumerak Mtns.
MM-11a-87	#33-1450	massive basalt	MzPzv	67.7521	162.1664	SW Maiyumerak Mtns.
MM-11b-87	#33-1451	pillow basalt	MzPzv	67.7521	162.1664	SW Maiyumerak Mtns.
MM-12a-87	#33-1452	basalt	MzPzv	67.7538	162.1598	SW Maiyumerak Mtns.
MM-12b-87	#33-1453	basalt	MzPzv	67.7538	162.1598	SW Maiyumerak Mtns.
MM-13a-87	#33-1454	basaltic dike	MzPzv	67.7523	162.1438	SW Maiyumerak Mtns.
MM-13b-87	#33-1455	massive basalt	MzPzv	67.7523	162.1438	SW Maiyumerak Mtns.
MM-13c-87	#33-1456	massive basalt	MzPzv	67.7523	162.1438	SW Maiyumerak Mtns.
MM-14-87	#33-1457	layered basalt	MzPzv	67.7462	162.1093	SW Maiyumerak Mtns.
MM-15a-87	#33-1458	basaltic dike	MzPzv	67.7448	162.1133	SW Maiyumerak Mtns.
MM-15b-87	#33-1459	basaltic dike	MzPzv	67.7448	162.1133	SW Maiyumerak Mtns.
MM-15c-87	#33-1460	basaltic dike	MzPzv	67.7448	162.1133	SW Maiyumerak Mtns.
MM-15d-87	#33-1461	basaltic dike	MzPzv	67.7448	162.1133	SW Maiyumerak Mtns.
MM-15e-87	#33-1462	basaltic dike	MzPzv	67.7448	162.1133	SW Maiyumerak Mtns.
MM-15f-87	#33-1463	basaltic dike	MzPzv	67.7448	162.1133	SW Maiyumerak Mtns.
MM-15g-87	#33-1464	basaltic dike	MzPzv	67.7448	162.1133	SW Maiyumerak Mtns.
MM-15h-87	#33-1465	basaltic dike	MzPzv	67.7448	162.1133	SW Maiyumerak Mtns.
MM-16a-87	#33-1466	basaltic sed.	MzPzv	67.7437	162.1119	SW Maiyumerak Mtns.
MM-16b-87	#33-1467	basalt	MzPzv	67.7437	162.1119	SW Maiyumerak Mtns.
MM-16c-87	#33-1468	basaltic sed.	MzPzv	67.7437	162.1119	SW Maiyumerak Mtns.
MM-50-87	#33-1469	dacite dike	MzPzv	67.7436	162.1302	SW Maiyumerak Mtns.
MM-51-87	#33-1470	gabbro	JPm	67.7323	162.0264	SE Maiyumerak Mtns.
MM-52a-87	#33-1471	gabbro	JPm	67.7311	162.0260	SE Maiyumerak Mtns.
MM-52b-87	#33-1472	gabbro	JPm	67.7311	162.0260	SE Maiyumerak Mtns.
MM-52c-87	#33-1473	gabbro	JPm	67.7312	162.0260	SE Maiyumerak Mtns.
MM-53a-87	#33-1474	limestone	MDl	67.7104	162.0179	Eli River
MM-53b-87	#33-1475	gabbro	JPm	67.7104	162.0179	Eli River
MM-54a-87	#33-1476	greywacke	Ko	67.7089	162.0087	Eli River
MM-54b-87	#33-1477	greywacke	Ko	67.7089	162.0087	Eli River
MM-55a-87	#33-1478	basaltic dike	MzPzv	67.7442	162.0612	SE Maiyumerak Mtns.
MM-55b-87	#33-1479	basaltic dike	MzPzv	67.7442	162.0612	SE Maiyumerak Mtns.
MM-55c-87	#33-1480	basaltic dike	MzPzv	67.7442	162.0612	SE Maiyumerak Mtns.
MM-55d-87	#33-1481	basaltic dike	MzPzv	67.7442	162.0612	SE Maiyumerak Mtns.
MM-55e-87	#33-1482	basaltic dike	MzPzv	67.7442	162.0612	SE Maiyumerak Mtns.
MM-55f-87	#33-1483	basaltic dike	MzPzv	67.7442	162.0612	SE Maiyumerak Mtns.
MM-55g-87	#33-1484	basaltic dike	MzPzv	67.7442	162.0612	SE Maiyumerak Mtns.
MM-55h-87	#33-1485	basaltic dike	MzPzv	67.7442	162.0612	SE Maiyumerak Mtns.
MM-55i-87	#33-1486	basaltic dike	MzPzv	67.7442	162.0612	SE Maiyumerak Mtns.
MM-55j-87	#33-1487	basaltic dike	MzPzv	67.7442	162.0612	SE Maiyumerak Mtns.
MM-56a-87	#33-1488	basaltic dike	MzPzv	67.7486	162.0666	SE Maiyumerak Mtns.
MM-56b-87	#33-1489	basaltic dike	MzPzv	67.7486	162.0666	SE Maiyumerak Mtns.

Sample #	USPS #	Lithology	Unit	Lat. (°)	Long. (°)	Location
MM-57a-87	#33-1490	pillow basalt	MzPzv	67.7480	162.0657	SE Maiyumerak Mtns.
MM-57b-87	#33-1491	massive basalt	MzPzv	67.7480	162.0657	SE Maiyumerak Mtns.
MM-58a-87	#33-1492	pillow basalt	MzPzv	67.7474	162.0617	SE Maiyumerak Mtns.
MM-58b-87	#33-1493	massive basalt	MzPzv	67.7474	162.0617	SE Maiyumerak Mtns.
MM-58c-87	#33-1494	jasper	MzPzv	67.7474	17.0000	SE Maiyumerak Mtns.
MM-59-87	#33-1495	basalt	MzPzv	67.7468	162.0629	SE Maiyumerak Mtns.
MM-60a-87	#33-1496	bas. pillow-marg	MzPzv	67.7464	162.0628	SE Maiyumerak Mtns.
MM-60b-87	#33-1497	bas. pillow-core	MzPzv	67.7464	162.0628	SE Maiyumerak Mtns.
MM-61-87	#33-1498	massive basalt	MzPzv	67.7458	162.0638	SE Maiyumerak Mtns.
MM-62-87	#33-1499	basalt	MzPzv	67.7361	162.0692	SE Maiyumerak Mtns.
MM-63a-87	#33-1500	basaltic dike	MzPzv	67.7382	162.0640	SE Maiyumerak Mtns.
MM-63b-87	#33-1501	basaltic dike	MzPzv	67.7382	162.0640	SE Maiyumerak Mtns.
MM-63c-87	#33-1502	basaltic dike	MzPzv	67.7382	162.0640	SE Maiyumerak Mtns.
MM-63d-87	#33-1503	basaltic dike	MzPzv	67.7382	162.0640	SE Maiyumerak Mtns.
MM-63e-87	#33-1504	basaltic dike	MzPzv	67.7382	162.0640	SE Maiyumerak Mtns.
MM-63f-87	#33-1505	basaltic dike	MzPzv	67.7382	162.0640	SE Maiyumerak Mtns.
MM-63g-87	#33-1506	basaltic dike	MzPzv	67.7382	162.0640	SE Maiyumerak Mtns.
MM-63h-87	#33-1507	basaltic dike	MzPzv	67.7382	162.0640	SE Maiyumerak Mtns.
MM-63i-87	#33-1508	basaltic dike	MzPzv	67.7382	162.0640	SE Maiyumerak Mtns.
MM-63j-87	#33-1509	pillow basalt	MzPzv	67.7382	162.0640	SE Maiyumerak Mtns.
MM-63k-87	#33-1510	basaltic dike	MzPzv	67.7382	162.0640	SE Maiyumerak Mtns.
MM-63l-87	#33-1511	stream sediment	MzPzv	67.7382	162.0640	SE Maiyumerak Mtns.
MM-64-87	#33-1512	basalt	MzPzv	67.7407	162.0631	SE Maiyumerak Mtns.
MM-65a-87	#33-1513	massive basalt	MzPzv	67.7419	162.0679	SE Maiyumerak Mtns.
MM-65b-87	#33-1514	pillow basalt	MzPzv	67.7419	162.0679	SE Maiyumerak Mtns.
MM-66a-87	#33-1515	basalt	MzPzv	67.7426	162.0503	SE Maiyumerak Mtns.
MM-66b-87	#33-1516	basalt	MzPzv	67.7426	162.0503	SE Maiyumerak Mtns.
MM-66c-87	#33-1517	basalt	MzPzv	67.7426	162.0503	SE Maiyumerak Mtns.
MM-67a-87	#33-1518	pyritic basalt	MzPzv	67.7433	162.0517	SE Maiyumerak Mtns.
MM-67b-87	#33-1519	basalt	MzPzv	67.7433	162.0517	SE Maiyumerak Mtns.
MM-67c-87	#33-1520	basalt	MzPzv	67.7433	162.0517	SE Maiyumerak Mtns.
MM-67d-87	#33-1521	basalt	MzPzv	67.7433	162.0517	SE Maiyumerak Mtns.
MM-67e-87	#33-1522	basalt	MzPzv	67.7433	162.0517	SE Maiyumerak Mtns.
MM-67f-87	#33-1523	basalt	MzPzv	67.7433	162.0517	SE Maiyumerak Mtns.
MM-68-87	#33-1524	basalt	MzPzv	67.7432	162.0538	SE Maiyumerak Mtns.
MM-69-87	#33-1525	breccia float	MzPzv	67.7432	162.0538	SE Maiyumerak Mtns.
MM-70-87	#33-1526	basalt	MzPzv	67.7438	162.0570	SE Maiyumerak Mtns.
MM-71-87	#33-1527	massive basalt	MzPzv	67.7444	162.0598	SE Maiyumerak Mtns.
MM-72a-87	#33-1528	basalt	MzPzv	67.7425	162.0640	SE Maiyumerak Mtns.
MM-72b-87	#33-1529	basalt	MzPzv	67.7425	162.0640	SE Maiyumerak Mtns.
MM-72c-87	#33-1530	basalt	MzPzv	67.7425	162.0640	SE Maiyumerak Mtns.
MM-72d-87	#33-1531	basalt	MzPzv	67.7425	162.0640	SE Maiyumerak Mtns.
MM-73a-87	#33-1532	pillow basalt	MzPzv	67.7471	162.0690	SE Maiyumerak Mtns.
MM-73b-87	#33-1533	massive basalt	MzPzv	67.7471	162.0690	SE Maiyumerak Mtns.
MM-73c-87	#33-1534	basalt	MzPzv	67.7471	162.0690	SE Maiyumerak Mtns.

[illegible]

[illegible]

[illegible]

Sample No.	Lithology	Unit	Lat. (°)	Long. (°)	Location
DH-1-87	red chert	PzPr	65.9392	149.8602	mi. 61.8
DH-2a-87	qtz-bio schist	PzPqs	67.4006	150.0864	mi. 185.9
DH-2b-87	musc. schist	PzPqs	67.4006	150.0864	mi. 185.9
DH-3-87	sandstone	Kpc	69.4033	148.7160	mi. 353
DH-4-87	sandstone	Kn	69.0230	148.8409	mi. 325
DH-5a-87	conglomerate	Kn	68.7401	149.0187	mi. 305.6, Slope Mtn.
DH-5b-87	conglomerate	Kn	68.7401	149.0196	mi. 305.6, Slope Mtn.
DH-6a-87	sandstone	Kfm	68.4923	149.4145	mi. 273, Galbraith Lake
DH-6b-87	conglomerate	Kfm	68.4901	149.4184	mi. 273, Galbraith Lake
DH-6c-87	sandstone	Kfm	68.4884	149.4231	mi. 273, Galbraith Lake
DH-6d-87	sandstone	Kfm	68.4864	149.4292	mi. 273, Galbraith Lake
DH-7-87	phyllite	Dwfv	67.9083	150.0163	mi. 229, East Doonerak
DH-8-87	fol. conglomerate	Mk	67.9141	149.9999	mi. 229, East Doonerak
DH-9-87	phyllite	Dhcp	67.9384	149.7990	mi. 229, East Doonerak
DH-10-87	conglomerate	Dhf	67.9562	149.7857	mi. 230, East Doonerak
DH-11-87	basalt	MzPzv	67.1705	150.3094	West Cathedral Mtn.
DH-12-87	basalt	MzPzv	67.1693	150.3113	West Cathedral Mtn.
DH-13-87	basalt	MzPzv	67.1683	150.3082	West Cathedral Mtn.
DH-14a-87	basalt	MzPzv	67.1676	150.3051	West Cathedral Mtn.
DH-14b-87	basalt	MzPzv	67.1676	150.3051	West Cathedral Mtn.
DH-15a-87	basalt	MzPzv	67.1652	150.3040	West Cathedral Mtn.
DH-15b-87	basalt	MzPzv	67.1652	150.3040	West Cathedral Mtn.
DH-16-87	basalt	MzPzv	67.1650	150.3043	West Cathedral Mtn.
DH-17-87	chert	MzPzc	67.1640	150.3058	West Cathedral Mtn.
DH-18a-87	basalt	MzPzv	67.1637	150.3075	West Cathedral Mtn.
DH-18b-87	basalt	MzPzv	67.1636	150.3073	West Cathedral Mtn.
DH-19-87	basalt	MzPzv	67.1627	150.3088	West Cathedral Mtn.
DH-20-87	basalt	MzPzv	67.1622	150.3094	West Cathedral Mtn.
DH-21-87	basalt	MzPzv	67.1609	150.3100	West Cathedral Mtn.
DH-22a-87	basalt	MzPzv	67.1641	150.2999	West Cathedral Mtn.
DH-22b-87	basalt	MzPzv	67.1641	150.2999	West Cathedral Mtn.
DH-22c-87	basalt	MzPzv	67.1641	150.2999	West Cathedral Mtn.
DH-22d-87	basalt	MzPzv	67.1641	150.2999	West Cathedral Mtn.
DH-23-87	basalt	MzPzv	67.1651	150.3011	West Cathedral Mtn.
DH-24-87	chert	MzPzc	67.1716	150.3096	West Cathedral Mtn.
DH-25a-87	foliated sandstone	PzPqs	67.2235	150.2341	mi. 172.3
DH-25b-87	schist	PzPqs	67.2235	150.2341	mi. 172.3
DH-26a-87	metagabbro	Dg	67.2273	150.2027	mi. 172.6
DH-26b-87	metagabbro	Dg	67.2273	150.2027	mi. 172.6
DH-26c-87	veined metag.	Dg	67.2273	150.2027	mi. 172.6
DH-26d-87	mafic schist	PzPqs	67.2273	150.2027	mi. 172.6
DH-27a-87	eclogite	Pze	67.2837	150.1394	mi. 177
DH-27b-87	eclogite	Pze	67.2837	150.1394	mi. 177
DH-27c-87	eclogite	Pze	67.2837	150.1394	mi. 177
DH-27d-87	eclogite	Pze	67.2837	150.1394	mi. 177
DH-28-87	schist	PzPqs	67.2825	150.1471	mi. 177
DH-29-87	schist	PzPqs	67.3387	150.1333	mi. 181.3

Sample No.	Lithology	Unit	Lat. (°)	Long. (°)	Location
DH-30-87	mafic schist	PzPqs	67.4319	150.0703	mi. 188
DH-31-87	schist	PzPqs	67.3616	150.1142	mi. 182.9
DH-32a-87	grit conglomerate	Ksc	67.0404	150.3044	mi. 157.7
DH-32b-87	conglomerate	Ksc	67.0407	150.3044	mi. 157.7
DH-33-87	cobble conglom.	Kic	66.9926	150.2926	mi. 154.2
DH-34a-87	basalt	MzPzv	66.7670	150.7010	mi. 135.5
DH-34b-87	chert	MzPzc	66.7668	150.7004	mi. 135.5
DH-34c-87	basalt	MzPzv	66.7670	150.7004	mi. 135.5
DH-34d-87	basalt	MzPzv	66.7668	150.7004	mi. 135.5
DH-34e-87	basalt	MzPzv	66.7670	150.7004	mi. 135.5
DH-35-87	andalusite schist	PzPr	66.7526	150.6771	mi. 130.3
DH-36a-87	basalt	QTb	66.0734	150.1606	mi. 75.5
DH-36b-87	basalt	QTb	66.0731	150.1612	mi. 75.5
DH-36c-87	basalt	QTb	66.0734	150.1612	mi. 75.5
DH-36d-87	vesicular basalt	QTb	66.0731	150.1612	mi. 75.5
DH-36e-87	weath. ves. basalt	QTb	66.0731	150.1612	mi. 75.5
DH-37-87	porph bio-granite	Kg	66.3576	150.4581	mi. 98.1
DH-38-87	harzburgite	Ju	66.4178	150.5803	mi. 103.6
DH-39-87	porph bio-granite	Kg	66.4557	150.6477	mi. 107
DH-40-87	porph bio-granite	Kg	66.4890	150.7163	mi. 109
DH-41a-87	basalt	MzPzv	66.4879	150.6835	mi. 109
DH-41b-87	phaneritic basalt	MzPzv	66.4879	150.6835	mi. 109
DH-41c-87	phaneritic basalt	MzPzv	66.4879	150.6835	mi. 109
DH-41d-87	phaneritic basalt	MzPzv	66.4879	150.6835	mi. 109
DH-41e-87	veined basalt	MzPzv	66.4879	150.6835	mi. 109
DH-42a-87	lamprophyre dike	PzPr	66.7396	150.6985	Gobbler's Knob
DH-42b-87	graphitic schist	PzPr	66.7396	150.6985	Gobbler's Knob
DH-42c-87	foliated marble	PzPr	66.7396	150.6985	Gobbler's Knob
DH-43-87	quartzite	MDk	68.2535	149.4097	mi. 256
DH-44-87	conglomerate	Dks	68.2839	149.3691	mi. 258.5
DH-45a-87	conglomerate	Dks	68.3141	149.3490	mi. 260.8
DH-45b-87	sandstone	Dks	68.3141	149.3490	mi. 260.8
DH-45c-87	conglomerate	Dks	68.3141	149.3490	mi. 260.8
DH-46-87	shale	Dhf	68.1557	149.4378	mi. 248.5
DH-47-87	sparse conglom.	Dhf	68.1339	149.4324	mi. 246.8
DH-48-87	wacke	Dhf	68.1683	149.4738	mi. 249.4
DH-49-87	sandstone	Dke	68.3494	149.3250	mi. 263.2
DH-50-87	graywacke	Dke	68.4106	149.3149	mi. 268
DH-51a-87	conglomerate	MDk	68.1298	149.4690	mi. 244.1
DH-51b-87	conglomerate	MDk	68.1318	149.4804	mi. 244.1
DH-51c-87	conglomerate	MDk	68.1270	149.5154	mi. 243.2
DH-51d-87	conglomerate	MDk	68.1204	149.5482	mi. 242.2
DH-52-87	sandstone	Dms	67.1792	150.2730	mi. 169
DH-53a-87	gabbro	Pzg	67.1769	150.2789	mi. 169
DH-53b-87	gabbro	Pzg	67.1775	150.2762	mi. 169
DH-54-87	bio-musc-gneiss	Dgr	67.3576	150.1573	mi. 181.3
DH-55-87	conglomerate	Mk			

Appendix IV

Publications

Abstracts

1985

- Bird, J.M., Wirth, K.R., Harding, D.J., and Shelton, D.H., 1985, Brooks Range ophiolites reconstructed: EOS, Transactions, American Geophysical Union, Fall Meeting, v. 66, no. 46, p. 1129. (Contract No. NAS5-28739)
- Harding, D.J., Wirth, K.R., Bird, J.M., and Shelton, D.H., 1985, Ophiolite emplacement, western Brooks Range, northern Alaska: EOS, Transactions, American Geophysical Union, Fall Meeting, v. 66, no. 46, p. 1129. (Contract No. NAS5-28739)

1986

- Wirth, K.R., Harding, D.J., Blythe, A.E., Bird, J.M., 1986, Brooks Range ophiolite crystallization and emplacement ages from $^{40}\text{Ar}/^{39}\text{Ar}$ data: 99th Annual Meeting of the Geological Society of America, San Antonio, Texas, Abstracts with Programs, v. 18, no. 6, p. 792. (Contract No. NAS5-28739)
- Harding, D.J., Wirth, K.R., Bird, J.M., 1986, Correlation of Angayucham Range and Copter Igneous Sequence basalts in the Brooks Range, Alaska, from Thematic Mapper data: 99th Annual Meeting of the Geological Society of America, San Antonio, Texas, Abstracts with Programs, v. 18, no. 6, p. 792. (Contract No. NAS5-28739)

1987

- Harding, D.J., Wirth, K.R., and Bird, J.M., 1987, Landsat TM studies, Brooks Range, Alaska: Cordilleran Section Meeting of the Geological Society of America, Hilo, Hawaii, Abstracts with Programs, v. 19, n. 6, p. 386. (Contract No. NAS5-28739)
- Wirth, K.R., Harding, D.J., and Bird, J.M., 1987, Basalt geochemistry, Brooks Range, Alaska: Cordilleran Section Meeting of the Geological Society of America, Hilo, Hawaii, Abstracts with Programs, v. 19, n. 6, p. 464. (Contract No. NAS5-28739)

*Technical Memoranda and Reports***1985**

Wirth, K.R., Harding, D.J., Shelton, D.H., and Bird, J.M., 1986, Mafic and ultramafic rocks in the Maiyumerak Mountains, Avan Hills, and at Asik Mountain, Noatak National Preserve, Alaska: 1985 Field Report to the U.S. National Park Service, Kotzebue, Alaska, 60 p., 4 plates. (Contract No. NAS5-28739)

1987

Bird, J.M., Harding, D.J., and Wirth, K.R., 1987, Recognition of hydrothermal metamorphism and alteration of basalts in the Brooks Range, Alaska, using Landsat Thematic Mapper data: in NASA Landsat Workshop, September 1-3, 1987, Laboratory for Terrestrial Physics, National Aeronautics and Space Administration, p. 115-120. (Contract No. NAS5-28739)

Wirth, K.R., Harding, D.J., Blythe, A.E., and Bird, J.M., 1987, Geology along the Noatak River and in western Brooks Range Ophiolites: Noatak National Preserve and Gates of the Arctic National Park, Alaska: 1987 Field Report to the National Park Service, Kotzebue, Alaska, 40 p., 5 plates. (Contract No. NAS5-28739)

*Newsletter Articles***1987**

Bird, J.M. and Harding, D.H., 1987, Landsat Thematic Mapper study of Alaskan ophiolites: The Clears Review, Cornell Laboratory for Environmental Applications of Remote Sensing, Cornell University, New York, v. 3, no. 1, p. 1-2. (Contract No. NAS5-28739)

Meetings Attended

American Association of Petroleum Geologists/Society of Economic and Petroleum Geologists/Society of Economic Geologists, May 22-24, 1985, Anchorage, Alaska. North Slope Seminar and field trip along the Dalton Highway attended by D. Harding.

NASA Landsat Science Investigations Workshop at the Fall Convention of the American Congress on Surveying and Mapping/American Society for Photogrammetry and Remote Sensing, Sept. 8-13, 1985, Indianapolis, Indiana. Attended by J. Bird, D. Harding, K. Wirth, and D. Shelton.

Fall Meeting of the American Geophysical Union, Dec. 9-11, 1985, San Francisco, California. Papers presented by D. Harding and K. Wirth. D. Harding also gave a talk at the U.S. Geological Survey, Menlo Park, on Cornell TM research in the Brooks Range.

NASA Landsat Science Investigations Workshop, Sept. 3-5, 1986, Greenbelt, Maryland. Attended by J. Bird and D. Harding.

Annual Meeting of the Geological Society of America, Nov. 10-13, 1986, San Antonio, Texas. Attended by D. Harding, K. Wirth, and A. Blythe. Papers presented by D. Harding and K. Wirth.

Cordilleran Section Meeting of the Geological Society of America, May 20-22, 1987, Hilo, Hawaii. Attended by K. Wirth and A. Blythe. Papers by D. Harding and K. Wirth presented at special session on the geology of the Brooks Range.

NASA Landsat Science Investigations Workshop, Sept. 1-3, 1987, Santa Barbara, California. Attended by J. Bird and D. Harding.

References Cited

- Abrams, M.J., Conel, J.E., and Lang, H.R., 1985, The Joint NASA/Geosat Test Case Project Final Report, v. 1, part 2..
- Balsley, J.R., Bromery, E.W., and Remington, E.W., 1960, Aeromagnetic map of the Kerby and part of the Grants Pass Quadrangles, Josephine and Curry Counties, Oregon, U.S. Geological Survey, Geophysical Investigations Map, GP-197.
- Barker, F., in press, Seamount origin for basaltic rocks of the Angayucham terrane, central Alaska: *Journal of Geology*.
- Barnard, J.B., Page, N.J., Ziemianski, W.P., Banister, C.A., and Giusso, J.R., 1981, Map showing distribution of serpentine minerals, density, and magnetic susceptibility of rocks from the Kalmiopsis Wilderness, southwestern Oregon, U.S. Geological Survey, Miscellaneous Field Studies Map, MF-1240-B.
- Barnes, D.F., 1970, Gravity and other regional geophysical data from northern Alaska: in Adkison, W.L., and Brosgé, W.P., editors, *Proceedings of the Geological seminar on the North Slope of Alaska, Pacific Section, American Association of Petroleum Geology*, p. I1-I19.
- Barnes, D.F. and TAILLEUR, I.L., 1970, Preliminary interpretation of geophysical data from the lower Noatak River Basin, Alaska: U.S. Geological Survey Open-File Report 70-18.
- Beaumont, C., 1981, Foreland Basins: *Geophysical Journal of the Royal Astronomical Society*, v. 65, p. 291-329.
- Beccaluva, L., Ohnenstetter, D., and Ohnenstetter, M., 1979, Geochemical discrimination between ocean-floor and island-arc tholeiites--application to some ophiolites: *Canadian Journal of Earth Science*, v. 16, p. 1874-1882.
- Bence, A.E., and Albee, A.L., 1968, Empirical correction factors for the electron microanalysis of silicates and oxides: *Journal of Geology*, v. 76, p. 383-402.

- Berger, G.W., and York, D., 1981, Geothermometry from $^{40}\text{Ar}/^{39}\text{Ar}$ dating experiments: *Geochimica et Cosmochimica Acta*, v. 45, p. 795-811.
- Bird, J.M., Harding, D.J., and Wirth, K.R., 1987, Recognition of hydrothermal metamorphism and alteration of basalts in the Brooks Range, Alaska, using Landsat Thematic Mapper data, in NASA Landsat Workshop, September 1-3, 1987: Laboratory for Terrestrial Physics, National Aeronautics and Space Administration, p. 115-120.
- Bird, J.M., Wirth, K.R., Harding, D.J., and Shelton, D.H., 1985, Brooks Range ophiolites reconstructed [abs.]: EOS (American Geophysical Union Transactions), v. 66, no. 46, p. 1129.
- Bird, K.J., 1977, Late Paleozoic carbonates from the south-central Brooks Range, in Blean, K.M., editor, U.S. Geological Survey in Alaska: Accomplishments during 1976, U.S. Geological Survey Circular 751-B.
- Blakely, R.J., and Page, N.J., 1980, Interpretation of aeromagnetic data over the Josephine peridotite, southwestern Oregon, and implications for marine magnetic anomalies [abs.]: EOS (American Geophysical Union Transactions), v. 206, p. 943.
- Boak, J.L., Turner, D.L., Moore, T.E., and Wallace, W.K., 1985, K-Ar ages of allochthonous mafic and ultramafic complexes and their metamorphic aureoles, western Brooks Range: 60th Annual Meeting of American Association of Petroleum Geologists, p. 37.
- Boak, J.M., Turner, D.L., Henry, D.J., Moore, T.E., and Wallace, W.K., 1987, Petrology and K-Ar ages of the Misheguk Igneous Sequence - an allochthonous mafic and ultramafic complex - and its metamorphic aureole, western Brooks Range, Alaska, in TAILLEUR, I. L., and WEIMER, P., editors, Alaska North Slope Geology, v. II: , Bakersfield, California, Pacific Section, Society of Economic Paleontologists and Mineralogists, p. 737-745.
- Box, S.E., and Patton, and W.W., Jr., 1985, Collided intraoceanic volcanic arc in the Yukon-Koyukuk basin, western Alaska: EOS (American Geophysical Union Transactions), v. 66, no. 46, p. 1102.

- Box, S.E., and Patton, and W.W., Jr., in press, Evolution of volcanic arcs during arc-continental collision: comparison of the Neogene Luzon Arc with the Cretaceous Koyukuk arc terrane of western Alaska: *Tectonophysics*.
- Brosgé, W.P., Dutro, J.T., Jr., Mangus, M.D., and Reiser, H.N., 1962, Paleozoic sequence in eastern Brooks Range, Alaska: *American Association of Petroleum Geologists Bulletin*, v. 46, no. 12, p. 2174-2198.
- Carey, S.W., 1958, The tectonic approach to continental drift, in Carey, S.W., editor, *Continental Drift, A Symposium* Tasmania University, p. 177-355.
- Churkin, M., Jr., and Trexler, J.H., Jr., 1980, Circum-arctic plate accretion: isolating part of a Pacific plate to form the nucleus of the Arctic Basin: *Earth and Planetary Science Letters*, v. 48, p. 356-362.
- Curtis, S.M., Ellersieck, I., Mayfield, C.F., and TAILLEUR, I.L., 1982, Reconnaissance geologic map of southwestern Misheguk Mountain quadrangle, Alaska: U.S. Geological Survey Open-File Report OF 82-611, scale 1:63,360.
- Curtis, S.M., Ellersieck, I., Mayfield, C.F., and TAILLEUR, I.L., 1983, Reconnaissance geologic map of DeLong Mountains A-1, B-1, and part of C-1 quadrangles, Alaska: U.S. Geological Survey Open-File Report 83-185, 53 p., scale 1:63,360.
- Curtis, S.M., Ellersieck, I., Mayfield, C.F., and TAILLEUR, I.L., 1984, Reconnaissance geologic map of southwestern Misheguk Mountain quadrangle, Alaska: U.S. Geological Survey Miscellaneous Investigations Map I-1502.
- Dahlstrom, C.D.A., 1969, Balanced cross-sections: *Canadian Journal of Earth Science*, v. 6, p. 743-757.
- Davis, P.A., and Berlin, G.L., Chavez, and P.S., Jr., 1987, Discrimination of altered basaltic rocks in the southwestern United States by analysis of Landsat Thematic Mapper data: *Photogrammetric Engineering and Remote Sensing*, v. 53, p. 45-55.

- Dodson, M.H., 1973, Closure temperature in cooling geochronological and petrological systems: *Contributions to Mineralogy and Petrology*, v. 40, p. 259-274.
- Ellersieck, I., Curtis, S.M., Mayfield, C.F., and TAILLEUR, I.L., 1982, Reconnaissance geologic map of south-central Misheguk Mountain quadrangle, Alaska: U.S. Geological Survey Open-File Report OF 82-612, scale 1:63,000.
- Ellersieck, I., Curtis, S.M., Mayfield, C.F., and TAILLEUR, I.L., 1984, Reconnaissance geologic map of south-central Misheguk Mountain quadrangle, Alaska: U.S. Geological Survey Miscellaneous Investigations Series Map I-1504, scale 1:63,000.
- Ewart, A., 1976, Mineralogy and chemistry of modern orogenic lavas - some statistics and implications: *Earth and Planetary Science Letters*, v. 31, p. 417-432.
- Fisher, D.E., 1972, U/He ages as indicators of excess argon in deep sea basalts: *Earth and Planetary Science Letters*, v. 14, p. 255-258.
- Foland, K.A., 1974, ^{40}Ar diffusion in homogeneous orthoclase and an interpretation of Ar diffusion in k-feldspars: *Geochimica et Cosmochimica Acta*, v. 38, p. 151-166.
- Frank, C.O. and Zimmerman, J., 1982, Petrography of nonultramafic rocks from the Avan Hills complex, De Long Mountains, Alaska: U.S. Geological Survey in Alaska: Accomplishments during 1980, U.S. Geological Survey Circular 844, p. 22-27.
- Funkhouser, J.G., Fisher, D.E., and Bonatti, E., 1968, Excess argon in deep sea rocks: *Earth and Planetary Science Letters*, v. 5, p. 95-100.
- Gottschalk, R.R., and Jr., 1987, Structural and petrologic evolution of the southern Brooks Range near Wiseman, Alaska, Unpublished PhD dissertation: Houston, Texas, Rice University, 263 p.

- Harding, D.J., 1988, Josephine peridotite tectonites: A record of upper-mantle plastic flow, Unpublished PhD dissertation: Ithaca, New York, Cornell University, 334 p.
- Harding, D.J., and Bird, J.M., 1984, Mapping ultramafic rocks using Landsat data: the Josephine peridotite, Oregon and California: Third Thematic Mapper Conference, Remote Sensing for Exploration Geology, Proceedings of the International Symposium on Remote Sensing, April 16-19, 1984, Colorado Springs, Colorado, p. 695-709.
- Harding, D.J., Wirth, K.R., and Bird, J.M., 1986, Correlation of Angayucham Range and Copter Igneous Sequence basalts in the Brooks Range, Alaska, from Thematic Mapper data [abs.]: Geological Society of America Abstracts with Programs, v. 18, no. 6, p. 628.
- Harding, D.J., Wirth, K.R., and Bird, J.M., 1987, Landsat TM studies, Brooks Range, Alaska [abs.]: Geological Society of America Abstracts with Programs, v. 19, no. 6, p. 386-387.
- Harding, D.J., Wirth, K.R., Bird, J.M., and Shelton, D.H., 1985, Ophiolite emplacement, western Brooks Range, northern Alaska [abs.]: EOS (American Geophysical Union Transactions), v. 66, no. 46, p. 1129.
- Harrison, T.M., 1981, Diffusion of ^{40}Ar in hornblende: Contributions to Mineralogy and Petrology, v. 78, p. 329-331.
- Harrison, T.M., Armstrong, R.L., Naeser, C.W., and Harakal, J.E., 1979, Geochronology and thermal history of the Coast Plutonic Complex, near Prince Rupert, B.C.: Canadian Journal of Earth Science, v. 16, p. 400-410.
- Harrison, T.M., Duncan, I.J., and McDougall, I., 1985, Diffusion of ^{40}Ar in biotite: temperature, pressure and compositional effects: Geochimica et Cosmochimica Acta, v. 49, p. 2461-2468.
- Harrison, T.M., and Gerald, J.D., 1986, Exsolution in hornblende and its consequences for $^{40}\text{Ar}/^{39}\text{Ar}$ age spectra and closure temperature: Geochimica et Cosmochimica Acta, v. 50, p. 247-253.

- Harrison, T.M., and McDougall, I., 1980a, Investigations of an intrusive contact, northwest Nelson, New Zealand-I: Thermal, geochronological and isotopic constraints: *Geochimica et Cosmochimica Acta*, v. 44, p. 1985-2004.
- Hitzman, M.W., Proffett, J.M., Jr, Schmidt, J.M., and Smith, T.E., 1986, Geology and mineralization of the Ambler District, northwestern Alaska: *Economic Geology*, v. 81, p. 1592-1618.
- Hitzman, M.W., and Smith, T.E., Proffett, and J.M., Jr., 1982, Bedrock geology of the Ambler district, southwestern Brooks Range, Alaska: Alaska Division of Geological and Geophysical Surveys, v. Geologic Report 75, p. scale 1:125,000.
- Humphris, S.E., and Thompson, G., 1978, Hydrothermal alteration of oceanic basalts by seawater: *Geochimica et Cosmochimica Acta*, v. 42, p. 107-126.
- Irvine, T.N., and Baragar, W.R.A., 1971, A guide to the classification of the common volcanic rocks: *Canadian Journal of Earth Science*, v. 8, p. 523-548.
- Jones, D.L., Silberling, N.J., Coney, P.J., and Plafker, G., 1984, in Silberling, N.J., and Jones, D.L., editors, Lithotectonic terrane map of Alaska (west of the 141st Meridian), Lithotectonic terrane maps of the North American Cordillera, U.S. Geological Survey Open-File Report 84-523, p. A1-A12.
- Jordan, T.E., 1981, Thrust loads and foreland basin evolution, Cretaceous, western United States: *American Association of Petroleum Geologists Bulletin*, v. 65, no. 12, p. 2506-2520.
- Kay, R.W., 1984, Elemental abundances relevant to identification of magma sources: *Philosophical Transactions of the Royal Society of London*, v. A 310, p. 535-547.
- Le Maitre, R.W., 1984, A proposal by the IUGS Subcommittee on the Systematics of Igneous Rocks for a chemical classification of volcanic rocks based on the total-alkali silica (TAS) diagram: *Australian Journal of Earth Sciences*, v. 31, p. 243-255.

- MacDonald, G.A., and Katsura, T., 1964, Chemical composition of Hawaiian lavas: *Journal of Petrology*, v. 5, p. 82-133.
- Masuda, A., Nakamura, N., and Tanaka, T., 1973, Fine structures of mutually normalized rare-earth patterns of chondrites: *Geochimica et Cosmochimica Acta*, v. 37, p. 239-248.
- Mayfield, C.F., Curtis, S.M., Ellersieck, I., and TAILLEUR, I.L., 1982, Reconnaissance geologic map of the southeastern part of the Misheguk Mountain Quadrangle, Alaska: U.S. Geological Survey Miscellaneous Investigations Series Map I-1503, scale 1:63,360.
- Mayfield, C.F., Curtis, S.M., Ellersieck, I., and TAILLEUR, I.L., 1983, Reconnaissance geologic map of the De Long Mountains A3, B3, and parts of A4, B4 Quadrangles, Alaska: U.S. Geological Survey Open File Report OF 83-183, 59 p., scale 1:63,360.
- Mayfield, C.F., Ellersieck, I., and TAILLEUR, I.L., 1987, Reconnaissance geologic map of the Noatak C5, D5, D6, and D7 Quadrangles, Alaska: U.S. Geological Survey Miscellaneous Investigations Map I-1814.
- Mayfield, C.F., TAILLEUR, I.L., and Ellersieck, I., 1983, Stratigraphy, structure, and palinspastic synthesis of the western Brooks Range, northwestern Alaska: U.S. Geological Survey Open File Report OF 83-779, 58 p.
- Miyashiro, A., 1974, Volcanic rock series in island arcs and active continental margins: *American Journal of Science*, v. 274, p. 321-355.
- Mullen, E.D., 1983, $MnO/TiO_2/P_2O_5$: a minor element discriminant for basaltic rocks of oceanic environments and its implications for petrogenesis: *Earth and Planetary Science Letters*, v. 62, p. 53-62.
- Nelson, S.W., and Nelson, W.H., 1982, Geology of the Siniktanneyak Mountain ophiolite, Howard Pass quadrangle, Alaska: U.S. Geological Survey Miscellaneous Field Studies Map MF-1441, scale 1:63,000.

- Nelson, S.W., Nockleberg, W.J., Miller-Hoare, M., and Mullen, M.W., 1979, Siniktanneyak Mountain ophiolite, in Johnson, K.M., and Williams, J.R., editors, U.S. Geological Survey in Alaska: Accomplishments during 1979, U.S. Geological Survey Circular 804-B, p. B14-B16.
- Noble, C.S., and Naughton, J.J., 1968, Deep-ocean basalts--inert gas content and uncertainties in age dating: *Science*, v. 162, p. 265-267.
- Oldow, J.S., Ave Lallemand, H.G., Julian, F.E., and Seidensticker, C.M., 1987, Ellesmerian(?) and Brookian deformation in the Franklin Mountains, northeastern Brooks Range, Alaska, and its bearing on the origin of the Canada Basin: *Geology*, v. 15, p. 37-41.
- Page, N.J., Cannon, J.K., Foose, M.P., Lipinn, B., Moring, B.C., Nicholson, M.G., Sawlin, M.G., Till, A., and Ziemianski, W.P., 1981, Geologic map of the Kalmiopsis Wilderness area, Oregon, U.S. Geological Survey, Miscellaneous Field Studies Map, MF-1240-A.
- Pallister, J.S., 1985, Pillow basalts from the Angayucham Range, Alaska: chemistry and tectonic implications [abs.]: EOS (American Geophysical Union Transactions), v. 66, no. 46, p. 1102.
- Pallister, J.S., and Budahn, J.R., in press, Pillow basalts of the Angayucham terrane: oceanic-plateau and island crust accreted to the Brooks Range: *Journal of Geophysical Research*.
- Parrish, R.R., 1983, Cenozoic thermal evolution and tectonics of the Coast Mountains of British Columbia 1. Fission track dating, apparent uplift rates, and patterns of uplift: *Tectonics*, v. 2, p. 601-631.
- Patton, W.W., and Jr., 1973, Reconnaissance geology of the northern Yukon-Koyukuk Province, Alaska: U.S. Geological Survey Professional Paper 774-A, p. A1-A17.
- Patton, W.W., Jr., TAILLEUR, I.L., Brosgé, W.P., and Lanphere, M.A., 1977, Preliminary report on the ophiolites of northern and western Alaska, in Coleman, R. G., and Irwin, W. P., editors, North American Ophiolites, Oregon Department Geology and Mining Industry Bulletin 95, p. 51-57.

- Pearce, J.A., 1982, Trace element characteristics of lavas from destructive plate boundaries, in Thorpe, R.S., editor, *Andesites* John Wiley and Sons, p. 525-548.
- Pearce, J.A., 1983, Role of sub-continental lithosphere in magma genesis at active continental margins, in Hawkesworth, C.J., and Norry, M.J., editors, *Continental Basalts and Mantle Xenoliths*, Nantwich, U.K., Shiva Publishers Ltd., p. 230-272.
- Pearce, J.A., and Cann, J.R., 1973, Tectonic setting of basic volcanic rocks determined using trace element analysis: *Earth and Planetary Science Letters*, v. 19, p. 290-300.
- Pearce, J.A., Lippard, S.J., and Roberts, S., 1984, Characteristics and tectonic significance of supra-subduction zone ophiolites, in Kokelaar, B.P., and Howells, M.F., editors, *Marginal Basin Geology*, Geological Society of London Special Publication, , Oxford, Blackwell Scientific Publications, p. 77-94.
- Reiser, H.N., Lanphere, M.A., and Brosgé, W.P., 1965, Jurassic age of a mafic igneous complex, Christian quadrangle, Alaska, Geological Survey Research 1965, U.S. Geological Survey Professional paper 525-C, p. C68-C71.
- Roeder, D., and Mull, C.G., 1978, Tectonics of the Brooks Range ophiolites, Alaska: *American Association of Petroleum Geologists Bulletin*, v. 62, p. 1696-1713.
- Rothery, D.A., and Hall, W., 1987, Improved discrimination of rock units using Landsat Thematic Mapper imagery of the Oman ophiolite: *Journal of the Geological Society of London*, v. 144, p. 587-597.
- Siegel, B.S. and Goetz, A.F.H., 1977, Effect of vegetation on rocks and soil type discrimination: *Photogrammetric Engineering and Remote Sensing*, v. 43, p. 191-196.

- Serri, G., 1981, The petrochemistry of ophiolite gabbroic complexes: A key for the classification of ophiolite into low-Ti and high-Ti types: *Earth and Planetary Science Letters*, v. 52, p. 203-212.
- Steiger, R.H., and Jäger, E., 1977, Subcommittee on geochronology: convention on the use of decay constants in geo- and cosmochemistry: *Earth and Planetary Science Letters*, v. 36, p. 359-362.
- Stern, C., and Elthon, D., 1979, Vertical variations in the effects of hydrothermal metamorphism in Chilean ophiolites: their implications for ocean floor metamorphism: *Tectonophysics*, v. 55, p. 179-213.
- Suppe, J., 1983, Geometry and kinematics of fault-bend folding: *American Journal of Science*, v. 283, p. 684-721.
- Suppe, J., and Medwedeff, D., 1984, Fault-propagation folding [abs.]: *Geological Society of America Abstracts with Programs*.
- Tailleur, I.L., 1973, Possible mantle-derived rocks in western Brooks Range, Geological Survey Research 1973; U.S. Geological Survey Professional Paper 850, p. 64-65.
- Tailleur, I.L., and Brosgé, W.P., 1970, Tectonic history of northern Alaska, in Adkison, W.L., and Brosgé, W.P., editors, *Proceedings of the Geological Seminar on the North Slope of Alaska*: American Association of Petroleum Geologists Pacific Section, p. E1-E19.
- Tarney, J., Saunders, A.D., Matthey, D.P., Wood, D.A., and Marsh, N.G., 1981, Geochemical aspects of back-arc spreading in the Scotia Sea and western Pacific: *Philosophic Transactions of the Royal Society of London*, v. A 300, p. 263-285.
- Telford, W.M., Geldart, L.P., Sheriff, R.E., and Keys, D.A., 1976, *Applied Geophysics*: Cambridge University Press, Cambridge, 860 p.

- Thompson, R.N., Morrison, M.A., Matthey, D.P., Dicken, A.P., and Moorbath, S., 1980, An assessment of the Th-Hf-Ta diagram as a discriminant for tectonomagmatic classifications in the detection of crustal contamination of magmas: *Earth and Planetary Science Letters*, v. 50, p. 1-10.
- Turner, D.L., 1984, Tectonic implications of widespread Cretaceous overprinting of K-Ar ages in Alaskan metamorphic terranes [abs.]: *Geological Society of America Abstracts with Programs*, v. 16, p. 338.
- Turner, D.L., Forbes, R.B., and Dillon, J.T., 1979, K-Ar geochronology of the southwestern Brooks Range: *Canadian Journal of Earth Science*, v. 16, p. 1789-1804.
- Vallance, T.G., 1974, Spilitic degradation of a tholeiitic basalt: *Journal of Petrology*, v. 15, p. 79-96.
- Wirth, K.R., Harding, D.J., and Bird, J.M., 1987, Basalt geochemistry, Brooks Range, Alaska: *Geological Society of America Abstracts with Programs*, v. 19, no. 6, p. 464.
- Wirth, K.R., Harding, D.J., Blythe, A.E., and Bird, J.M., 1986, Brooks Range ophiolite crystallization and emplacement ages from $^{40}\text{Ar}/^{39}\text{Ar}$ data [abs.]: *Geological Society of America Abstracts with Programs*, v. 18, no. 6, p. 792.
- Wood, D.A., 1980, The application of a Th-Hf-Ta diagram to problems of tectonomagmatic classification and to establish the nature of crustal contamination of basaltic lavas of the British Tertiary Volcanic Province: *Earth and Planetary Science Letters*, v. 50, p. 11-30.
- Wood, D.A., Joron, J.-L., and Treuil, M., 1979, A re-appraisal of the use of trace elements to classify and discriminate between magma series erupted in different tectonic settings: *Earth and Planetary Science Letters*, v. 45, p. 326-336.
- York, D., 1969, Least squares fitting of a straight line with correlated errors: *Earth and Planetary Science Letters*, v. 5, p. 320-324.

Zeitler, P.K., 1985, Cooling history of the NW Himalaya, Pakistan: *Tectonics*, v. 4, no. 1, p. 127-151.

Zimmerman, J., and Frank, C.O., 1984, Possible obduction-related metamorphic rocks at the base of the ultramafic zone, Avan Hills complex, De Long Mountains, in Coonrad, W.L., editor, *The U.S. Geological Survey in Alaska: Accomplishments during 1980*, U.S. Geological Survey Circular 844, p. 27-28.